INVESTIGATION OF DIMENSIONAL ACCURACY ON SLANT TYPE TAPER CUTTING BY WEDM OF Ni-BASED SUPERALLOY FOR HIGH-TEMPERATURE APPLICATIONS

Thesis

Submitted in partial fulfillment of the requirements for the degree of

DOCTOR OF PHILOSOPHY

By

MANOJ.I.V

(177117/177ME006)

DEPARTMENT OF MECHANICAL ENGINEERING

NATIONAL INSTITUTE OF TECHNOLOGY KARNATAKA,

SURATHKAL, MANGALORE - 575025

JULY, 2022

INVESTIGATION OF DIMENSIONAL ACCURACY ON SLANT TYPE TAPER CUTTING BY WEDM OF Ni-BASED SUPERALLOY FOR HIGH-TEMPERATURE APPLICATIONS

Thesis

Submitted in partial fulfillment of the requirements for the degree of

DOCTOR OF PHILOSOPHY

By

MANOJ.I.V

(177117/177ME006)

Under the guidance of

Dr. NARENDRANATH S

Professor

DEPARTMENT OF MECHANICAL ENGINEERING

NATIONAL INSTITUTE OF TECHNOLOGY KARNATAKA, SURATHKAL,

MANGALORE - 575025

JULY – 2022

DECLARATION

I hereby declare that the Research Thesis entitled **"Investigation of Dimensional Accuracy on Slant Type Taper Cutting by WEDM of Ni-Based Superalloy for High-Temperature Applications"** which is being submitted to the **National Institute of Technology Karnataka, Surathkal** in partial fulfillment of the requirements for the award of the degree of **Doctor of Philosophy** in **Mechanical Engineering** is a *bonafide report of the research work carried out by me*. The material contained in this Research Thesis has not been submitted to any other Universities or Institutes for the award of any degree.

MANOJ.I.V

Register Number: **177117/177ME006**

Department of Mechanical Engineering

Place: NITK-Surathkal

Date: 25/7/2022

CERTIFICATE

This is to certify that the Research Thesis entitled **"Investigation of Dimensional Accuracy on Slant Type Taper Cutting by WEDM of Ni-Based Superalloy for High-Temperature Applications"** submitted by **Mr. Manoj.I.V (Register Number: 177117/177ME006)** as the record of the research work carried out by him, *is accepted as the Research Thesis submission* in partial fulfillment of the requirements for the award of the degree of **Doctor of Philosophy.**

Research Guide(s)

Dr. Narendranath S.

Professor

Department of Mechanical Engg.

Chairman - DRPC

Date: 25·7·2022

ACKNOWLEDGEMENTS

ॐ नमः शिवाय

Dedicated to …

My Beloved Parents who have helped, supported and encouraged me throughout my life.

My teachers who have guided, shaped and inspired me throughout my career.

My friends who always encouraged me with their positive thoughts.

ABSTRACT

The demand for the usage of superalloys has increased due to their good mechanical properties in extreme atmospheric conditions. The aerospace industry uses about 60-70% of superalloys. They have an austenitic face-centred cubic having advantages such as better mechanical properties, higher modulus, higher solubility of alloying elements and systems of gliding plane. They can be classified as nickel, iron and cobalt-base superalloys. As nickel-based superalloys pose a higher fraction of melting temperature, therefore more favourable than cobalt-based and iron-nickel-based superalloys.

Nickel-based superalloys have mechanical properties like good surface stability, high-temperature mechanical strength, resistance to corrosion or oxidation, and resistance to thermal creep deformation. These alloys can be used over a wide temperature having an operational range from -217°C to 700°C. Nickel-based superalloys can be strengthened through solid solution and precipitation. They can be used in different application as they have excellent fabricability, high-temperature corrosion resistance, and weldability but lower mechanical strength.

Hastelloy-X is a nickel-chromium-iron-molybdenum alloy named after 'Haynes Stellite Alloy'. As the Matrix stiffening is delivered by the molybdenum content results in high strength in a solid-solution alloy having good fabrication characteristics. It is one of the nickel-based superalloys which has applications in afterburners, gas turbine engines components, tailpipes, cabin heaters and flame holders etc. Nickel-based superalloys pose a major challenge during machining due to low thermal diffusivity and high-temperature strength. The conventional process leads to many surface defects like tearing, feed mark, surface crack, burr and tool defects like flank wear, creator wear, edge chipping, welding and adhesion of coated surface.

Non-conventional machining techniques are the alternate methods used for machining such hard to cut materials with minimal surface and tool damage. From the literature, it was noted that nickel-based alloys can also be machined Laser Beam Machining, Abrasive Jet Machining and Electric Discharge Machining. Among different non-conventional machining process wire electric discharge machining (WEDM) was found to be the most

precise and high-quality finishing. Although wire electric discharge machining is most accurate there will be minute errors during machining due to the complexity of the component. These errors are caused due to the flexible nature of the wire (electrode). The complexity of the component also demands accuracy in tapering operation which is achieved by making the wire slant or taper to the required angle through the movement of guideways during machining. This method has many drawbacks like insufficient flushing, wire bending, guide wear, wire break, angular inaccurate, surface damage.

In the literature, it was seen that to achieve tapering was performed using convention tapering, change in wire circulation mechanisms and use hard materials as wire guides which avoids guide wear. For the present studies, an economic aluminium slant type fixture was employed to achieve tapering which is eaiser to manufacture. It was developed and fabricated to achieve tapering eliminating the major disadvantage i.e. bending of wire during conventional tapering in WEDM. This fixture provided the required angle to the workpiece (Hastelloy-X) where the required taper component can be machined. The cutting speed parameters like pulse on time, servo voltage, wire feed and servo feed were fixed based on the different performance parameters like cutting speed, surface roughness, surface crack density, angular error and kerf width for different taper angles (0°, 15°, 30°, 45° and 60°). As most of the application have taper angle ranging between 0-30° for different profiles i.e. triangular, square and cicular profiles were considered for three different angles such as 0°,15° and 30°. Further, the profiling parameters i.e. wire guide distance (WGD), corner dwell time (CDT), wire offset (WO) and cutting speed override (CSO) were explored in the machining of triangular, square and circular profiles at different taper angles (0°,15° and 30°). Output response parameters such as profiling speed, surface roughness, profile area, angular error, corner errors, recast layer thickness and microhardness were studied in detail to explore the effects of profiling parameters on triangular, square and cicular profiles and also the effect of taper angles on triangular, square and cicular profiles was also analyzed. Artificial neural network (ANN) and adaptive neuro-fuzzy interference (ANFIS) system were used to predict the profiling speed

and surface roughness. Finally, different responses during taper profiling of Hastelloy-X using WEDM were explored and discussed in detail.

CONTENTS

LIST OF FIGURES

x

LIST OF TABLES

LIST OF ABBREVIATIONS AND SYMBOLS

Abbreviation	Description
ANFIS	Adaptive Neuro-Fuzzy Inference System
ANN	Artificial Neural Network
ANOVA	Analysis of variance
AWJM	Abrasive water jet machining
CDT	Corner Dwell Time (s)
CE	Corner Error (μm^2)
CMM	Co-ordinate Measuring Machine
CS	Cutting Speed (mm/min)
CSO	Cutting Speed Override (%)
DOE	Design of Experiments
ECM	Electro chemical machining
EDM	electric discharge machining
Hv	Microhardness
LBM	Laser beam machining
MSD	Mean Square Deviation
PS	Profiling speed (mm/min)
SCD	Surface Crack Density ($\mu m/\mu m^2$)
SEM	Scanning Electron Microscope
SF	Servo Feed (mm/min)
SR	Surface roughness (μm)
SV	Servo Voltage (V)
Toff	Pulse off time (μs)
Ton	Pulse on time (μs)
WEDM	Wire electric discharge machining
WF	Wire Feed (m/min)
WGD	Wire Guide Distance (mm)
WO	Wire Offset (μm)

λ	Taper angle
SSE	sum of squares of error
SST	sum of squares of treatment
MST	mean square of treatment
MSE	mean square of error

CHAPTER 1

INTRODUCTION

1.1 BACKGROUND

Nowadays increase in the application has demanded the usage of conventional alloys to superalloys due to their good mechanical properties at extreme atmospheric conditions. These superalloys are used in many areas such as aerospace, chemical, marine, nuclear etc. These applications demand the machining of such suitable superalloys to the required shape and specifications. Machining is a subtractive manufacturing process that removes the excess material through various methods and finally converting the raw material into an acceptable finished product. Achieving accuracy with an excellent surface finish during the machining of these alloys is the major challenge faced by many manufacturers.

1.2 SUPERALLOYS

Superalloys are heat resistant alloys that are used more than 0.7 times the absolute melting point. In general, they have the operating temperatures surpasses 1050°C with occasional working temperature up to 1200 °C. Based on the composition, superalloys are classified mainly into Cobalt-based, Iron-based and Nickel based alloys. It can also be further sub-classified into the cast, wrought, and alloys processed by powder metallurgy. As a result, superalloys have vast applications in high-temperature areas because of their properties like good surface stability, high-temperature mechanical strength, resistance to corrosion or oxidation, and resistance to thermal creep deformation (Benjamin, 1970; Nowotnik, 2016). These superalloys are segregated mainly into three alloy systems as shown in fig.1.1 (Choudhury et al., 1998).

The primary applications of these superalloys are in: (i) aircraft gas turbines, e.g. disks, combustion chambers, blades, vanes, etc.; (ii) steam turbine power plants, e.g. bolts, stack gas reheaters blades; (iii) reciprocating engines, e.g. super and turbocharger, exhaust

valves, etc.; (iv) metal processing, e.g. dies and tooling; (v) pharmaceutical applications, e.g. dentistry uses, prosthetic devices; (vi) aeronautical and aerospace components; (vii) heat-treating furnace components; (viii) nuclear power generating stations; (ix) petrochemical and chemical industries; (x) pollution control equipment; and (xi) liquefaction and coal gasification systems. (Mali and Unune, 2017; Mouritz, 2012)

1.3 NICKEL BASED SUPERALLOYS

As nickel is a versatile element and is easily soluble with various other metals, hence many different alloys can be formed. Nickel superalloys contain 50% of nickel due to which superalloys have properties like relatively higher strength at elevated temperatures and high hardness. In the present investigation, the Hastelloy-X was used as highlighted in fig.1.1.
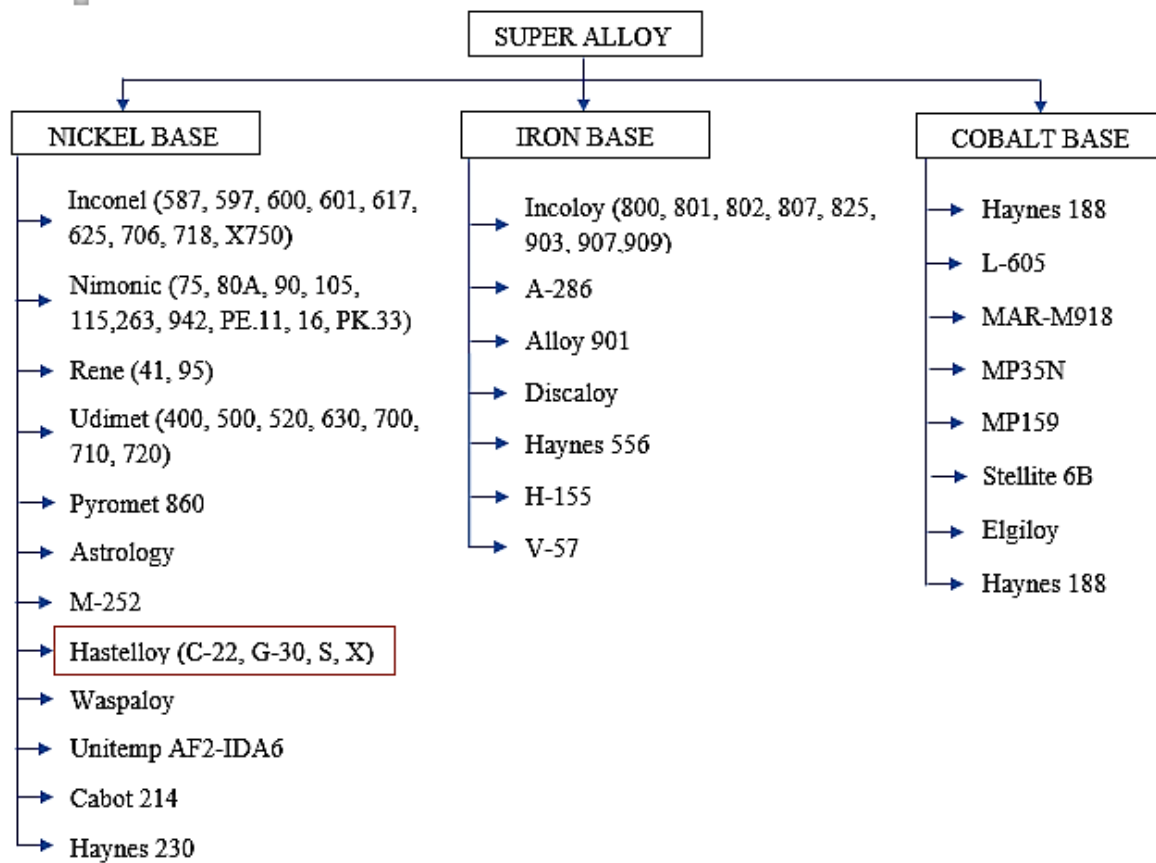
Figure 1.1. Classification of superalloys (Choudhury et al., 1998).

2

Fig.1.2 shows the different type of materials and their specific strength at different temperatures that are used in aerospace. The nickel alloys can be observed at relative higher operating ranges and can withstand up to 10000C. These properties were observed in the presence of many alloying elements. Different alloying components like cobalt, tungsten, chromium, molybdenum, titanium, iron, vanadium and aluminium etc. are all solid-solution strengtheners present in nickel superalloys. These elements not only improve the mechanical properties but also enhances other properties of the nickel-based superalloy as shown in table 1.1. The high-temperature strength and other superior properties oppose a major challenge in the machining of nickel alloys.
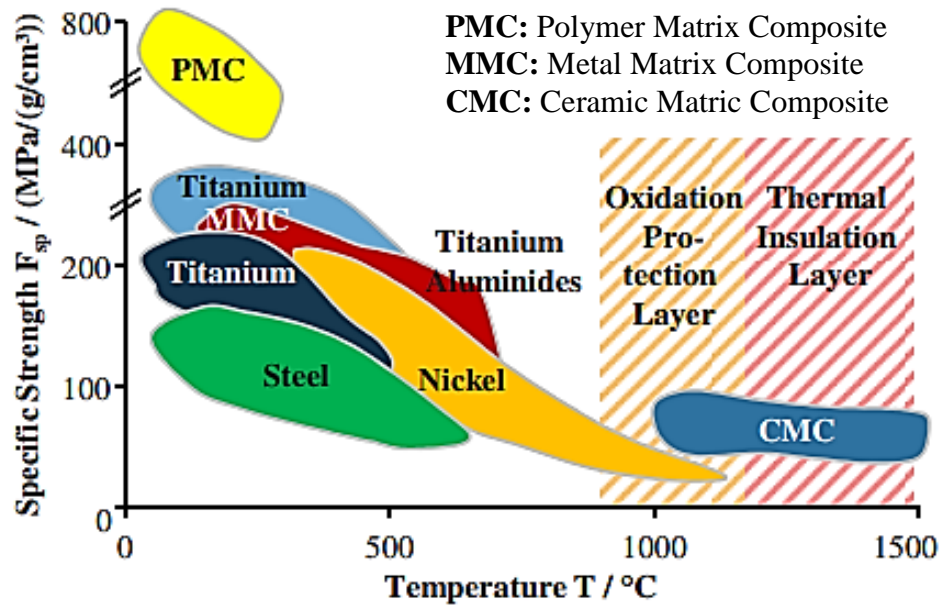
Figure 1.2. Specific strength variation with temperature potential of materials (Klocke et al., 2013)

Table 1.1 Effect of different alloying elements on nickel-based alloys (Davis, 2000).

Sl. No.	Alloying Element	Enhanced Properties
1	Aluminium, Titanium and Niobium	Oxidation resistance, Creep rupture properties.
2	Iron	Improves the economy of alloy but decrease their oxidation resistance.

3	Cobalt	Slight solid solution strengthening and reduces the solubility of aluminium and titanium.
4	Molybdenum, Tungsten and Tantalum	Solid-solution strengthening at high temperature.
5	Boron and Zirconium	Creep strength and ductility.
6	Carbon	Creep strength due to the formation of carbides.
7	Calcium, Magnesium and Yttrium	Improve workability, oxidation resistance, etc.
8	Hafnium	Ductility and strength at low and intermediate temperatures.
9	Copper	Resistance to reducing acids and salts
10	Silicon	Oxidation strength
11	Sulphur	Improves machinability

1.4 APPLICATIONS OF NICKEL BASED ALLOYS

Because of its exceptional and superior properties like high-temperature strength, low creep, non-magnetic, corrosion and oxidation resistance, and high fatigue strength etc. These superalloys are extensively employed in the manufacturing of different components and structures for aerospace, chemical, marine, nuclear power generation and process industries. Table 1.2 shows different applications of nickel-based alloys in various fields of engineering.

Table 1.2 General applications of nickel-based alloys (Bochenek and Basista, 2015; Heilmaier et al., 2009; Oriňáková et al., 2006; Davis, 2000)

Nickel-Based Alloys	Applications
Inconel	Gas turbine blades, seals, combustors, nuclear steam generators tubes, jet engine fan containment applications.
Nimonic	Gas turbine components (discs and blades), Steam turbine values, bolts, nuclear boiler tube supports, engine cylinder valves, die-casting inserts and cores.
Rene	Aircraft turbine blades, hot gas path components of gas turbines
Udimet	Warm segments of aircraft and land-based gas turbine, industrial furnace applications, for instance, liner/muffles in

	higher temperature kilns, bearing races, ball bearings, springs and heart valve, etc.
Hastelloy	Piping industries, land-based and marine gas turbines, power generation equipment, aircraft and space shuttle engines, and submarines.
Waspaloy	Gas turbine components like disks, compressor parts, shafts and cases.
Incoloy	Nuclear steam generators tubes and chemical industries.
Haynes	Gas turbine, applications, like advanced ultra-supercritical steam, supercritical CO_2.

1.5 HASTELLOY AND ITS APPLICATIONS

Haynes International, Inc., company filed a patent for nickel-based alloy called Hastelloy in 1922. The name Hastelloy derived from the first letters of the words Haynes Stellite Alloy. Soon after the invention, the company introduced twelve high-temperature corrosion resistance alloys. The aircraft gas turbine engine market has traditionally been the major user of HASTELLOY® and HAYNES® High-temperature alloys. There are different grades in Hastelloy namely B-3, C-4, C-22, C-22HS, C-276, C-2000, G-30 etc. (Haynes In.). Hastelloy-X or Alloy-X alloy can be called nickel-chromium-iron-molybdenum alloy. This was invented by Howard R. Spendelow, Jr and Walter Crafts. This is a wrought alloy that possesses high mechanical properties and the first commercial-scale production was in 1955. It has different commercial names called Nickelvac® HX, Microfer® 4722, Altemp® HX, Inconel® HX. Inconel HX®. This alloy is wide use in afterburners, gas turbine engine components, tailpipes, cabin heaters and flame holders as highlighted in fig.1.3. The properties and composition of Hastelloy-X are as shown in table 1.3 and table 1.4 respectively (Ott et al., 2014; Haynes In.). Machining is the most important manufacturing process that shapes the raw material into the component of the intended design. These alloys undergo hardening rapidly and during machining built-up edge forming on cutting tool surfaces. They also generate high heat levels at the interface due to low thermal diffusivity which poses a challenge during machining.
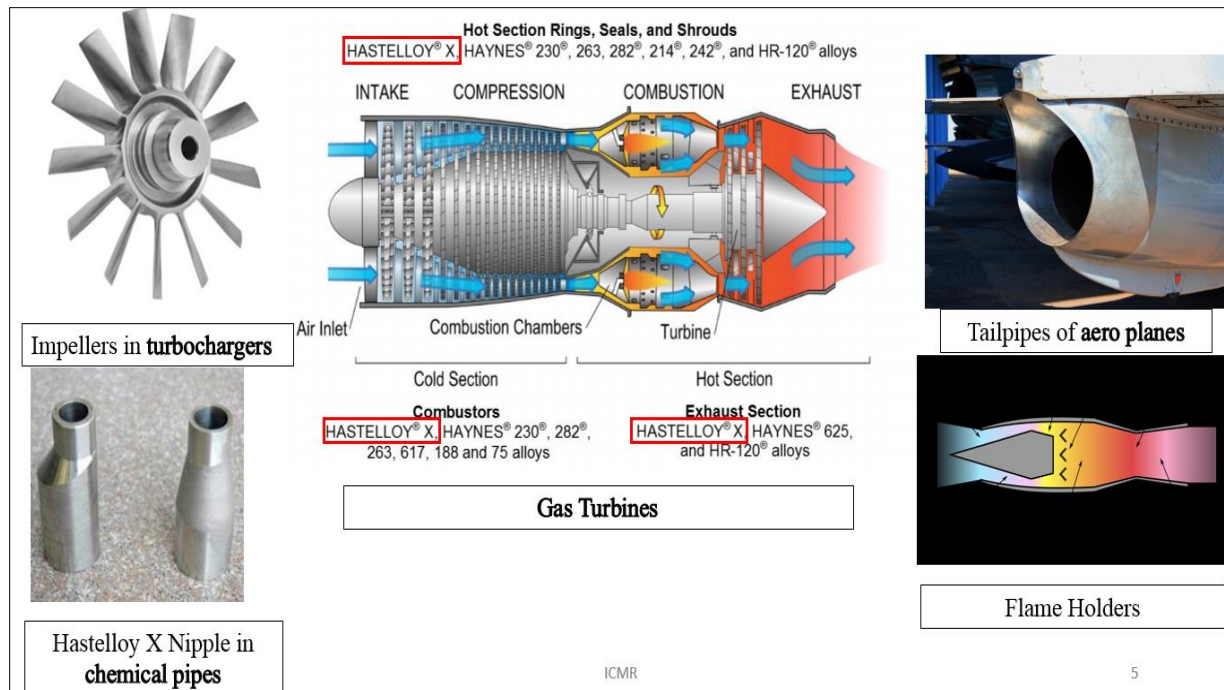
Figure 1.3 Application of Hastelloy-X (Griffiths, 2019; Ott et al., 2014; Haynes In.).

Table 1.3 Properties of Hastelloy-X (Haynes In.,)

Sl. no.	Properties	Values
1	Density	8.22 g/cm^3
2	Melting Range	1260 - 1355°C
3	Thermal conductivity	10 W/m.K
4	Yield strength (0.2% offset)	340 Mpa
5	Ultimate Tensile Strength	760 MPa
6	Elongation	48.9%

Table 1.4 Composition of Hastelloy-X (Haynes In.,)

E	C	Mn	P	S	Si	Cr	Ni	Mo	Fe	Ti	Al	Co	B
P	.05 - .15	1.00 max	.040 max	.030 max	1.00 max	20.5 - 23	38-42	8-10	17 - 20	.15 max	.50 max	.50- 2.5	.01 max

*E- Element, P- Percentage

6

1.6 MACHINING OF SUPER ALLOYS

There are many types of machining operations such as turning, drilling, milling, shaping, planing, boring, broaching and sawing. However tapering is the most popular machining operation, where there is a gradual reduction in diameter can be achieved on a workpiece. From fig. 1.3 we can notice many complex tapering and intricate structures where different operations are required to manufacture such a precision components.

Different unfavourable properties like affinity to react with the tool materials and low thermal diffusivity makes the machining process more difficult and challenging. This is observed due to the existence of nickel in nickel superalloys (Ezugwu et al., 1999, 2005). The applications of nickel-based alloys like Hastelloy, Inconel, Rene, nimonic etc. triggers the manufacturing and machining process to meet the market demand. Many researchers and manufacturers have explored machining such alloys in both conventional and non-conventional methods.

1.6.1 Conventional Machining Process

In conventional machining, the material is removed from the workpiece with the aid of a tool by the principle of shear deformation and controlled fracture. Machining of nickel-based superalloys using the conventional process was explored by many researchers (Liu et al., 2015; Sharman et al., 2004, 2008; Razak et al., 2014; Zhu et al., 2013; Akhtar et al., 2014). The nickel-based superalloys have exhibited superior properties at elevated temperature, low thermal diffusivity and work hardening effect during machining. This leads to an increase in temperature in the machining zone. Due to the higher temperature in the machining zone, it was observed that there were many surface defects on the workpieces and the tool was prone to damages. These may lead to catastrophic failure of the component. Some of the surface and tool defects are highlighted in the following section.

1.6.1.1 Surface and Tool Defects

Different researchers have machined various nickel-based alloys, to study the surface defects of the machined workpiece and the machining tool. (Thakur and Gangopadhyay, 2016; Ezilarasan et al., 2013; Axinte et al., 2004; Thakur et al., 2014, 2015). The surface defects like tearing, smearing, surface cracks, chatter marks etc. and damages on the tool like flank wear, edge chipping, creator wear etc. for the different process is as shown in fig.1.4. As the degree of tool and workpiece damage during conventional machining was found to be high, it forced the researchers to look towards non-conventional machining. Meanwhile, it is difficult to produce intricate shapes with tight tolerances in conventional machining.
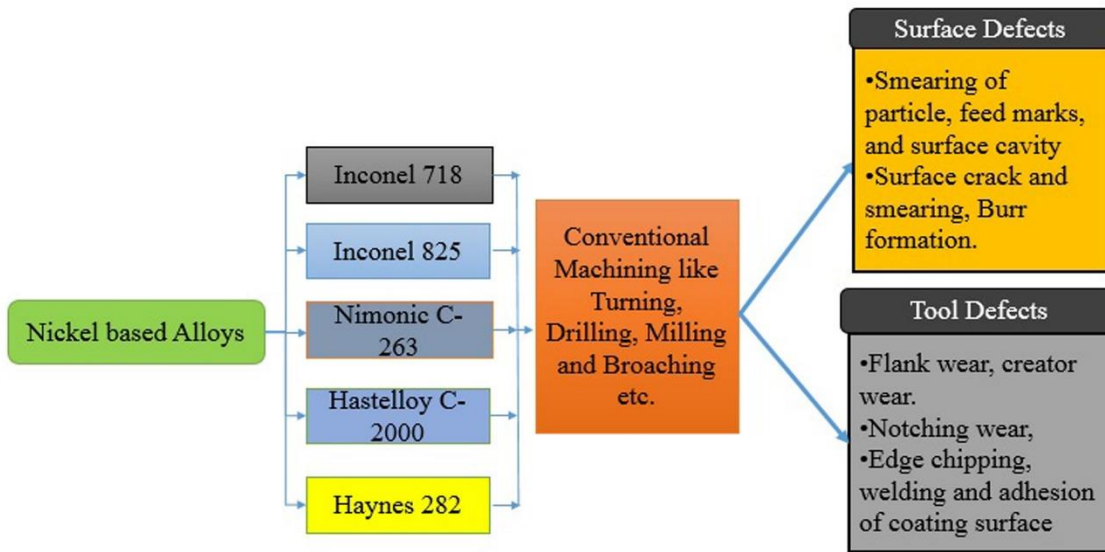
Figure 1.4 Different defects observed in conventional machining of nickel alloys

1.6.2 Non-Conventional Machining Process

To overcome the disadvantages of conventional machining processes has forced the researchers and industries to shift from traditional machining process to non-conventional machining process. It provides a promising solution as it would cut exotic materials with accuracy and good surface integrity. Fig. 1.5 shows different manufacturing process

capabilities of conventional and non-conventional machining. The tolerance range of various process of non-conventional machining is shown at the top and bottom. It can be inferred that electric discharge machining has a tolerance range of 0.05-0.0035mm which is comparable to the finishing process like the electrochemical grinding which possesses approximately the same tolerance.
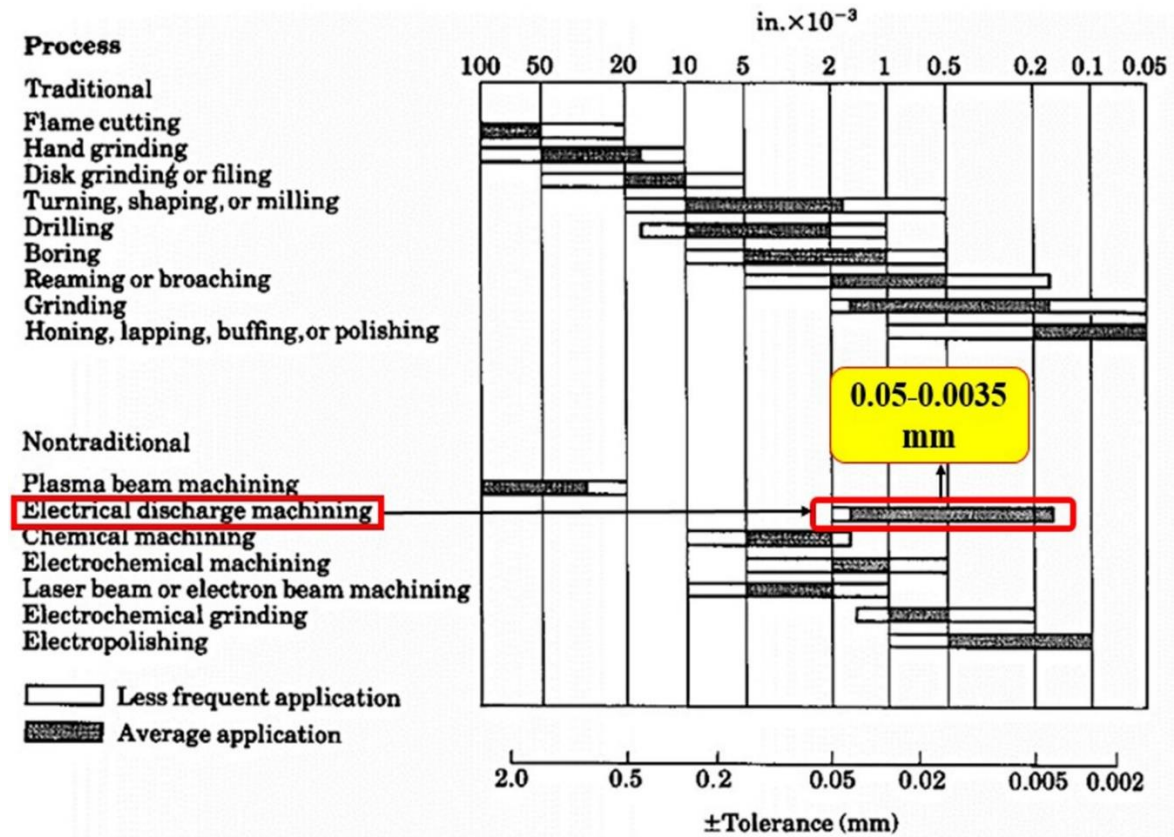
Figure 1.5 Different tolerance ranges of the different manufacturing process (Kalpakjian, 1989)

Apart from the process capability, different researchers have machined nickel-based alloys using different non-conventional processes like laser beam machining, abrasive waterjet machining, electrochemical machining, electric discharge machining and wire electric discharge machining as discussed below.

Abrasive waterjet machining has a high initial cost and low material removal rate. Hence it cannot be used for machining components. The taper in the machined part is a problem with AWJM in the case of thick materials. The taper occurs as the jet exits the workpiece

at a different angle than it enters the workpiece. This causes dimensional inaccuracy in the machining of nickel-based alloys (Nair and Kumanan, 2018; Cárach et al., 2016). In laser beam machining heat-affected zone, will appear and it damages the machined surface. However minimum deviation and taper kerf were observed in laser machining (Genna et al., 2015; Reddy et al., 2018). In the case of electrochemical machining, for complicated shapes, initial tooling have to be prepared which is time-consuming and costly. Besides, there should be a constant flow of electrolyte with a constant voltage for uniform material removal. The overcut, difficulty in machining complex profiles, corners that may lead to tool wear was observed in electric discharge machining of Inconel based alloys. (Caiazzo et al., 2015; Wei, 2002; Jothimurugan and Amirthagadeswaran, 2016). Table 1.5 shows the different nickel-based superalloys machined using a different non-conventional machining process.

Table 1.5 Nickel alloys machined by different non-conventional processes

Nickel-based superalloys	AWJM	LBM	ECM	EDM	WEDM
Inconel	✓	✓	✓	✓	✓
Hastelloy		✓		✓	✓
Nimonic		✓			✓
Rene				✓	
Waspaloy				✓	✓
Incoloy	✓				✓
Monel				✓	✓
Udimet				✓	✓
*✓-can be Machinable or Machined					

From fig.1.5 and table 1.5, it can be concluded that to obtain better dimensional accuracies and surface integrity nickel-based alloys can be machined in WEDM. Although it can be seen from table 1.5 that Hastelloy-X has been machined in LBM, AJM and EDM. But LBM possesses difficulty in the machining of the thicker workpiece and higher heat-affected zone (Razzell, 2000). However, in AWJM kerf is a major drawback while cutting the material. Whereas the EDM produces a relatively small amount of sub-surface damage on the cut surfaces compared to LBM and AJM (Müller and Monaghan, 2000). In the case of WEDM, it can achieve high tolerances and better accuracy of components (Kunieda

and Furudate, 2001). Hence, WEDM is the most preferred machining method, as lower surface damage and tight tolerances and closer accuracy can be achieved with complex geometries.

1.7 WEDM AND ITS WORKING PRINCIPLE

The WEDM forms the most ideal solution in terms of accuracy and surface integrity in the machining of difficult to cut nickel-based superalloys. Many nickel-based alloys including Hastelloy have been machine by WEDM. It is a non-contact process where the machining depends on the thermal conductivity of the workpiece.
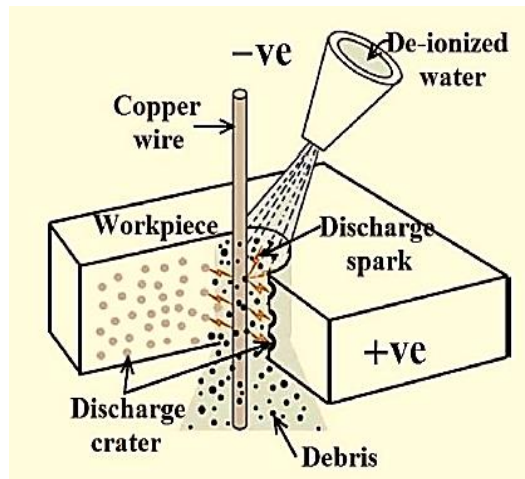
Figure 1.6 Mechanism of WEDM Process (Hsieh et al., 2009)

Wire electric discharge machining is an electro-thermal spark erosion machining process that removes material by a series of sparks that is generated between the workpiece and electrode engulfed by dielectric fluid. During WEDM, the workpiece is placed in a positive charged terminal and wire is the negatively charged terminal as shown in fig.1.6. The dielectric fluid is continuously flushed, the material that is melted is cooled and carried away in the form of debris from the machining zone. There is a strong potential difference that is developed between the wire and workpiece engulfed by a dielectric medium. A series of electrons hit the medium and there is an accumulation of ion and electrons at the plasma that comes out as spark. As the spark strikes the workpiece there is an intense heat

generated that is capable of melting and vaporizing the material, forcing the workpiece material to clear the path of the wire (Shahane and Pande, 2016).

1.7.1 Taper Cutting in WEDM
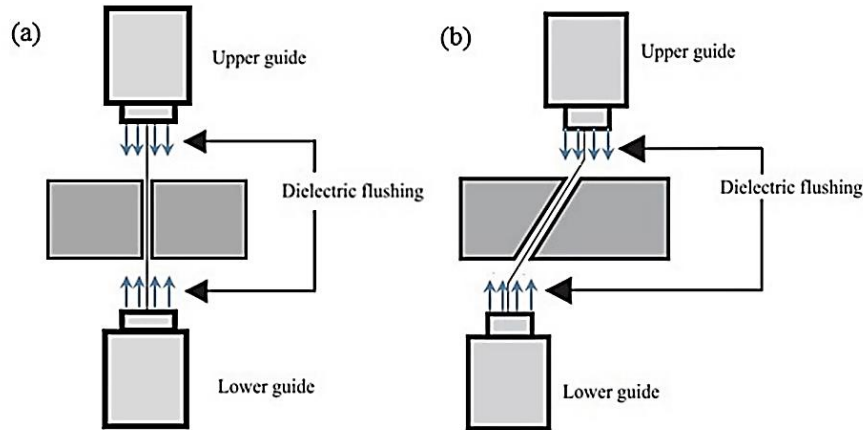
Figure 1.7 (a) Straight cut in WEDM (b) Shift of upper and lower guide's ways in taper cutting (Sanchez et al., 2016)

The tapered surface can be machined in WEDM by varying the wire guide alignment. The machine possesses a mechanism where one of the wire guides is pushed left or right making the wire slant as shown in fig.1.7. The dielectric fluid flushing in such a distributed manner that it forms a water curtain around the taper machining zone. In this mechanism the major disadvantages are (a) the water flushing from the guide is distributed irregularly throughout the slant distance while machining (b) the wire is bent with a radius due to which it leads to breakage of wire and (c) as each wire has its strength the bending soft and hard wires would be different causing inaccuracies in the machining of the workpiece.

The hard wires have tensile strength, is straighter and more impervious to wire breakage during cutting compared to soft wire. As hardwire offers resistance to the true programmed wire path, it can lead to poor surface finish or wire breakage. While machining with any type of wire there can be intolerable marks on the workpiece and inaccuracies in angle as shown in eq.1.1. The favourable solution for cutting tapers by WEDM is with the help of a soft wire. As soft wire possess low-tensile-strength, they

bend and follow the correct path traversed by the CNC controller which provides a higher surface finish and accurate cuts. The tapered surface has many applications like from rocket skirts to simple machine components.

Taper error (Degrees) = Measured angle-programmed angle   (1.1)

1.7.2 Wire Material and Dielectric Fluid

In general, the coated wires have a very thin deposition (2-3μm) of pure zinc applied to a brass or copper core. The Zinc coated copper wires of 0.25mm were used as the electrode for the machining. Zinc coated wires would machine at a rapid rate and breakage of wire is less frequent compared to brass wires. These wires would generate an excellent surface finish, enhanced surface integrity and is always engulfed with deionized water during machining. The deionized water was used as a dielectric fluid for machining in WEDM. The deionized water has favourable properties like low viscosity, high cooling rate, non-hazardous, non-flammable and pollution-free. It has good fluidity due to low viscosity which enables it to efficiently flow thereby decreasing the temperature.

1.8 WEDM PARAMETERS USED FOR PROFILING

The WEDM is a machining process that involves a combination of thermodynamic, hydrodynamic, electrodynamics and electromagnetic actions. The machining action in WEDM can be controlled by many input parameters such as pulse off time, flushing pressure, pulse on time, wire-speed, servo voltage, and input current. So among these input parameters a very few parameters influences on the profile.

1.8.1 Machining Parameters in WEDM for Profiling

As WEDM gives a high precision finish cutting, hence it can be used in complex component manufacturing (Kunieda and Furudate, 2001). With the dimensional accuracy of slant profile as the main focus, in the present study, the following input parameters are

taken into consideration as it influences the machining accuracies during profiling through WEDM.

1. *Wire distance between guides (WGD)*

The distance between the upper and lower wire guide during cutting is called wire distance between guides or guide span. It is denoted by L as shown in fig. 1.8. The lower guide is fixed and the upper guide is moveable. As the WGD increases, the tension in the wire decreases which leads to an increase in wire vibration (Puri and Bhattacharyya, 2003; Habib and Okada, 2016). This increase in wire vibration causes lower cutting velocity due to variation in spark gap (Chaudhary et al., 2019; Habib, 2017). The WGD parameter enables the machine to cut the material of different thickness and their orientation. This affects the cutting speed, surface roughness, corners, recast layer thickness, micro-hardness.
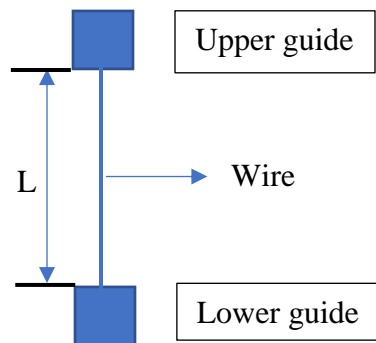
Figure 1.8 Wire distance between guides

2. *Corner dwell time (C-dwell time) (CDT)*

C-dwell time is a feature measure through a period where the wire guide waits at specific coordinates until the wire travels to that coordinate and overcoming the lag in the wire. As it helps to recover the lag, it is used to machine sharper corners. It can be varied from 0 to 99 seconds. CDT default fixed in the machine is 3 sec and which is the recommended value. This parameter helps to reduce corner error or uncut region in the profiling for various shapes and at the different workpiece orientation. (Read and Zenyth, 2010).

3. Cutting speed over-ride (CSO)

Cutting speed over-ride is an online parameter that is provided to control the cutting speed in percentage without modifying the set machining parameters in the progression of machining. This feature provides better control of the corner edges, for larger taper angles in taper cutting and complex profiling avoiding the risk of breakage of wire (Read and Zenyth, 2010). It can be varied in terms of percentage mainly 25%, 50%, 75%, 100% (full cutting speed).

4. Wire offset (WO)
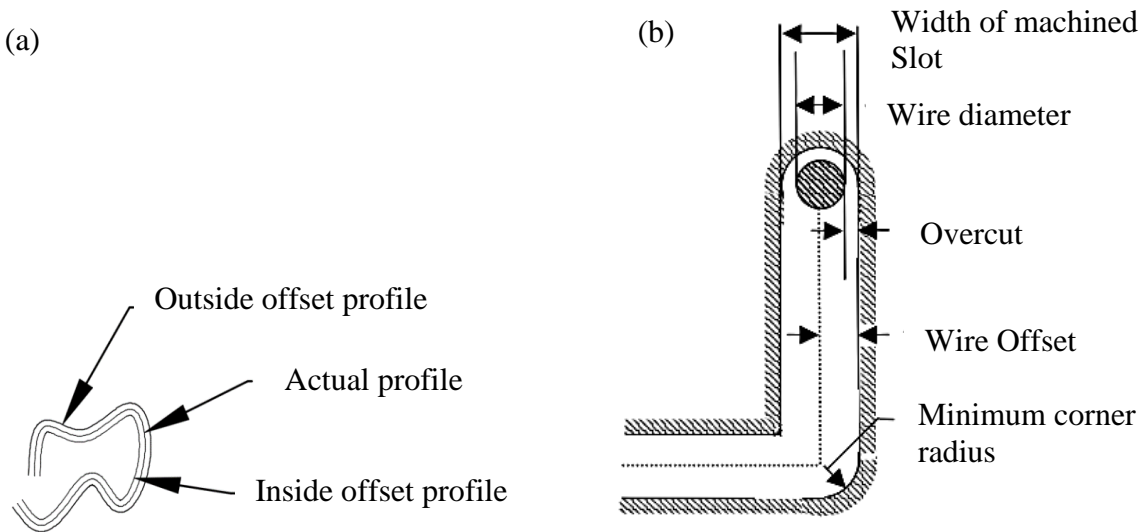
Figure 1.9 (a) Offset of a profile (b) Wire offset of a slot (Sarkar et al. 2006)

Wire offset is the parallel distance that is provided to the wire while cutting the profile on the workpiece to avoid overcut (Read and Zenyth, 2010). The wire is made to move a fixed perpendicular distance from the programmed profile that leads to an increased profile area. The wire moves out or inside parallel to the actual profile as shown in fig.1.9 (a). It is represented in micrometres where it is taken to be the sum half of the wire diameter and spark gap (Sarkar et al. 2005) as in fig. 1.9 (b) and eq. 1.2.

$$\text{Wire Offset (μm)} = \frac{\text{Wire Diameter}}{2} + \text{Spark gap} \qquad\qquad 1.2$$

5. Taper Angle (TA)

The WEDM employs slant/inclined wire to machine taper components varying from 0-60° as shown in fig. 1.10. This taper angle or wire inclination can be adjusted through the controlling wire guide movement. In the present investigation an in-house developed fixture is used to machine taper components.
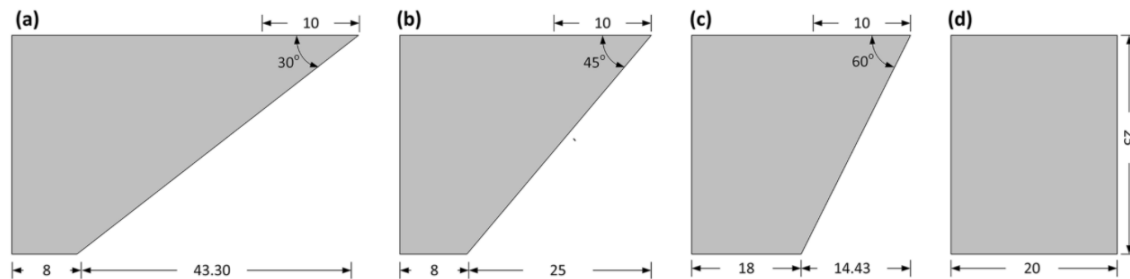
Figure 1.10 Tapered angled components machined by WEDM (Wasif et al., 2020).

1.8.2 Response Characteristic Parameters of Profiles

From the input profile parameters and taper angle during profiling for different basic profile like triangular, square and circular shapes were machined. The following machining parameters WGD, CDT, WO, CSO and TA affects the profile and its accuracy of a component. The effect of the machining parameters was analyzed by using output responses for different profiles at 0°, 15°, and 30° taper angles. These output responses are briefly discussed below

1. Profiling speed

Profiling speed is the cutting speed of the profile or rate at which the profile is machined. It is defined as the rate of length of cut (Azam et al. 2016). It was taken as the average of all the instantaneous speed required to cut a profile.

2. Surface roughness

Surface roughness is the measure of irregularities that were formed during WEDM on the machined surface. These irregularities were due to the melting and solidification of the

layer on the machined surface. The machined surface finally inclusive of micro-voids, micro-globules, debris, crater and micro-holes leads to surface roughness (Sen et al. 2020). To achieve better machined surface with other output responses like cutting speed, surface crack density and kerf width, optimal input parameters were selecting through trial runs.

3. Profile area

The profile area is the area of the profile that was machined. In the present study, the basic shapes like triangular, square and circular profiles were machined based on CNC programming. It was calculated after measuring the sides of the machined profile. The effects of dimensional shift can be observed due to the change in the area after machining.

4. Corner error

The corner error is the uncut region at the corners due to the wire lag. These error were caused due to the elastic nature of the wire (Abyar et al., 2018). For the corner formation the wire have to change its course after coming to the programmed co-ordinates. Due to its elastic in nature it changes its course before the programmed co-ordinates leading to formation of uncut region on the profile.

5. Recast layer thickness and Micro-hardness

Recast layer is the layer formed on the WEDM surface due to melting and re-solidication during the machining process. As WEDM is a spark erosion technique the sparks heat the surface to melting state and the dielectric cools the layer instantaneously. This leads to the formation a layer having variable hardness due to metallurgical changes. The micro hardness gives the changes on the WEDMed surface indicating the effects that occurs after machining on the surface.

1.9 TAPER MACHINING AND PROFILING OF DIFFERENT BASIC SHAPES

WEDM gives high precision finishing cuts, hence further avoiding finishing processes (Kunieda and Furudate, 2001; Huang et al., 1999). Occurrence of wire lag, overcut leads to corner errors, profile area and dimensional shift during profiling. This leads to variation in the final machined profiles. These effects can be minimized by analyzing the impacts of machining parameters. In the present investigation, the input parameters like wire guide distance, wire offset cutting speed override and corner dwell time are the parameters used for profiling. These parameters control the accuracy during the profiling of complex shapes, tapering and the formation of sharp corners, so they can be called profiling parameters. These parameters can be used to control and increase the dimensional aspect during profiling.

1.10 PROFILING BASIC SHAPES AT VARIOUS TAPER ANGLES.

The cutting speed parameters like pulse off time, flushing pressure, pulse on time, wire-speed, servo voltage, and input current have to be chosen to get optimal profiling conditions. Initial experiments were performed at different slant angles namely 0°, 15°, 30°, 45° and 60°. These angles were achieved with the help of an in-house developed slant type fixture. Based on the responses like cutting speed, surface roughness, surface crack density, kerf width and angular error the profiling parameters were decided. The cutting speed parameters were chosen such that the parameters were suitable for profiling at all the taper angles and with less wire consumption. Further investigation was carried out using profiling parameters. One factor at a time experiments were carried out for simple square profile at 0°, 15° and 30° taper angles The profile of 1mm, 3mm and 5mm square was programmed in WEDM. The behaviour of the profiling parameters on each response parameters like profiling speed, surface roughness, corner error, residual stresses, micro-hardness and metallurgical changes in the component were studied. Based on similar lines basic shapes like triangle, square and circle of 1mm, 3mm and 5mm were programmed and were machined on Hastelloy-X were machined at 0°, 15° and 30° taper angles. The profiling parameters like wire guide distance, wire offset cutting speed override and corner

dwell time were used at different combinations. Although the profiling parameters influenced similarly to the profiling speed and surface roughness. The corner dwell time parameter influences differently for triangular and square profiles. This was due to the change in the angle for different profiles. The variation in taper was also considered and its effect on output responses was highlighted. These responses can be predicted by many prediction tools to find suitable parameters giving an optimal profile.

1.11 PREDICTION OF RESPONSES USING SOFT COMPUTING IN WEDM

As profiling in WEDM requires more time and resources, hence the prediction of responses becomes important. Soft computing can be used to predict the machinability of the profile, some of the computing techniques like a neural network, fuzzy system and evolutionary computation forms the most promising tool for the prediction of many parameters. In our studies, the network like artificial neural networks (ANN), adaptive neuro-fuzzy inference system (ANFIS) is used for prediction due to its greater prediction accuracy. The ANN mimics the actual process by forming a neural network-based training of the input and output responses. The ANFIS is the combination of both fuzzy and neural networks. It can not only be used for the prediction but also can be used to map the variation of response parameters. A 3-dimensional plot of the variation of response parameter along with the machining parameters can be obtained from the ANFIS system. In the current study, ANN and ANFIS were employed to predict the profiling speed and surface roughness. Validation of the predicted responses was also carried out by experimentation.

1.12 SUMMERY

Most nickel-based alloys could be machined by WEDM with high precision. Basic profiles such as triangular, square and circular shapes of different dimensions were machined at 0°, 15° and 30° taper angles. Some of the machining parameters like WGD, CDT, WO, CSO and taper angle were identified and their effects were analyzed by output responses. The output parameters like profiling speed, surface roughness, profile area, corner error, recast

layer thickness and micro-hardness were assessed. ANN and ANFIS soft computing technique was used for the prediction of output parameters. ANFIS mapping was used for analyzing the effects of input parameter on the machined surface.

1.13 THESIS ORGANISATION

Profiling is performed at different slant angles with the aid of slant type fixture on Hastelloy-X using WEDM. Simple profiles like triangle, square and circular profiles were machined at various machining parameters and responses were analyzed. This is divided into eight chapters as follows.

CHAPTER-1

In this chapter, superalloys have been defined and different types of superalloys have been introduced. Nickel-based superalloys and various applications have been outlined. Hastelloy-X has been concentrated and different machining methods were discussed. The significance in machining such alloys and tapering in WEDM was highlighted. Different profiling parameters employed with prediction methods were explained.

CHAPTER-2

This chapter gives a summary of the literature that was performed using WEDM using nickel-based alloys. Research on different responses like surface roughness, surface crack density, dimensional shift, corner error, wire lag and numerical modelling that was used in WEDM have been reported. Research gaps from which the objectives were derived was also emphasized.

CHAPTER-3

Different experimentation techniques adopted for the investigation were stated in this chapter. The instruments used in that with specifications of the model with make and slant

type taper fixture details were specified. Artificial neural network and adaptive neural fuzzy logic interference system used for prediction were explained.

CHAPTER-4

This section indicates different parameters like pulse on, servo voltage, wire speed and servo feed were fixed for profiling. The machining was performed at various slant angles from 0° to 60°. Based on parameters fixed one factor at a time (OFAT) approach was adopted for a simple square profile. Profiling speed, surface roughness, taper angle, recast layer formation, microhardness, residual stresses and elemental changes were examined.

CHAPTER-5

The triangular profile was machined using a slant type taper fixture for different machining parameters at 0°, 15° and 30° slant angles. Profiling speed, surface roughness, profile areas angular error, corner error, corner deviation, recast layer and microhardness were characterized. The variation of the response parameter with the slant angle were highlighted.

CHAPTER-6

This chapter details the square and circular profile machined at various parameters that were characterized for all at 0°, 15° and 30° slant angles. Different characteristic response like profiling speed, surface roughness, profile areas angular error, corner error, recast layer and microhardness were measured from the profiled components.

CHAPTER-7

This section of the thesis deals on artificial neural network and adaptive neural fuzzy logic interference system that was employed in the prediction of profiling speed and surface

roughness. The neural networks were formed for prediction and validation of the optimal prediction model were also performed.

CHAPTER-8

The conclusion has been formulated from the experimental trials in this section. Different characteristics that effects the profiles were underlined. This chapter also emphasizes the future scope of machining in WEDM based on the literature and present study.

CHAPTER 2

LITERATURE REVIEW

2.1 INTRODUCTION

The machining of nickel-based superalloys both by conventional and non-conventional have been highlighted. Among the several non-conventional machining processes, WEDM was the most promising method for machining of different alloys. As WEDM is a complex process it has many input parameters that influence the output responses. A detailed study of the literature is highlighted on parameters influencing the output responses in this chapter. The input response parameter like cutting speed, surface roughness, surface crack density, micro-hardness, recast layer thickness, kerf width, and residual stress were explored.

2.2 MACHINING OF NICKEL BASED SUPERALLOYS

Among the superalloys, the Ni-based super-alloys are having most widely used as it has excellent mechanical properties. Nickel is one of the most versatile elements because of its solubility with several other metals, many different alloys are fabricated easily (Davis et al., 2000). They possess a face-centred cubic structure (FCC) having a solid solution precipitation tendency with topologically close-packed (TCP) phases (Gowthamana and Jeyakumar, 2019). These alloys have high strength due to its precipitation when compared to other superalloys (Mouritz, 2012). They pose a challenge for machining due to the following reasons (a) properties like high hardness, high strength at high temperature, (b) chemical affinity to react with the tool materials, (c) work hardening, (d) low thermal diffusivity, (e) tough and continuous chip leads to wear or damage in the tool (f) built-up edge formation onto the cutting tool materials makes the machining operation more difficult and challenging (Ezugwu et al., 1999).

2.2.1 Conventional machining

Many researchers have tried to machine nickel-based alloys using conventional machining like turning, drilling, milling, shaping, planing, and broaching. Fig.1.4 shows different types of tool and surface defects that were identified in the conventional machining process. During machining the high temperature developing at the chip and tool interface leads to damage to the machined surface and the cutting tool.
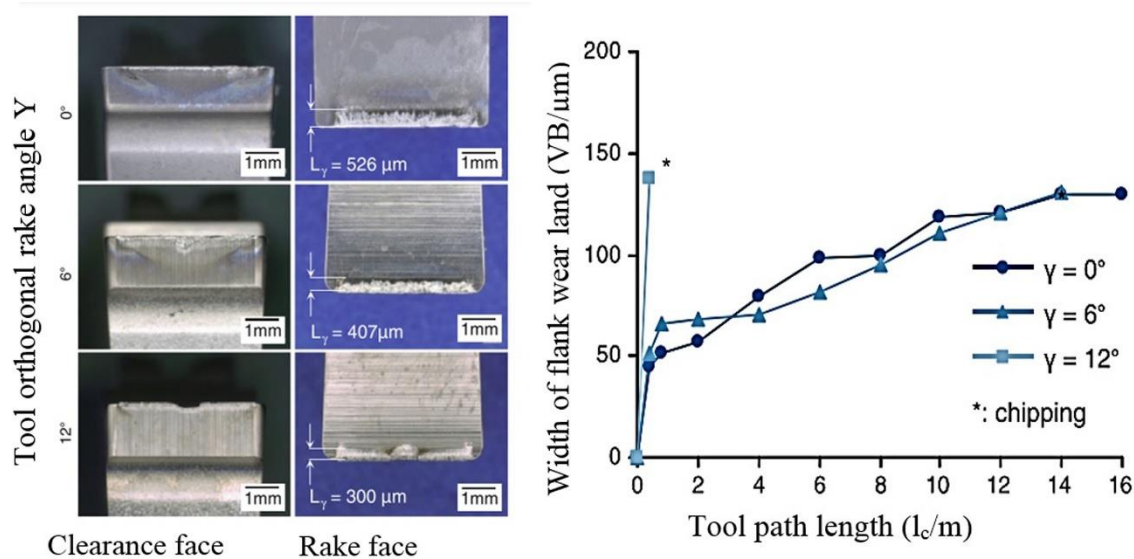
Figure 2.1 Tool wear formation for different rake angles (Klocke et al., 2013)

The Inconel 718 a nickel-chromium-molybdenum alloy was machined by broaching machine and the results were reported by Klocke et al. (2013). The machinability, process forces, tool wear and chip formation were evaluated after the process. The wear on the tool face was as shown in fig.2.1. Similar studies were performed on milling machine by Liu et al. (2015), where they were observed to have build-up edge, tear, groove and cavity on the tool face and machined surface of Inconel 718. Sharman et al. (2006) explored the damages during turning on Inconel 718 operation, where the cracked carbide particles and surface cavities were formed on the work surface. The tool defects like tool wear or scar on the flank face and feed marks on the tool were highlighted. Axinte and Chiffre (2008) reported turning, milling, grinding of Inconel 718. From the metallurgical inspections of machined subsurface damages, anomalies e.g. plucking, laps, cracks, white layers were revealed.

Ranganath et al. (2009) and Özel and Arisoy (2014) examined the formation of white layer and bent grains in the finishing of a nickel superalloy Inconel-100 during turning operation. Thakur et al. (2015) stated abrasion, adhesion, and diffusion wears were found to be dominating tool wear mechanism during dry machining of Inconel 825. During the drilling operation of Inconel 713C (Lee et al., 2007) porosity and feed marks on the work surface were commonly found on the workpiece. Ezilarasan et al. (2013a) performed turning on Nimonic C263 superalloy where wear on cutting edge and flank wear were noticed on the tool surface. Whereas the machined surface showed rough and smeared surface, chip particles, feed marks as shown in fig.2.2.
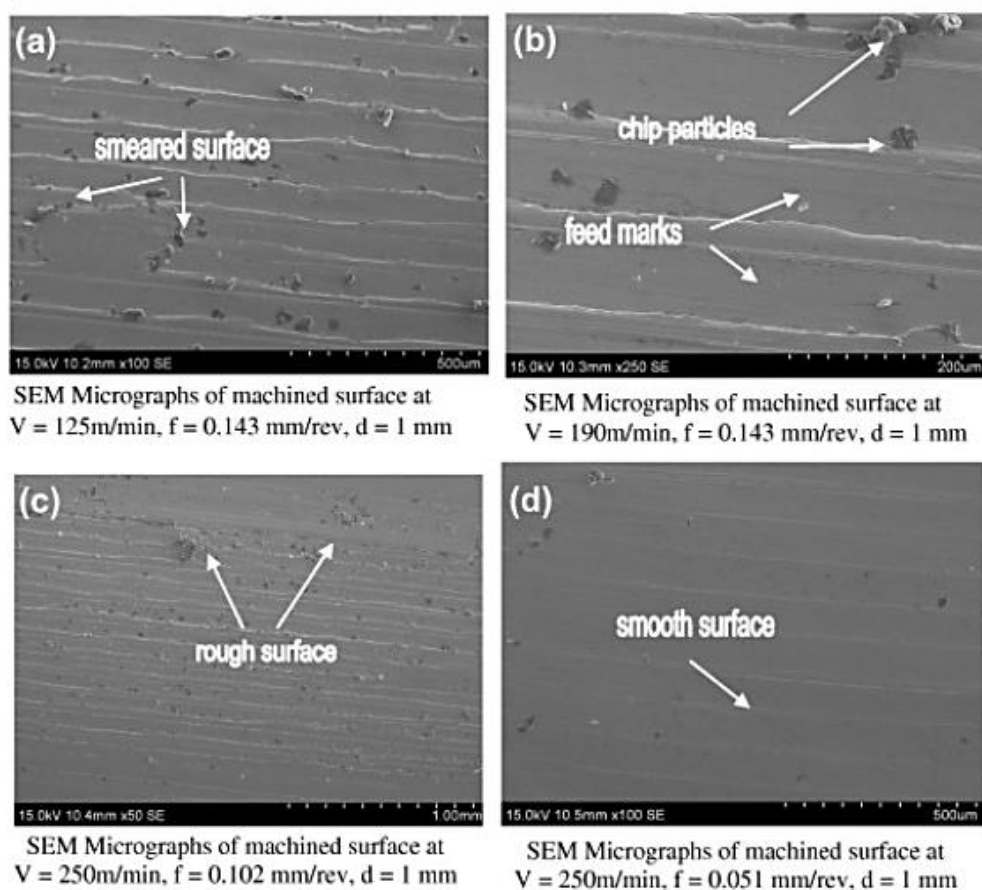
Figure 2.2 Wear on the cutting tool (Ezilarasan et al., 2013a)

Further Nimonic 105 and 75 were machined through turning operation, here it was concluded micro-adhesion wear (attrition) was observed on the tool while machining such

nickel-based alloys. A new nickel-based superalloy, Haynes 282 was machined in milling, they observed flank wear and grain deformation/damage to a maximum depth of ~15 µm. They also reported surface/subsurface microstructural damage with deformed grain boundaries up to a depth of ~15 µm and the white layer of up to ~6 µm from the machined surface (Hood et al., 2011, 2012). In the case of Hastelloy C 2000, machined by milling operation where feed marks, chip redeposition to the surface, adhered material particles and surface cavities were observed on the machined surface (Razak et al., 2012). These clearly show different conventional machining used for machining of different superalloys which ended with poor surface and tool damage.

2.2.2 Non-conventional machining

The defects in the machining of nickel-based alloys during different kinds of conventional machining forced the researchers and industries to explore non-conventional machining. Some of the non-conventional machining processes from which nickel-based alloys can be machined are as given in table 1.5 i.e. abrasive waterjet machining, laser beam machining, electrochemical machining and electric discharge machining.
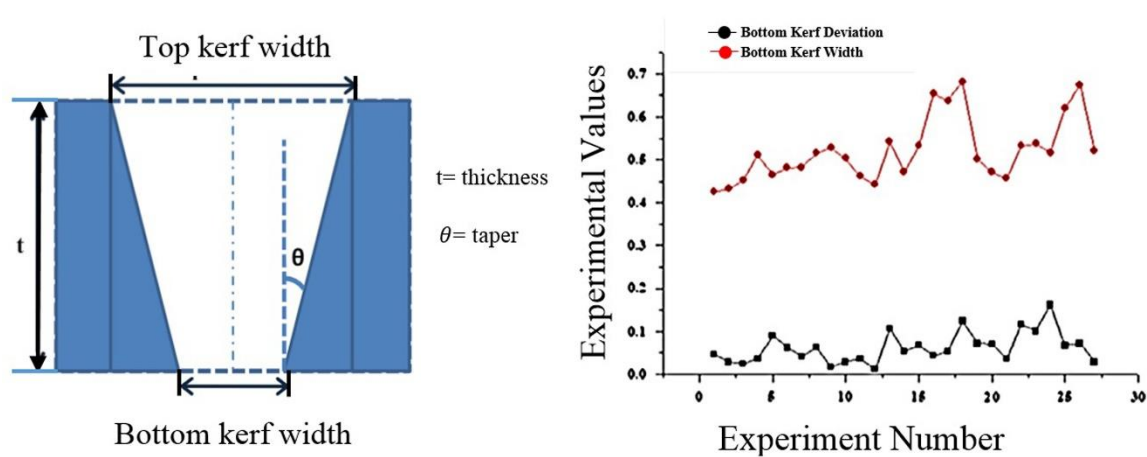
Figure 2.3 Kerf width in laser beam machining (Shrivastava et al., 2018)

During the abrasive waterjet machining of Inconel 617 and Incoloy alloy 925, the dimensional aspects like overcut, taper angle of the hole where the main disadvantage caused during machining. (Nair and Kumanan, 2018; Cárach et al., 2016). Laser beam

machining was used for machining of Inconel-718, NIMONIC® C263, Hastelloy C276 (Shrivastava et al., 2018; Reddy et al., 2018; Genna et al., 2015). It was observed that there is taper formation in the kerf as shown in fig.2.3 and it was only admissible in thin sections. Lynch et al. (2021) have attempted machining of Inconel 718 it was seen that the electrolyte flow must be maintained for uniform and proper machining of the material. As it involves hazardous chemicals, controlling them for dimensional accuracy becomes difficult. The next favourable process is electric discharge machining it was seen that most of the nickel-based alloys like Inconel, Hastelloy, Rene, Waspaloy, Monel, Udimet etc. can be machined with greater accuracy.

2.3 WEDM OF NICKELBASED SUPERALLOYS

Among the non-conventional machining processes, WEDM is the best method for machining intricate shapes to get precise components (Lin and Liao, 2009) and superior surface integrity (Newton, 2009) than EDM. In WEDM many response parameters can be controlled and by optimizing the different process parameters for different materials. Many researchers have machined different nickel-based alloys in WEDM and the detailed discussions as given below.

2.3.1 Parameters Affecting Cutting Speed

The cutting speed is defined as the rate of length of the cut (Azam et al., 2016). The higher the cutting speed higher will be the material removal rate. Cutting speed depends on many machining parameters like pulse time, open-circuit voltage, wire-speed, input current, pulse off time, servo voltage, wire tension dielectric fluid pressure etc. and other aspects like workpiece material, thermal conductivity, the orientation of workpiece, dielectric fluid, wire diameter, wire material etc. It was stated in an investigation by Tosun, (2003) that an increase in open-circuit voltage increases cutting speed and material removal rate due to higher spark energy. This lead to larger craters, in turn, increasing the surface roughness of the WEDMed surface. Shandilya et al. (2013) have reported that among

different input parameters voltage was the most significant parameter affecting the cutting speed. ANN was used for accurate prediction of cutting speed in SiCp/6061 Al metal matrix composite machining. In a study carried out by Azam et al. (2016), WEDM of HSLA steel by moly wire was used. They observed that the pulse off-time, power and pulse frequency were the significant parameters influencing the cutting speed. Fig. 2.4 shows the variation of cutting speed for pulse off-time and power. In a parametric analysis during WEDM of stainless-clad steel optimization of cutting speed was performed. This resulted in a 20% improvement in cutting speed during machining (Ishfaq et al., 2018).
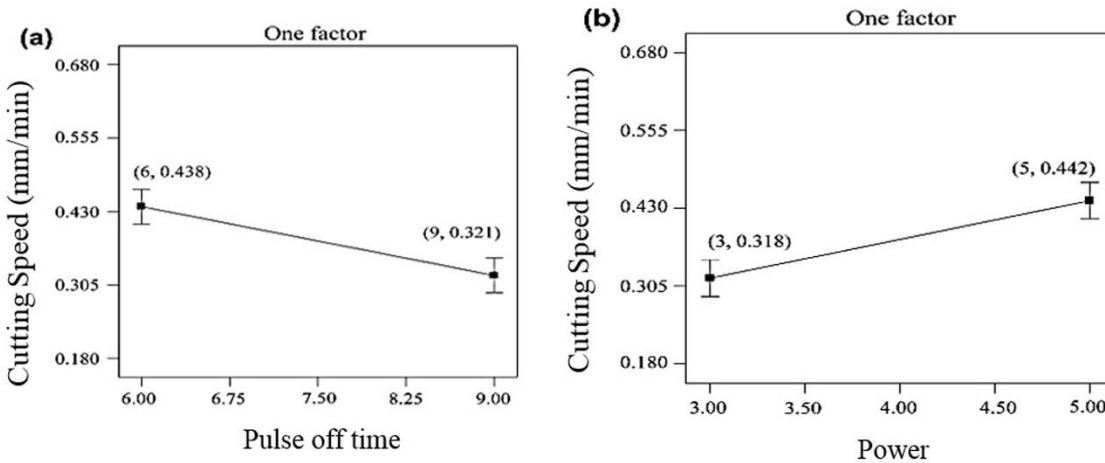
Figure 2.4 Variation of cutting speed with (a) pulse off-time (b) power (Nain et al., 2018)

Mouralova et al. (2019) have investigated the effects of machining parameters on cutting speed and surface quality. The optimum cutting speed was experimentally confirmed for efficient machining to get a good surface quality. During wire electrical discharge machining (WEDM) of 2D C/SiC composite. He et al. (2019) have investigated that fiber orientation also affects the machining speed and surface roughness. Response surface method with grey relation analysis was opted for the analysis by Chaudhari et al. (2020) to obtain optimal parameter setting. During the WEDM process of pure titanium, the cutting rate was maximized while reducing surface roughness. Kumar et al. (2020) have reported optimal kerf width and cutting speed in the machining of AleSiCeB4C composites using response surface methodology with input parameters like current, pulse on time, wire feed rate and the content of B4C in aluminium. Response surface modelling and optimization

of cutting rate and surface roughness was performed by Vivek Aggarwal et al. (2015). The prediction models were developed having 5% prediction errors during machining of Inconel 718 alloy.

2.3.2 Influence of Machining Parameters on Surface Roughness

Surface roughness is a component of surface texture that indicates the condition of the machined surface. As the damages like craters, micro and deep cracks, porosity, cavities and inclusions. on the surface leads to poor surface quality of the product, hence these flaws should be minimized by selecting optimal input process parameters. Researchers have attempted many combinations to obtain a favourable surface. The influence of WEDM and the grinding process on Inconel 718 were analyzed by Ayesta et al. (2016), they reported like transverse and longitudinal surface roughness, heat-affected layer influenced fatigue behaviour of the manufactured component. Li et al. (2016) have studied the surface integrity of the machining of Inconel 718 alloy for different cuts namely one rough and three trim. The distribution of surface roughness using probability density for different cuts was highlighted.
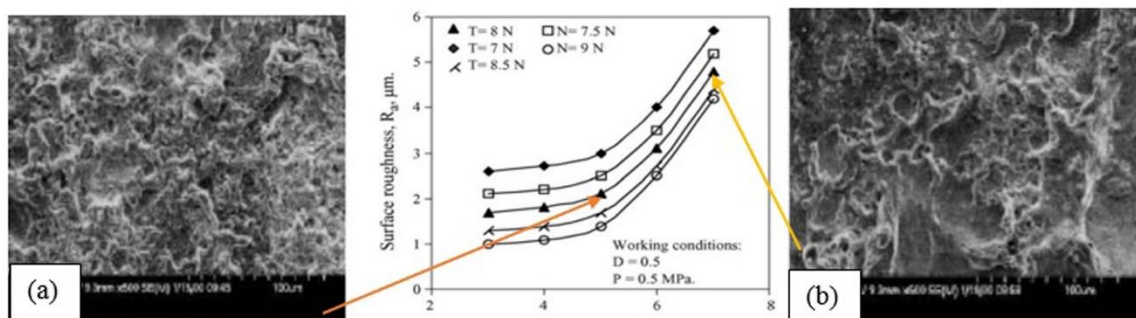
Figure 2.5 Variation of surface roughness and peak current a. SEM micrograph at 5A b. SEM micrograph at 7A (Hewidy et al., 2005)

A hybrid PCA-grey relational analysis was used for prediction and compensation between cutting time and surface roughness by Majumder et al. (2017) in WEDM of Inconel 800. It was proved to be accurate than the traditional grey relational analysis. Sharma et al. (2015) have investigated response parameter like surface roughness, material removal rate

for WEDM of Inconel 706 and they were concluded that Inconel 706 can be a substitute for Inconel 718 for different applications. With the aid of response surface methodology, a mathematical model was established on the surface roughness, metal removal rate, and wear ratio by Hewidy et al. (2005) during WEDM of Inconel 601, and cutting wire as brass wire (CuZn377). Fig.2.5 (a) and (b) shows a variation in effect of peak current on surface roughness and SEM micrographs shows the depth of the crater depend on the discharge heat energy at different levels.

Rajyalakshmi and Venkata Ramaiah (2013) have optimized of process parameters during WEDM of Inconel 825 using Grey relational theory. Mathematical equation was formulated for surface roughness including all process parameters using regression modelling. The machining effects of Udimet 720 nickel-based superalloy was revealed during an investigation by Antar et al. (2011). Surface roughness, recast layer was analyzed using a different variation of the coated and uncoated electrode system. It was observed that there was a 70% increase in productivity in uncoated brass wires. During WEDM of shape memory alloy, Manjaih et al. (2015) reported that a higher pulse on time causes greater discharge energy, leading to higher surface roughness. It was found that the servo voltage and pulse off time affected the surface roughness adversely compared to pulse on time. Further Mandal et al. (2016, 2017) have investigated surface morphology, surface roughness, elemental composition, microhardness and residual stress of the WED machined surface of Nimonic alloy at the rough cut and finish cut.

The surface integrity of Udimet 720 during WEDM with uncoated brass material tool combination was studied by Antar et al. (2012). Different machined workpiece damages with microcracks, microholes and subsurface integrity were highlighted. It was established that WEDM a feasible alternate solution for machining critical aerospace components. Study of suitable machinability of alloys like Inconel-825, Incoloy-800 and Monel-400 in wire EDM was carried out by Ajay et al. (2017). The optimization of the four parameters in terms of machining rate and surface roughness were carried out during machining aerospace materials.

Baburaja et al. (2017) have studied the variation of surface roughness in terms of roughness average (Ra), Skewness (Rsk), and Kurtosis (Rku) of WEDMed Hastelloy C 276 and aluminium. Varying machining parameters to compare adequate erosion rates with brass wire. Many other researchers have reported for different alloys such as Nimonic C276 (Rao and Venkaiah, 2015), 80A (Goswami and Kumar, 2014), Waspolly (Kus and Motorcu, 2017), Monel 400 (Kumar and Babu, 2018, 2017), for investigating different aspects for different machining parameters.

2.3.3 Parameters Affecting Surface Crack Density (SCD$_i$)

Surface cracks are common surface flaws that are observed in the machining surface. The surface crack density (SCD$_i$) can be defined as the average crack length (LC$_i$) present on each sample divided by the area of the micrograph (A). Kumar et al. (2016) have examined SCD and it was found that surface crack density and recast layer thickness were influenced by pulse on time, pulse off time and peak current.
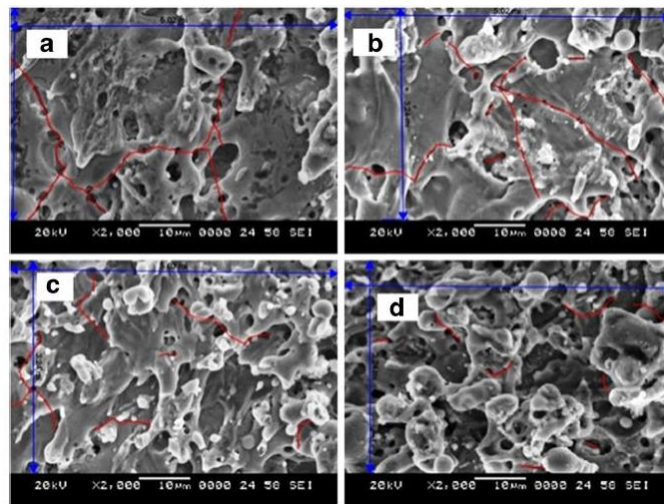
Figure 2.6 Surface crack density analysis measured at (a) higher cutting speed (b) higher surface roughness (c) lower cutting speed lower surface roughness (Soni et al.2017)

Soni et al. (2017) have reported SEM results shown in fig.2.6 that surface crack density was higher at higher cutting speed while it is lower at the lower cutting speed. Moreover, Zhang et al. (2015) have investigated the surface crack density using a tungsten tool YG15

in WEDMed surface. Naveen Beri et al. (2010) have reported about the effects of powder metallurgy processed electrodes on the machined surface and they have observed surface cracks were reduced. Hasçalýk and Çaydas (2004) have examined surface cracks in AISI D5 tool steel after machining with WEDM. Aspinwall et al. (2008) have explored surface cracks of machined surface in WEDM in titanium alloy and Inconel 718. Guu (2005) have investigated micro-crack of EDMed AISI D2 tool steel surface process were characterized with aid of the atomic force microscopy (AFM). Zhang et al. (2016) have established that ultrasonic vibration-assisted magnetic field during WEDM gave a superior surface quality based on surface crack density. The surface crack density of WEDMed Ni55.95Ti44.05 shape memory alloy was measured by Bisaria and Shandilya (2020) in their investigation. It was observed that servo voltage and pulse of time was proportional to the surface crack density, whereas pulse on time was inversely proportional to surface crack density indicated in fig. 2.7.

2.3.4 Variation of Micro-hardness and Recast Layer Thickness

During machining, the temperature increases in the machining zone this is due to the discharge energy. This melts the material and the molten metal is cooled by the dielectric fluid. A part of it is carried away as debris and the remaining part forms as a recast layer at the top of the machined surface. This machined layer have different hardness when compared to the base material due to the metallurgical changes after WEDM. Sharma et al. (2018) highlighted the metallurgical changes affecting the recast layer thickness and micro-hardness during WEDM of Inconel 706. The micro-hardness of the WEDMed surface was minimum for the higher pulse on time and vice versa. In the case of recast layer, lower pulse on time recorded minimum recast layer and vice versa. Mussada et al. (2018) reported that in WEDM of die steel increase in the wire speed and servo feed increases the recast layer thickness. The hardness increased due to the presence of C, Cr, Cu, and Fe in the recast layer. Kumar et al. (2017) have reported that high discharge energy yielded higher recast layer thickness having forms deep craters of large size diameters on

the machined surface. Chaudhary et al. (2019) have investigated that the increase in wire tension, leads to a slight reduction in the recast layer and micro-hardness.
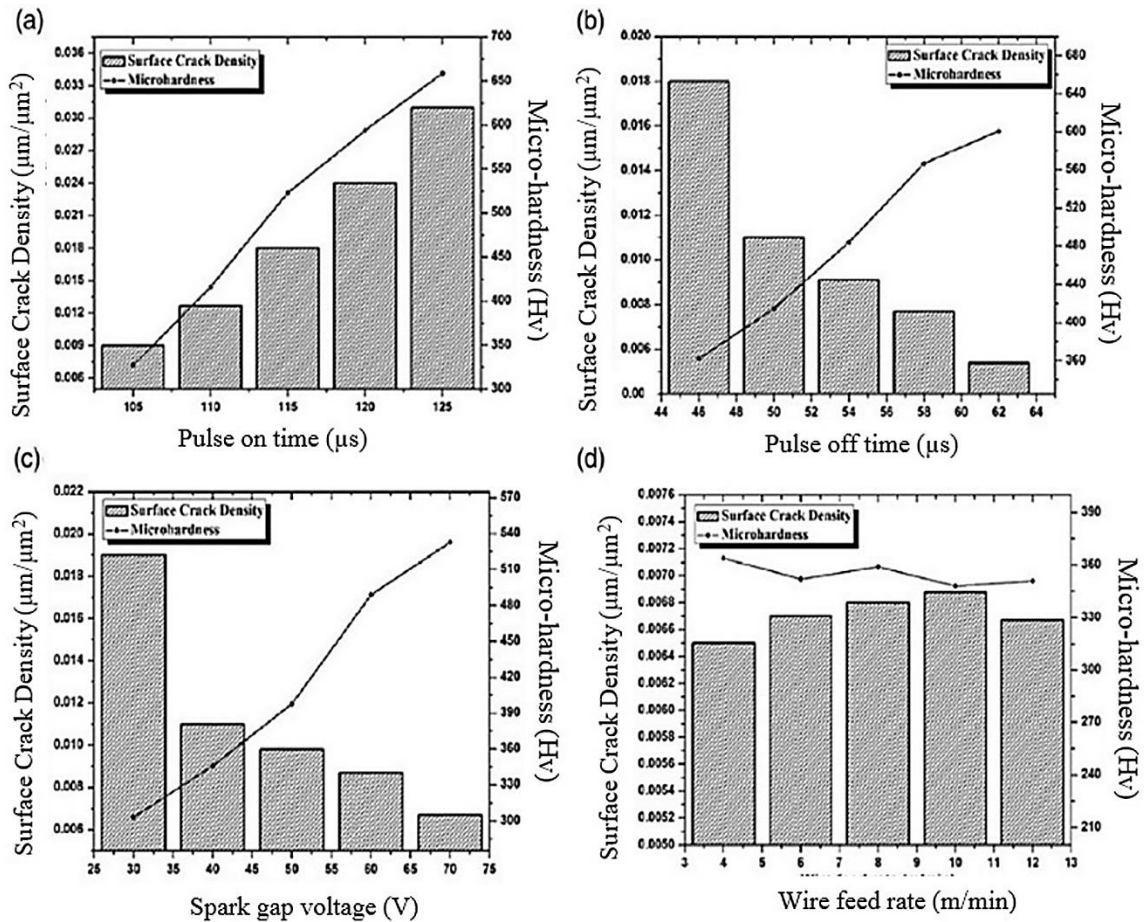
Figure 2.7 Microhardness variation across the WEDMed surface (Bisaria and Shandilya, 2020)

Manjaiah et al. (2015) have investigated wire electro-discharge machining of Ti50Ni50-xCux shape memory alloy. The escalation in the pulse on time leads to an increase in the thickness of the recast layer and the micro-hardness at the WEDMed surface. During Ni55.95Ti44.05 shape memory alloy (SMA) of WEDM, Bisaria and Shandilya (2020) explored that spark gap voltage, pulse off time and pulse on time are the major influential parameters. It was concluded that with the increase in pulse on, pulse off and servo gap voltage the micro-hardness also increases as shown fig. 2.7. Soni et al. (2017) have

examined the microhardness of WEDMed TiNiCo shape memory alloy. It was observed that the microhardness of the surface initially increased and later it decreased to the base material hardness. Kumar et al. (2017) explored microhardness during machining of Nimonic-90 on wire electrical discharge machining. It was noticed that the hardness at the machined surface was lower due to surface damage during the WEDM process.

2.3.5 Influence of Machining Parameter on kerf width

The width of cut is also known as kerf width. Many machining parameters influence the kerf width which affects the accuracy of the machined surface. Some of the studies have been reported in this section. During the WEDM of Al-Si metal matrix composite, teaching-learning-based (TLBO), graph theory and utility concept (GTUC) were used to the optimum working parameters. The kerf width was found 2.8% less compared to kerf obtained from GTUC optimization by Reddy et al. (2021). In an investigation carried out by Bose and Nandi (2021), it was concluded that kerf width and overcut was influenced by power, peak current and pulse off time during machining of titanium hybrid composite. Shinde and Pawade (2020) have stated that kerf width variation decides the accuracy of the component during wire electrical discharge machining of copper-coated Y2O3 stabilized ZrO2. Based on kerf width and other response, it was concluded that graphite powder mixed with distilled water can substitute the kerosene dielectric. A squeeze-casted composite Al6061-7.5% SiC was machined by Ishfaq et al. (2020) where the surface roughness, cutting rate and kerf width were measured. The current and voltage beside smaller pulse yields influenced kerf width as shown in fig. 2.8. The multi-objective genetic algorithm gave minimal kerf width and surface roughness with optimal cutting rate. Ali et al. (2020) have analyzed the top and the bottom kerf during dry micro-wire EDM. It was concluded not only machining parameters but the supply of compressed air at the top and bottom during machining also varied that kerf. Roy et al. (2019) have studied the cutting rate and kerf width while machining (TiNiCu) shape memory alloy. During which the upward-direction flow gives more debris than the downward-direction flow of the

dielectric fluid. It was concluded that wire tension doesn't influence kerf width by Chaudhary et al. (2019) during machining of AISI 304 stainless steel by WEDM.
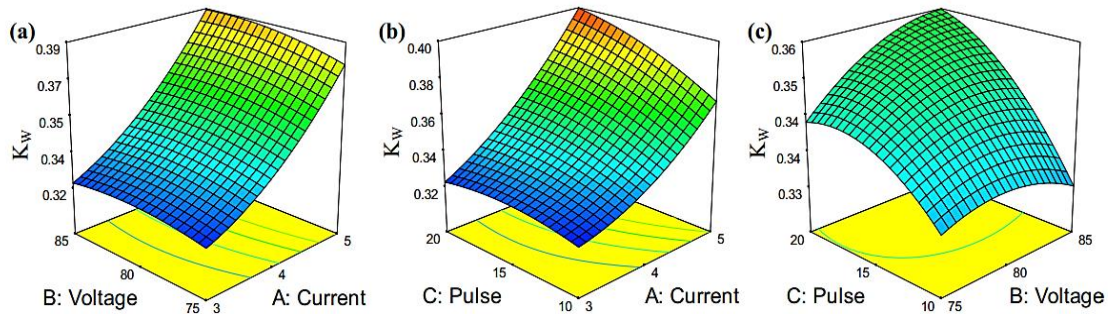
Figure 2.8 Variation of kerf width with (a) voltage and current, (b) pulse and current, (c) pulse and voltage (Ishfaq et al., 2020)

Chopra et al. (2019) observed that kerf width increases with servo voltage, pulse on time, wire feed during EN31 Steel by WEDM. Jadam et al., (2019) have reported zinc-coated brass wire offers a relatively narrow kerf width than brass. It was also seen that rough and trim cuts influence the kerf width. During WEDM machining of IN718 with Cu and Zn electrodes, Reolon et al. (2019) noticed that the kerf width is influenced by the discharge energy and wire run off speed. It was concluded that zinc-coated copper wire performed better than uncoated brass wire for all the experiments.

2.3.6 Influence of Machining Parameter on Residual Stress

During WEDM, the heat generated during the sparking is unevenly distributed in the material, sudden cooling is taking place by the dielectric fluid. This thermal cycle repeats during machining and hence there is internal stress generated on the machined surface. This internal stress produce cracks and further damages to the material. The current section reports some of the researchers work on the effect of residual stress on the machined surface. During the WEDM of powder metallurgical tool steels, Hatami et al. (2012) observed the diffusion of Cu and Zn into the WEDMed surface. The other parameters like surface roughness and residual stress exhibited an insignificant change. Ahmad and Fitzpatrick (2016) have investigated the WEDM cutting parameters to identify the

optimum conditions for the contour method of residual stress measurements. This contour method improved the residual stress magnitude up to 150 MPa which was also validated by X-ray diffraction, incremental centre hole drilling, and neutron diffraction. Sharma et al. (2016) reported residual stress increases with an increase in discharge energy. Among different wire materials, the hard brass wire offers comparatively less residual stresses as shown in fig.2.9. In a study during WEDM of Cu based shape memory alloy, Manjaiah et al. (2017) investigated that the thicker recast layer implied a larger tensile residual stress and vice versa. Besides, the high servo voltage produced the lowest residual stresses and had the least impact on the surface integrity of the material. An attempt was made by Kumar et al. (2018) to optimize the residual stresses and erosion rate during WEDMed of High Carbon High Chromium D2 tool steel. It was found that high peak current and duty cycle depreciate the surface creating high tensile residual stresses. Das and Joshi, 2020 have explored the residual stress of the wire electrode during WEDM. It was observed that residual stress causes microcracks, voids and pits which increases the probability of wire rupture. It also helps in the prediction of the wire breakage phenomenon easing the machinability detection for different materials.
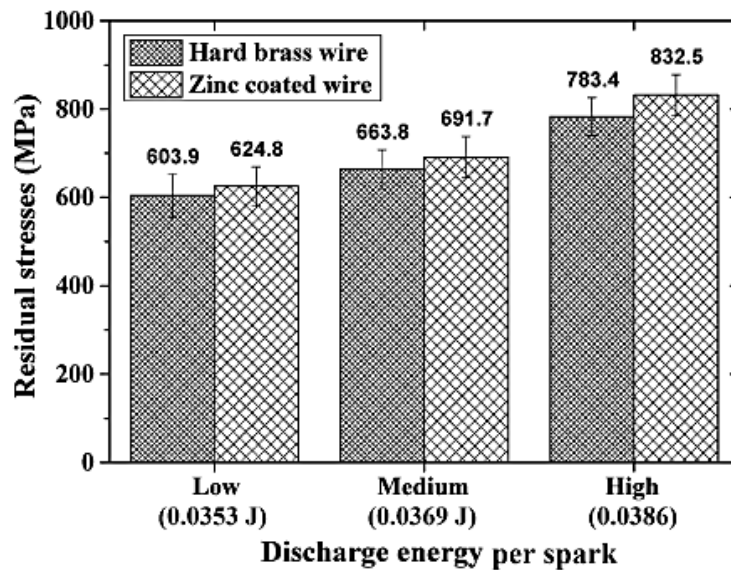
Figure 2.9 Residual stresses generated within WED machined material. (Sharma et al., 2016)

2.4 TAPER MACHINING IN WEDM

Tapering is a process of machining having the diameter of a cylindrical workpiece gradually decreases from one end to another. This tapered structure has vast applications such as dies, slant vents, rocket skirts, tool draft angles etc. Kinoshita et al. (1987, 1984) were one of the first researchers to highlight the problems in taper machining achieved by bending the wire. The problems are (i) as the bending couldn't be sharp, (ii) it produces geometrically inaccurate surface angles and (iii) wire breakage chances are more. Further to overcome these problems. Many authors have conducted their study to suggest mechanism to machine taper structure. The problems and their outcomes are reviewed and reported in the following section.

2.4.1 Taper Machining and Angular Error

Machining taper structure in WEDM is very critical as the electrode (wire) has to be bent. Machining such components using difficult to cut materials is challenging as both accuracy and the angle of taper have to be considered. Fig. 2.10 (a) shows inaccuracies in angle during taper machining as explored by Nayak and Mahapatra (2014, 2016). They reported that the multi-objective optimization in WEDM of austenitic stainless steel 304. The performance parameters like surface roughness, cutting speed for taper angles viz. 5°, 6°, 7° were considered in their study. Selvakumar et al. (2016) have studied the optimization of response parameters such as surface roughness, cutting speed, and the taper error in taper machining viz. 2°, 16°, 30° of AISI D3 tool steel by considering various machining parameters. Martowibowo and Wahyudi (2012) have reported the optimization of taper motion for taper angles 0°, 5°, 10° in the WEDM process on carbon steel (ASSAB 760). The influence of different parameters on the surface roughness and material removal rate were highlighted. Sanchez et al. (2008) devised a quadratic equation to numerically predict angular error in the taper machined surface for taper angles 10°, 20°, 30°. The electrical parameters were taken into account in the machining of tool steel as shown in fig. 2.10 (b).

Wasif et al. (2020) concluded in their study that taper angle influences different response parameters such as wire wear, material removal rate, kerf width and surface roughness.
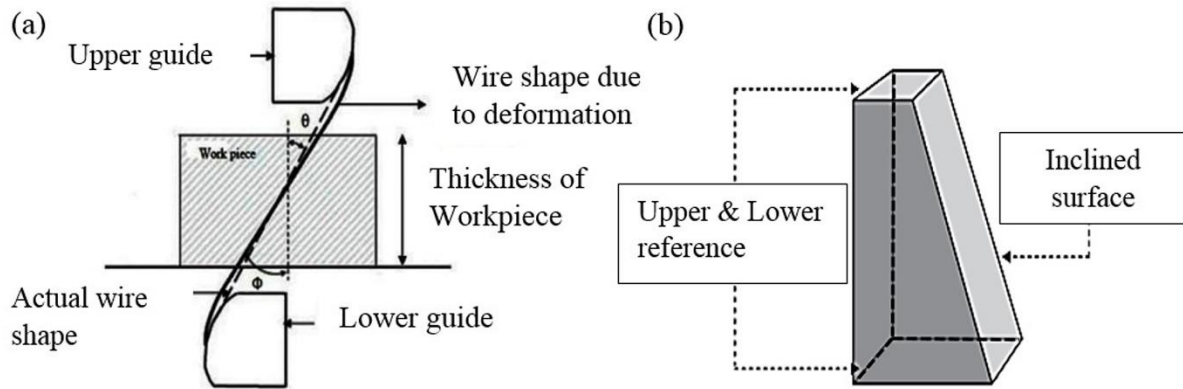
Figure 2.10 (a) Cause of inaccurate taper while machining (Nayak and Mahapatra, 2014)
(b) Taper Structure (Sanchez et al., 2008)

Naveed et al. (2019) have investigated arced profiles are to be machined at a certain taper angle. It was noticed that the optimal machining parameters reduced 33.3% and 14.3% in angular error and radial error respectively. Plaza et al. (2009) have formulated two models that predicted the taper error for angles 5°-30°. The equation was derived from the quadratic regression equation and finite-element model considering different machining parameters. This reduced the experimental trial and errors adapting such methodologies. Deka et al. (2020) have investigated taper angle, circularity error, overcut and material removal rate during the micro-electrical discharge machining (μEDM) process. It was concluded that the taper angle in silicon was higher than german silver due to the higher electrical resistivity of silicon. Hsue and Su, (2004) feasible discharge power and wire tension were maintained based on the material requirement rate for better dimensional accuracy. Selvakumar et al. (2016) have analyzed that taper angle influences cutting speed, surface roughness they observed taper accuracy and taper accuracy is independent of cutting speed.

2.5 PROFILE ACCURACY IN WEDM

Profiling\Dimensional accuracy is one of the most significant output response other than surface roughness, material removal rate, wire wear. Profiling inaccuracies occur majorly due to incorrect parametric selection, wire lag, corner error and dimensional shift in WEDM. The different researchers have concentrated on achieving the machining accuracy and their observations were discussed below.

2.5.1 Influence of Input Parameter on Profile Accuracy

Profiling a process where a closed profile or actual component profile is machined. Many parameters in WEDM influences the accuracy, some of the investigations are reported. During WED turning of micro-rod, Sun et al. (2017) have investigated accuracies that were achieved. A 70 µm diameter rods were machined with the diametrical deviation of the micro-rod of 0.65 µm using different machining parameters at rough, semi-finishing and finishing trim cut. Yueqin et al. (2016) studied the machining of Cr12, where the size error of 2µm, was reported due to dense passive film on a workpiece causing variation in thermal conductivity. Nani (2017) have explored enhancing the performance of the WEDM, where a special device for ultrasonic activation of the wire electrode increasing the dimensional accuracy of the profile and decreased the error of shape and the machined surface roughness. Zhu et al. (2018) have investigated the dimensional accuracy of the cylindrical parts in WEDM. The machined cylindrical workpiece was having good shape accuracy and geometrical precision were attained. The dimensional accuracy of the machined profile was controlled within 2 µm. During WEDM, Straka et al. (2017) investigated variation in errors of geometrical accuracy and deviation influenced by the process parameters. The graphical dependencies were used to predict the maximum deviation of flatness as shown in fig. 2.11. The meso/micro-sized spur gear was manufactured by Ali et al. (2010) employing micro and conventional WEDM. The gears manufactured in conventional WEDM were having 1.8 µm surface roughness and 2-3 µm of dimensional accuracy. This was acceptable for many micro-engineering applications which proved the capability of conventional WEDM.
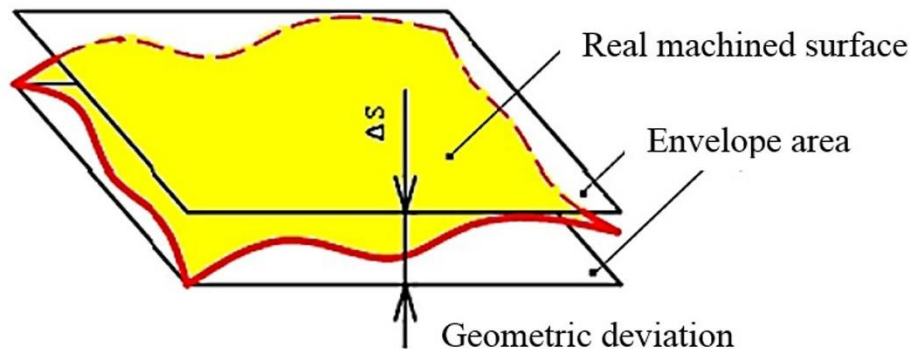
Figure 2.11 Geometric deviation in Machined surface (Straka et al., 2017)

Pramanik et al. (2019) have utilized Pareto analysis of variance to study the parametric influence on circularity, cylindricity, and diametral errors. Flushing pressure, pulse on time and wire tension were the three noticeable parameters influencing the accuracy. Alshemary et al. (2018) have stated that pulse on time, pulse off time and low wire tension contributes to 13%, 16% and 7% diameter error respectively. This can be avoided by maintaining optimal parameters such as medium pulse on time, and low pulse off time and low wire tension.

Azam et al. (2016) explored that high strength low-alloy (HSLA) steel, when machined with reusable moly wires showes improved dimensional accuracies. Garg et al. (2012) have studied different machining parameters on the dimensional deviation. The dimensional deviation was influenced by pulse on and pulse off time. As the spark discharge energy increased, the dimensional deviation was also increased during machining. During machining of K460 tool steel by Kanlayasiri and Jattakul (2013), it was noticed that the dimensional accuracy was influenced by peak current and offset distance. The surface quality was affected by peak current. The wire-tool vibration was analyzed by Puri and Bhattacharyya (2003) as dimensional accuracy depends on wire vibration. The controlled wire movement leads to precise component machining. The Inconel 617 was machined by Kumanan and Nair (2017) to investigate the material removal rate, surface roughness, wire wear rate and dimensional accuracy like circularity, cylindricity, perpendicularity and parallelism for different machining parameters. The profile was machined at different input

machining parameters and the output parameters were mapped to understand variation with input parameters using ANFIS. Manikandan et al. (2020) have studied, Incoloy 825, Inconel 603 XL, Monel K400 and Inconel 600 using WEDM. The optimal process parameters were derived for all the materials. However, it was found that Monel K400 showed the better straightness, perpendicularity and surface roughness compared to other alloys.

2.5.2 Effect of Wire Lag on Profile Accuracy
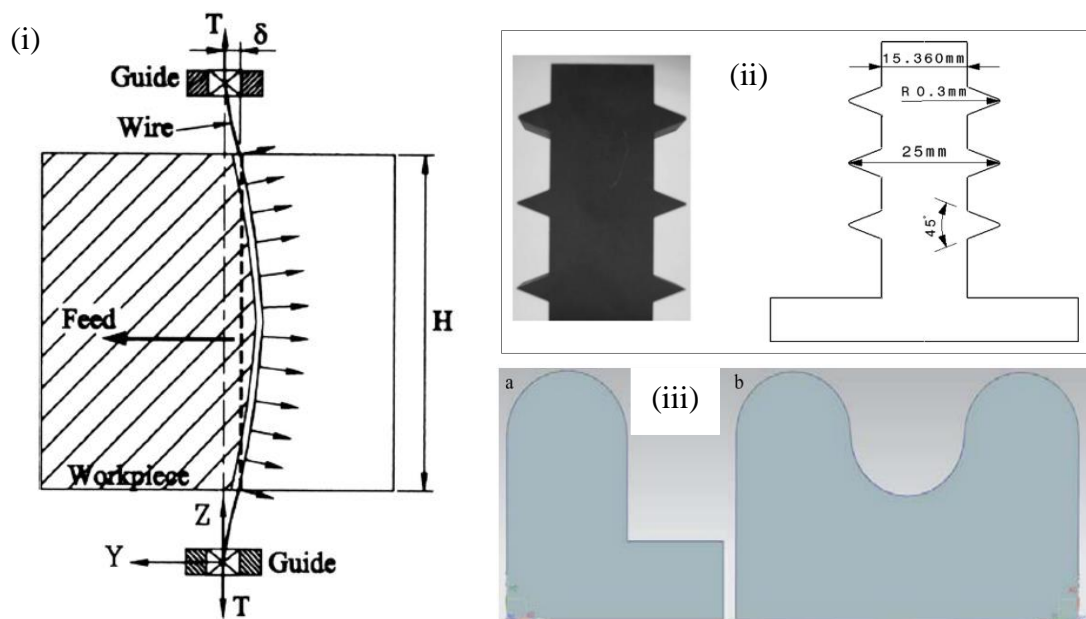
Figure 2.12 (i) Wire bending which causes lag (Firouzabadi et al., 2015) (ii) Specimen shapes (Firouzabadi et al., 2015) (iii) Circular profile of the workpiece (Conde et al., 2016)

Wire lag is a gap/delay in the wire to travel to a co-ordinate due to its elastic nature. This causes corner error and dimensional shift during profiling. This lag may be caused due to various other reasons also. A parametric investigation was carried out by Puri and Bhattacharyya (2003) using WEDM. It was discovered that the reason for wire lag were forces from the gas bubbles coming out during the erosion, hydraulic forces due to flushing, electrostatic force and electrodynamics forces. The author also highlights there should be

a tradeoff between surface quality and geometrical accuracy due to the lag of wire, to get the highest productivity with accuracy.

Firouzabadi et al. (2015) have reported wire bending as shown in fig. 2.12 (i) leading to wire lag is the main reason for corner error, where the tip of the corner is removed by the lag in wire and heat concentration. They have also highlighted that the corner errors were caused due to lag in the wire, wire vibrations, and increased discharges at machining of corners for the profiles shown in fig 2.12 (ii). Beltrami et al. (1996) reported improvement in dimensional accuracies by creating a feedback loop. The deviations are measured by online monitoring and controlling of the wire with the aid of the optical sensor the deviations were eliminated. These are some of the methods where the corner inaccuracies were eliminated. A. Conde et al. (2016) have identified the main reason for inaccuracies like wire-lag and concavity shape caused by electromagnetic and electrostatic forces on the workpiece while machining curved profiles as in Fig. 2.12 (iii). From simulations, it was established that for circles of radius r (3 mm < r) effect of wire lag is negligibly found by mathematical simulation of the 'pursuit curve' for free-form geometries. Different micro-geometry gear manufacturing errors and parameters influencing the errors were highlighted by Jain et al. (2013) during micro gear machining. The escalation in discharge energy was due to the higher voltage and pulse on-time lead to an increase in the electro-dynamic forces. These forces deviate the wire from its path during sparking contributing to errors. The wire lag was the major factor influencing the error, which was high during high pulse on time. As the generation of excessive forces caused by gas bubbles. But, in the case of lower pulse off time, the hydraulic force of flushing pressure influenced wire lag. Sarkar et al. (2016) have reported a unique technique to estimate the wire deflection and gap force intensity with the help of an analytical model. The inaccuracies could be compensated which was calculated to eliminate the errors. The authors observed that the programmed radius was inversely related to wire lag compensation.

During machining of titanium-based alloy, Ghodsiyeh et al. (2014) have reported a study on the behaviour of sparking gap, surface roughness, white layer thickness, wire wear ratio, and wire lag. The servo voltage and peak current influences the lag of the wire. The pulse

on time and peak current was directly proportional to wire lag, whereas it was inversely proportional to pulse off time and servo voltage which was showed to be very significant. The behaviour of machining parameter on multi-walled carbon nanotubes (MWCNT) filled alumina composites was investigated by Singh et al. (2017). At 5 vol. % of MWCNT, the wire lag was observed due to a decrease in thermal conductivity in the workmaterial.

2.5.3 Corner Error Affecting Profile Accuracy
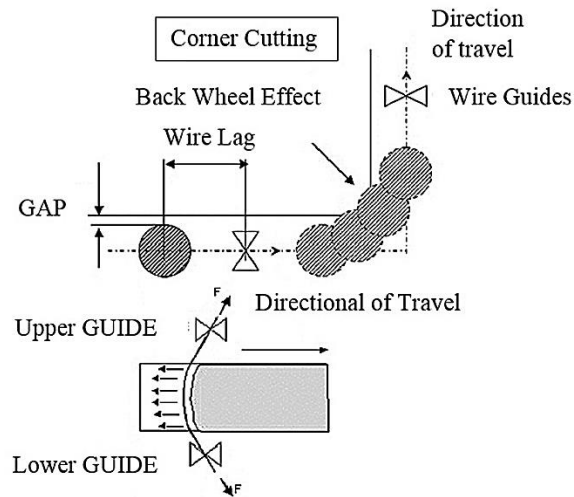
Figure 2.13 Bending of wire leading to back wheel effect. (J.A. Sanchez et al., 2007)

The corner error is the uncut region in the profile during machining. This mainly reduces the profile area, as the area is lesser than the programmed area. In research carried out by Sanchez et al. (2007), the limitation in cutting speed and wire lag while machining of corners was explored. This also affects the errors at different zones of corners in both rough and finishing cut as shown in fig. 2.13. The authors established that the results depend on wire offset and by optimizing the process parameters, the errors can be reduced by increasing the number of finished cuts. Han et al. (2007) have simulated the movement of wire between the wire path and the NC path during different corners at an acute angle, right angle, and obtuse angle machining was performed. This path was simulated based on the geometry and wire vibration analysis which was experimentally validated.

Lin et al. (2001) have reported the corner error may occur because of wire defection and vibration which was controlled using a strategy based on fuzzy logic. A multivariable fuzzy logic controller was used to considering the percentage of sparking force that can be accounted for controlling the machining accuracy at the optimal cutting speeds were achieved. A dynamic model using a PI controller from which the dynamic performance of the wire tension control mechanism was developed by Yan and Huang (2017). This is a closed-loop system having dynamic absorbers to the idle rollers in the wire transportation system. A 7% of satisfactory steady-state error was observed and washing of the apex edge along the thickness during machining was reduced by 50% and 40% in contrast to the open-loop mechanism.

During WEDM, Hsue et al. (2007) investigated conventional rotary motor drivers with linear synchronous motors. They were both furnished with linear scales having a sub-micrometre resolution. It was found that linear synchronous motors were more accurate even when the feed direction was changed at higher feeds. Dodun et al. (2009) have reported machining of the corners' radii and angles in small thickness workpieces of aluminium and steel. It was observed that there was a small bending of a sharp corner during the machining of the profile. The reasons for the corner error inaccuracies was wire deflection caused by unbalance of the external load. The discharge concentration can be reduced by optimizing the control factors as highlighted by Chen et al. (2014). An elliptical model was proposed to predict the corner error that fitted the right and obtuse angle corner-cutting, but a deviation was observed at the acute angle due increase in discharge energy at corners. Farooq et al. (2020) have machined convex and concave profiles using WEDM in Ti6Al4V alloy. It was seen that machining with optimal parameters yielded 0.250% overcut in convex and 0.236% undercut in concave profiles. Yan et al. (2020) observed corner deformation although WEDM was a noncontact machining process. This deformation was influenced by pulse on time and discharge peak current and reduces along with pulse-off time. By the optimal process parameter, corner deformation was reduced to 34.3 μm. Abyar et al. (2019) have examined successive machining stages during straight and curved paths. It was observed that the first finishing stage gave an accuracy of 78%

and the second finishing yielded an accuracy of 83%. Bisaria and Shandilya (2019) machined corner error for acute angle (60°), right angle (90°) and obtuse angle (120°) triangular profiles using WEDM of Ni50.89Ti49.11 shape memory alloy. It was concluded that at low pulse parameters, the corner error decreased by 43.38%, 31.12%, and 29.04%, respectively.

2.5.4 Dimensional Shift Influencing Profile Accuracy

The dimension shift is the shift or offset of the machined profile compared to the programmed profile. Many factors in WEDM influences the dimensional shift which in turn affects the profile accuracy. A controller based on genetic algorithm-based fuzzy logic was designed by Yan and Fang (2008) to maintain a constant tension value and smooth wire flow. The results concluded that fuzzy logic control fitted to the wire transport system was found to have a lesser error as it has a quicker transient response and lesser steady-state error. Wang et al. (2017) investigated the machining of gear teeth made of the X153CrMoV12 workpiece using micro-WEDM. The self-centring flexible fixture was employed to achieve a sharp corner. By appropriate process parameters, minimum kerf width can be obtained by choosing suitable open voltage and discharge capacitance. Sarkar et al. (2017) used an artificial neural network based on the Bayesian regularization method to predict the accuracy for the response parameter like cutting speed, surface roughness and dimensional shift. The variation of dimensional shift with cutting speed and surface roughness were mapped. Selvakumar et al. (2018) during machining aluminium 5083 (AA5083) investigated the output responses such as cutting speed, surface roughness, corner error and dimensional shift. The authors noticed that it was not a real response in turn it was caused due to the offset (overcutting/undercutting). It can be avoided by giving compensation to enhance the dimensional accuracy of the workpiece. The Genetic Algorithm Approach was followed during a study conducted by Padhi et al. (2016) to optimize the dimensional deviation during EN-31 steel WEDM. Ishfaq et al. (2020a) have optimized kerf width, axial and lateral dimensional errors. It was observed an improvement of 13.5%, 49%, and 27% from the optimal parameters respectively. Chalisgaonkar and

Kumar (2015) have highlighted that wire type, pulse on time and wire offset are the most significant parameters during WEDM. Fig. 2.14 (a) and (b) shows the different path during the rough and trim cut indicating the accuracy of the cut profile. Ishfaq et al. (2020b) reported a reduction of 13.5%, 49%, and 27% of kerf width, axial, and lateral dimensional errors by parametric variation. The open voltage, pulse on and off time were found to be the most important influential factors on dimensional accuracy. Nain et al. (2018) have concluded that cutting speed, dimensional deviation and wire wear ratio increases as the pulse on time increases. The optimization was carried out to get the high cutting speed and lowest dimensional deviation and wire wear ratio. Further Saleh et al. (2020) concluded that microchannels quality (surface integrity and dimensional accuracy) is influenced by pulse on time, pulse off time and servo gap voltage during WEDM of Monel 400. Arindam Mukhuti et al. (2006) have minimized the machining time and overcut by adapting Taguchi's methodology using MOORA method during WEDM of Inconel 600.
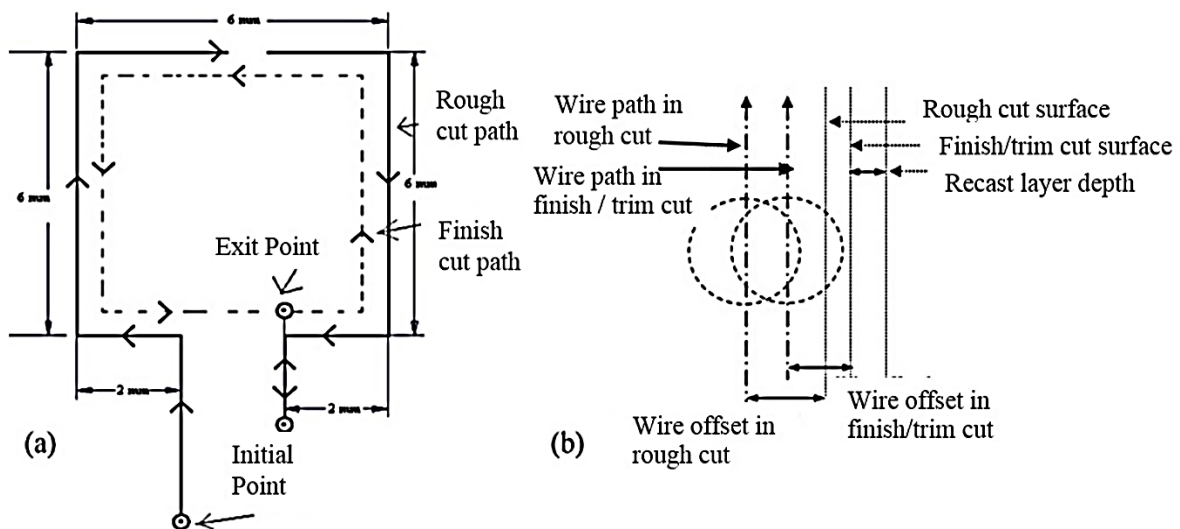
Figure 2.14 (a) Wire path profile during machining. (b) Wire offset in rough cut and trim cut. (Chalisgaonkar and Kumar, 2015)

2.6 PREDICTION OF RESPONSE PARAMETERS IN WEDM

Numerical studies mostly used in the prediction, simulation and optimization of the input parameters. Many information before occurrence can be formulated making the behaviour

of the system more predictable and simulation gives a better understanding of the process. The researches carried out by different investigators in WEDM are highlighted below. A multi-spark thermo-physical model that was upgraded by altering the single spark thermal heat transfer model was formulated by Shahane and Pande (2016). This model considers overlapping multi sparks for the prediction of the temperature distribution and material removal rate in the workpiece of aluminium. Banerjee and Prasad (2010) have modelled thermal models for the prediction of safe operating ranges, random pulse and clusters models that are recommended for predicting thermal load distribution. Singh et al. (2018) modelled using finite element and finite volume method, a 2-D numerical model to understand the influence of assisting electrode on material removal rate. Garg et al. (2016) have developed predictive models with the aid of response surface methodology to predict the material removal rate and spark gap for Al/ZrO2 (p)-MMCs. Wang et al. (2017) have formulated a model for forecasting the surface roughness with an error of less than 1% using regression equation from the root mean square and arithmetic mean roughness values of acoustic emission. However soft computing can also be used for predictions and optimization of input parameters in the WEDM process. It can be defined as a group of computational techniques based on artificial intelligence and natural selection that provides a quick and cost-effective solution to very complex problems. Among many soft computing techniques, artificial neural network (ANN) and adaptive neuro-fuzzy interference system (ANFIS) were prominent. It can be applied in WEDM for the prediction of different response parameters. In our research work, soft computing methods like artificial neural networks and adaptive neural fuzzy interference system were used for prediction of output parameters during WEDM.

2.6.1 Artificial Neural Network (ANN)

Artificial neural networks, computing systems inspired by the biological neural networks in brains. These neural networks with different input and output combinations give the output for the required input set. Artificial neural networks have been applied to the

prediction of WEDM response characteristics. Some of the researcher's observations and findings have been highlighted below in table 2.1.

Table 2.1 Different published research work on artificial neural network.

Sl. No.	Author	ANN model	A brief description of the response parameters used for predicting the outcome of the work
1	Yusoff et al. (2019)	Feedforward back propagation neural network (FFNN) with 5–6–6–4 architecture was used.	The material removal rate, surface roughness, cutting speed and width of kerf was predicted using ortho ANN. The best-predicted results were less than 10% error.
2	Saha et al. (2008)	Feed-forward back-propagation neural network (BPNN) model having 4-11-2 architecture was used.	ANN model prediction was found more accurate than regression model prediction with 3.29% overall mean prediction while the prediction of cutting speed and surface roughness.
3	Singh and Mirsa (2019)	Feedforward BPNN with Levenberg-Marquardt (4-10-2) was employed	The ANN-BPNN models are more efficient than the RSM models because of the lower values of RMSE and PEP in the prediction of surface roughness.
4	Sarkar et al. (2010)	Bayesian regularization and early stopping method.	Prediction of trim cutting speed, average surface roughness and dimensional sift using the ANN model.
5	Conde et al. (2018)	Elman-based Layer Recurrent Neural Network	Prediction of wire paths of variable radius for machining of the component and A deviation below 6 μm occurred in machined components
6	Nain et al. (2018)	BP-ANN model	The BP-ANN model proves more accurate over the fuzzy-logic model for both surface roughness and waviness of machining Udimet-L605.
7	Phate and Toney (2019)	-	ANN model was concluded to be superior to the dimensional analysis model in the prediction of material removal rate and surface roughness.

8	Yusoff et al. (2018)	Cascade forward backpropagation neural network	During the prediction of surface roughness cutting speed and sparking gap an average of 5.16% error is generated.
9	Ramakrishnan and Karunamoorthy, (2008)	Back-propagation algorithms	ANN models predicted the performance characteristics of the WEDM process more accurately in the prediction material removal rate and surface roughness.
10	Jafari (2017)	Bayesian regularization algorithm	An assessment was performed to know the variation of the surface roughness with process parameters. The coefficient of determination of 99.5 % was obtained indicating the efficiency of prediction.
11	Ming et al. (2016)	ANN-LWPA	Both surface roughness and material removal rate were predicted and the average errors are 19.70 and 18.01 % respectively.

ANN is a well-known prediction method that can be used in knowing the outcomes of different parametric combination in WEDM. From the above table, it can be seen that different ANN model combinations have been used by the researchers for prediction. The most popular ANN model, the back-propagation neural network has been employed for prediction in our research work to predict the output responses of WEDM.

2.6.2 Adaptive neural fuzzy interference system (ANFIS)

Adaptive neural fuzzy interference system is similar to neural networks and it is the integration of both neural networks and fuzzy logic principles. It has five layers that are used to construct this inference system. This method can be used for the prediction of different response parameters in WEDM as it has many machining parameters that influence the response characteristics. Some of the researchers who have carried out their work by ANFIS in their WEDM study are tabulated briefly in table 2.2.

Table 2.2 Different researchers worked on adaptive neuro-fuzzy interference system

Sl. No.	Author	A brief description of the parameters used for prediction and outcome of the work
1	Çaydas et al. (2009)	Estimation of the average surface roughness and the white layer thickness (WLT) with various machine parameters

2	Maher et al. (2016)	Prediction of the white layer thickness using process parameters like pulse on time, wire tension, pulse off time, wire-speed, and peak current.
3	Fard et al. (2013)	Prediction of cutting velocity and surface roughness. The mapping relationship between process inputs and main responses.
4	Abhilash and Chakradhar (2020)	It was used to predict the wire breakage situations using the ANFIS model. It was concluded that a higher value of mean gap voltage variation resulted in greater wire wear and inferior part quality. It was found average prediction error was 2.61% compared to experimental values
5	Manikandan et al. (2019)	Predicting output like material removal rate, surface finish, overcut, circularity error and perpendicularity error.
6	Kumanan and Nair (2017)	ANFIS was used to analyze the effect of each parameter on the grey grade.
7	Krishnan and Samuel (2013)	Prediction of material removal rate, and surface roughness, which is important for increasing the productivity and quality of the products.
8	Sarkheyli et al. (2015)	Among different models, the adaptive network-based fuzzy inference system with a modified genetic algorithm was concluded as an accurate tool for prediction.
9	Aldas et al. (2014)	Modelling with different membership functions was used in the prediction of the surface roughness.
10	Azhiri et al. (2014)	Cutting velocity and surface roughness was predicted using ANFIS. A clear mapping of output response with input parameters was derived from ANFIS.
11	Naidu et al. (2020)	A hybrid Grey ANFIS was utilized as an intelligent decision-making tool to predict desired multi-performance index.
12	Maher et al. (2015)	Prediction of cutting speed, surface roughness, heat-affected zone and ANFIS mapping for knowing the variation of response parameters to pulse on time, wire tension, peak current and spark energy.

As ANFIS integrates both neural networks and fuzzy logic principles for the prediction of response parameters in WEDM. In most of the cases, the ANFIS has been an accurate predictor compared to other models. This not only predicts the output responses but also helps in mapping the response parameters. This mapping provides a better understanding of the behaviour of the output parameter at different input parameters.

2.7 SUMMARY OF THE LITERATURE SURVEY

The above literature shows different output responses that were measured at different machining input parameters. It was observed that there is a requirement for taper machining of nickel-based alloys due to the demand in various applications. The traditional tapering mechanism in WEDM and the disadvantages that were observed during the conventional tapering operation due to bending of wire was highlighted. Different errors that occur during WEDM was outlined in this chapter. The ANN and ANFIS models used for the prediction of different response characteristics were tabulated in this section. Based on the detailed literature review the research gaps and objectives were derived as stated below

2.8 RESEARCH GAP FROM THE LITERATURE SURVEY

The different research gaps have been noticed based on the above literature and systematically summarized below and the same work has been carried out

1. To explore suitable cutting parameters for profiling from input parameters such as like pulse on time, pulse off time, servo voltage, wire-speed, servo feed based on output parameters such as cutting speed, surface integrity and angular error on Hastelloy-X during tapering using WEDM.

2. The investigation profiling parameters such as WGD, CDT, WO, CSO and TA during triangular profile for different taper angles like 0°, 15°, 30° and further many performance characteristics like profiling speed, surface integrity, angular error can be examined.

3. To understand the effects of profiling parameters in taper machining and its dimensional characteristics of corner error and dimensional shift for different shapes like square, and circular have been investigated.

4. ANN and ANFIS soft computing methods can be used for the prediction of output performance parameters like cutting speed, surface roughness for different combinations of input parameters during taper profiling.

2.9 OBJECTIVES OF THE RESEARCH WORK

From the above literature and research gaps, the dimensional characteristics with surface aspects have to be taken into account during the machining in WEDM. Different effects of WEDM parameters like wire guide distance (WGD), wire offset (WO), cutting speed override (CSO) and corner dwell time (CDT) were studied on basic profiling shapes like triangular, square and circular profiles on Hastelloy-X. Prediction of response parameters at different parametric conditions is also important for achieving efficient machining with dimensionally accurate profiles. Keeping all this as a focus, the specific objectives of the research work are derived as follows.

1. To investigate slant taper cutting for different cutting speed at different angles like 0°,15°, 30°, 45° & 60° and to choose suitable parameters for profiling based on performance characteristics of angular error, width of cut, surface roughness and surface crack density.

2. Examine the input profiling parameters like wire distance between guides (WGD), corner dwell time (CDT), wire offset (WO), cutting speed override (CSO) using one factor at a time (OFAT) approach on profiling speed, surface roughness, corner error, recast layer and micro-hardness for simple square profile at different taper angles like 0°, 15° and 30°.

3. Explore the effects of machining slant taper cutting of triangular slot in WEDM with different control parameters like WGD, CDT, WO and CSO at different taper angles like 0°, 15° and 30° on dimensional and machining performance characteristics of profiling speed, surface roughness, angular error, corner error, profile area, recast layer thickness and micro-hardness.

4. Investigation of profiling speed, surface roughness, recast layer thickness, micro-hardness, profile area and corner error on simple slant type taper profiling of square and circular slot profiles at different taper angles i.e. 0°, 15° and 30°.

5. To develop the prediction models using artificial neural network (ANN) and adaptive neuro-fuzzy inference system (ANFIS) for the prediction of profiling speed, surface roughness in slant taper cutting at different angles i.e. 0°, 15° and 30° and comparison of prediction results of the optimal models with experimental data in slant taper cutting.

2.10. NOVELTY OF THE WORK

The aim of the present research is to achieve taper profiling without bending of the wire unlike conventional Wire EDM. In the literature it was seen that to achieve tapering most of the researcher have opted for conventional tapering. But in our method it is simple which eliminates the bending of the wire, as we have used newly designed slant type taper fixture. In the literature the following parameters are studied in detail such as pulse on time, pulse off time, servo voltage, wire feed, input current, servo feed and wire tension on surface roughness, cutting speed, recast layer, and micro hardness.

However, in our research we have focused on basic profiles like triangular, square and circular shapes in normal and tapered conditions. For this study the following in put parameters were considered viz, wire distance between guides (WGD), corner dwell time (CDT), wire offset (WO), cutting speed override (CSO). Based on this the following output parameters i.e. profiling speed, surface roughness, profile area, corner error, recast layer thickness and micro hardness were studied.

CHAPTER 3

EXPERIMENTAL SETUP

3.1 INTRODUCTION

In the present chapter different layout of experimental procedure adapted to investigate various response parameters for simple taper and different profiles are discussed. Further, this chapter discusses the steps followed in material procurement, instruments used for processing, characterization and different methods used for prediction of parameters by using artificial neural networks (ANN) and artificial neural interference system (ANFIS). The response parameters that were related to dimensional aspects and surface integrity with cutting speed was investigated for a simple taper cut. The features like cutting speed, surface roughness, slant angle, profile area, recast layer and corner error are examined for slant profiles of triangle, square and circle on the workpiece.

3.2 SELECTION OF MATERIALS

Superalloys are mainly of three types based on their composition mainly nickel, iron-nickel, and cobalt-nickel. They are a good amalgamation of mechanical strength and high temperature. Hastelloy-X is known as nickel-chromium-iron-molybdenum alloy used for many applications at high-temperature because of its superior properties. The applications like flame holder, turbine blades, tailpipes, spray bars and flame holders having taper structures. Hence, Hastelloy-X was selected for our research work.

3.2.1 Material Procurement

The Hastelloy X was acquired from Narendra Steels Pvt. Ltd, Mumbai, India. It was subjected to EDX analysis at MIT, Manipal, Mangalore, Karnataka, India for conformation of its composition and the same as shown in fig.3.1. It was also confirmed from spectral

analysis tested from "SpectraMax 130779" at Quality Test Laboratory, Mumbai, India. Table 3.1 shows the elemental percentage present in the material and the required range of composition.

Element	Weight%
C	7.75
Al	0.41
Si	0.11
Ti	0.13
Cr	18.33
Mn	0.75
Fe	17.34
Co	0.48
Ni	44.53
Cu	1.41
Mo	7.83
W	0.95

Full Scale 562 cts Cursor: 16.461 (0 cts)
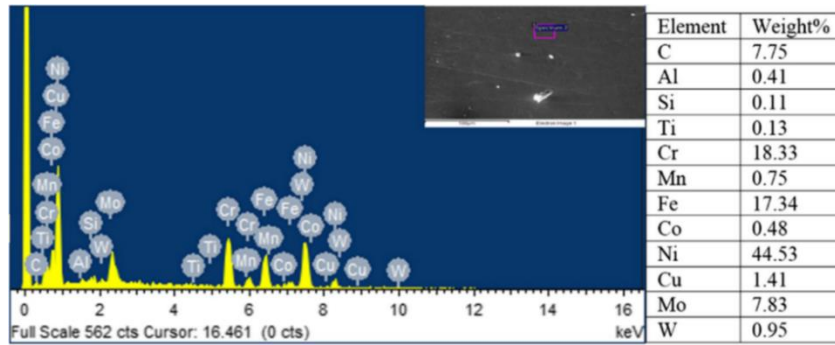
Figure 3.1 EDX of Hastelloy-X

Table 3.1 Chemical composition of Hastelloy-X superalloy

%	C	Si	Mn	P	S	Cr	Mo	Fe	Co	W	Ni
C	0.06	0.21	0.65	0.027	0.01	20.65	8.24	18.05	0.69	0.29	50.88
RC	0.05-0.15	<1	<1	<0.04	<0.03	20.5-23.0	8-10	17-20	0.5-2.5	0.2-1	50-60

*C-Composition, *RC- Required Composition

3.3 EXPERIMENTAL SETUP

The experimental set up mainly consists of WEDM (model: ECOCUT ELPLUS15) purchased from Electronica machine tools, Pune, India. The machine comprises of mountable table, wire guide system, wire supply system, dielectric fluid supply, filter storage tank and wire collector bin. The mounting table can be moved 1µm in both X and Y directions having a size of 370mm×600mm with a workpiece height of 200mm and 300kg maximum weight. The worktable can be simultaneously controlled by a remote on X, Y, u and v axes, which has other facilities of starting and stopping of machining, changing the speed of the table movement etc. It is provided with M8 threaded holes where the workpiece can be fixed using clamps. The wire guide system comprises guides that hold the wire and wire supply mechanism supplying wire from the spool. The guideways are of specific diameters which can be replicable with a tolerance of 5µm. The spool wound

with the wire is fixed in the machine which unwinds as the cutting operation progresses. The deionized water as used dielectric fluid and the machine is provided with a storage tank of capacity of 140 litres. The filter system having a filter paper of 10 µ single cartridge. The wire collector bin collects the machined wire where it has to be emptied after a certain time. The machine is also provided with ELCAM a software that allows reading and simulate the drawing in the system with USB 2.0 for data transfer. The ELCAM software generates system-specific NC codes based on the part drawing to be machined. The WEDM setup was shown in fig. 3.2.

Figure 3.2 Wire Electric Discharge Machine Setup

3.3.1 Experimental Procedure

Initially based on material-tool combination basic cutting parameters like pulse on time, pulse off time, wire feed, servo voltage, servo feed that could be employed for profiling were investigated. Further, the experimental parameters like wire guide distance, wire offset, corner dwell time and cutting speed override were studied using one factor suitable for profiling one factor at a time approach. This provided an outline to understand the effect of experimental parameters. The flow chart of the experimental plan has been shown in fig. 3.3. However, a

detailed experimental procedure has been described below:

- Hastelloy X, a nickel-based superalloy was chosen for the present study. It is difficult to machine, material that is chemically stable and corrosion-resistant. It has many precision applications like gas turbine impellers, dies and stampings, nozzles etc. The initial cutting parameters were chosen based on the trial experiments.

- A fixture that was capable of providing a slant angle to the workpiece was designed. This slant type fixture was made of aluminium and machined through CNC as shown in fig.3.10. It could easily lock the workpiece at different angles and could be easily fixed to the WEDM bed.

- To determine the range of cutting parameters like pulse on time, pulse off time, servo voltage and wire feed were used in angular machining giving simple taper profiles at different slant angles. The favourable cutting parameters were determined and these cutting parameters were used for further investigation in profiling.

- As the cutting parameters were fixed the experiments were performed considering one factor at a time approach (OFAT). A simple square profile was employed to study the effect of various control parameters on the WEDM performance characteristics. The profile parameters were wire guide distance, wire offset, corner dwell time and cutting speed override where the simple profile was chosen.

- The significant control parameters are considered to evaluate the effect of different wire diameters on the WEDM performance characteristics such as cutting speed, surface roughness, recast layer formation, subsurface micro-hardness, microstructural and elemental changes.

- As the cutting and the profile parameters were chosen different shapes were machined at 0°, 15° and 30° slant angles. The .NC files were programmed using ELCAM for different profiles namely triangle, square and Circular of 1mm, 3mm and 5mm dimensions. The Taguchi L16

57

orthogonal array was employed at different slant angles.

- With the aid of the slant fixture as simple triangular shape profile was machined taking profile parameters at different slant angles. The performance characteristics like cutting speed, surface roughness, profile area, corner error, taper angle, recast layer thickness and micro-hardness were investigated.

- The next profile machined using the slant fixture was a simple square at different angles. The characteristics like cutting speed, surface roughness, profile area, corner error, taper angle, recast layer thickness, metallurgical changes and micro-hardness at different regions were examined.

- Similarly cutting speed, surface roughness, profile area, taper angle, recast layer thickness, metallurgical changes and micro-hardness were characterized for circular shaped profiles using different profile parameters at 0°, 15° and 30° slant angles.

- The Artificial neural network was used for process modelling, trained for the prediction of cutting speed, surface roughness and profile area of all the profile shapes at different slant angles. The prediction was validated with experimentation at different profile parameters.

- The Adaptive Neuro-Fuzzy Interference System (ANFIS) was used in the prediction of cutting speed and surface roughness for different profiling shapes. The profiling parameters and the slant angle were considered as input parameters. The ANFIS also gave the input and output characteristic mapping were helped in understanding the variation of performance characteristics for different profiling parameters.

- The ANN, ANFIS and experimental values of cutting speed and surface roughness were compared to evaluate an accurate prediction method with errors used for prediction in taper machining.

3.3.2 Experimental Methods

1. One Factor at a Time (OFAT)

This is an experimental method that helping in problem solving technique to identify the critical causes for an effect from a pool of parameters. When there are different parameters this method provides to study the effects of individual parameters. This can be achieved by varying single parameter at different levels and keeping the other parameters constant. By doing this the effect of each level of each parameter on the output variables can be analyzed easily. In our experimentation we have four parameters namely Wire guide distance (WDG), Corner dwell time (CDT), Wire offset (WO) and Cutting speed override (CSO). We analyses each and every parameter in chapter 4 by varying one parameter and keeping others constant. For example in our investigation we have 4 parameters in table 4.12. As shown in table 3.2 each individual parameters are varied keeping the other parameters in minimal level.

Table 3.2 One factor at a time experiments

Trials	Wire guide distance (WGD) (mm)	Corner Dwell Time (CDT) (s)	Wire Offset (WO) (μm)	Cutting speed Override (CSO) (%)
1	90	0	0	31
2	100	0	0	31
3	110	0	0	31
4	120	0	0	31
-	-	-	-	-
-	-	-	-	-
-	-	-	-	-
-	-	-	-	-
n-3	90	0	0	31
n-2	90	0	0	54
n-1	90	0	0	77
n	90	0	0	100

2. ANOVA (Analysis of Variance)

Analysis of variance (ANOVA) is a statistical analysis tool that splits an observed aggregate variability found inside a data set into two parts: systematic factors and

random factors. The ANOVA test to determine the influence that independent variables have on the dependent variable in a study. In our experimentation we have used the ANOVA for finding percentage contribution of the parameter on output variable and significant parameter that influences on output parameter. In our investigation we have used ANOVA as shown in chapter 5 and chapter 6. Steps for calculating ANOVA table

1. Calculate the sample means for each of our samples as well as the mean for all of the sample data.

2. Calculate the sum of squares of error. Here within each sample, we square the deviation of each data value from the sample mean. The sum of all of the squared deviations is the sum of squares of error, abbreviated SSE.

3. Calculate the sum of squares of treatment. We square the deviation of each sample mean from the overall mean. The sum of all of these squared deviations is multiplied by one less than the number of samples we have. This number is the sum of squares of treatment, abbreviated SST.

4. Calculate the degrees of freedom. The overall number of degrees of freedom is one less than the total number of data points in our sample, or n - 1. The number of degrees of freedom of treatment is one less than the number of samples used, or m - 1. The number of degrees of freedom of error is the total number of data points, minus the number of samples, or n - m.

5. Calculate the mean square of error. This is denoted MSE = SSE/(n - m).

6. Calculate the mean square of treatment. This is denoted MST = SST/m - `1.

7. Calculate the F statistic. This is the ratio of the two mean squares that we calculated. So F = MST/MSE.

8. Once the F value is determined the P value can be calculated using F distribution table.

Experimental Plan
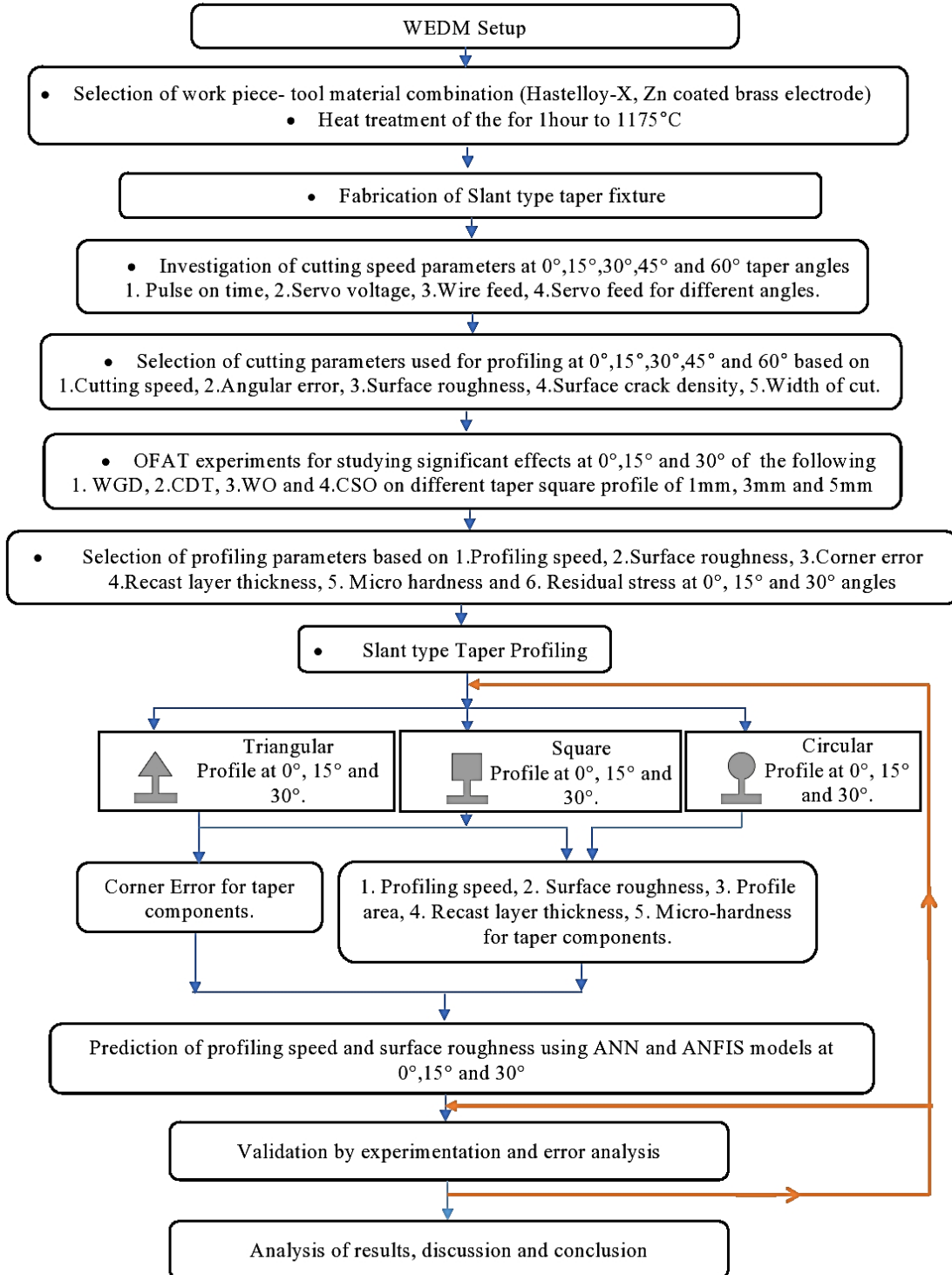
Figure 3.3 Flowchart of the plan of experiments

3.4 PERFORMANCE CHARACTERISTICS OF THE MACHINED PROFILES

The performance characteristics that were assessed in the investigation are profiling speed, surface roughness, corner error, slant area, taper angle, microhardness and recast layer thickness.

3.4.1 Cutting Speed/ Profiling Speed

The cutting speed is a vital parameter that helps in the finding of productivity in machining. The cutting speed varies with the thickness and orientation of the workpieces. The cutting speed of the specimen was calculated using Eq. (3.1). Total path length was calculated, whereas total machining time was recorded using a digital stopwatch (accuracy of 0.01 s).

$$\text{Cutting Speed (mm/min)} = \frac{\text{Total path length (mm)}}{\text{Total machining time (min)}} \qquad (3.1)$$

3.4.2 Surface Roughness Tester

The surface roughness tester of Model SURFTEST SJ-301 form MITUTOYO, Japan as shown in fig.3.4. It is used to measure the surface roughness of the surface machined by WEDM. It consists of a stylus which is made of diamond. The stylus is moved with a sampling length, where the surface peaks and valleys is generated at a certain speed and presented in the form of graph. The stylus tip diameter is 2µm and force of 0.75N used to measure surface roughness. The stylus tip has an angle of 60°. The speed generally is 0.25mm/sec. A random evaluation length within the range of 0.3 mm - 12.5 mm (Unit: 0.1 mm) can be set. It was also equipped with a printer facility through which the R_a profile can be documented.

Figure 3.4 Surface Roughness Tester

3.4.3 Optical Microscope

Specimens after machining WEDM is observed by Optical microscopy is as shown in fig.3.5. The microscope is connected to a computer having BIOVIS material plus software for different analysis. The microscope is having a magnification from 4X to 1000X. Images such as corner edges and corner damages can be investigated by using this microscope.

Figure 3.5 Optical Microscope

3.4.4 Scanning Electron Microscope (SEM)

The scanning electron microscope of model JEO JSM- 638OLA from JEOL, USA was used for investigation as shown in fig. 3.6 (a). The resolution of the equipment is from 3nm

to 3,00,000 X having an aperture size of 30µm and acceleration voltage of 20kV. SEM is used to measure the profiles and to observe the behaviour of the edges that were been machined from wire EDM. The corner edges, errors and radius was measured by using SEM.
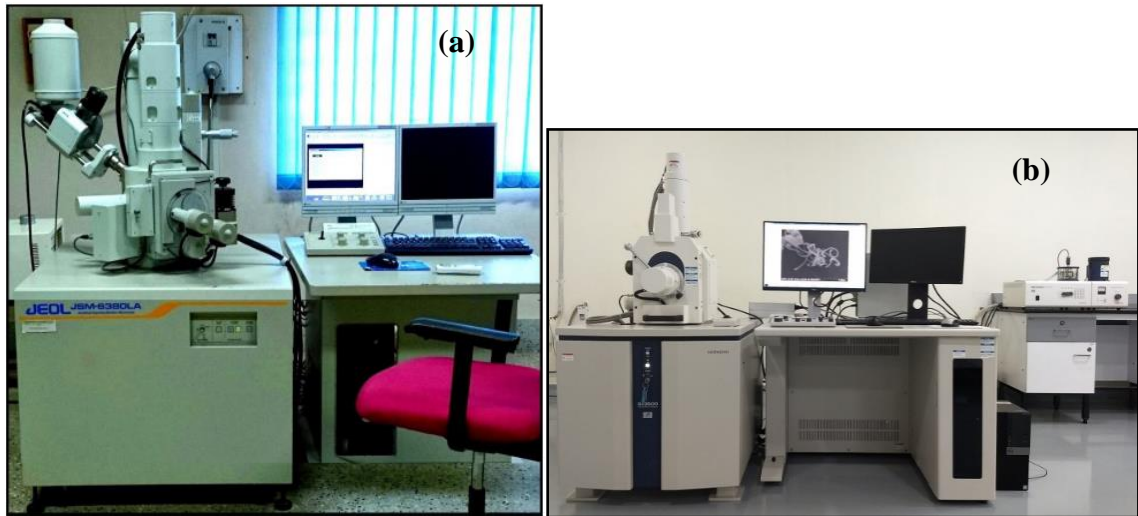
Figure 3.6 SEM (a) JEO JSM- 638OLA model (b) Hitachi S 3500 model

The SEM of Hitachi S 3500 make were also used for observing the surface morphology, recast layer thickness etc. This facility was available at "Centre for Incubation, Innovation, Research and Consultancy (CIIRC®)" Bangalore as shown in fig.3.6 (b). The resolution of from this equipment was 30nm. The resolution varies up to 3,00,000 X. The acceleration voltage varied from 0.3 to 30 kV. The corner radius was measured using SEM images by elliptical curve fitting method (Cheng et al. 2014) where the image was fitted to an ellipse that can inter lap the corners formed, where wire lag(δ) can be approximately taken as half of the length of the major axis of the ellipse that is fitted to corner radii.

3.4.5 Coordinate Measuring Machine (CMM)

The accuracy of the machined profile was measured using a co-ordinate measuring machine of model TESA MICRO-HITE 3D from Hexagon SD, the United States. This facility is available at Tespa Calibration Services, Bangalore, India as shown in fig.3.7. It contains a rotary axis along with measuring a range of X-600mm, Y-950mm, Z-430mm

with a high-speed scanning probe head and can measure co-ordinates with a minimum resolution of 0.1µm. It was claimed that CMM can reproduce or replicate within the tolerance range of ±5µm. The probe traverses across the specimen after fixing on the work table where the coordinates are recorded different characteristics such as distance, angle, parallelism etc. The machine is connected to a computer having licensed software TESA-REFLEX. The part drawing in the form of .iges format is fed to the system. The probe equipped with a sensor moves to the specific co-ordinates sensing the features of the part to be inspected. The different characteristics like profile area, taper angle can be measured.

Figure 3.7 Co-ordinate measuring Machine

3.4.6 Micro-hardness
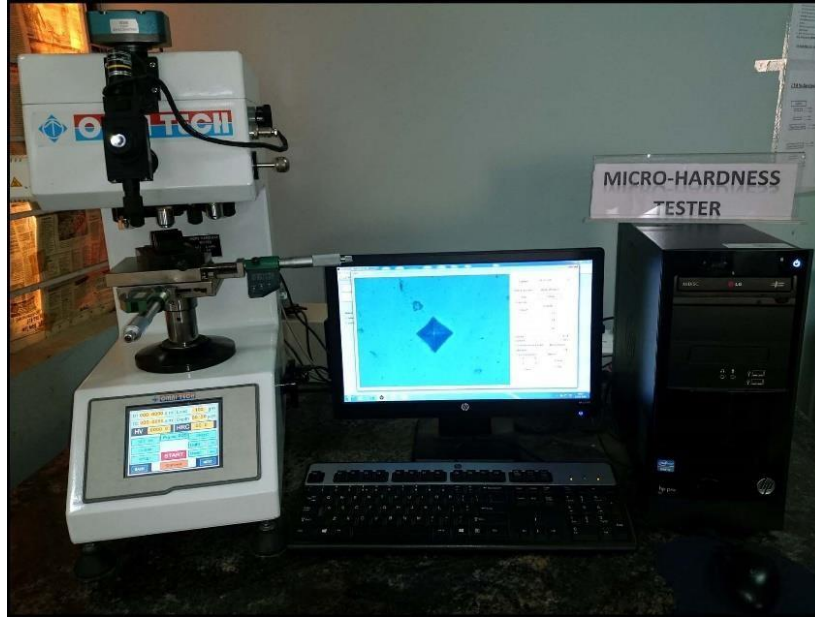
Figure 3.8 Micro-hardness Tester

The subsurface microhardness of the WEDMed surface was characterized by microhardness tester (Model: MVH–S–AUTO from OMNI TECH, PUNE, INDIA) as shown in fig.3.8. This machine is capable of measuring hardness in terms of Knoop and Vickers hardness number. The Vicker hardness was employed in measuring the hardness of the machined surface. The weight of 200gms with a dwell time of 10 sec was followed for the indentation. The indentation was in the form of rhombus where the opposite corners were measured and hardness was calculated as per the eq. 3.2 with the help of the preloaded software "QuantimetMHT". For repeatability purpose we measured at different locations. An average of 5 indentation values of hardness were taken for the investigation.

$$Hv = \frac{2*F*\sin(136°/2)}{d^2} = 1.854\frac{F}{d^2} \qquad (3.2)$$

Where Hv= Vickers hardness of sample,

F=Applied Load,

d=Mean diagonal length of a square pyramid.

3.4.7 Residual Stress

Residual stresses are the stresses which the material retains after removing thermal or mechanical loads. These stresses are retained due to the lack of elasticity in the material. In WEDM, due to sparks and dielectric medium, the material is always subjected to a sudden heating /cooling cycle due to which there is residual stress-induced inside the machined surface. For residual stress measurement samples were prepared as per the equipment requirement with dimensions of 3 x 3 x 5 mm. Fig.3.9 shows the residual stress equipment used for measurement. The residual stress measurement was done using X-Ray Diffraction (XRD) technique in IIT Bombay (model EMPYREAN, PANalytical).

$$\sigma_r = \frac{m}{d^2} \left[\frac{E}{1+\gamma} \right] \tag{3.3}$$

The residual stress (Mpa), σ_r is calculated using equation (3.3). Here, E is Young's modulus, γ is the Poisson's ratio, m is the slope.
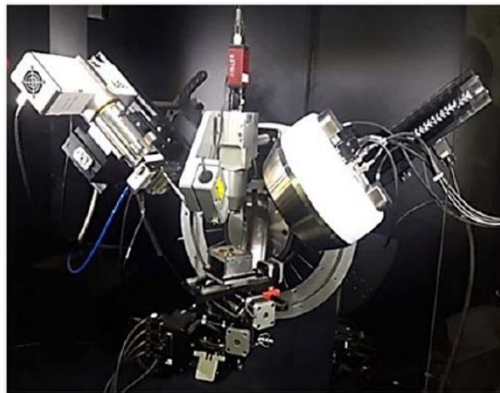
Figure 3.9 Setup for residual stress analysis.

3.5 FABRICATION OF SLANT FIXTURE

The fixture was made up of Aluminium H9 series procured form Hi-Tech Sales Corporation, Mangalore, India. It was placed on the mount table with the help of M8 Allen screws. The fixture mainly consists of a base plate, side plate and angle plate. The whole

fixture is assembled with the help of M5 screws. The base plate ensures a firm grip to fixture and supports the side plate and angular plate. The angular plate can be locked at a required angle based on the side plate with M8 Allen screws. The workpiece to be machining can be place and fix on the angular plate with the help of M8 Allen screws.

3.5.1 Slant type taper fixture Specifications
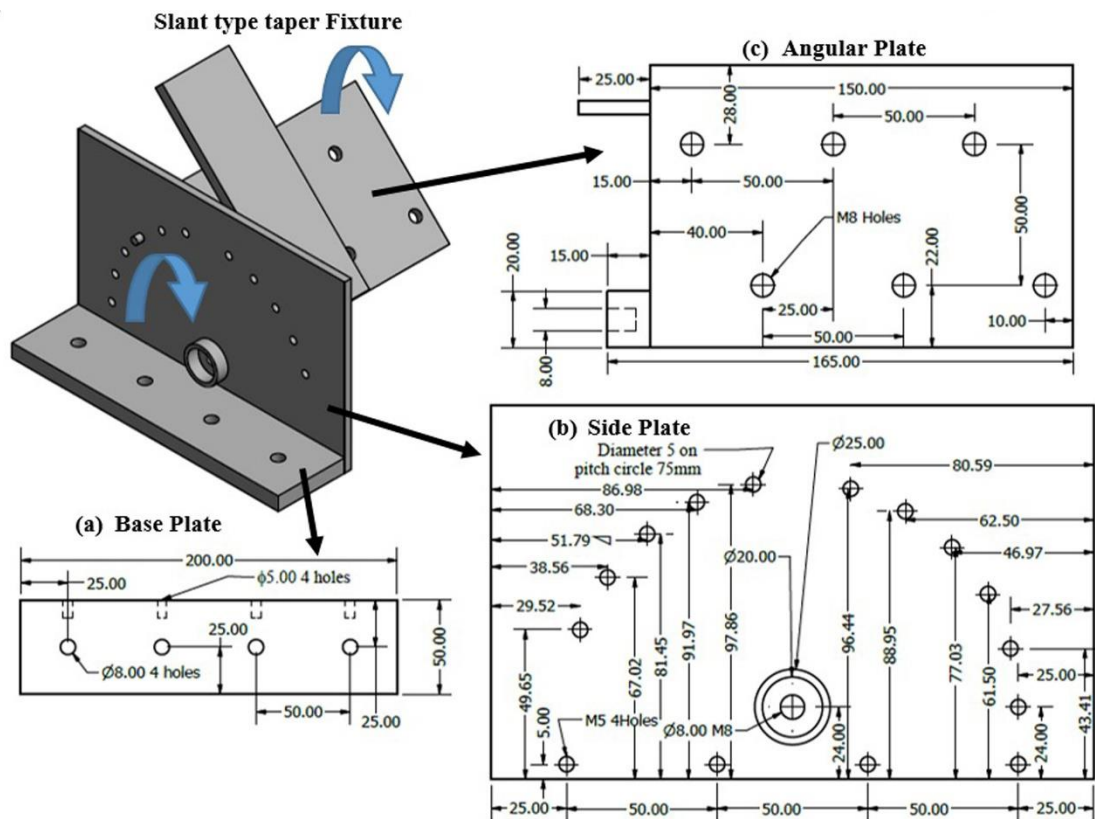
Figure 3.10 Slant type taper Fixture part specification (Manoj et al., Copyrights: Diary Number: 2378/2019-CO/L., Reg. No: L-81981/2019)

The fixture was modelled in Autocad Inventor Professional 2016 software consisting of base, side and angular plates. This was fabricated by GOVT. TOOL ROOM & TRG CENTRE (GTTC) Mangalore, Karnataka, India as shown in fig.3.10. The parts were assembled and fixed to the WEDM table as shown in fig. 3.11(a). The angle plate can be rotated for the required angle by slots on the side plate. Fig 3.11(b) shows the position of the workpiece in between the guideways for different angles of 0°, 15°, 30°, 45°, 60°, 20°,

35°, 50° and 80°. Indian copyright (Copyrights: Diary Number: 2378/2019-CO/L., Reg. No: L-81981/2019) was obtained to this fixture that was used for machining of taper components.
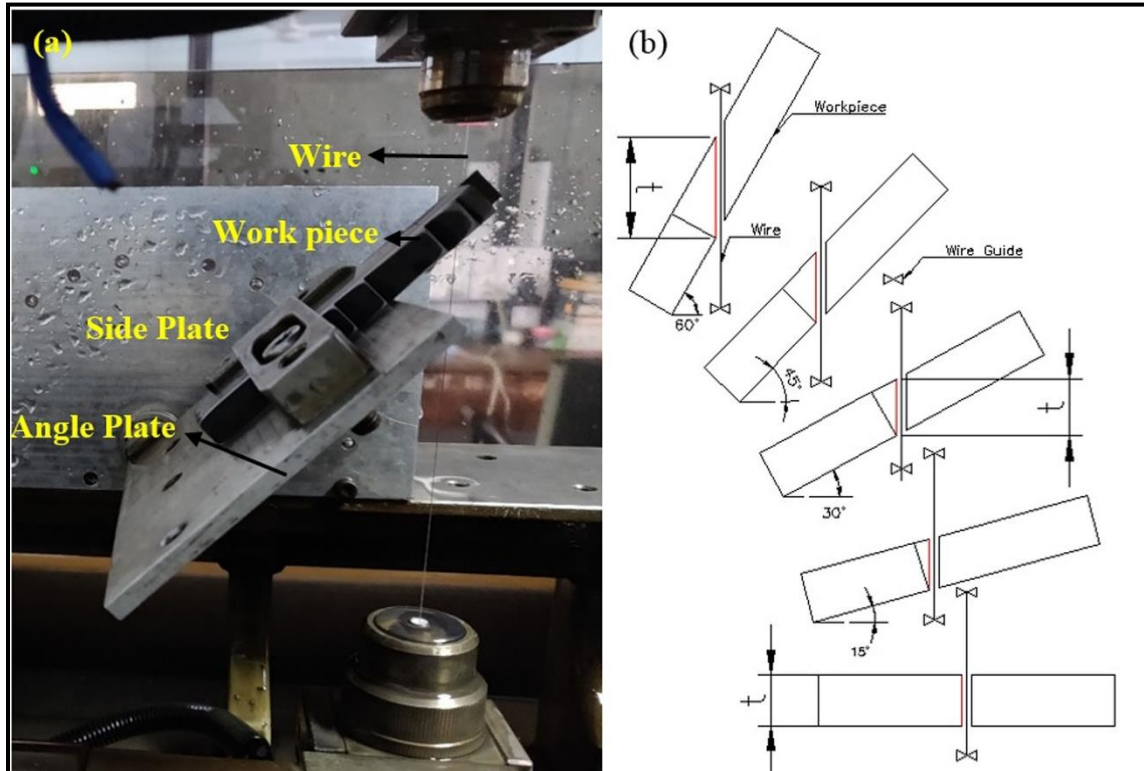
Figure 3.11 (a) Slant type taper fixture (b) Slant cut at different angles

3.6 NUMERICAL MODELLING FOR PREDICTION

3.6.1 Artificial Neural Network Prediction

A neural network can be defined as the logical assembly used for multiple processing elements that communicate and links with each other by the interconnections present between the processors. It follows a principle followed by the human neural system which passes the signals or impulses for communication. In our study, different input parameters like wire guide distance, corner dwell time, cutting speed over-ride, wire offset and taper angle were considered for the prediction of profiling speed and surface roughness at different taper angles 0°, 15° and 30° as shown in fig. 3.12. Mainly the log sigmoid, tan

sigmoid and pure line functions were used for the formation of neural network. Based on the 48 iterations of the profile the neural network was trained and the optimal network was modelled. From the experiment, total sets were divided randomly into 70% for training, 15% for validation and 15% for testing the model by the software. Since the backpropagation neural network (BPNN) integrated with the Levenberg- Marquardt (LM) algorithm is most efficient as stated in the literature (Nain et al., 2018; Singh and Mirsa, 2019; Saha et al., 2008). Similar network and algorithm combinations are used to train the neural network for the prediction of response parameters.
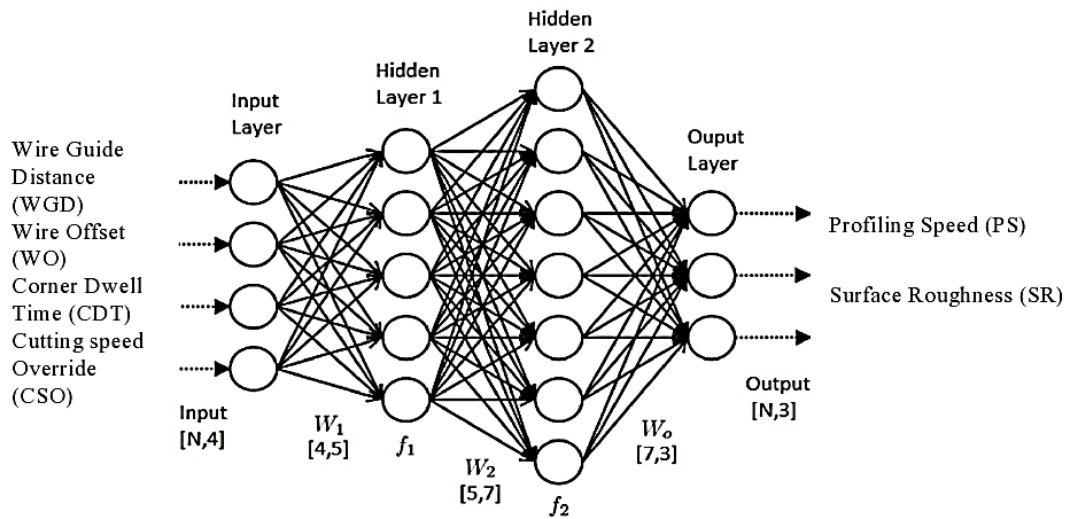
Figure 3.12 Different layers in ANN

3.6.2 Adaptive Neuro-Fuzzy Interference System Prediction

The ANFIS is known to be a universal estimator as it has the learning capability to approximate nonlinear functions obtained from the interference system. It can be used for the prediction of response parameters for the input parameters. The input parameters are wire guide distance, corner dwells time, cutting speed over-ride, wire offset and taper angle for prediction of profiling speed and surface roughness. The prediction of output parameters at different experimental parameters. The profiling speed, surface roughness can be predicted at different angles namely 0°, 15° and 30°. In the normalization stage, all the parameters are entered especially the maximum and minimum limits of the data where

the ANFIS is trained and in the second stage, there is feature reduction based on influential parameters on the output parameters are considered in case of prediction of each parameter. In the third stage, the prediction of required parameters was carried out as shown in fig.3.13.
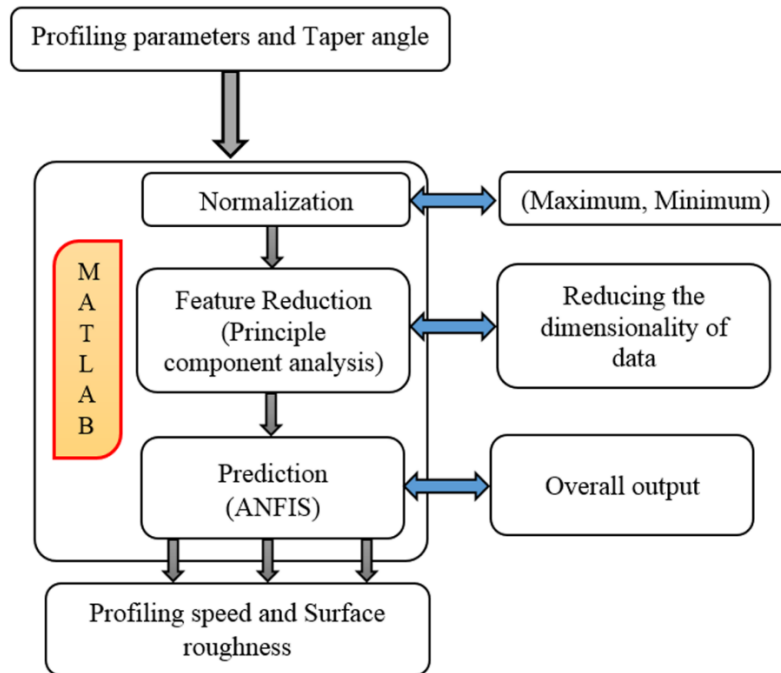
Figure 3.13 Prediction of profiling speed and surface roughness using ANFIS

3.7 SUMMARY

This section of the thesis shows selection of machining material Hastelloy-X and the material composition were highlighted. The influence of experimental parameters like WGD, WO, CDT, CSO and taper angle were characterized by using different experimental facilities. This also explains the details of the tools used. Different output parameters like profiling speed, surface roughness, profile area, corner error, angular error, recast layer thickness and micro-hardness were investigated. The slant type taper fixture was used to obtain tapering surface at different angles namely 0°, 15°, 30°, 45° and 60°. The specifications of the copyrights obtained for slant type taper fixture are mentioned. Prediction of profiling speed and surface roughness were made using ANFIS and ANN model during the investigation were emphasized in this chapter.

71

CHAPTER 4

ASSESSMENT OF WEDM PARAMETERS ON RESPONSE CHARACTERISTICS

4.1 INTRODUCTION

In this chapter, the WEDM cutting parameters i.e. pulse on time, servo voltage, wire feed and servo feed for machining Hastelloy-X using the zinc-coated copper wire was highlighted. Different output parameters viz. surface roughness, surface crack density, angular error and kerf width based on cutting speed were recorded and cutting parameters were chosen. Once the cutting parameters were fixed the different profiling parameters i.e. WGD, WO, CDT and CSO were used carried out to study the effects on square profile. All the trial experiments were carried on slant type taper fixture that was fixed on the WEDM table. The effect of WEDM parameters on response characteristics based on one factor at a time (OFAT) approach. The output response characteristics such as cutting speed, surface roughness, taper angle, recast layer formation, micro-hardness, residual stress and elemental changes on the WED machined surface was studied.

4.2 EXPERIMENTAL DETAILS

The machining parameters were chosen through initial experiments for machining the alloy using power pulse mode (Pulse current of 12A) and pulse off time as 44μs as shown in table 4.1 were kept constant. From the initial experiments, it was seen that the pulse off time had minor significance on cutting speed and surface roughness. All the angular machining was carried out at a wire guide distance of 140mm from 0°, 15°, 30°, 45° and 60° angle of cut. The parameters were selected based on the machining capability during machining of Hastelloy-X. Table 4.2 represents Taguchi's L_9 experiments that were performed at different angles with various machining parameters such as pulse on time,

servo voltage, wire feed and servo feed. The cutting speeds were recorded and five distinct cutting speed parameters were chosen for each angle, it was shown in table 4.3. The five ditinct cutting speeds included the lowest (T_{on}=105 μm, SV=60 V, WF=8 m/min and SF=20 m/min) and highest (T_{on}=125 μm, SV=40 V, WF=8 m/min and SF=15 m/min) cutting speeds parameters. These parameters were used to machine the Hastelloy-X at different taper or slant angles to obtain the tapered surface of 5mm thickness as shown in fig. 4.1.

Table 4.1 Constant machining parameters

Sl. No.	Parameters	Specifications
1	Wire diameter (μm)	250
2	Wire Material	Zinc coated copper wire
3	Dielectric Fluid	Deionized water
4	Polarity	Positive
5	Peak Current (A)	12
6	Pulse on time T_{on} (μs)	105,115,125
7	Servo voltage SV (V)	40,50,60
8	Wire feed WF (m/min)	6,7,8
9	Servo feed SF (mm/min)	10,15,20
10	Pulse off time T_{off} (μs)	44
11	Wire guide distance (mm)	140

Table 4.2 Taguchi's L_9 Design for different cutting speed parameter

Sl. No.	Pulse on time (μs)	Servo voltage (V)	Wire feed (m/min)	Servo feed (mm/min)
1	105	40	6	10
2	105	50	7	15
3	105	60	8	20
4	115	40	7	20
5	115	50	8	10
6	115	60	6	15
7	125	40	8	15
8	125	50	6	20
9	125	60	7	10

Table 4.3 Selected parameters for angular machining in WEDM

Trial No.	Pulse on time (μs)	Servo voltage (V)	Wire feed (m/min)	Servo feed (mm/min)	Cutting Speed (mm/min) Angles (°)				
					0°	15°	30°	45°	60°
1	105	60	8	20	0.471	0.365	0.336	0.261	**0.162**
2	115	50	8	10	0.670	0.602	0.522	0.442	0.287
3	115	40	7	20	0.925	0.811	0.701	0.572	0.383
4	125	50	6	20	1.393	1.307	1.233	0.838	0.675
5	125	40	8	15	**2.494**	1.941	1.629	1.161	0.852
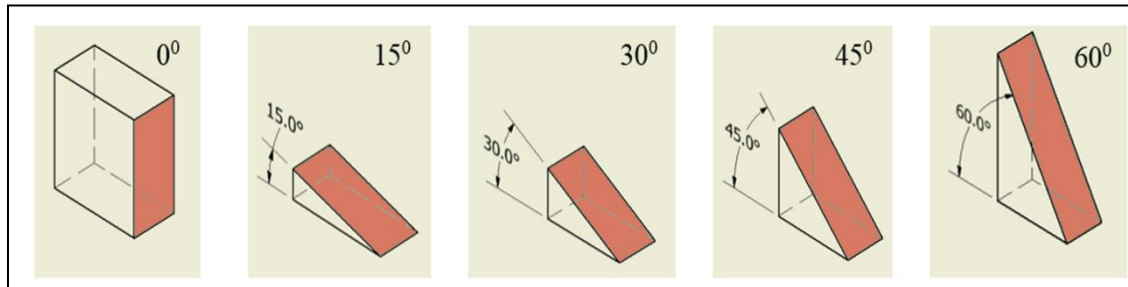
Figure 4.1 Taper cut samples at 0°, 15°, 30°, 45° and 60° angle of cut

4.2.1 Variation of cutting speed with different angle of cut

The parameters for machining that were decided from the initial experiments, the slant type taper machining of Hastelloy-X was carried out. It was observed form table 4.3 that the cutting speed ranging from 0.16 to 2.494 mm/min for different cutting parameters and at various angles. The cutting speed increased from trial 1 (lowest cutting parametrs) to trial 5 (highest cutting parametrs) in all the angle of cut as as shown in fig. 4.2. From the trial 1 parameters it is seen that the servo voltage is highest and pulse on time is least as in table 4.3. So the trial 1 shows the lowest cutting speeds at all the angles. It can be observed in table 4.3 that although trials 2, 3 have same pulse on time i.e. 115 µs. There is increase in cutting speed from trials 2 to 3 due the decrease in servo voltage This leads to an increase in discharge energy during machining irrespective of there angles. Similarly the trials 4, 5 shows increase in cutting speed with same pluse on time with 125 µs. According to initial experiments it can be observed that as the pulse on time increases the discharge energy also increased. This was due to an increase in the intensity of sparks, but in the case of servo

voltage, an increase in servo voltage increases the spark gap. This reduces the number of sparks striking the workpiece decreasing the discharge energy. Similar trends were observed by Sharma et al. (2015) for the machining of nickel-based alloy. The cutting speed is influenced by sparking conditions which are controlled by parameters like pulse duration, workpiece orientation, servo voltage, wire diameter, and dielectric fluid (Ishfaq et al., 2018; Samanta et al., 2016). Trial 1 recorded the lowest cutting speed of 0.162 mm/min at 60° taper angle and trial 5 yielded the maximum speed of 2.49 mm/min at 0° angle in table 4.3. Trail 5 had a noticeable increase in 79.15% in cutting speed from trial 4 at 0° due to the increased discharge energy. Fig.4.2 shows the decrease in cutting speed with an increase in the angle of cut for the chosen machining parameters. This reduction in cutting speeds was observed due to an increase in the length of cutting thickness with increasing angle of cut. For the specifically chosen parameter, as the angle of cut increases, the cutting thickness also increases. This causes an increase in the area for melting compared to a straight cut, as the melting of the workpiece takes more time for the same sparking conditions which results in decreasing cutting speeds (Joy et al., 2019;Samanta et al., 2016).
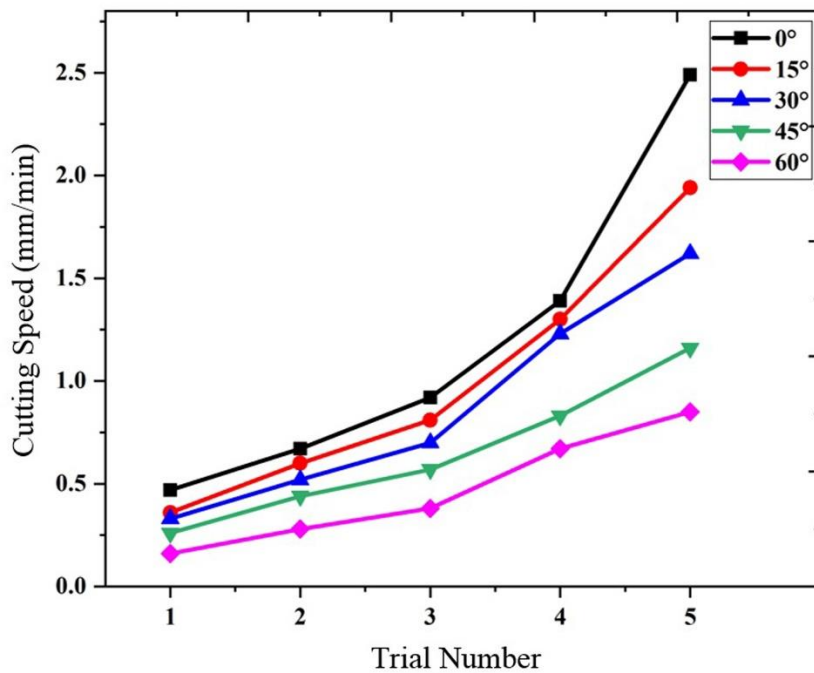
Figure 4.2 Variation of cutting speeds with different angle of cut

4.2.2 Variation of angle error with cutting speed.

The slant type fixture was measured for angular dead errors before machining. Table 4.4 shows dead angular errors that were measured for different angles. The angular error is the difference in machined angle and the true angle. The actual machined angle can be obtained by deducting the dead errors from CMM measured angle and angular error was calculated with the help of Eq. (1) & (2) (Rabinovich, 2016). Table 4.5 shows the actual error that the sample carries after machining by using slant type taper fixture. Fig. 4.3 shows the behaviour of angular error at different cutting speed parameters for the various angle of cut. Each angle was machined using five different chosen cutting speed parameters in table 4.3. These parameters with different cutting speeds influenced the amplitude of wire vibration as observed by Habib (2017). The machining was not always performed at the mid-span of the wire length due to tilt, there would be a change in vibrational forces and flushing conditions as observed by Habib et al. (2016). Due to this change, the vibrational amplitude of wire is leading to form errors on the machined surface. Trial 5 was observed to have maximum and minimum angular errors among all the angle of cut. The cutting speed parameters in table 4.3 gave minimum angular errors at 0°, 30°, 45° and 60° and maximum error at 15°. It can be observed that at 60° taper angle of cut, there was a change in angular error from positive (7'20") to negative (-0'53") for trial 5. This behaviour in angular error was due to the maximum vibrational amplitude that occurs at the highest discharge frequency and higher cutting thickness (Puri and Bhattacharyya, 2003; Samanta et al., 2016). These vibrational amplitudes may increase or decrease the angular error during slant type taper machining. From fig. 4.3 the angular errors was observed to be shifted from negative to positive from 15° to 30° angles and this shift was noticed due to the manufacturing imprecisions and stochastic wire vibration (Puri and Bhattacharyya, 2003). The angular accuracy was found to be influenced by wire vibration and wire tension as reported by Selvakumar et al. (2016) but it is independent of cutting speed.

Actual angle = CMM angle - Dead error   (4.1)

Angular Error = Actual angle -True Angle   (4.2)

Table 4.4 Dead Errors on slant type taper fixture

Angle in degrees	CMM Angle of the fixture (degrees)	Dead angular Error (degrees)
0°	00°28'30"	28'30"
15°	15°12'01"	12'01"
30°	29°59'52"	-00'08"
45°	45°00'08"	00'08"
60°	60°04'48"	04'48"
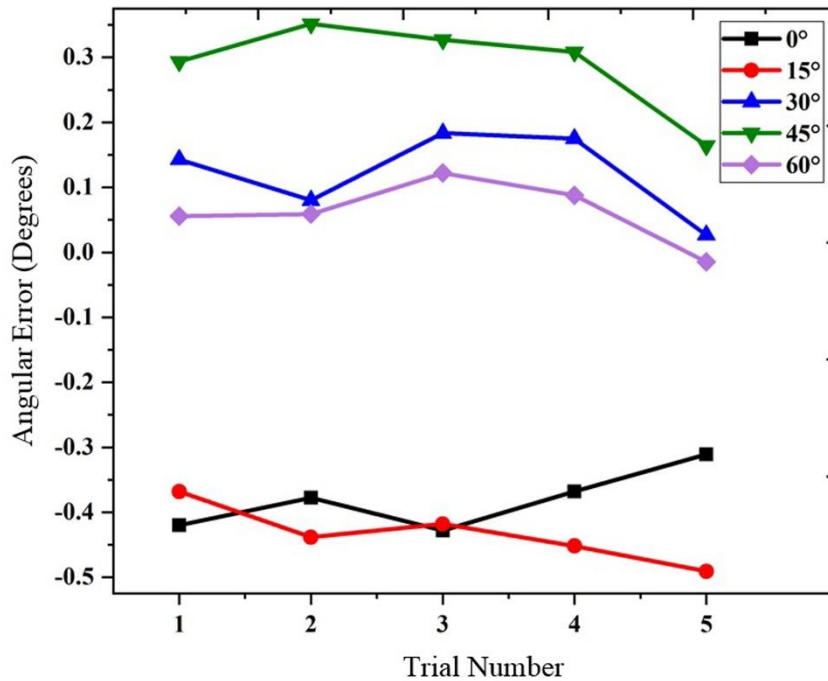
Figure 4.3 Variation of Angular error at different trials

Table 4.5 Variation of angular error at different trials

True Angle (degrees)	Trial No.	Measured Angle (Degrees)	Dead Error (degrees)	Actual angle (degrees)	Angular Error (degrees)
0°	1	0°03'19"	28'30"	-0°26'49"	-26'49"
	2	0°05'50"	28'30"	-0°23'20"	-23'20"
	3	0°02'48"	28'30"	-0°26'18"	-26'18"
	4	0°06'25"	28'30"	-0°23'55"	-23'55"
	5	0°09'17"	28'30"	-0°19'20"	-19'20"
15°	1	14°49'56"	12'01"	14°37'55"	-22'05"
	2	14°45'52"	12'01"	14°33'51"	-26'09"
	3	14°46'56"	12'01"	14°34'55"	-25'05"

	4	14°44'54"	12'01"	14°32'53"	-27'07"
	5	14°42'34"	12'01"	14°30'33"	-29'27"
30°	1	30°08'27"	-00'08"	30°08'35"	08'35"
	2	30°04'40"	-00'08"	30°04'48"	04'48"
	3	30°10'53"	-00'08"	30°11'01"	11'01"
	4	30°10'22"	-00'08"	30°10'30"	10'30"
	5	30°01'29"	-00'08"	30°01'37"	01'37"
45°	1	45°17'45"	00'08"	45°17'37"	17'37"
	2	45°20'47"	00'08"	45°20'39"	20'39"
	3	45°19'46"	00'08"	45°19'38"	19'38"
	4	45°18'38"	00'08"	45°18'30"	18'30"
	5	45°09'59"	00'08"	45°09'51"	09'51"
60°	1	60^{0}09'09"	04'48"	60^{0}03'21"	3'21"
	2	60^{0}07'10"	04'48"	60^{0}03'32"	3'32"
	3	60^{0}12'08"	04'48"	60^{0}07'20"	7'20"
	4	60^{0}10'04"	04'48"	60^{0}05'16"	5'16"
	5	60^{0}03'55"	04'48"	59^{0}59'07"	-0'53"

4.2.3 Variation of surface roughness with cutting speed for different angle of cut

The surface roughness is a vital parameter that can be used as a measure of surface integrity. Table 4.6 shows the variation of surface roughness for varying cutting speeds. Fig.4.4 shows the trends of surface roughness with cutting speed at different angle of cut. It was observed that as the cutting speed increases the surface roughness also increases. The surface roughness of the machined surface was 3.574 µm at the highest cutting speed of 2.494 mm/min at 0° and 1.734 µm at the lowest cutting speed of 0.162 mm/min at 60°. During WEDM, the surface roughness was due to craters produced on the machined surface by the spark to melt the workpiece reported by Sharma et al. (2017). The surface roughness was found to be influenced by pulse on time and servo voltage. The increase in pulse on time leads to a higher intensity of sparks causing more craters which increases the surface roughness of the machined angular surface. The increase in sparks also increases the discharge energy which offers higher cutting speeds in the machining of the material. But in the case of servo voltage, as it increases the spark gap between electrode and material becomes more, it reduces the number of sparks hitting the workpiece (Sharma et al., 2017; Kumar et al., 2015). Therefore there is a decrease in the discharge energy reducing the

number of craters with a decrease in cutting speed. Fig. 4.5 shows SEM micrograph of the lowest (0.162 mm/min) and highest (2.494 mm/min) cutting speeds. Fig. 4.5 (a) shows reduced micro holes and micro globules due to the lowest discharge energy with the lowest cutting speed (0.162 mm/min) on the machined surface. From fig. 4.5 (b) observation, the SEM image for the machined angular surface at the highest cutting speed (2.494 mm/min) shows more number of micro-craters, micro globules and micro-holes which contributes to higher surface roughness. The highest surface roughness was measured to be 3.991 µm for a cutting speed of 0.852 mm/min at 60°. This increase in surface roughness at lower cutting speed was due to high cutting thickness this was because of an increase in the angle of cut. This behaviour was observed due to the increased discharge energy and the variation in gap voltage at trial 5. However, similar results as reported by Samanta et al. (2016) for varying job height condition during WEDM.

Table 4.6 Surface roughness observed for varying cutting speed and angle of cut

Trial No.	0°		15°		30°		45°		60°	
	CS (mm/min)	SR (µm)	CS (mm/min)	SR (µm)	CS (mm/min)	SR (µm)	CS (mm/min)	SR (µm)	CS (mm/min)	SR (µm)
1	0.471	1.791	0.365	1.881	0.336	1.957	0.261	1.751	**0.162**	**1.734**
2	0.670	2.905	0.602	2.802	0.522	2.183	0.442	2.301	0.287	2.587
3	0.925	3.112	0.811	2.991	0.701	2.752	0.572	2.967	0.383	2.649
4	1.393	3.493	1.307	3.813	1.233	3.584	0.838	3.838	0.675	3.712
5	**2.494**	**3.574**	1.941	3.854	1.629	3.931	1.161	3.954	0.852	3.991

* CS- cutting speeds, SR-surface roughness
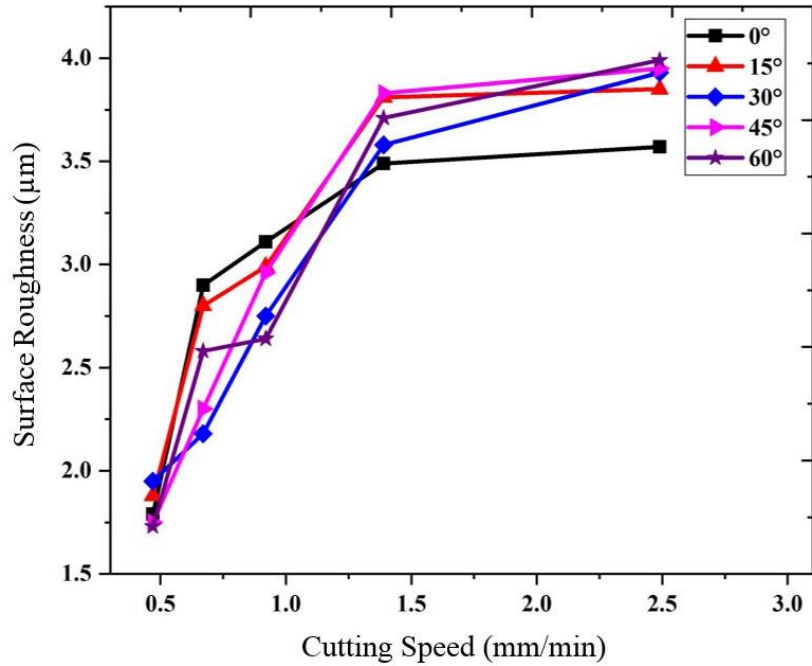
Figure 4.4 Variation of surface roughness with different cutting speeds
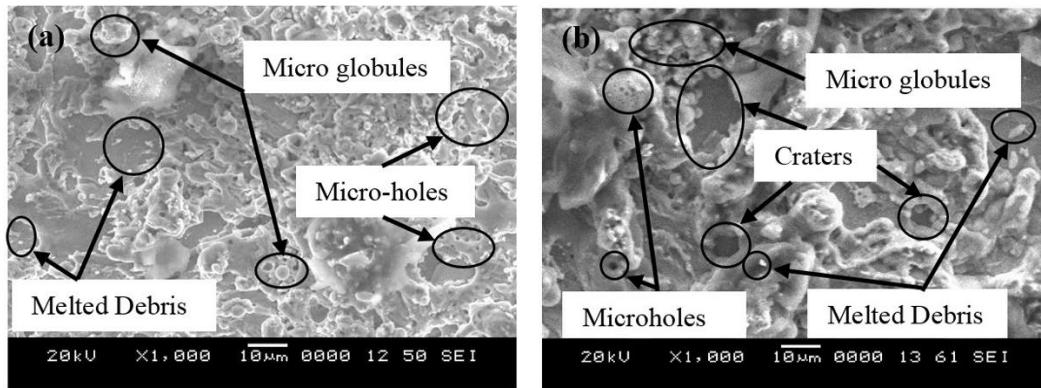
Figure 4.5 SEM micrographs of (a) lowest cutting speed (0.16mm/min) at taper angle of 60° (b) highest cutting (2.49mm/min) speed at taper angle of 0°

4.2.4 Variation of Surface crack density with cutting speed

Table 4.7 shows the calculated surface crack density for different cutting speeds at various angle of cut. It was observed from fig. 4.6 as the cutting speed increases the surface crack density also increases. It was calculated that surface crack density at the highest cutting speed of 2.49mm/min was 0.257 μm/μm^2 at taper angle 0° and at the lowest cutting speed of 0.16mm/min, the surface crack density was 0.328 μm/μm^2 at 60°. During the WEDM

process workpiece experiences instantaneous heating and cooling cycles, due to the machining. The material melting and simultaneous flushing out at the cutting region. This rapid heating and cooling cycles lead to the formation of thermal stress on the machined surface. This thermal stress on the surface causes cracks which may lead to failure of the component (Kumar et al., 2016). With the increase in cutting speeds the number of heating and cooling cycles increases, this leading to more thermal stress on the machined surface, causing more cracks. Hence the surface crack density increases with an increase in cutting speed as observed by Soni et al. (2018). The highest surface crack density was calculated as 0.455 μm/μm^2 at 60° for cutting speed of 0.85mm/min. From fig. 4.6 it can be observed that the surface crack density increases although the cutting speed decreased with an increase in the angle of cut. As the angle of cut increases, the cutting thickness also increases. The cutting thickness increase was calculated to be 41.42% from 45° to 60° and 22.47% from 30° to 45° taper/slant angles which were highest when compared to other angles of cut. With an increase in cutting thickness the area that is required to melt is also increasing. As the surface area of angular machined part that is subjected to the heating and cooling cycle also increases. It induces more cracks due to increased thermal stress, although there is a decrease in cutting speed making the curve linear in fig. 4.6 for 60° comparing to other angles. Similar results were outlined by Zhang et al. (2015) in their investigation. Fig. 4.7 (a) and (b) shows the SEM images with cracks for angular specimens at 0° and 60° for the highest (2.19mm/min) and lowest (0.16mm/min) cutting speeds at respective angles. The larger microcracks were observed in fig. 4.7 (a) i.e. in the machined surface at 0°. From fig. 4.7 (b) shows smaller micro-cracks at 60° angular machined surfaces due to lowest cutting speed.

Table 4.7 Surface crack density at different cutting speeds for various angle of cut

Trial No.	0°		15°		30°		45°		60°	
	CS (mm/ min)	SCD (μm/ μm²)	CS (mm/ min)	SCD (μm/ μm²)	CS (mm/ min)	SCD (μm/ μm²)	CS (mm/ min)	SCD (μm/ μm²)	CS (mm/ min)	SCD (μm/ μm²)
1	0.471	0.188	0.365	0.218	0.336	0.256	0.261	0.293	**0.162**	**0.328**
2	0.670	0.197	0.602	0.231	0.522	0.269	0.442	0.312	0.287	0.349
3	0.925	0.207	0.811	0.241	0.701	0.282	0.572	0.322	0.383	0.370
4	1.393	0.233	1.307	0.264	1.233	0.298	0.838	0.338	0.675	0.386

| 5 | **2.494** | **0.257** | 1.941 | 0.293 | 1.629 | 0.339 | 1.161 | 0.395 | 0.852 | 0.455 |
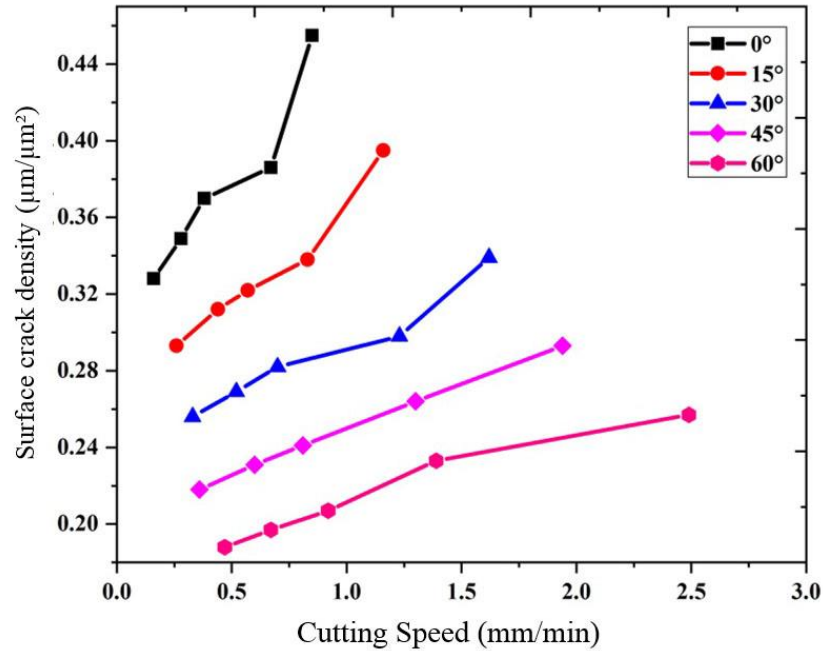
Figure 4.6 Variation of surface crack density with different cutting speeds
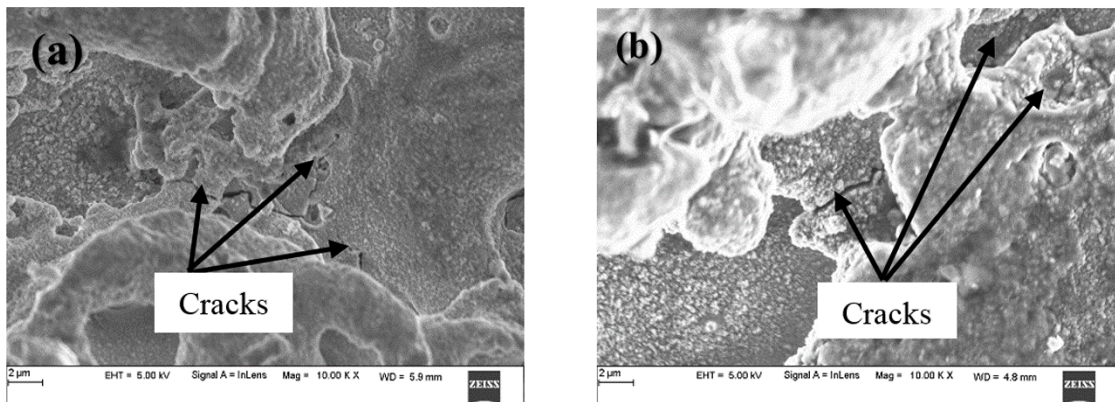
Figure 4.7 SEM images of angular cut specimen at (a) highest cutting speed
(2.49mm/min) at 0° (b) lowest cutting speed (0.16mm/min) at 60°.

4.2.5 Variation of the width of cut for different angle of cut

The width of cut is also known as kerf width, is the distance of cut perpendicular to the
direction of the wire path in WEDM. The different width of cut that was measured by using

SEM at various angle of cut is as shown in Table 4.8. Fig. 4.8 shows the variation of the width of cuts at different chosen parameters in table 4.3 that were cut at different angles of cut. Fig.4.9 shows SEM micrograph of the different width of cut at 0°, 15°, 30°, 45° and 60° angles of cut at different cutting speed parameter in table 4.3. The width of cut mainly depends on wire vibration, servo voltage, servo feed, amplitude of vibration and job height (Samanta et al., 2016; Habib, 2017; Chen et al., 2018). The lowest width of cut was observed in trial 1 which was varying from 280.678 μm to 380.276 μm at 0° and 60° respectively. Trial 1 measured lowest cutting speed with a lower width of cuts as it has the highest servo feed in all angle of cut. However, trial 5 offers the highest width of cut varied from 358.97 μm to 425.678 μm at 0° and 60° respectively and it has the least servo feed with the highest cutting speed. During sparking if the servo feed is least, the distance of wire movement inside the material is reduced. This makes a larger width of cut as the material around the wire is exposed to sparking for a longer time than the normal cutting (Habib, 2017; Chen et al., 2018). The highest width of cut was observed at 60° for all the trials. It was noticed that for all the individual cutting speed parameter in table 4.3 the width of cut increases with an increase in the angle of cut. As cutting thickness increases the amplitude of wire vibration also increases, hence it increases the width of cut (Habib, 2017; Samanta et al., 2016). In all the trials the width of cut increased but there was a noticeable increase in the width of cut for 45° and 60° as shown in fig. 4.8. This behaviour is due to the rapid increase in the cutting thickness from 15.56mm to 20mm, which in turn increases the amplitude of wire vibration as reported by Samanta et al. (2016).

Table 4.8 Width of cut observed for different taper angles

Trial No.	Width of cut (μm)				
	0°	15°	30°	45°	60°
1	**280.678**	305.789	318.642	332.375	380.276
2	308.821	320.033	331.200	345.600	390.706
3	316.700	331.769	349.500	362.840	405.623
4	340.500	351.801	365.648	379.820	411.670
5	358.970	369.058	387.740	400.270	**425.678**
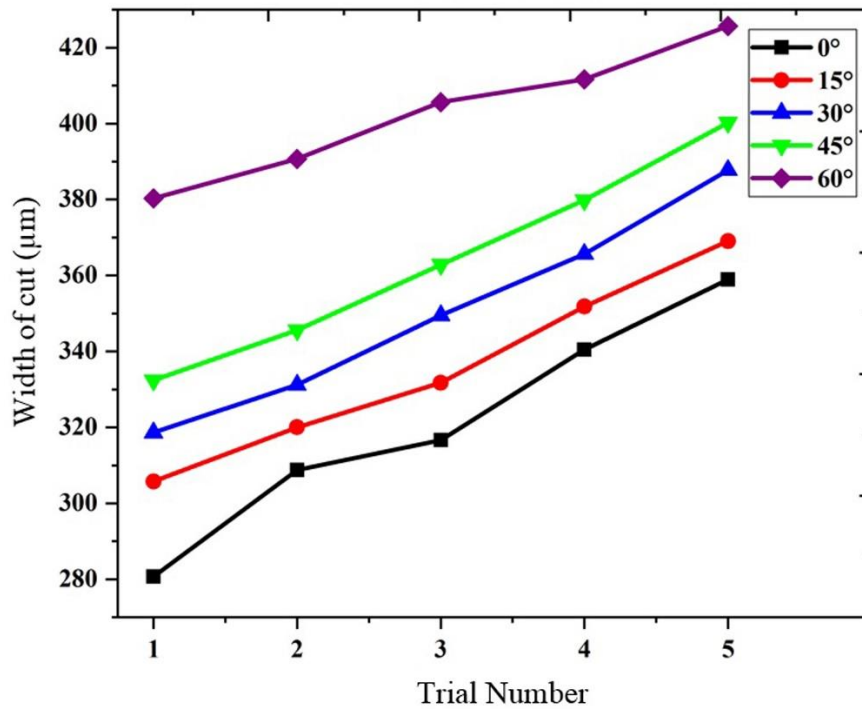
Figure 4.8 Variation of width of cut for different angle of cut
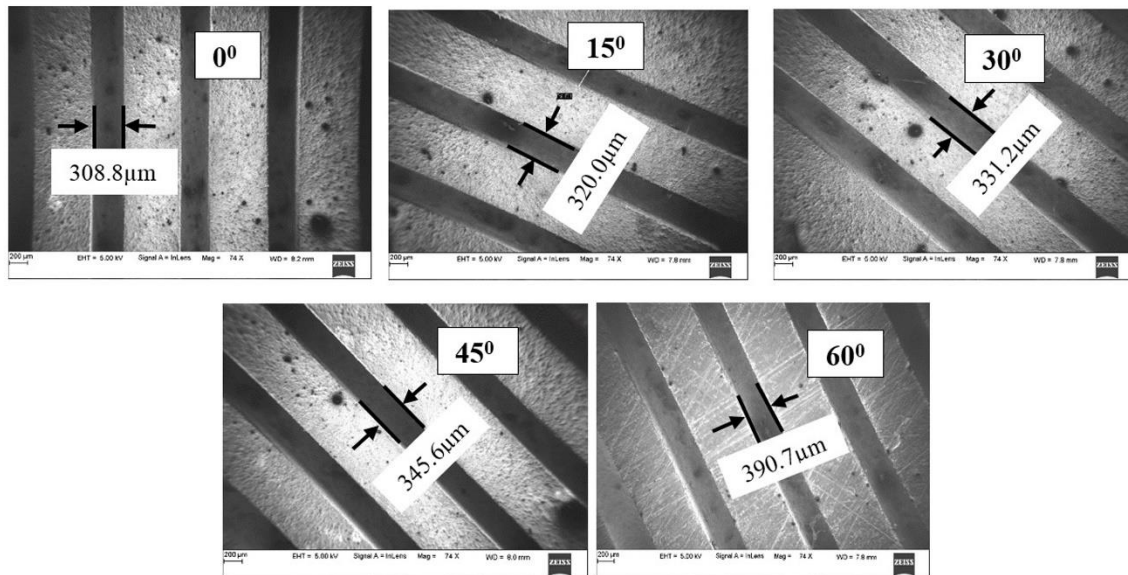
Figure 4.9 SEM images of width of cut at 0°,15°,30°,45° and 60° angles.

4.2.6 Selection of Profiling Parameters

Based on the above experimentation the basic cutting parameters i.e. pulse on time, pulse off time, wire feed, servo feed and servo voltage and their constant values were chosen for

profiling as shown in table 4.9. Among the trials in table 4.3, trial 1 and 2 are very slow cutting parameters as they yielded lower profiling speeds. Whereas trail 4 and 5 are parameters having the highest surface roughness, surface crack density and width of cut. Therefore the trial 3 in table 4.3 was chosen as cutting parameters for machining profiles as in table 4.9. These parameters were found to be machinable in all the slant/taper angles. The wire feed was set as 6 m/min as it was optimal which was found from the trial experiments and change in wire feed does not influence the surface. Although the preliminary experiments were carried out at 0°, 5°, 30°, 45° and 60° only 0°, 15° and 30° were chosen for profiling. This was due to the more applications having ≤ 30° and also lesser workpiece thickness leads to more angular errors (Sanchez et al., 2006). The profiling at 45° and 60° takes more time, wire and the angular error will also increase. The cutting parameters were kept constant throughout the experiment for examination of the effects of different profiling parameters such as wire guide distance (WGD), wire offset (WO), corner dwell time (CDT) and cutting speed override (CSO) on profiles. Square profiles of 1mm, 3mm and 5mm was machined using One factor at a time (OFAT) experiment at different taper angles viz. 0°, 15° and 30°. Based on the observation of OFAT experiments further detailed investigation were performed for three triangular, square and circular profiles at different taper angles.

Table 4.9 Constant Parameter

EDM Parameters	Settings
Pulse off time T_{off} (µs)	44
Servo Feed SV (mm/min)	20
Wire Feed WF (m/min)	6
Pulse on time T_{on} (µs)	115
Servo voltage SV (V)	40

4.3 ONE FACTOR AT A TIME (OFAT) APPROACH

One Factor at a Time was used for profiling square profiles keeping all profiling parameters constant and varying a single parameter with fixed cutting parameters as in fig.4.10. The input experimental parameters like wire guide distance, corner dwell time, wire offset, cutting speed override and taper angle. Table 4.10 shows the range of input parameters

used for square profiling. These parameters were chosen based on the machining capability and initial experiments. The output response characteristics cutting speed, surface roughness, corner error, recast layer thickness, micro-hardness, metallurgical changes and residual stresses was studied. The wire guide distance was chosen as such that the profiling could be easily performed with minimal vibration for all three type of taper angles as shown in table 4.10. One factor at a time was followed in the experimental approach. In this approach, apart from one parameter others were maintained to minimal (level 1) to know the individual effects on response parameters. Fig. 4.10 (a) shows the different slant type taper fixture at WEDM table and different taper position in 4.10 (b) and (c). Fig. 4.11 shows machined profiles using the fixture.
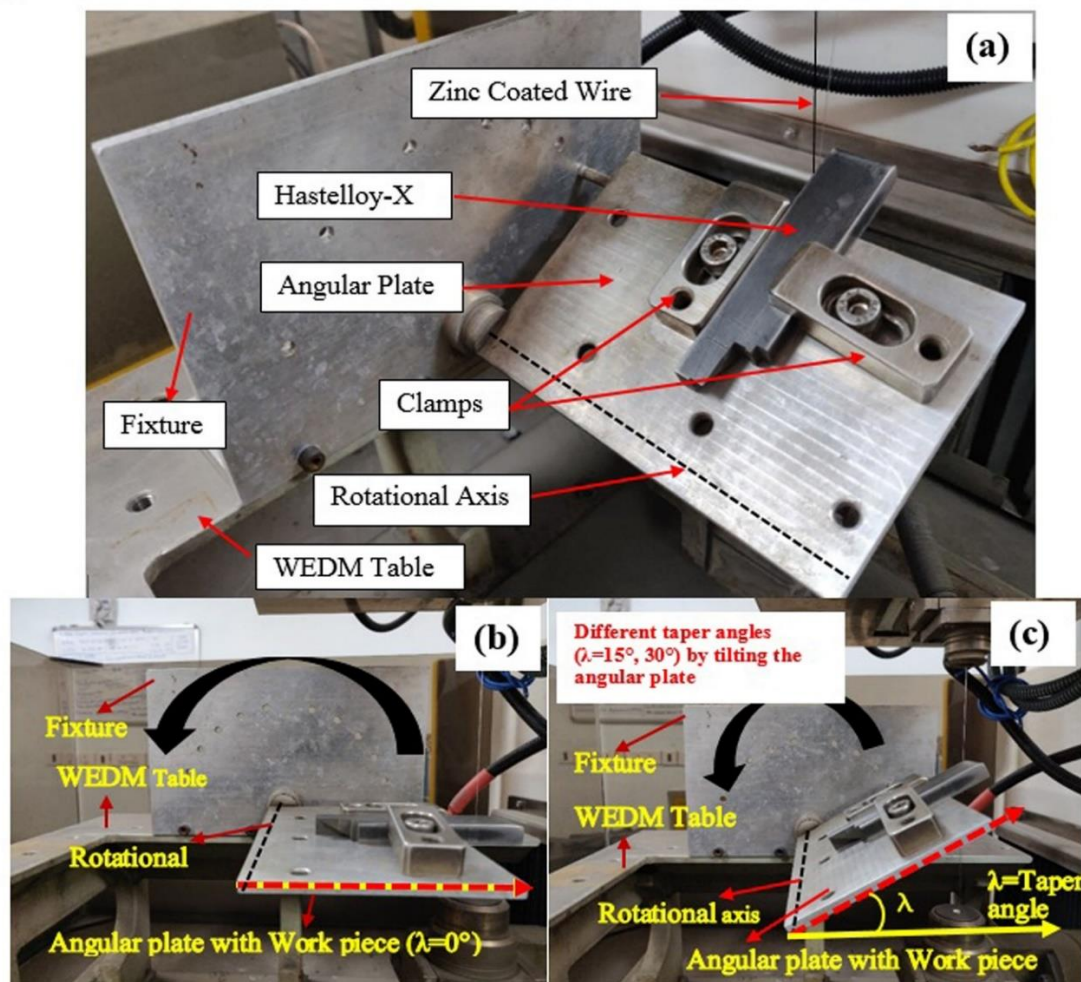
Figure 4.10 (a) Fixture fixed to WEDM table, fixture position at (b) 0° taper angle (c) 15° or 30° taper angle
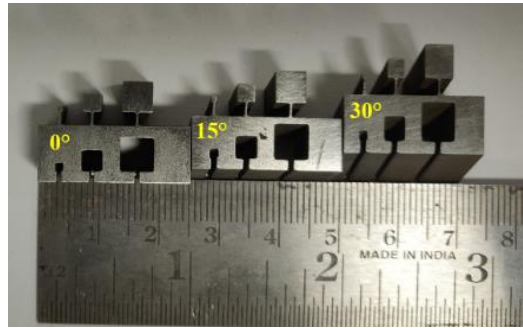
Figure 4.11 Square profiles machined at 0°, 15° and 30° taper angles

Table 4.10 WEDM Parameters

Parameters	Level 1	Level 2	Level 3	Level 4
Wire guide distance (WGD) (mm)	90	100	110	120
Cutting speed override (CSO) (%)	31	54	77	100
Wire offset (WO) (µm)	0	40	80	120
Corner dwell time (CDT) (s)	0	33	66	99

4.3.1 Analysis of Profiling Speed

The behaviour of the profiling speed for the different input parameters WGD, CDT, WO and CSO as shown in fig.4.12 (a), (b), (c) and (d). The wire guide distance is the distance between the upper guide and the lower guide. As the WGD increases, the tension in wire tends to reduce and the tendency of wire vibration also increases (Chaudhary et al., 2019). These wire vibration that occurs in the chaotic nature. So there is a decrease in profiling speed as shown in fig.4.12 (a). In fig. 4.12 (b) shows the profiling speed variations with the CDT. The CDT mainly affects the corners during complex shape profiling (Read and Zenyth, 2010). It shows the lower variation of profiling speed as the CDT increases. This effect is due to vibrations caused during sparking (Habib, 2017). The WO controls the fixed perpendicular distance from the machined profile to the programmed profile. According to the observations by Habib and Okada (2016), as the WO increases, the wire vibration decreases because the wire has to cover the larger part of profile circumference. This increases the profiling speed as wire vibration decreases as shown in fig. 4.12 (c). The CSO is an online parameter that varies the profiling speed without altering the machining

parameter (Read and Zenyth, 2010). The CSO controls the discharge during machining which in turn controls the profiling speed. So as the CSO increases the profiling speed also increases due to the increase in discharge energy (Habib and Okada, 2016). It can be observed from all the plots the 0° taper angle produced the highest profiling speed followed by 15° and 30°. This was observed due the increase in cutting thickness. As the taper angle increases the cutting thickness also increases. As the cutting thickness increases the discharge energy during machining gets distributed (Joy et al., 2020a). This decreases the profiling speed, so the 30° taper angle has the least profiling speed as it machines the highest cutting thickness. Whereas the 0° taper angle yielded the highest profiling speed while machining the lowest cutting thickness.
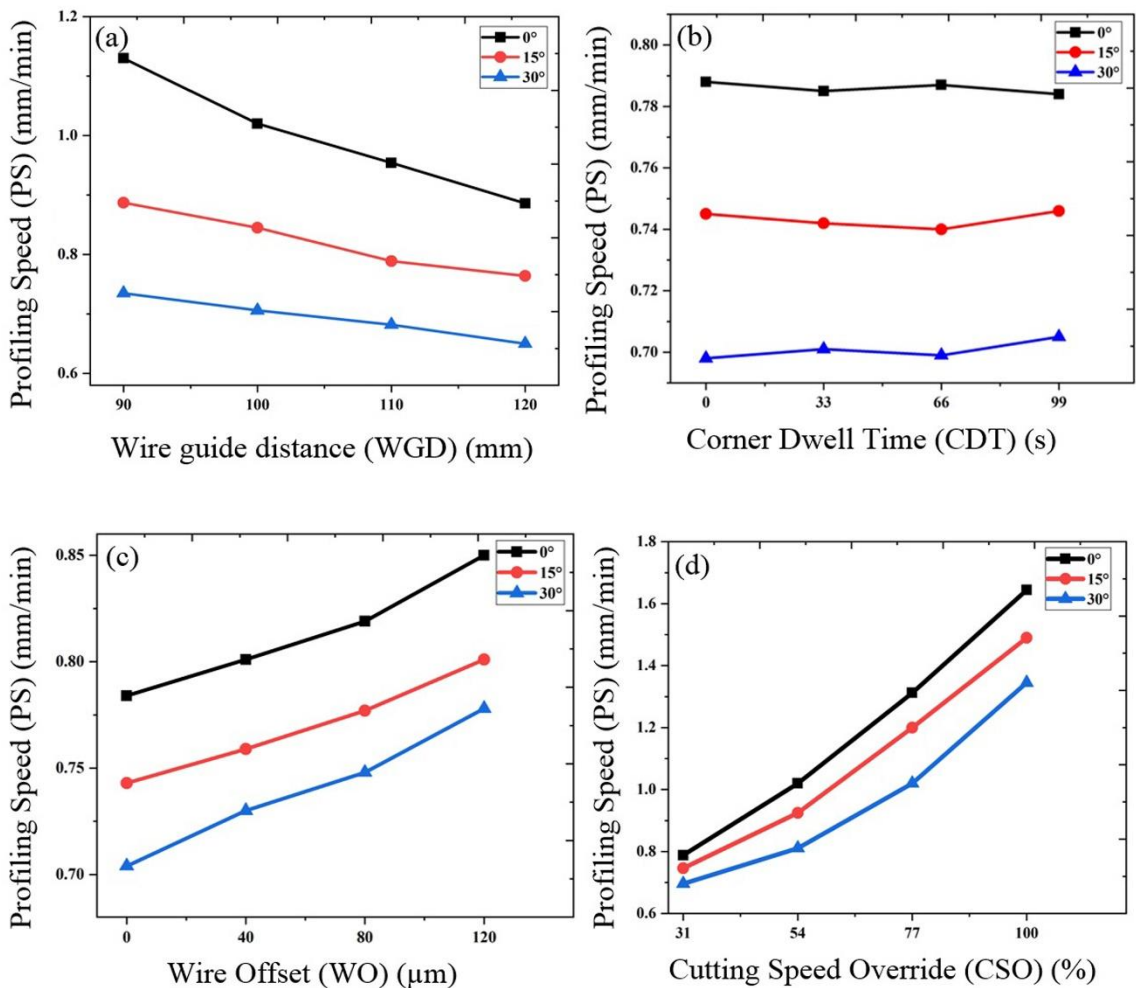
Figure 4.12 Effect of machining parameters on profiling speed

4.3.2 Analysis of surface roughness

The variation of surface roughness with different input parameters such as WGD, CDT, WO and CSO was as shown in fig. 4.13. From the fig. 4.13 (a) the surface roughness increases as the WGD this is due to the decrease in wire tension. Puri and Bhattacharyya, (2003) and Chaudhary et al. (2019) have noticed in their investigation that as the wire tension decreases because of the impact force on the wire during machining. This occurs due to the high frequency produced during sparking. Hence the wire vibration increases, which gives multiple irregular sparking on the machining surface. Therefore the surface roughness increases with the WGD due to the wire vibration. Fig.4.13 (b) shows the variation of CDT on surface roughness. As it can be observed that the CDT have no effect on surface roughness. From fig. 4.13 (c) it can be seen as the WO increases the surface roughness also increases. The WO controls the perpendicular distance from the machined profile to the programmed profile. As the perpendicular distance increases the wire vibration decreases which gives higher profiling speed in turn increasing surface roughness (Habib, and Okada, 2016). The CSO controls the discharge energy during machining. As the discharge energy increases the profiling speed increases, this gives a surface with higher roughness. So the surface roughness increases as the CSO increases which were observed and reported in Fig.4.13 (d).
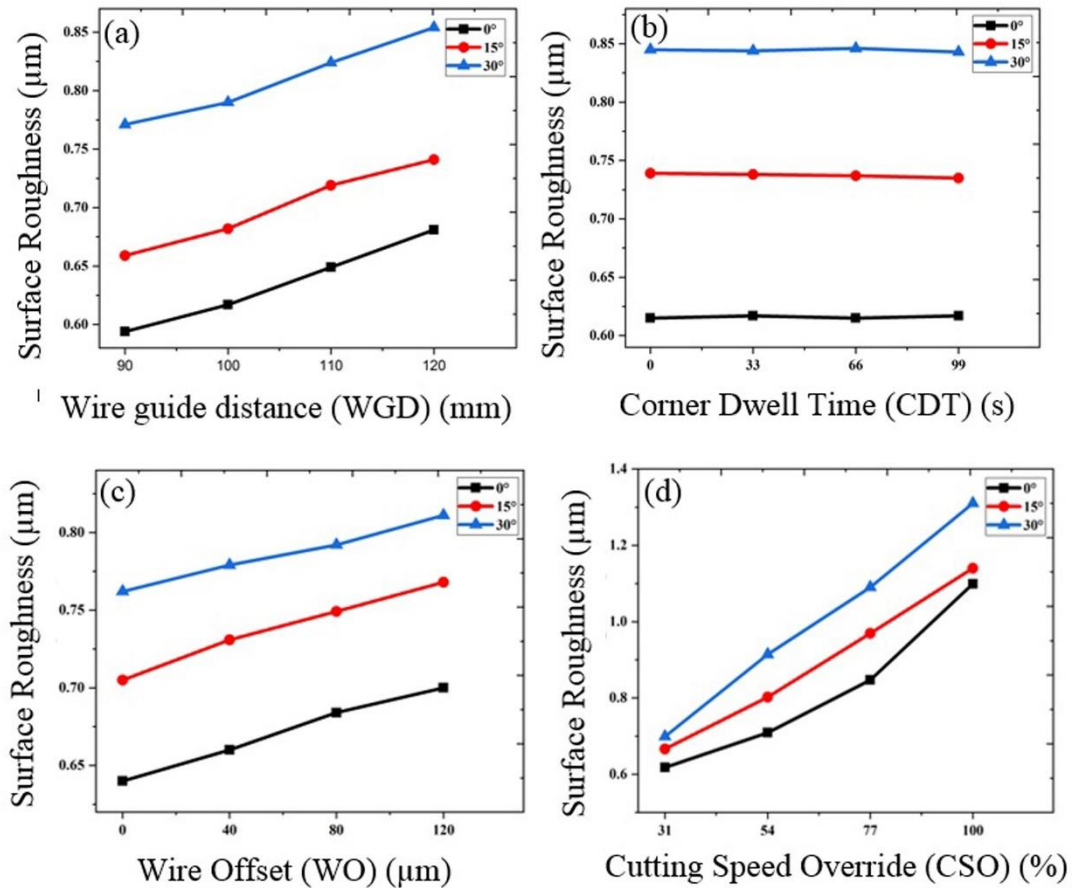
Figure 4.13 Effect of machining parameters on surface roughness

It can be observed that the surface roughness of 30° taper angle was recorded highest followed by 15° and 0° taper angle. As the cutting thickness increases the surface roughness also increased although the profiling speed was decreased. This behaviour was observed due to the flushing efficiency of the dielectric fluid. It leads to re-solidification of the melt on the machined surface due to rapid cooling by the dielectric fluid (Goswami et al., 2017). The SEM images for the lowest (WGD=120mm, CDT=0s, WO=0μm, CSO=31%) and highest (WGD=90mm, CDT=99s, WO=120μm, CSO=100%) machining speed parameters are shown in fig. 4.14 (a) to (d). The SEM images in fig.4.14 (a) shows lesser craters, bigger micro globules, micro-holes which results in lower surface roughness (0.681 μm) at 0°. Fig.4.14 (b) shows more number of smaller craters, larger micro globules, micro-holes which gives higher peaks and valleys on the machined surface increases the surface roughness (0.854 μm) at 60°for lowest machining speed parameters. Similarly, in the case

90

of the highest machining speed parameters, fig.4.14 (a) shows lesser craters, bigger micro globules, micro-holes leading to lower surface roughness (0.919 Ra) compared to fig.4.14 (b) at 0°. Whereas fig.4.14 (b) has larger micro globules and micro-holes and presence of debris giving the highest surface roughness (1.13 Ra) at 60° taper angle.
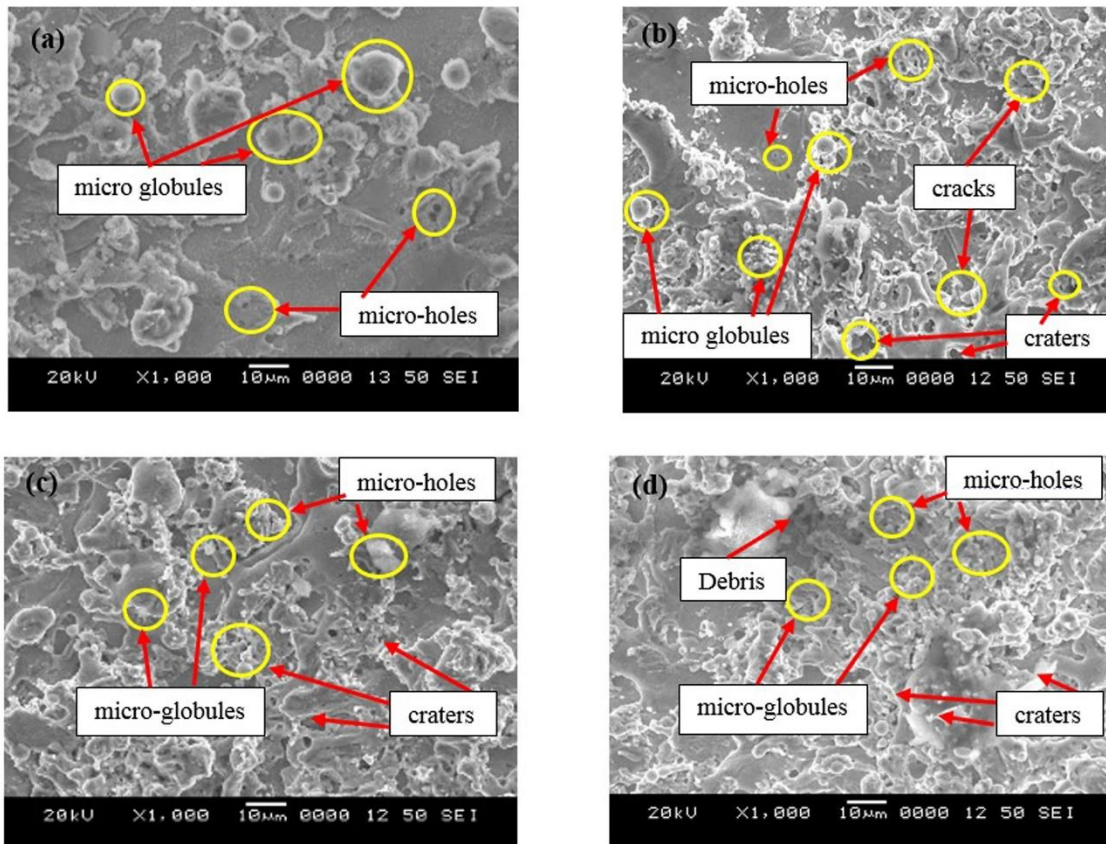
Figure 4.14 SEM images for WEDMed surface at (a) (c) 0° and (b) (d) 60° taper angles

4.3.3 Analysis of Corner error

Fig. 4.15 shows the variation of corner error for different input parameters during machining of taper square profile. As WGD increases the tendency of the wire to deflect, due to the lower wire tension (Puri and Bhattacharyya, 2003). With the increase in wire deflection, the corner error also increases (Chen et al., 2018). Hence, as WGD increases the corner error also increases as observed in fig. 4.15 (a). As the CDT decreases the corner error increases as shown in fig. 4.15 (b). This corner error occurs due to wire lag. The CDT

makes the wire dwell at a specific coordinate to decrease the wire lag. The wire deflection is the main reason for wire lag where the wire remains behind the actual coordinates. However Sakar et al. (2011) observed in their investigation that as the wire lag decreases the corner error also decreases, which is similar to the present context. Fig. 4.15 (c) explains the behaviour of corner error with the increase in the WO. Habib and Okada (2016) have observed in their work as the WO increases the wire deflection also increases. This was noticed because the wire has to cover higher circumference than the programmed profile. This increases the corner error due to an increase in wire deflection as the wire has to machine more area of profile. The CSO controls the discharge energy which in turn governs the profiling speed. It was observed from fig.4.15 (d) that as the CSO parameter increased the corner error was also increased. This phenomenon was noticed due to the increase in wire lag. As the CSO increases the wire has to move faster due to an increase in discharge energy. But it is observed the wire delay causing wire lag, as it cannot travel as fast as the wire guide coordinate. This increases the corner error as the CSO increases as shown in Fig.4.15 (d). Overall, it can be observed that the 30° yielded a higher corner error than 0° and 15° taper angles. This effect results due to the higher cutting thickness of the workpiece. As cutting thickness increases the wire tend to deflect more which causes wire deflection (Sakar et al., 2011). So as the wire deflection was highest at 30° it gives the highest corner errors followed by 15° and 0° taper angles.

The machined surface obtained from the highest machining speed parameters (WGD=90mm, CDT=99s, WO=120µm, CSO=100%) and the lowest machining speed parameters(WGD=120mm, CDT=0s, WO=0µm, CSO=31%), were studied by SEM. The SEM images exported in Image J software to measure the corner error. The corner error increased due to the increase in thickness leading to the wire deflection. This increases the wire lag leading to higher corner error. It can be seen in both fig.4.15 at the highest and lowest speed parameters, the profiling speed decreases and the corner error increases as the taper angle increases. This was contrasting to behaviour reported by Selvakumar et al. (2018). Fig.4.15 and 4.16 shows the corner errors at the lowest and highest machining speed parameters. At the lowest machining speed parameters it was found to be

65005.45µm² and 72014.10µm² at 0° and 30° taper angles respectively as shown in fig.4.16 (a) and (b). It was 68737.99µm² and 79541.61µm² for the highest machining speed parameters at respective taper angles as indicated in fig.4.16 (c) and (d).
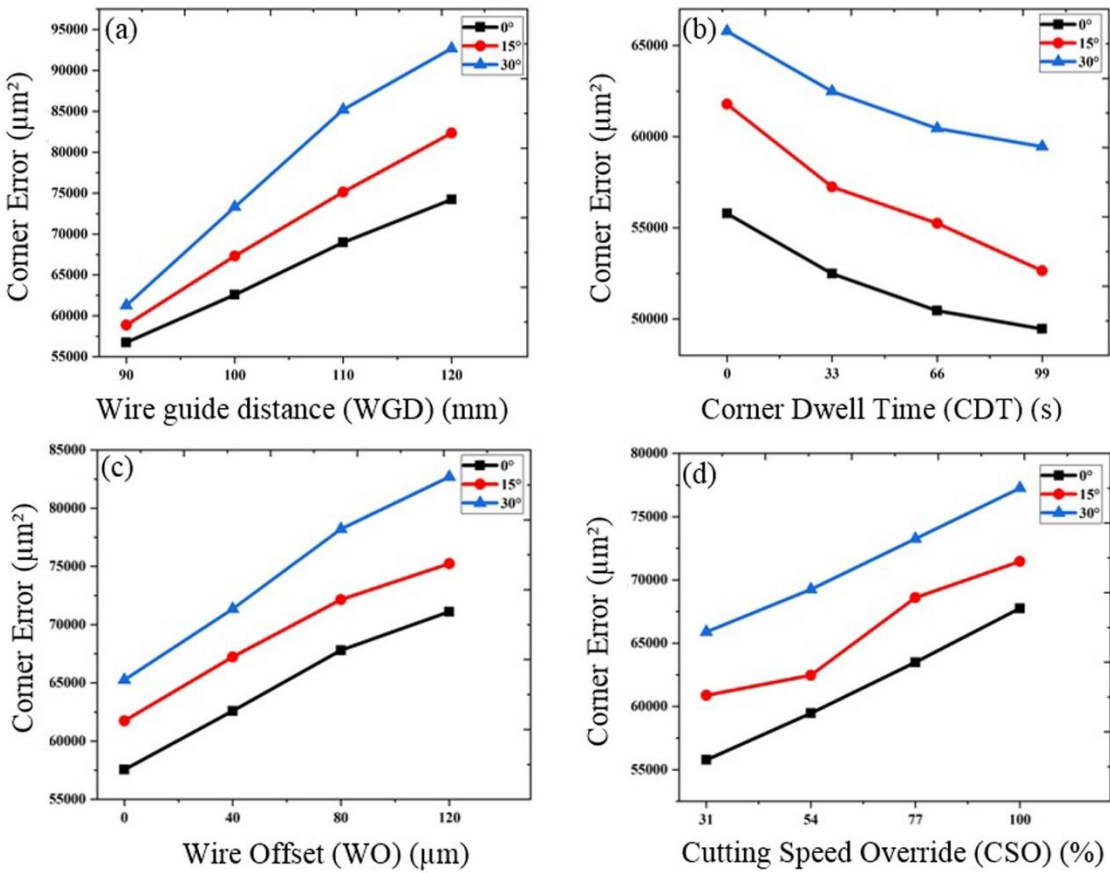
Figure 4.15 Effect of machining parameters on corner error
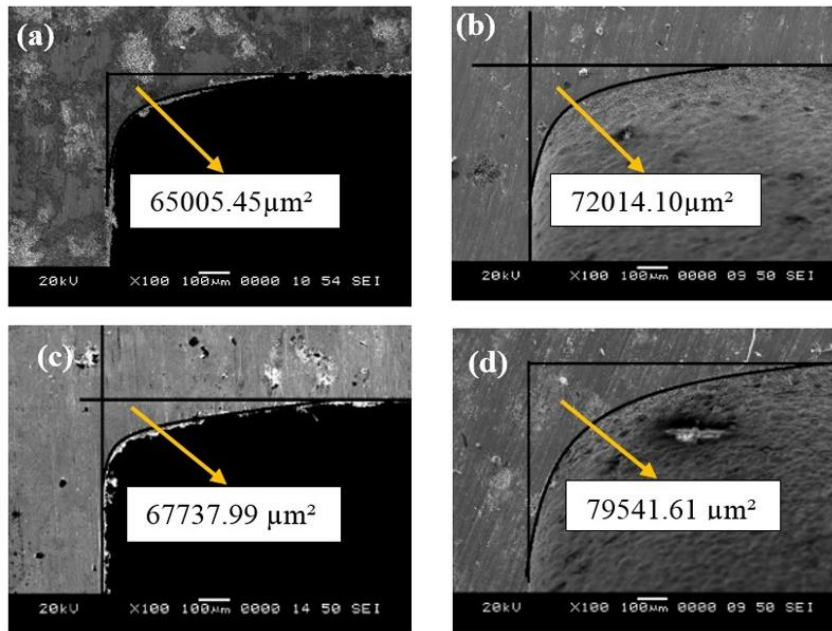
Figure 4.16 SEM images for profile corners at (a) (c) 0° and (b) (d) 60° taper angles for lowest and highest cutting speed respectively.

4.3.4 Variation of Profiling speed, Surface roughness and corner error at different taper angles

Fig. 4.17 shows the variation of profiling speed, corner error and surface roughness at different taper angle for the lowest and highest machining speed parameters. It can be seen that both the lowest and highest machining speed parameters have similar effects on the response parameter. As the taper angle increases the cutting thickness also increases. With an increase in cutting thickness the profiling speed decreases as the discharge energy gets distributed. The profiling speed decreases due to the decrease in the rate of length of cut (Puri and Bhattacharyya, 2003). The profiling speed was found to be 1.57mm/min, 1.44mm/min and 1.39mm/min for 0°, 15° and 30° taper angle respectively for the highest machining parameters (WGD=90mm, CDT=99s, WO=120μm, CSO=100%). For the lowest machining parameters lowest (WGD=120mm, CDT=0s, WO=0μm, CSO=31%), it was 0.886mm/min, 0.764mm/min and 0.65mm/min at respective taper angles.
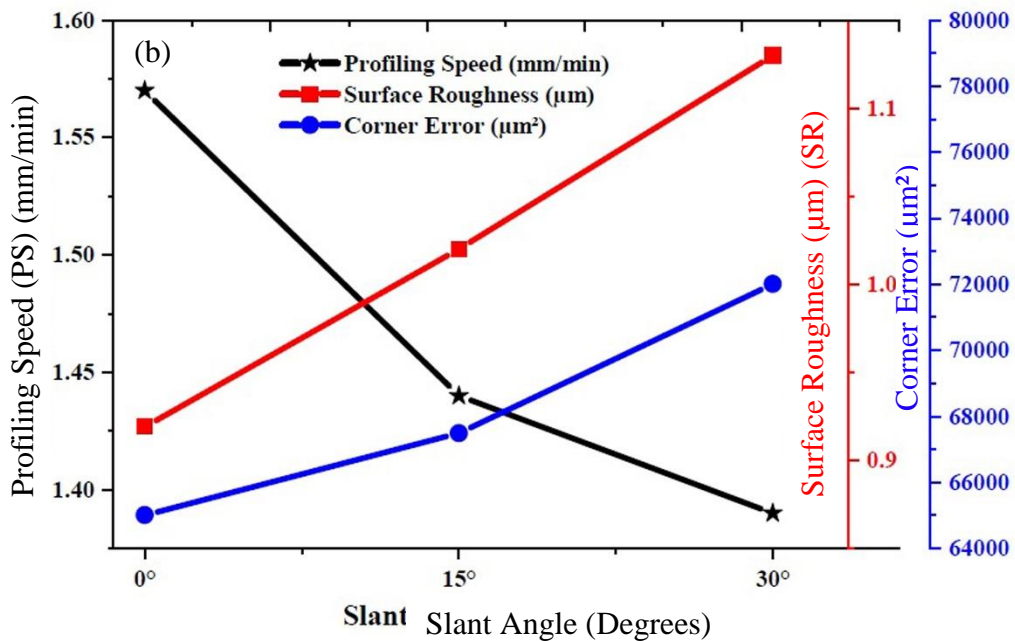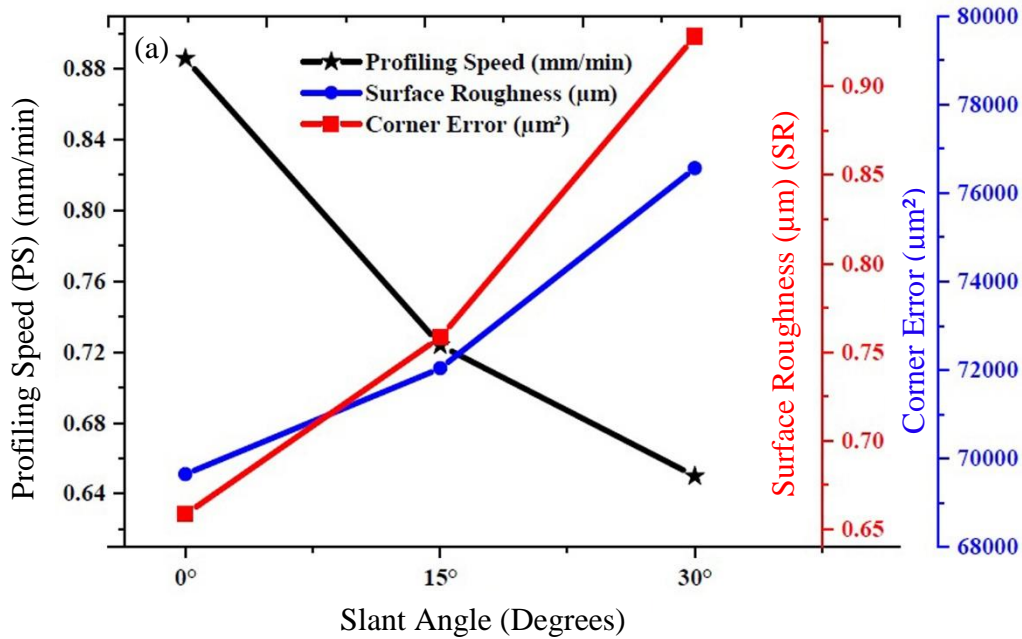
Figure 4.17 Variation of profiling speed, corner error and surface roughness at different taper angle for (a) lowest (WGD=120mm, CDT=0s, WO=0μm, CSO=31%) and (b) highest (WGD=90mm, CDT=99s, WO=120μm, CSO=100%) machining speed parameters

In case of corner error, due to the increase in thickness the wire deflection also increased. This increases the wire lag leading to higher corner error. It can be seen in fig.4.17 at the highest and lowest parameters the profiling speed decreases and the corner error increases as the taper angle increases. This was contrasting to behaviour reported by Selvakumar et al. (2018). The SEM images in fig.4.16 show the corner errors at the lowest and highest machining speed parameters. At the lowest machining parameters (WGD=120mm, CDT=0s, WO=0µm, CSO=31%) it was found to be 65005.45µm², 67487.25µm² and 72014.10µm² at 0°, 15° and 30° taper angles respectively. It was 68737.99µm², 74731.78µm² and 79541.61µm² for the highest machining parameters (WGD=90mm, CDT=99s, WO=120µm, CSO=100%) at respective taper angles.

In the case of surface roughness, as the taper angle increased the surface roughness also increased although the profiling speed decreased. This was due to the increase in cutting thickness. Due to the thickness, the flushing efficiency also decreases as melted material cannot be flush properly. It leads to re-solidification on the machined surface due to the rapid cooling by the dielectric (Goswami et al., 2017). So there is an increase in surface roughness (Samanta et al., 2019). For highest profling speed parameters (WGD=90mm, CDT=99s, WO=120µm, CSO=100%) it measured 0.919, 1.02 and 1.13 µm at 0°, 15° and 30° taper angle respective. Whereas, the lowest profling speed parameters (WGD=120mm, CDT=0s, WO=0µm, CSO=31%) surfaces measured 0.681, 0.741 and 0.854µm at respective taper angles. The SEM images in fig.4.14 shows the morphology of the surface at highest and lowest profling speed parameters.

4.3.5 Variation of recast layer thickness and microhardness

SEM images in fig.4.18 (a) to (f) shows the variation of recast layer thickness at different taper angles. During machining, the temperature increases in the machining zone due to the discharge energy. This melts the material and the molten metal is cooled by the dielectric fluid. A part of it re-solidifies on the machined surface and the remaining portion is carried away by dielectric fluid as debris. Hence the re-solidified melt forms as a recast layer at the top of the machined surface. It was observed that both at the lowest

(WGD=120mm, CDT=0s, WO=0µm, CSO=31%) and highest (WGD=90mm, CDT=99s, WO=120µm, CSO=100%) machining speed parameters, the recast layer thickness decreased as the taper angle increased. This effect was observed because the cutting thickness increased although the discharge energy with which the profiling was performed remained constant. As the cutting increases, the discharge energy gets distributed. This distribution of discharge energy results in a decrease in the recast layer thickness for higher tapered components as shown in fig.4.18. It was seen that the recast layer decreased (72.63%) from 12.73 to 3.48µm and (62.75%) from 14.150 to 5.27 µm for lowest and highest machining speed parameters as taper angle increased from 0° to 30°. The 15° was in between 0° and 30° taper angle always. Recast layer can be observed from SEM image in fig. 4.18 that there are minute voids or porosity in the recast layer, this was due to the gas bubbles gets entrapped during solidification which leads to voids on the machined surface. Therefore the surface roughness increases eventually. This can also be noticed in SEM images fig. 4.14 (a) to (d) minute voids, creates, micro-holes that contribute to the surface roughness. This SEM figures shows that the maximum recast layer thickness was caused at 0° taper profiles which was due to lower distribution of discharge energy.
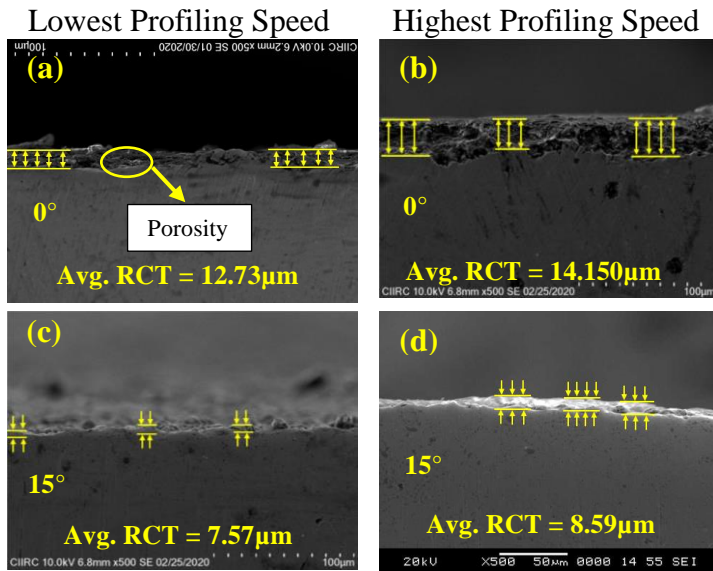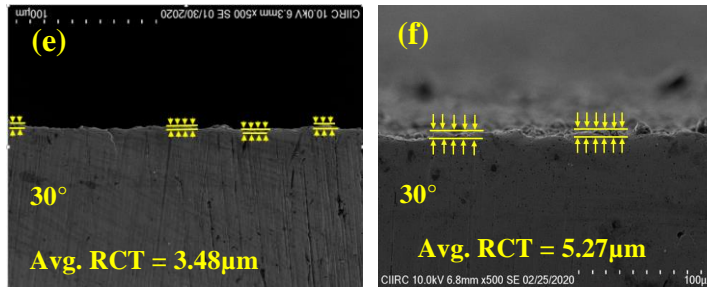
Figure 4.18 Variation of recast layer thickness with an increase in taper angle
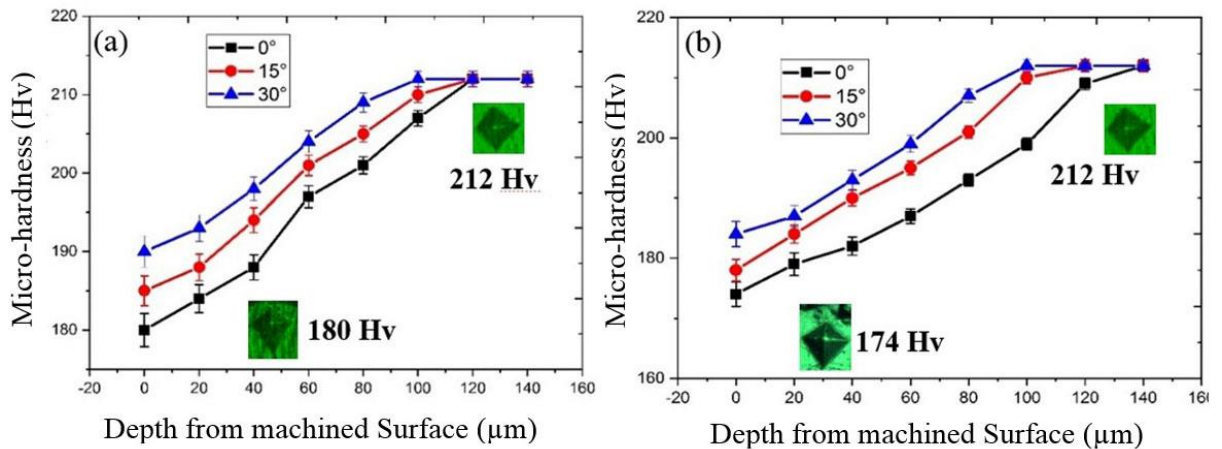
Figure 4.19 Micro-hardness at (a) Lowest (WGD=120mm, CDT=0s, WO=0μm, CSO=31%) (b) Highest (WGD=90mm, CDT=99s, WO=120μm, CSO=100%) Profiling speed parameters

Fig.4.19 (a) and (b) shows the micro-hardness for both the lowest (WGD=120mm, CDT=0s, WO=0μm, CSO=31%) and highest (WGD=90mm, CDT=99s, WO=120μm, CSO=100%) machining speed parameters respectively. It was observed that for both the WEDMed surface hardness decreases as the taper angle increases. For both machining speed parameters highest decrease was in 0° taper angle. The percentage decrease was found to be 15.09% and 17.92% for lowest and highest profiling parameters respectively. Fig. 4.19 (a) shows the least hardness to be 180, 175 and 190 HV for 0°, 15° and 30° taper angles respectively. Similarly Fig. 4.19 (b) shows the least hardness to be 182, 178 and 174 HV for respective taper angles. As the cutting thickness increases the discharge energy distributed. This distribution of discharge energy decreases the recast layer thickness for

higher tapered components (Joy et al., 2019). This indicates that the amount of layer thickness affected by WEDM process decreases as shown in SEM fig. 4.18.
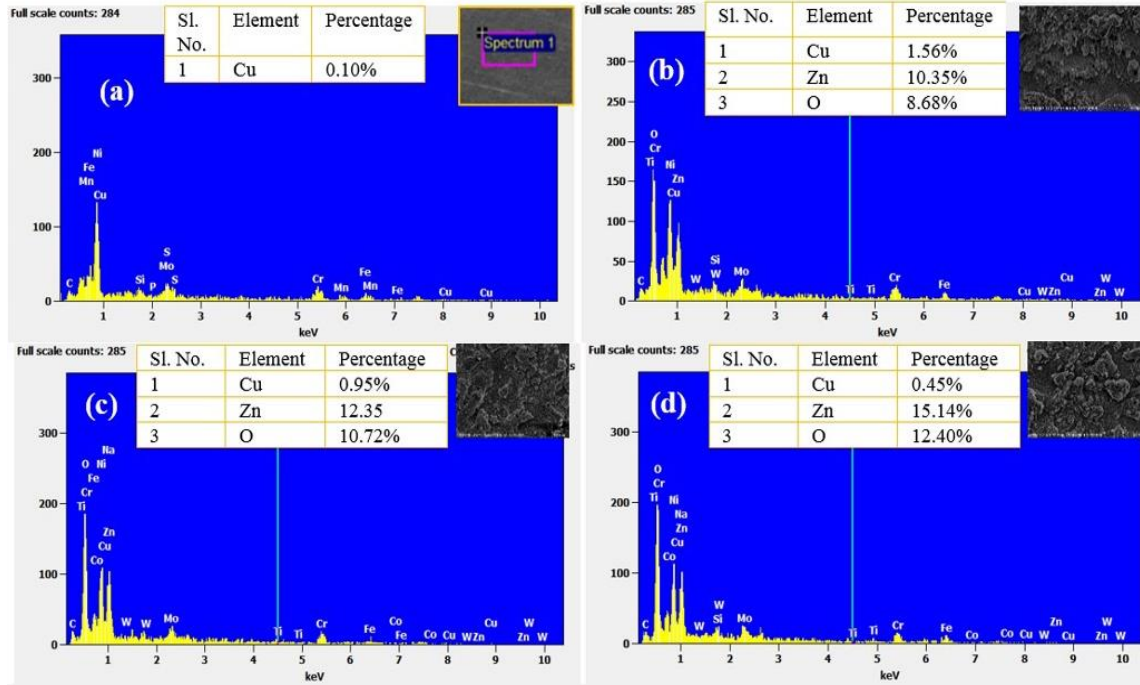
Figure 4.20 EDS of (a) As received material, (b) 0°, (c) 15°and (d) 30° tapered WEDMed surface at highest machining parameters (WGD=90mm, CDT=99s, WO=120μm, CSO=100%)

This decrease in recast layer thickness and material degradation in 30° taper angle causes an increase in the micro-hardness at higher taper angles compared to 0° taper angle as shown in fig.4.20 (a) and (b). Similar results were obtained in Joy et al. (2019). Therefore the thermal degradation also decreased which was validated by micro-hardness. This decreased in micro hardness was noticed due to the material degradation (metallurgical changes) at the machined surface. Soni et al. (2018) and Sharma et al. (2016) also observed the similar results in their investigation. The EDS in fig.4.20 (a) to (b) shows the EDS of the as received material and WEDM machined surface at different taper angles. It can be conclude that as the taper angle increases the elements like Cu, Zn and O were observed on the machined surface which decreased the hardness of the component. The Cu and Zn was induced because of the zinc-coated wire used for machining. The O was induced due

to the dielectric fluid. The addition of these elements may form a softer recast layer on the machined surface which was caused due to thermal effects.

4.3.6 Residual Stress

During machining, ionization occurs at the spark gap that induces spark intensity. This melts the material, the molten metal on the parent metal is heated by spark intensity and suddenly cooled by the dielectric fluid. This cycle is repeated as the machining progresses. These heating and cooling cycles will induce metallurgical changes in the parent material. At 30° taper angle, the cutting thickness is the highest. The amount of parent material affected due to the discharge energy decreases due to better heat distribution. The machined surface and the recast layer are subjected to heating and cooling cycles, which induce tensile residual stress. The tensile residual stress decreases in material indicating low thermal degradation as the taper angle increases (Manjaiah et al., 2017). In case of 0° taper angle, the residual stress are the highest as the heat distribution is minimal compare to 15° and 30° taper angle. This is because of the smaller cutting thickness that was subjected to heating and cooling cycles. The residual stress was tested for the WEDMed taper components after machining at highest profiling parameters (WGD=90mm, CDT=99s, WO=120µm, CSO=100%) and as received alloy as shown in fig.4.21. Manjaiah et al. (2017) have clearly stated that a thick recast layer implied a large tensile residual stress and vice versa. So it can be concluded that 0° taper angle components had larger residual stress as shown in fig.4.21 from the recast layer thickness in fig. 4.18. These stresses are produced in non- homogeneous, plastically deformed surface causes metallurgical transformation as shown in EDX in fig.4.21. The continuous heating and cooling cycles causes mainly flaws on the surface. All the WED machined surface flaws like creates, globous, cracks as shown in fig. 4.14 affects the residual stress (Ekmekri, 2007). These residual stress affect the fatigue properties of the profile/component. The metallurgical transformation and recast layer thickness are high at 0° so the micro hardness was found to be least at 0° taper angle as shown in fig. 4.19. The relation of tensile residual stresses with micro-hardness was been

reported by Sines and Carlson (1952). Sharma et al. (2018) also found similar trends in residual stress distribution in WEDMed Inconel surface.
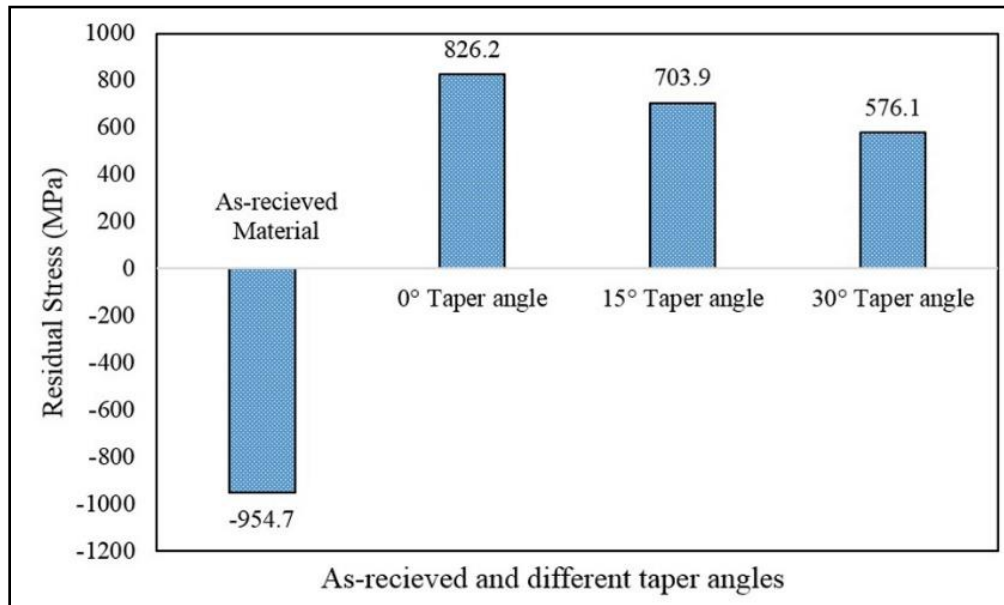
Figure 4.21 Residual Stress of as received material and different tapered profiles

4.4 SUMMARY

This section of the thesis highlights the preliminary experiments for finding cutting parameters were carried out. A suitable cutting parameter for profiling was selected and further the angles were chosen to be 0°, 15° and 30° for profiling. Further, the profiling parameters such as WGD, WO, CDT and CSO for investigation was studied for a simple profile using one factor at a time experiment. Different output responses like profiling speed, surface roughness, corner error, recast layer thickness, micro-hardness and residual stress of the profile were highlighted. Based on the experimental work the following conclusions were drawn.

1. The cutting speed decreased with an increase in angle of cut, and there was the highest reduction of 65.57% in cutting speed observed from 2.49 to 0.85 mm/min due to increase in cutting thickness.

101

2. The highest response parameters i.e.surface roughness (3.99µm), surface crack density (0.455µm/µm²) and width of cut (425.67 µm) were observed at 60° taper angle.

3. The suitable parameters for profiling were chosen as T_{on}=115µs, T_{off}=44µs, SF=20mm/min, WF=6m/min and SV=40V. It was observed that at higher taper angles 45° and 60° the errors are more due to the thickness (10mm) they were neglected for further study. Therefore the profiling was performed at 0°, 15° and 30° taper angles.

4. As the taper angle increases from 0° to 30°, at the highest profiling parameters, the profiling speed decreases by 12.53%, surface roughness and corner error increases by 22.95% and 15.72% respectively. A similar trend was found in the lowest profiling parameters the profiling speed decreased, whereas surface roughness and corner error increased by 26.64%, 25.40% and10.78% respectively.

5. The recast layer thickness decreased by 62.76 -72.66% and the hardness at the WEDM surface increases by 4.59-5.56% and as the taper angle increased by 0°, 15° and 30° at both highest and lowest parameters respectively. The EDS and XRD confirm the presence of Cu, Zn and O in WED machined surface which makes the material softer.

6. The as-cast material had compressive stresses (-954.7 Mpa) and after machining the samples exhibited tensile stresses. As the taper angle increased 0°, 15° and 30° the residual stresses decreased by 30.27% due to heat distribution.

CHAPTER 5

INVESTIGATION OF PROFILING SPEED, SURFACE ROUGHNESS AND PROFILE AREA FOR A DIFFERENT PROFILES

5.1 INTRODUCTION

In this chapter, the suitable cutting parameters (Ton=115µs, Toff=44 µs, SF=20mm/min, WF=6m/min and SV=40V) from the previous experiments were used for profiling triangular profile. The slant type taper fixture was used in machining this profile at different taper angles namely 0°, 15° and 30°. The effects on profile with different input profiling parameters like wire guide distance (WGD), corner dwell time (CDT), wire offset (WO) and cutting speed override (CSO) were examined in detail for each taper angle for different profiles. Different output response characteristics like profiling speed, surface roughness, and profile area. The influence of the taper angle on these parameters was also highlighted.

5.2 EXPERIMENTAL DETAILS

The triangular, square and circular profile were programmed using numerically controlled codes as shown in annexure-1 for different WO. These are converted into .WC files for the required machining conditions by the CNC profiling software called ELCAM. The .WC files were instructions for the machine for profiling with specific conditions like shape, distance, offset and curvature. This .WC file is loaded in Electronica 'ELPLUS 15 CNCWEDM' where the wire machines the programmed path as shown in fig.5.1 (a), (b) and (c). The slant type taper fixture facilitates the taper profiling by giving a tilt to the clamped workpiece. This enables profiling in different taper angles namely 0°, 15° and 30°. The orthogonal views of the machined profile are shown in fig.5.2. As there were four

parameters L_{16} Taguchi's orthogonal array for each angle were utilized for the study and fig.5.3 (a), (b) and (c) shows the different machined taper profiles.
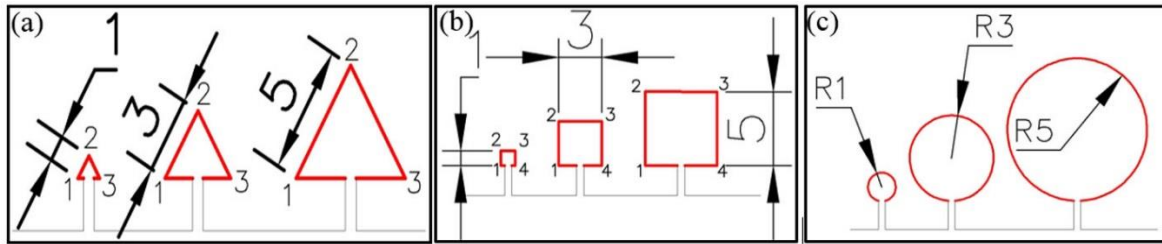
Figure 5.1 (a) Triangular (b) Square and (c) Circular Profiles with dimensions for machining
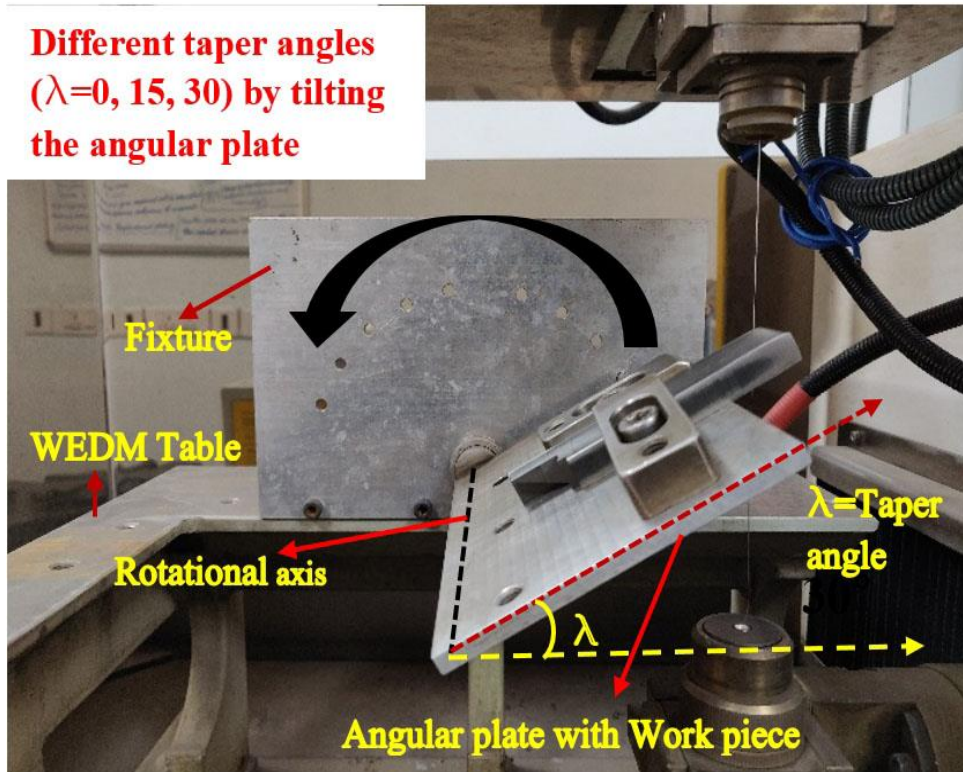
Figure 5.2 Slant type taper fixture fixed on WEDM with workpiece
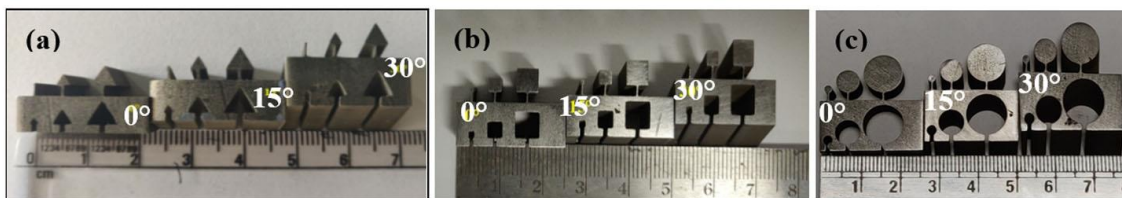
Figure 5.3 (a) Triangular (b) Square and (c) Circular machined profiles

104

5.3 EFFECT OF PROFILING SPEED ON DIFFERENT PROFILES

Different profiles like triangular, square and circular profiles were machined using slant type taper fixture. Table 5.1 shows the profiling speed for various machining parameters at different taper angles. The average profiling speed (PS) was calculated as an average of all the instantaneous cutting speed during machining of the profile.

Table 5.1 Variation of profiling speed for different profiles

Trial No.	WGD (mm)	CDT (s)	WO (μm)	CSO (%)	Triangular	Square	Circular
					PS (mm/min)		
0° Taper angle							
1	40	0	0	31	0.749	0.769	0.756
2	40	33	40	54	0.952	1.126	0.990
3	40	66	80	77	1.256	1.427	1.392
4	40	99	120	100	1.425	1.616	1.537
5	50	0	40	77	1.266	1.501	1.337
6	50	33	0	100	1.409	1.599	1.510
7	50	66	120	31	0.659	0.898	0.748
8	50	99	80	54	0.801	1.000	0.881
9	60	0	80	100	1.403	1.558	1.501
10	60	33	120	77	1.371	1.523	1.399
11	60	66	0	54	0.812	0.889	0.879
12	60	99	40	31	0.631	0.739	0.718
13	70	0	120	54	0.750	0.908	0.898
14	70	33	80	31	0.602	0.749	0.729
15	70	66	40	100	1.508	1.718	1.677
16	70	99	0	77	1.326	1.495	1.393
15° Taper angle							
1	75	0	0	31	0.523	0.723	0.719
2	75	33	40	54	0.637	0.876	0.850
3	75	66	80	77	1.089	1.289	1.263
4	75	99	120	100	1.403	1.49	1.501
5	85	0	40	77	1.137	1.345	1.263
6	85	33	0	100	1.399	1.507	1.468
7	85	66	120	31	0.520	0.754	0.712
8	85	99	80	54	0.667	0.855	0.838
9	95	0	80	100	1.399	1.493	1.456

10	95	33	120	77	1.111	1.479	1.274
11	95	66	0	54	0.663	0.876	0.843
12	95	99	40	31	0.550	0.708	0.701
13	105	0	120	54	0.656	0.858	0.813
14	105	33	80	31	0.558	0.715	0.693
15	105	66	40	100	1.477	1.628	1.602
16	105	99	0	77	1.091	1.427	1.311
30° Taper angle							
1	100	0	0	31	0.483	0.695	0.620
2	100	33	40	54	0.566	0.718	0.703
3	100	66	80	77	1.000	1.160	1.106
4	100	99	120	100	1.384	1.467	1.405
5	110	0	40	77	0.977	1.297	1.089
6	110	33	0	100	1.361	1.499	1.383
7	110	66	120	31	0.494	0.698	0.682
8	110	99	80	54	0.571	0.779	0.718
9	120	0	80	100	1.383	1.449	1.405
10	120	33	120	77	1.046	1.369	1.074
11	120	66	0	54	0.586	0.834	0.696
12	120	99	40	31	0.470	0.693	0.607
13	130	0	120	54	0.586	0.856	0.708
14	130	33	80	31	0.500	0.698	0.614
15	130	66	40	100	1.450	1.468	1.457
16	130	99	0	77	1.006	1.406	1.088

5.3.1 Analysis of profiling speed

The analysis of variance was done using Minitab software. Fig. 5.4, 5.5 and 5.6 represents main effect plots and table 5.2 shows ANOVA indicating the effect and significance of each parameter respectively. It can be observed from ANOVA that profiling speed was influenced by cutting speed override (CSO). The CSO parameter is an online parameter that can override the given machining parameter based on the shape of the profile (Read and Zenyth, 2010). In the case of the profiling speed according to the main effects plot in fig. 5.4, 5.5 and 5.6 the profiling parameters apart from CSO, remaining are least influential for all the profiles. The CSO influences the discharge energy, as the CSO increases the discharge energy increases. This increase in discharge energy increases the ionization

which escalates the sparking intensity. With the increase in sparking intensity, the metal melts faster and it increases the rate of metal cutting. It can be seen from fig. 5.4, 5.5 and 5.6 a small variations during increase in profiling speed. These variation are at 54% and 77% of CSO for different profiles in the main effect graphs. This variations is due to the increase in sparking as CSO increases during profiling (Habib 2017). It was observed profiling speed is highest at 0° and lowest at 30° due to increase in cutting thickness as the taper angle increases.
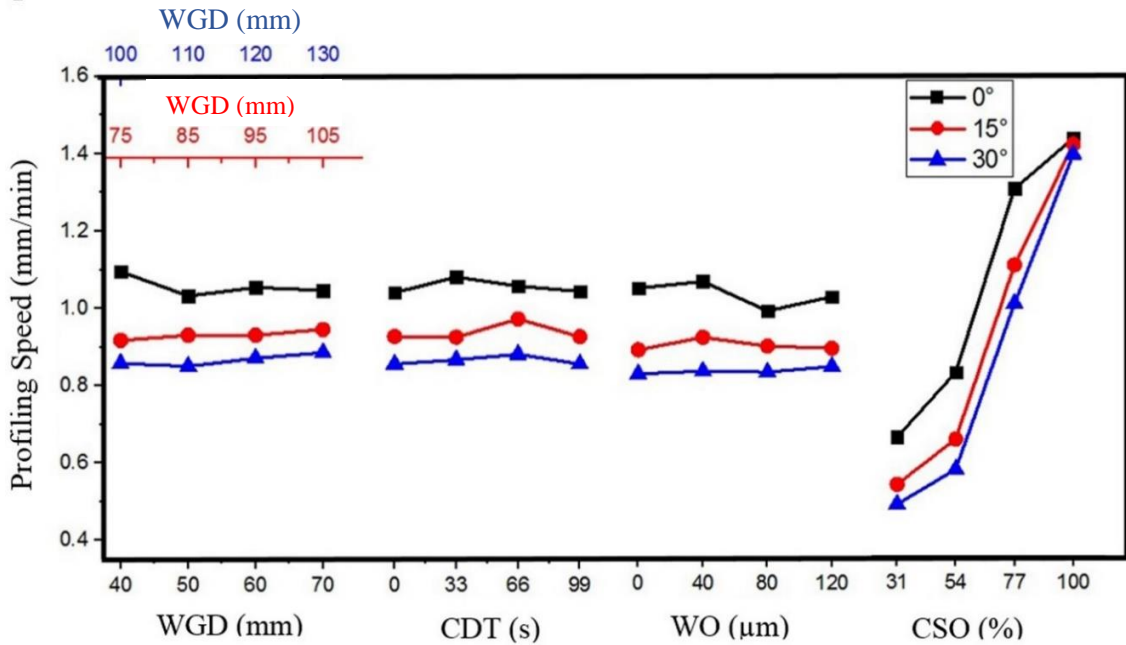
Figure 5.4 Effects plot for triangular profiling speed at different taper angles
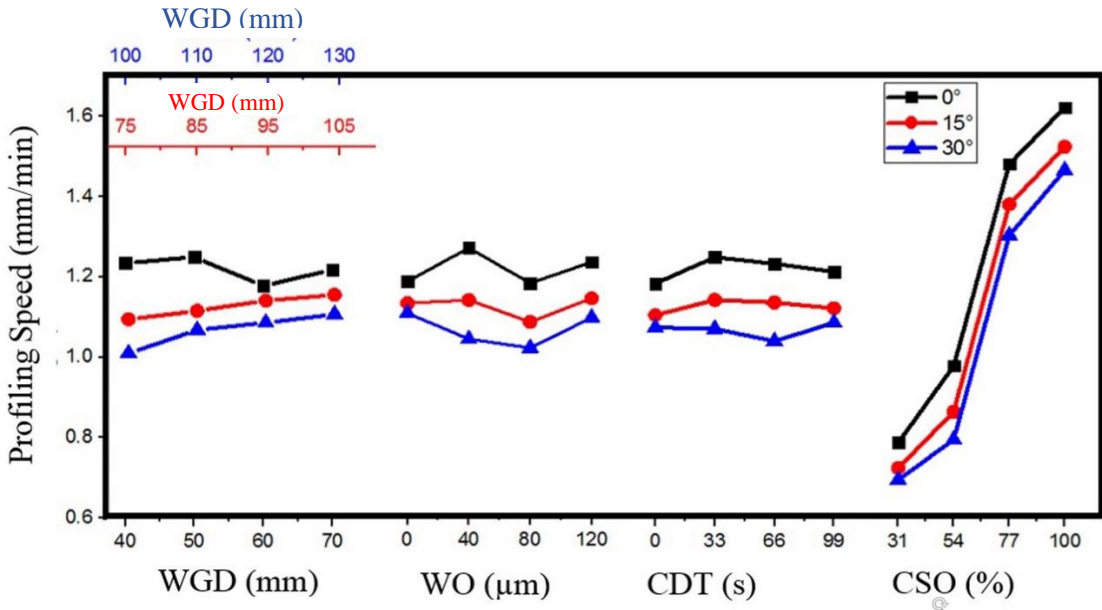
Figure 5.5 Effects plot for square profiling speed at different taper angles
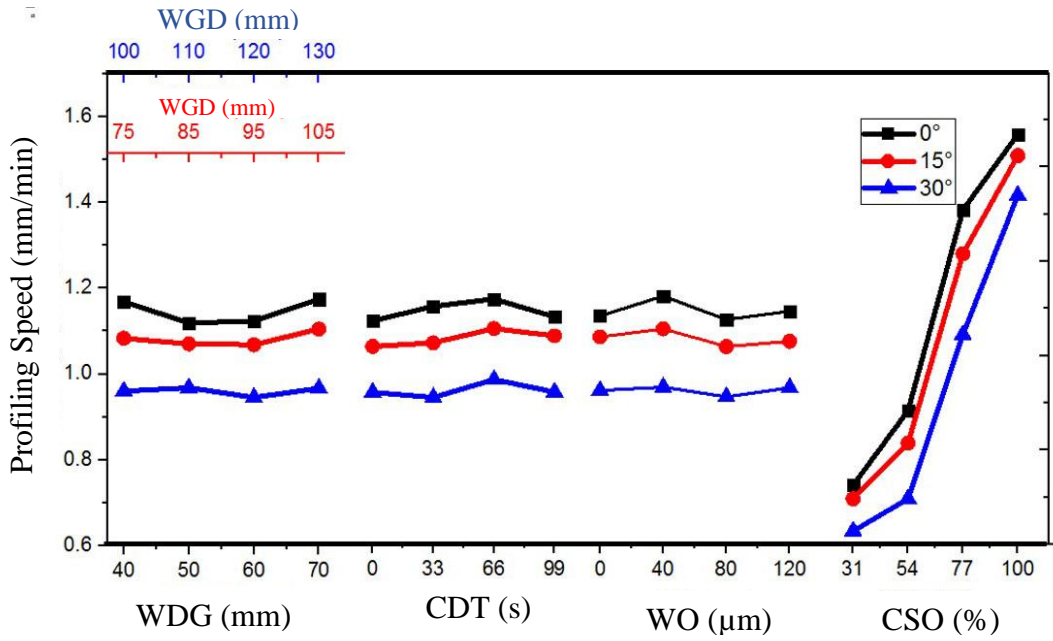
Figure 5.6 Effects plot for circular profiling speed at different taper angles

Table 5.2 Profiling speed ANOVA table for all the profiles

Sl. No.	Factor	DF	Adj SS (E-02)	Adj MS (E-02)	F-Value	P-Value	% Contribution
Triangular Profile							

	0° Taper angle						
1	WGD(mm)	3	0.889	0.296	0.34	0.798	0.521
2	CDT (s)	3	0.397	0.133	0.15	0.921	0.233
3	WO (µm)	3	1.214	0.405	0.47	0.725	0.711
4	**CSO (%)**	**3**	**165.558**	**55.186**	**63.92**	**0.003**	**97.017**
5	Error	3	2.590	0.863			
6	Total	15	170.649				
	15° Taper angle						
1	WGD(mm)	3	0.216	0.072	0.77	0.581	0.107
2	CDT (s)	3	0.030	0.010	0.11	0.950	0.014
3	WO (µm)	3	0.235	0.078	0.84	0.556	0.017
4	**CSO (%)**	**3**	**200.040**	**66.680**	**715.10**	**0.001**	**99.621**
5	Error	3	0.280	0.093			
6	Total	15	200.801				
	30° Taper angle						
1	WGD(mm)	3	0.286	0.095	1.14	0.459	0.136
2	CDT (s)	3	0.173	0.058	0.69	0.617	0.082
3	WO (µm)	3	0.076	0.025	0.30	0.823	0.035
4	**CSO (%)**	**3**	**210.587**	**70.196**	**838.11**	**0.001**	**99.628**
5	Error	3	0.251	0.084			
6	Total	15	211.373				
	Square Profile						
	0° Taper angle						
1	WGD (mm)	3	0.089	0.030	0.34	0.798	0.522
2	CDT (s)	3	0.040	0.013	0.15	0.921	0.234
3	WO (µm)	3	0.121	0.040	0.47	0.725	0.709
4	**CSO (%)**	**3**	**16.556**	**5.519**	**63.92**	**0.003**	**97.017**
5	Error	3	0.259	0.086			1.518
6	Total	15	17.065				
	15° Taper angle						
1	WGD (mm)	3	0.087	0.029	0.58	0.670	0.465
2	CDT (s)	3	0.034	0.011	0.23	0.873	0.182
3	WO (µm)	3	0.088	0.029	0.59	0.663	0.471
4	**CSO (%)**	**3**	**18.334**	**6.112**	**121.70**	**0.001**	**98.069**
5	Error	3	0.151	0.050			0.808
6	Total	15	18.695				
	30° Taper angle						
1	WGD (mm)	3	0.209	0.070	13.08	0.031	1.176
2	CDT (s)	3	0.046	0.015	2.89	0.203	0.259
3	WO (µm)	3	0.209	0.070	13.03	0.032	1.176
4	**CSO (%)**	**3**	**17.285**	**5.762**	**1077.34**	**0.001**	**97.293**
5	Error	3	0.016	0.005			0.090

6	Total	15	17.766				
Circular Profile							
0° Taper angle							
1	WGD	3	0.010	0.003	1.21	0.440	0.559
2	CDT	3	0.006	0.002	0.77	0.581	0.357
3	WO	3	0.007	0.002	0.83	0.559	0.383
4	**CSO**	**3**	**1.778**	**0.593**	**212.72**	**0.001**	**98.240**
5	Error	3	0.008	0.003			
6	Total	15	1.810				
15° Taper angle							
1	WGD	3	0.003	0.001	0.72	0.604	1.979
2	CDT	3	0.004	0.001	0.90	0.535	0.247
3	WO	3	0.003	0.001	0.79	0.574	0.217
4	**CSO**	**3**	**1.618**	**0.561**	**359.87**	**0.001**	**99.062**
5	Error	3	0.005	0.002			
6	Total	15	1.698				
30° Taper angle							
1	WGD	3	0.001	0.001	1.14	0.458	0.081
2	CDT	3	0.004	0.001	3.38	0.172	0.238
3	WO	3	0.001	0.001	0.96	0.513	0.067
4	**CSO**	**3**	**1.582**	**0.527**	**1412.68**	**0.0001**	**99.543**
5	Error	3	0.001	0.001			
6	Total	15	1.590				

5.3.2 Comparison of profiling speeds for different profiles at different angles
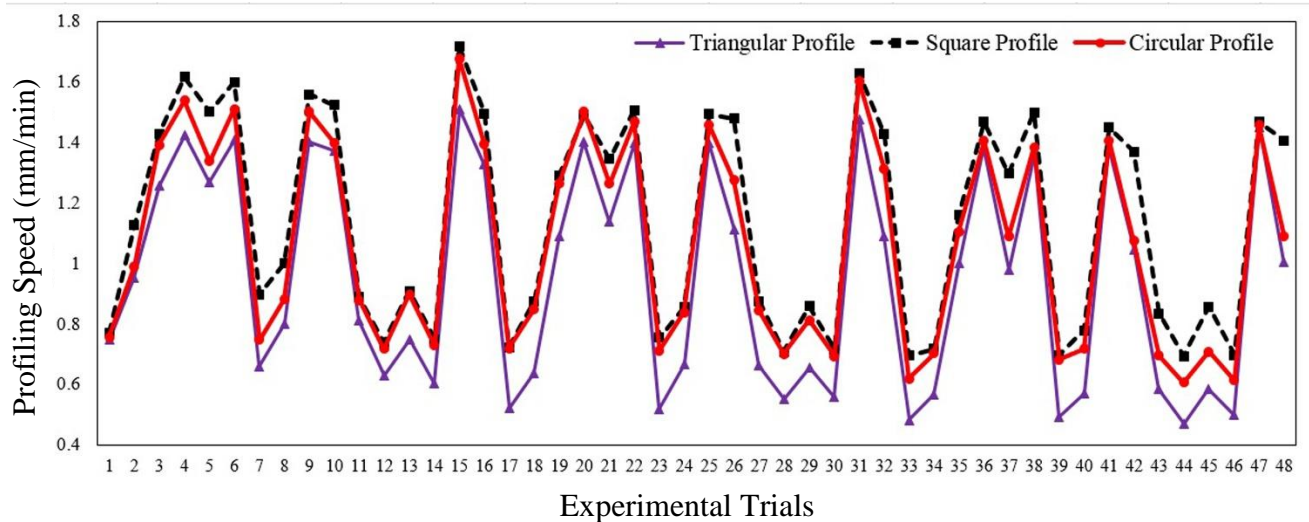
Figure 5.7 Variation of profiling speed for different experimental trials

The fig. 5.7 shows the profiling speed for different profiles. It can be seen at square profile have the highest profiling speed and triangular profile have the least profiling speed. During machining of the profiles, the instantaneous profiling speed increases or decreases gradually at the corners of the profile and then it comes back to the original profiling speed at straight edge cuts due to the CSO parameter. The CSO parameter detects the corners (acute-angled corners or right-angled corners) in the profile geometry and changes conditions during machining. It automatically tunes the speed to increases or decreases for obtaining the sharp corners in case of square and triangular profiles without changing the machining parameters (Read and Zenyth, 2010). Acute angled corners (triangular shape) need more time leading to lesser speed for its machining. So the square profiles have the highest profiling speed due to geometry, although it has a higher number of corners compared to triangular profiles. In the case of circular profiles, the wire have to traverse by changing the direction at every point. This movement of the wire in a curved way that changes the direction very instant decreasing the profiling speed. This makes the cutting speed of the circular profiles lower compared to the square profile. But comparing the triangular profile, the circular profile has a higher cutting speed due to the geometry of the profile and CSO parameter. Similar trends are found all the profiles which were machined at 15° and 30° slant angle.

5.4 EFFECT OF SURFACE ROUGHNESS ON DIFFERENT PROFILES

Table 5.3 shows the surface roughness for various machining parameters at different taper angles for all the three profiles namely triangular, square and circular profiles. The average surface roughness (SR) was calculated as an average of 3 surface roughness values of machined surface for all the profiles.

Table 5.3 Variation of surface roughness for different profiles

Trial No.	WGD (mm)	CDT (s)	WO (μm)	CSO (%)	Triangular	Square	Circular
					SR (μm)		
0° Taper angle							
1	40	0	0	31	0.447	0.551	0.542
2	40	33	40	54	0.519	0.696	0.612

3	40	66	80	77	0.577	0.696	0.65
4	40	99	120	100	0.756	0.941	0.848
5	50	0	40	77	0.657	0.766	0.683
6	50	33	0	100	0.692	0.859	0.774
7	50	66	120	31	0.476	0.644	0.495
8	50	99	80	54	0.621	0.792	0.672
9	60	0	80	100	0.799	1.025	0.834
10	60	33	120	77	0.794	0.96	0.79
11	60	66	0	54	0.518	0.659	0.582
12	60	99	40	31	0.427	0.582	0.497
13	70	0	120	54	0.663	0.843	0.686
14	70	33	80	31	0.567	0.739	0.602
15	70	66	40	100	0.909	1.108	0.945
16	70	99	0	77	0.736	0.918	0.763
15° Taper angle							
1	75	0	0	31	0.477	0.595	0.576
2	75	33	40	54	0.549	0.689	0.617
3	75	66	80	77	0.627	0.762	0.678
4	75	99	120	100	0.786	0.984	0.871
5	85	0	40	77	0.687	0.839	0.712
6	85	33	0	100	0.722	0.906	0.805
7	85	66	120	31	0.516	0.641	0.531
8	85	99	80	54	0.661	0.823	0.719
9	95	0	80	100	0.859	1.03	0.887
10	95	33	120	77	0.834	0.996	0.851
11	95	66	0	54	0.578	0.692	0.618
12	95	99	40	31	0.477	0.592	0.522
13	105	0	120	54	0.693	0.854	0.715
14	105	33	80	31	0.607	0.73	0.622
15	105	66	40	100	0.949	1.137	1.001
16	105	99	0	77	0.766	0.919	0.783
30° Taper angle							
1	100	0	0	31	0.512	0.615	0.596
2	100	33	40	54	0.571	0.699	0.637
3	100	66	80	77	0.692	0.822	0.746
4	100	99	120	100	0.821	1.054	0.891
5	110	0	40	77	0.732	0.849	0.782
6	110	33	0	100	0.757	0.906	0.835
7	110	66	120	31	0.561	0.651	0.569

8	110	99	80	54	0.693	0.843	0.749
9	120	0	80	100	0.904	1.1	0.917
10	120	33	120	77	0.899	1.098	0.921
11	120	66	0	54	0.63	0.742	0.657
12	120	99	40	31	0.512	0.592	0.552
13	130	0	120	54	0.725	0.884	0.735
14	130	33	80	31	0.64	0.75	0.642
15	130	66	40	100	0.984	1.207	1.031
16	130	99	0	77	0.821	0.959	0.843

5.4.1 Analysis of Surface Roughness (SR)

In the case of the surface roughness, the main effects plot for all the profiles is as shown in fig. 5.8, 5.9 and 5.10 with ANOVA in table 5.4 for all the profiles. It can be noticed from both main effect plots and the table that the cutting speed override (CSO) is the most influential and corner dwell time (CDT) was found to be the least influential. CDT is a corner controlling parameter, it helps in the formation of complex corners in the profile (Read and Zenyth, 2010). So the CDT doesn't affect the profiling speed. The CSO was the most contributing and significant factor on surface roughness as shown in fig. 5.8, 5.9, 5.10 and Table 5.4. Both CDT and CSO are used to the machining of intricate shapes by controlling the profiling speed.

5.4.1.1 Effect of Cutting Speed Override (CSO) on Surface Roughness

The CSO increases from 31% to 100%, the profiling speed also increases as observed in fig. 5.8, 5.9 and 5.10. This increase in CSO escalates the profiling speed by increasing the intensity of sparking. The higher intensity of sparking increased the discharge energy in the machining zone. This led to an increase in the craters, partially melted surface with micro globules, micro-holes and metal debris, cracks on the machined surface due to the higher discharge energy. Sharma et al. (2018) also observed similar phenomenon in their investigation. This causes higher peaks and valleys which increases the surface roughness. So higher profiling speed leads to higher surface roughness. Fig. 5.8, 5.9 and 5.10 shows a small variation at 54% to 77% these small variations in trends are resulting from increase in discharge energy due to sparking (Habib 2017).
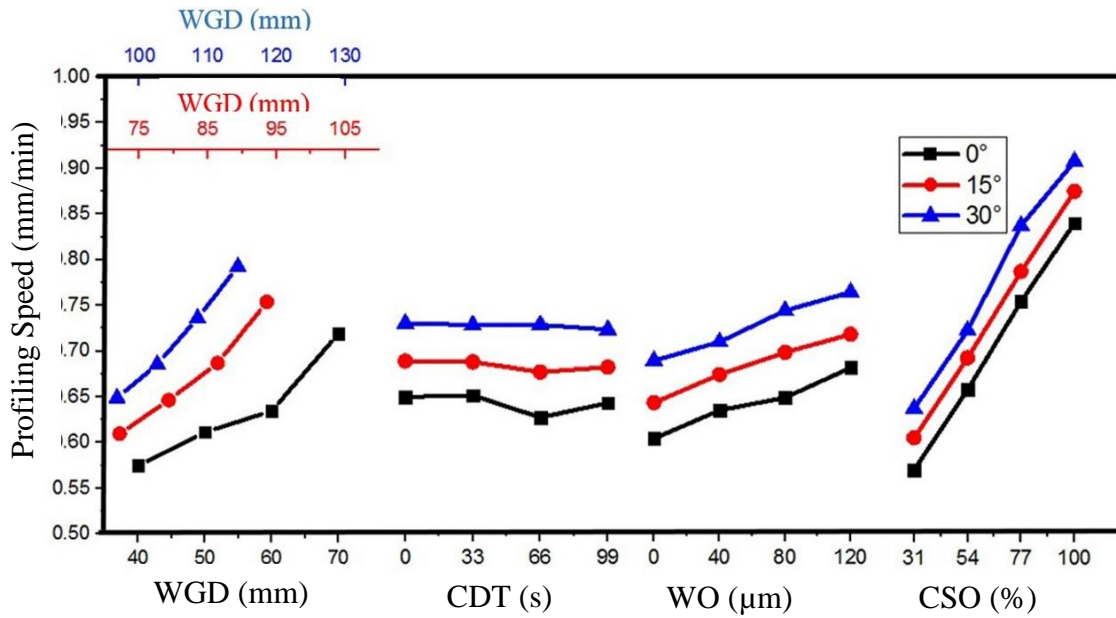
Figure 5.8 Effects plot for triangular profile surface roughness at different taper angles
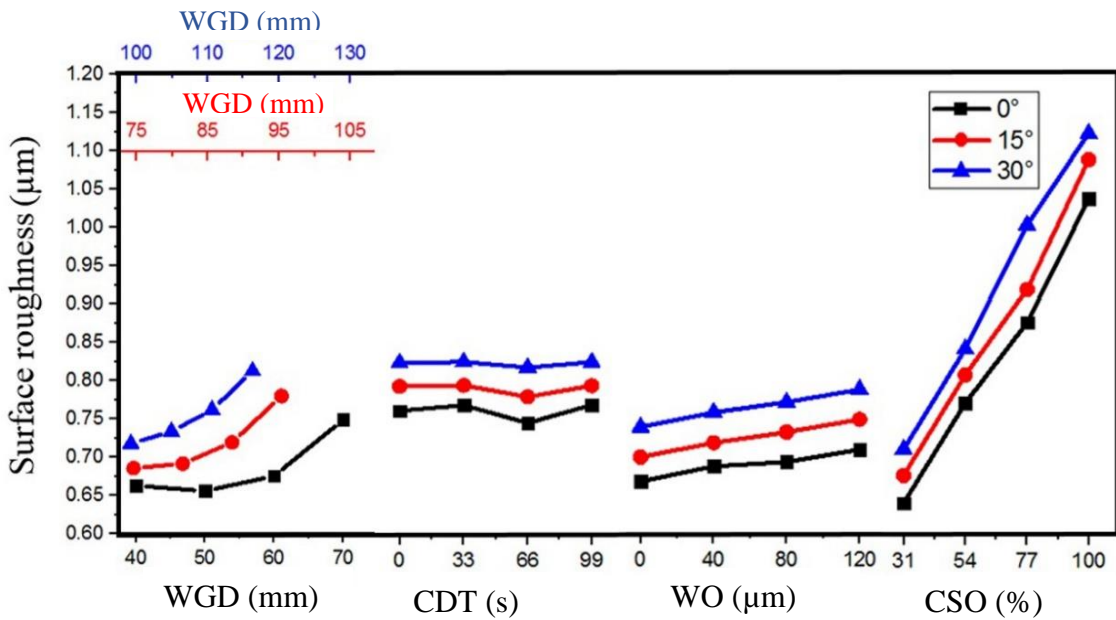
Figure 5.9 Effects plot for square profile surface roughness at different taper angles
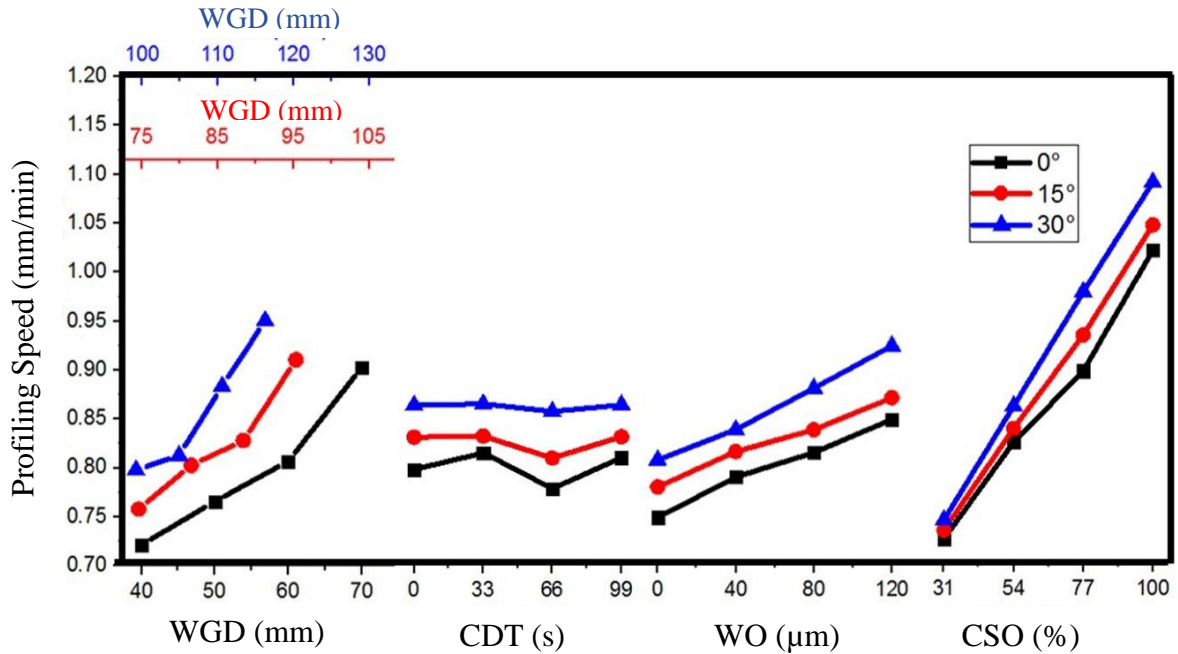
Figure 5.10 Variation of surface roughness at different machining parameters

Table 5.4 Surface roughness ANOVA table for all the profiles

Sl. No.	Factor	DF	Adj SS (E-03)	Adj MS (E-03)	F-Value	P-Value	% Contribution
Triangular Profiles							
0° Taper angle							
1	WGD(mm)	3	44.913	14.971	2.04	0.287	15.163
2	CDT (s)	3	1.333	0.444	0.06	0.977	0.450
3	WO (μm)	3	11.364	3.788	0.52	0.700	3.847
4	**CSO (%)**	**3**	**216.524**	**72.175**	**9.82**	**0.046**	**73.105**
5	Error	3	22.050	7.350			7.445
6	Total	15	296.183				
15° Taper angle							
1	WGD(mm)	3	45.792	15.264	2.19	0.268	15.579
2	CDT (s)	3	0.343	0.114	0.02	0.997	0.117
3	WO (μm)	3	11.477	03.826	0.55	0.683	3.904
4	**CSO (%)**	**3**	**215.420**	**71.807**	**10.30**	**0.043**	**73.296**
5	Error	3	20.911	6.970			7.114
6	Total	15	293.943				
30° Taper angle							
1	WGD(mm)	3	59.242	19.747	1.46	0.382	11.515
2	CDT (s)	3	0.154	0.051	0.00	1.000	0.030
3	WO (μm)	3	30.925	10.308	0.76	0.586	6.011
4	**CSO (%)**	**3**	**383.515**	**127.838**	**9.43**	**0.049**	**74.542**

5	Error	3	40.656	13.552			7.902
6	Total	15	514.491				
Square Profiles							
0° Taper angle							
1	WGD(mm)	3	0.716	0.0239	2.63	0.224	18.312
2	CDT (s)	3	0.032	0.0011	0.12	0.945	0.818
3	WO (µm)	3	0.214	0.0071	0.79	0.576	5.473
4	**CSO (%)**	**3**	**2.675**	**0.0892**	**9.82**	**0.046**	**68.414**
5	Error	3	0.272	0.0091			
6	Total	15	3.910				
15° Taper angle							
1	WGD(mm)	3	0.492	0.164	1.95	0.298	12.275
2	CDT (s)	3	0.014	0.005	0.06	0.979	0.349
3	WO (µm)	3	0.176	0.059	0.70	0.612	4.391
4	**CSO (%)**	**3**	**3.073**	**1.024**	**12.19**	**0.035**	**76.672**
5	Error	3	0252	0.084			
6	Total	15	4.008				
30° Taper angle							
1	WGD(mm)	3	0.592	0.198	1.46	0.382	11.506
2	CDT (s)	3	0.002	0.001	0.00	1.000	0.039
3	WO (µm)	3	0.309	0.103	0.76	0.586	6.006
4	**CSO (%)**	**3**	**3.835**	**1.278**	**9.43**	**0.049**	**74.538**
5	Error	3	0.407	0.136			
6	Total	15	5.145				
Circular Profiles							
0° Taper angle							
1	WGD(mm)	3	0.022	0.007	1.39	0.396	8.551
2	CDT (s)	3	0.001	0.001	0.12	0.942	0.742
3	WO (µm)	3	0.003	0.001	0.20	0.889	1.245
4	**CSO (%)**	**3**	**0.214**	**0.071**	**13.57**	**0.030**	**83.331**
5	Error	3	0.015	0.005			
6	Total	15	0.257				
15° Taper angle							
1	WGD(mm)	3	0.022	0.007	0.86	0.548	7.785
2	CDT (s)	3	0.001	0.001	0.03	0.991	0.284
3	WO (µm)	3	0.005	0.002	0.18	0.903	1.642
4	**CSO (%)**	**3**	**0.232**	**0.077**	**8.96**	**0.049**	**81.231**
5	Error	3	0.026	0.008			
6	Total	15	0.286				
30° Taper angle							
1	WGD(mm)	3	0.021	0.007	0.79	0.574	6.884
2	CDT (s)	3	0.001	0.001	0.01	0.999	0.065

3	WO (µm)	3	0.005	0.002	0.18	0.906	1.543
4	**CSO (%)**	**3**	**0.249**	**0.083**	**9.53**	**0.048**	**82.833**
5	Error	3	0.026	0.009			
6	Total	15	0.301				

5.4.1.2 Effect of Wire Guide Distance (WGD) on Surface Roughness

The next highest contributing factor was WGD as shown in table 5.4. The WGD controls the wire distance between the guides. As the WGD increases the tension between the wire decreases due to the increase in wire span between the guides (Chen et al., 2018). As the wire tension decreases the vibration of the wire escalates which leads to increases in surface roughness. This causes irregular sparking which increases the surface roughness, Chaudhary et al. (2019) also outlined similar results in their investigation where the decrease in wire tension lead to the increase in surface roughness. So it can be observed in fig. 5.8, 5.9 and 5.10 a gradual increase in the surface roughness as the WGD increases. Small variations were observed during the increase of surface roughness at different taper angle of 50 mm to 60mm due to the irregular sparking (Chaudhary et al., 2019).

5.4.1.3 Effect of Wire Offset (WO) on Surface Roughness

The WO is the offset or the perpendicular distance given during the machining of a profile. As the WO increases the wire has to traverse a larger part of the circumference. This increases the tension in the wire which leads to increase in the profiling speed. As the profiling speed increases there is an increase in surface roughness as stated by Habib and Okada (2016). So it can be observed in fig. 5.8, 5.9 and 5.10 the surface roughness increases with an increase in WO. There were small variations observed in the increase of the surface roughness at 40 and 80mm for all the profiles. This was because of the variation in wire tension during sparking as reported by Habib (2017).

5.4.2 Effect of Taper angle on Profiling Speed and Surface Roughness for different profiles.
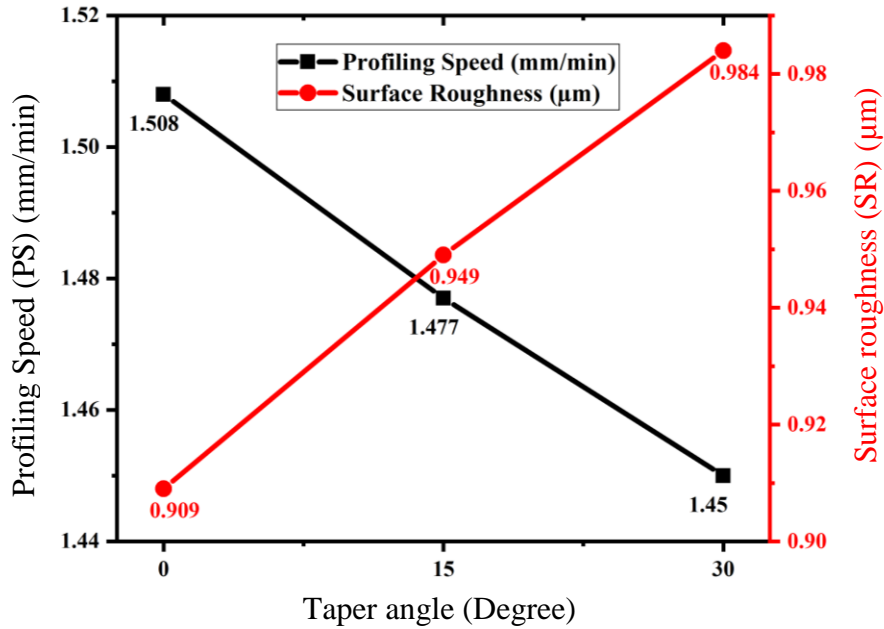
Figure 5.11 Variation of profiling speed and surface roughness for highest profiling parameters (WGD=70mm at 0°,105mm at 15°,130mm at 30°, CDT=66s, WO=40μm, CSO=100%)
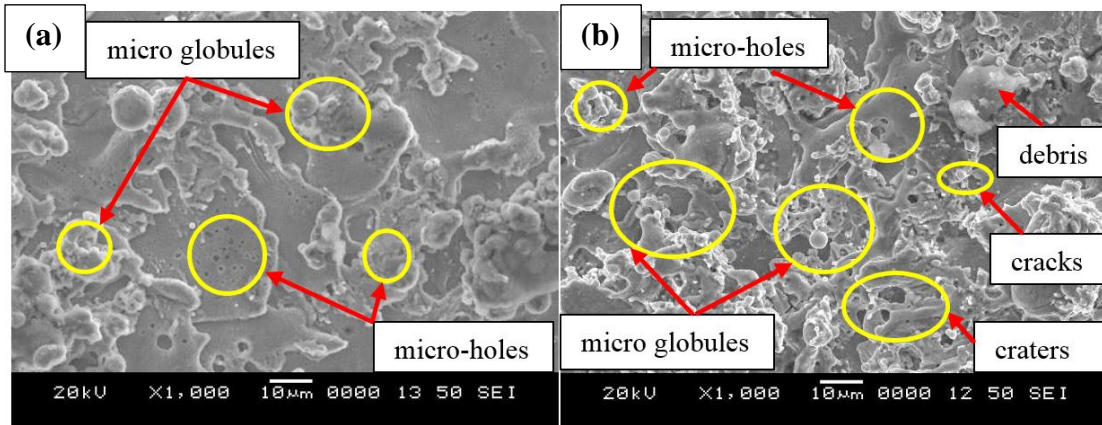
Figure 5.12 SEM images of triangular surface at (a) 0° (at PS=1.508μm, SR=0.909mm/min) and (b) 30° (at PS=1.450mm/min, SR=0.984μm) taper angles

Fig. 5.11 shows that as the taper angle increases the surface roughness also increases but profiling speed decreases. The surface roughness increases from 0.909 to 0.989μm as the

taper angle increase from 0° to 30°. This is because the rapid cooling provided by the dielectric fluid increases the number of smaller craters, larger micro globules, micro-holes as indicated in SEM fig. 5.12 (b). The re-solidification of the melt occurs before the dielectric fluid enters the machining zone at 30° taper angle, this is due to the increase in cutting thickness. Contrastingly, the 0° taper angle shows lesser craters, micro globules, micro-holes as in fig. 5.12 (a). Goswami et al. (2017) also observed similar results in surface roughness due to the rapid cooling by the dielectric fluid. Similar trends have been observed in our studies and shown in section 5.4.1, where 30° taper angle yields maximum surface roughness than 0° taper angle at all the profiling parameters. In the case of the profiling speed, this decrease with the increase in taper angle was observed due to the increase in cutting thickness. As the cutting thickness increases the material that has to be cut increases because of the increase in taper angle. This decreases the profiling speed from 1.508 to 1.450 mm/min as it takes more time to melt the material. Fig. 5.4, 5.5 and 5.6 also shows similar trends where the 30° taper angle has the least profiling speed and the 0° taper angle has the highest profiling speed. Similar trends have been followed by square and circular profiles. The profiling speed for square profiles were 1.719, 1.628 and 1.468 mm/min and surface roughness were 1.109, 1.137 and 1.207 µm for 0°, 15° and 30° taper angles. In case of circular profiles, the profiling speed for were 1.677, 1.602 and 1.457 mm/min and surface roughness were 0.945, 1.001 and 1.031 µm for respective taper angles. The SEM images in fig. 5.13 and 5.14 shows the machined surfaces.
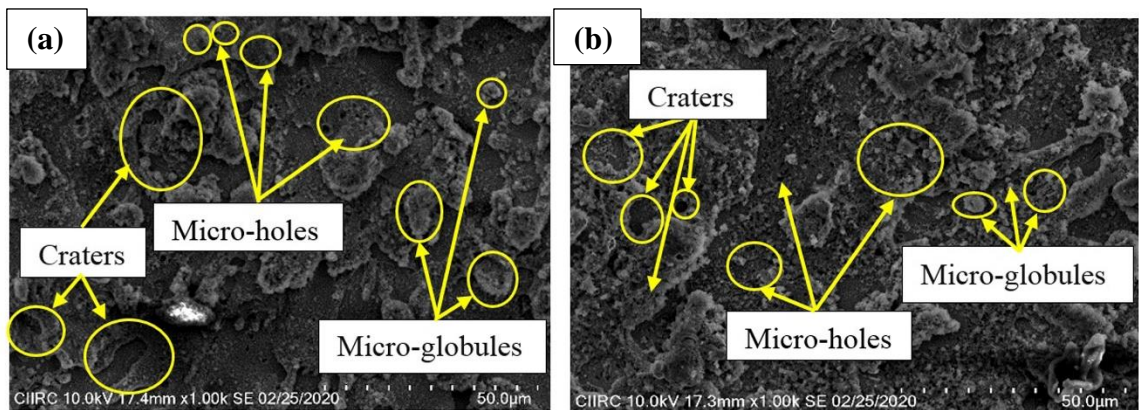
Figure 5.13 SEM images of square surface at (a) 0° (at PS=1.719mm/min, SR=1.109µm) and (b) 30° taper angles (at PS=1.468mm/min, SR=1.207µm)
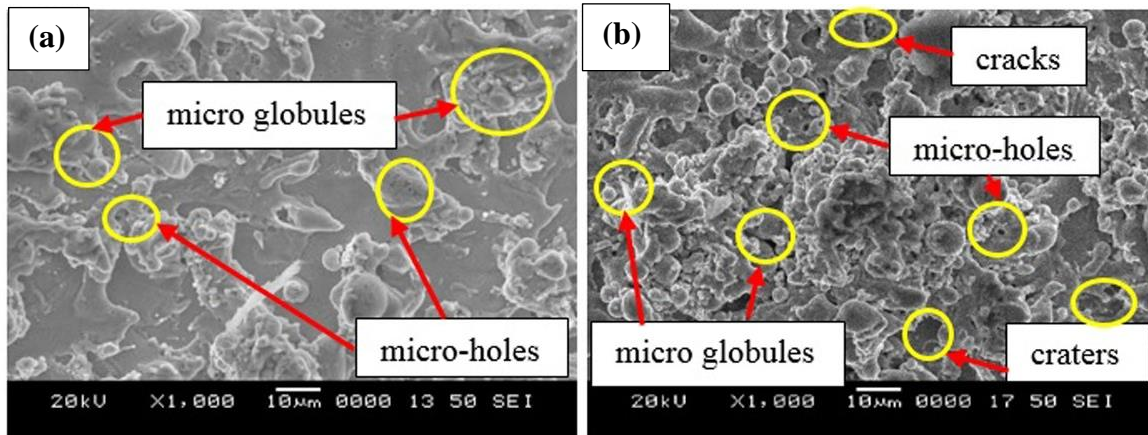
Figure 5.14 SEM images of circular surface at (a) 0° (PS=1.677mm/min, SR=0.945μm) and (b) 30° taper angles (PS=1.457mm/min, SR=1.031μm)

5.4.3 Comparison of surface roughness for different profiles at different angles

From section 5.3.2 it can be noticed that the square profiles have highest cutting speed although it has more corners than triangular profiles. The triangular profiles takes more time to machine as it has acute angled corners where the CSO parameter machines in lower speed than square profiles to ensure minimum damage to the corners (Read and Zenyth, 2010). The circular profiles have profiling speed in between the triangular profiles and square profiles as the wire have to change its direction at every point due to the curved path. So in case of surface roughness, it is highest in square profiles due to higher profiling speed. Similarly triangular profiles have lowest surface roughness due to lower cutting speed as shown in fig. 5.15. As the CSO increases the profiling speed also increases due to the increase in discharge energy. This increases the surface roughness of the profiles due to the sparking and rapid melting of workpiece. Similar results were observed by Sharma et al. (2016).
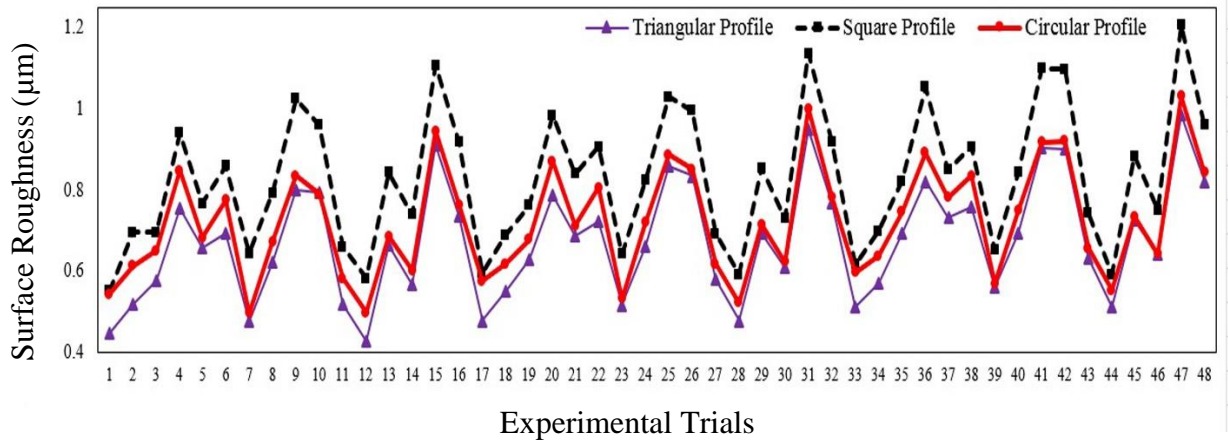
Figure 5.15 Comparison of surface roughness of different profiles for different trials

5.5 VARIATION OF PROFILE AREAS FOR DIFFERENT PROFILES
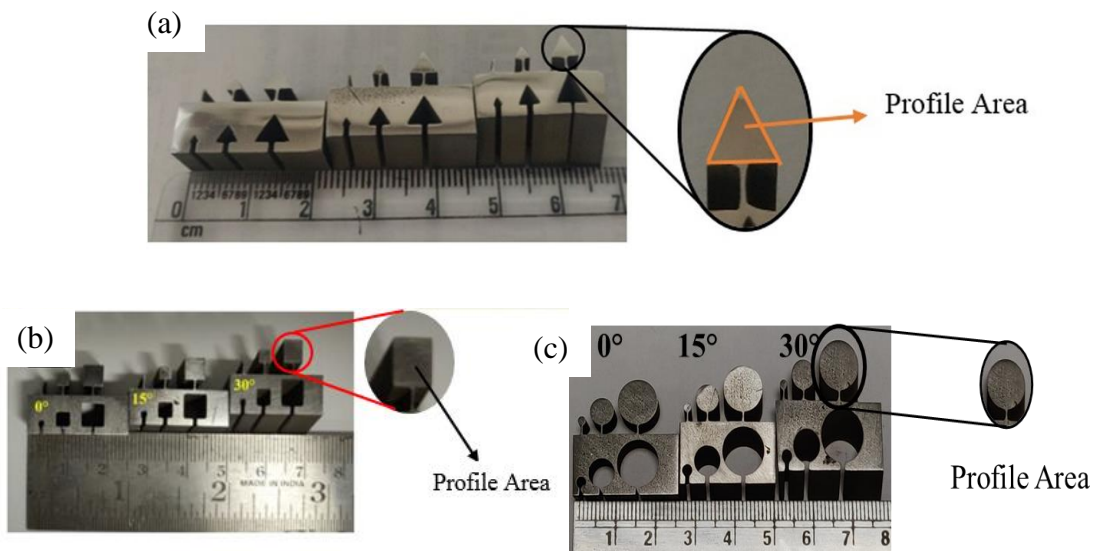
Figure 5.16 Profile areas for (a) triangular, (b) square and (c) circular profiles
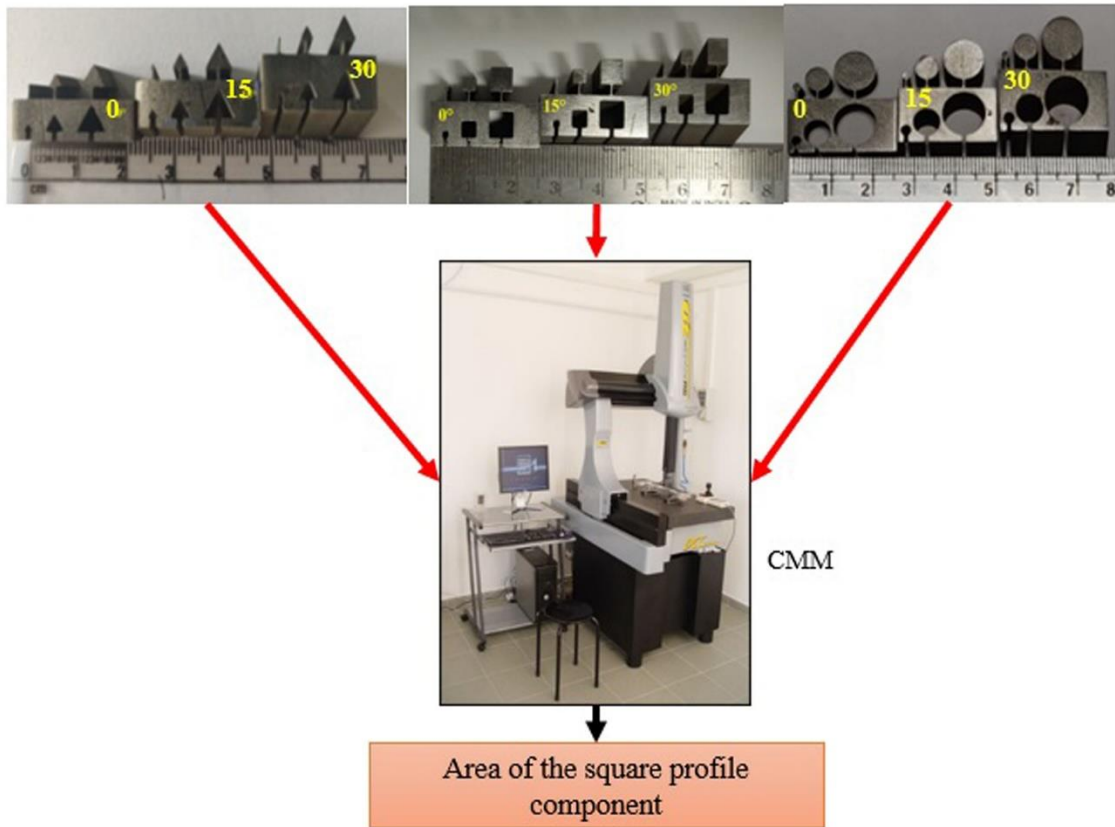
Figure 5.17 Profile areas measured from CMM

The machined profiles namely triangular, square and circular profiles with the aid of slant type taper fixture at different taper angles like 0°, 15° and 30° is as shown in fig.5.16. A different phenomenon like overcut, undercut, dimensional shift and its variation to profiling parameters like WDG, WO, CDT and CSO. The profile area was taken as a response parameter so that the dimensional variation during WEDM can be tracked. The variation in profile area was recorded and measured using CMM. The 1mm, 3mm and 5mm triangular, square and circular profiles were measured using CMM as shown in fig. 5.17.

5.5.1 Analysis of profile areas

Table 5.5 shows the profile areas at different parameters for 0°, 15° and 30° taper angles. The ANOVA and main effect plots were obtained from the Minitab software. Table 5.6 shows the ANOVA recorded at different parameters for various taper angles. From ANOVA table and main effects plot in fig. 5.18 to 5.20, it can be concluded that the profile area was mostly influenced by the WO. WO also contribute majorly (82.36-49.08%) during

slant profiling. The next contributing parameter is WDG followed by CSO and CDT. The CDT parameter influences only on corner of the profile as observed in section 6.2. It can be noticed that wire offset and wire guide distance are the most significant factor in most of the cases at all taper angles.

Table 5.5 Areas of different profiles at different angles

Sl. No.	Area of triangle (mm²)			Area of Square (mm²)			Area of Circle (mm²)		
	1mm	3mm	5mm	1mm	3mm	5mm	1mm	3mm	5mm
0° Taper angle									
1	0.27	2.89	9.101	0.773	7.66	23.086	2.599	25.659	74.990
2	0.293	2.888	9.412	0.786	7.622	22.969	2.750	26.459	75.878
3	0.37	2.843	9.81	0.986	8.265	23.112	2.906	25.839	77.085
4	0.434	3.043	10.007	1.059	8.797	24.131	3.170	26.601	78.419
5	0.25	2.928	8.904	0.690	7.392	22.323	2.582	25.358	75.785
6	0.153	2.699	8.557	0.664	7.194	21.914	2.350	23.841	74.394
7	0.422	3.511	10.02	1.033	8.689	24.284	3.136	27.474	78.099
8	0.316	2.802	9.597	0.765	8.249	23.432	2.832	26.366	77.100
9	0.231	2.855	9.359	0.701	7.672	23.032	2.652	26.123	75.931
10	0.362	3.058	9.492	0.822	8.138	23.633	2.841	26.030	77.260
11	0.205	2.627	8.338	0.588	6.989	21.826	2.488	24.732	73.868
12	0.236	2.788	9.019	0.806	7.676	22.425	2.541	25.458	76.284
13	0.354	3.278	9.518	0.938	8.206	23.392	2.814	25.765	76.161
14	0.305	2.891	9.361	0.865	7.956	22.766	2.795	26.003	76.642
15	0.169	2.943	8.209	0.529	6.877	22.13	2.377	24.312	73.953
16	0.111	2.565	8.106	0.460	6.787	21.754	2.313	24.245	72.439
15° Taper angle									
1	0.28	3.159	10.75	0.953	9.019	25.486	3.029	27.859	76.490
2	0.339	3.147	11.004	0.957	8.872	25.369	3.110	28.759	77.378
3	0.393	3.89	12.087	1.166	9.261	25.612	3.266	28.339	78.585
4	0.466	3.771	12.189	1.239	9.454	26.431	3.440	28.901	79.719
5	0.291	3.942	10.819	0.855	8.555	24.723	2.942	27.658	76.918
6	0.19	2.86	10.371	0.833	8.293	24.213	2.650	26.141	75.294
7	0.473	3.903	12.709	1.198	9.603	26.584	3.536	29.774	79.199
8	0.336	4.244	11.802	0.926	9.218	25.832	3.162	28.566	78.200
9	0.309	4.048	11.484	0.881	8.905	25.332	2.932	28.223	76.903
10	0.395	3.723	11.328	1.006	9.262	26.033	3.171	28.130	78.069
11	0.243	3.195	10.328	0.751	8.214	24.126	2.798	26.732	75.007
12	0.248	3.014	10.48	0.986	8.484	24.825	2.861	27.458	77.082
13	0.389	4.195	11.805	1.100	9.094	25.792	3.154	27.665	77.361
14	0.366	3.773	11.590	1.049	8.872	25.166	3.145	27.903	77.642
15	0.203	3.385	9.710	0.709	8.411	24.330	2.627	26.312	75.153

16	0.145	3.136	9.782	0.640	8.012	24.154	2.583	26.345	73.439
30° Taper angle									
1	0.37	3.663	11.686	1.253	9.160	25.946	4.429	32.841	78.190
2	0.383	3.651	11.99	1.247	9.192	26.205	4.510	34.351	78.778
3	0.481	3.234	12.09	1.476	9.765	26.760	4.666	35.928	79.585
4	0.521	3.946	12.416	1.539	10.197	27.869	4.840	39.487	80.919
5	0.33	3.789	11.66	1.215	8.862	25.582	4.342	33.240	78.784
6	0.237	3.714	10.781	1.143	8.594	24.845	4.050	29.952	76.794
7	0.519	4.199	12.801	1.538	10.089	27.656	4.936	38.981	80.699
8	0.403	3.321	12.124	1.316	9.549	26.384	4.562	35.732	79.600
9	0.379	4.202	11.755	1.181	9.172	26.209	4.432	33.278	78.331
10	0.454	3.979	11.72	1.276	9.638	26.863	4.471	34.948	79.269
12	0.252	3.698	11.383	1.091	8.489	24.728	4.098	30.207	76.568
13	0.341	3.636	11.161	1.286	9.146	25.563	4.161	31.344	78.384
14	0.495	4.310	11.491	1.440	9.706	26.433	4.454	34.823	78.506
15	0.412	3.704	12.001	1.309	9.456	26.381	4.445	34.185	79.642
16	0.284	3.210	10.997	1.009	8.447	24.915	3.927	28.772	76.653

Table 5.6 ANOVA for different profile areas at three taper angles

Sl. No.	Factor	DF	1mm		3mm		5mm	
			Sum of squares (E-01)	% Contribution	Sum of squares (E-01)	% Contribution	Sum of squares (E-01)	% Contribution
Triangular Profile								
0° Taper angle								
1	WDG	3	0.027	19.424	0.202	23.962	1.327	23.708
2	CDT	3	0.001	0.719	0.004	0.474	0.038	0.713
3	**WO**	**3**	**0.099**	**71.223**	**0.584**	**69.276**	**3.896**	**69.519**
4	CSO	3	0.009	6.475	0.043	5.101	0.285	5.169
5	Error	3	0.003	2.158	0.010	1.186	0.045	0.891
15° Taper angle								
1	WDG	3	0.019	13.768	0.214	16.449	1.786	15.498
2	CDT	3	0.002	1.449	0.002	0.154	0.082	0.693
3	**WO**	**3**	**0.107**	**77.536**	**0.984**	**75.634**	**8.848**	**76.623**
4	CSO	3	0.006	4.348	0.063	4.842	0.507	4.416
5	Error	3	0.004	2.899	0.038	2.921	0.321	2.771
30° Taper angle								
1	WDG	3	0.019	12.752	0.113	12.047	1.020	25.823
2	CDT	3	0.002	1.342	0.004	0.426	0.050	1.266
3	**WO**	**3**	**0.120**	**80.537**	**0.774**	**82.516**	**1.940**	**49.114**
4	CSO	3	0.007	4.698	0.024	2.559	0.304	7.595

5	Error	3	0.001	0.671	0.023	2.452	0.640	16.203
				Square Profile				
				0° Taper angle				
1	WGD	3	0.960	21.371	9.319	16.543	14.734	16.014
2	CDT	3	0.004	0.089	0.743	1.319	0.569	0.618
3	**WO**	**3**	**2.683**	**59.728**	**42.440**	**75.340**	**68.701**	**74.669**
4	CSO	3	0.458	10.196	3.365	5.974	4.186	4.550
5	Error	3	0.387	8.615	0.464	0.824	3.818	4.150
				15° Taper angle				
1	WGD	3	0.961	21.384	7.083	21.277	16.550	17.463
2	CDT	3	0.005	0.111	0.252	0.757	0.844	0.891
3	**WO**	**3**	**2.685**	**59.746**	**23.539**	**70.709**	**69.577**	**73.414**
4	CSO	3	0.473	10.525	1.356	4.073	4.618	4.873
5	Error	3	0.370	8.233	1.060	3.184	3.184	3.360
				30° Taper angle				
1	WGD	3	1.006	22.405	8.662	16.302	31.501	19.858
2	CDT	3	0.029	0.646	0.110	0.207	0.122	0.077
3	**WO**	**3**	**2.664**	**59.332**	**40.532**	**76.280**	**118.871**	**74.936**
4	CSO	3	0.407	9.065	3.361	6.325	6.923	4.364
5	Error	3	0.384	8.552	0.471	0.886	1.212	0.764
				Circular profile				
				0° Taper angle				
1	WGD	3	0.182	18.440	2.314	16.599	7.576	19.095
2	CDT	3	0.010	1.034	0.0577	0.414	0.411	1.035
3	**WO**	**3**	**0.725**	**73.381**	**7.927**	**56.873**	**28.933**	**72.919**
4	CSO	3	0.042	4.235	2.184	15.670	2.010	5.066
5	Error	3	0.029	2.910	1.458	1.458	0.748	1.886
				15° Taper angle				
1	WGD	3	0.264	22.783	4.304	27.619	10.059	24.381
2	CDT	3	0.005	0.463	0.029	0.186	0.101	0.245
3	**WO**	**3**	**0.750**	**64.797**	**8.017**	**51.445**	**28.470**	**69.003**
4	CSO	3	0.115	9.914	1.664	10.678	1.907	4.622
5	Error	3	0.024	2.044	1.569	1.068	0.722	1.749
				30° Taper angle				
1	WGD	3	0.444	32.524	42.055	26.491	8.604	23.357
2	CDT	3	0.009	0.624	0.310	0.195	0.126	0.343
3	**WO**	**3**	**0.798**	**58.489**	**106.802**	**67.276**	**23.729**	**64.420**
4	CSO	3	0.077	5.645	5.229	3.294	3.014	8.183
5	Error	3	0.037	2.717	4.357	2.745	1.362	3.697

5.5.1.1 Effect of wire offset (WO) on Profile area

The WO offset contributes most on profile areas of all the profiles. From Fig. 5.17, 5.18 and 5.20, it can be concluded that as the WO increases, the profile areas also increases. This increase is due to an increase in offset distance given to wire during profiling. The wire is moved to a fixed perpendicular distance from the programmed profile that leads to an increased profile area (Kumar et al., 2016; Selvakumar et al., 2018). The amount and direction of shift of the wire can be controlled through part programming. Fig. 5.17, 5.18 and 5.20 shows a clear increase of profile areas as the WO increases for 1mm triangle, 1mm square and 5mm circle. It can be noticed that there was a variation in the increase in form 40µm to 80µm at 15° and 30° respectively. This phenomenon was observed due to the variation in wire tension at higher values of offsets. As the wire offset values increase the wire have to cut the workpiece with a larger part of profile circumference with fixed wire length (WGD). So wire tension differs as compared to normal machining as stated by Habib and Okada (2016).
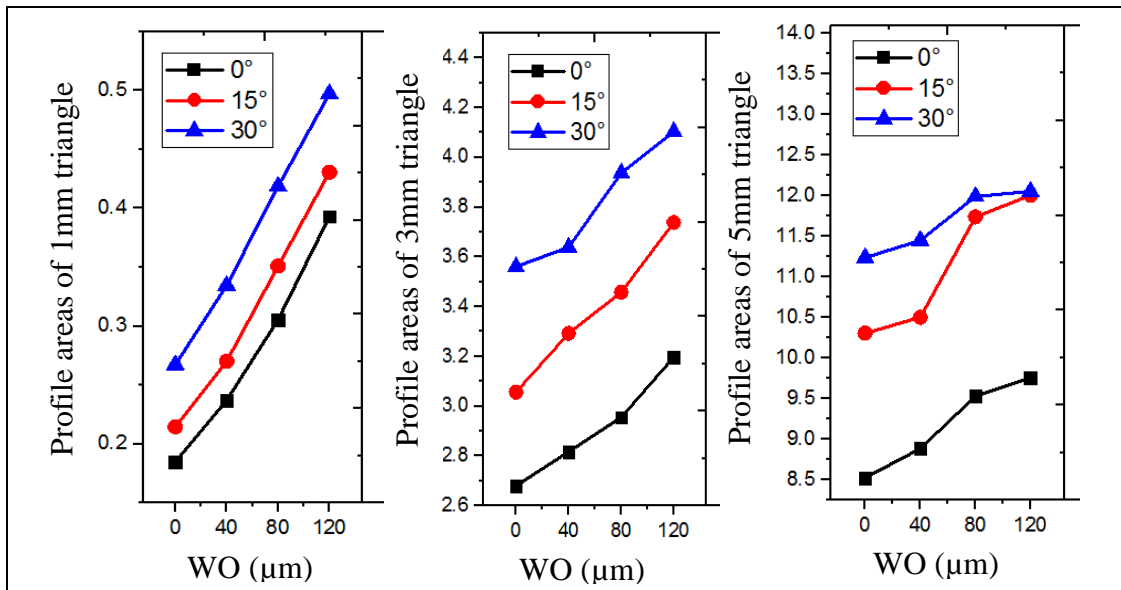
Figure 5.18 Effect wire offset (WO) on triangular profile areas

126
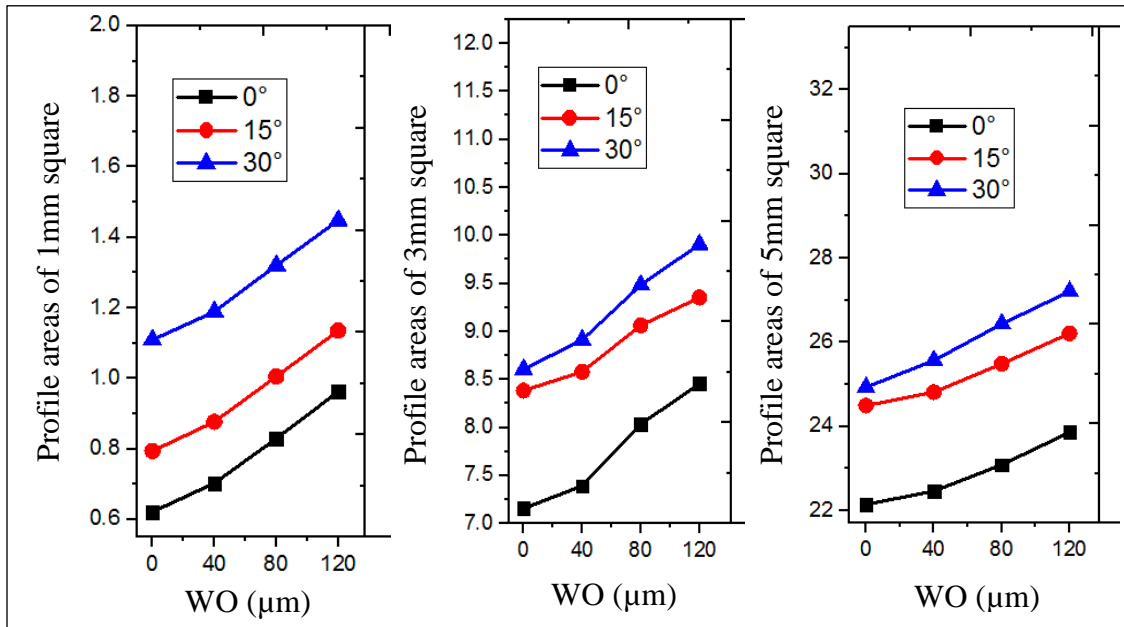
Figure 5.19 Effects plots for wire offset (WO) parameter on square profile areas
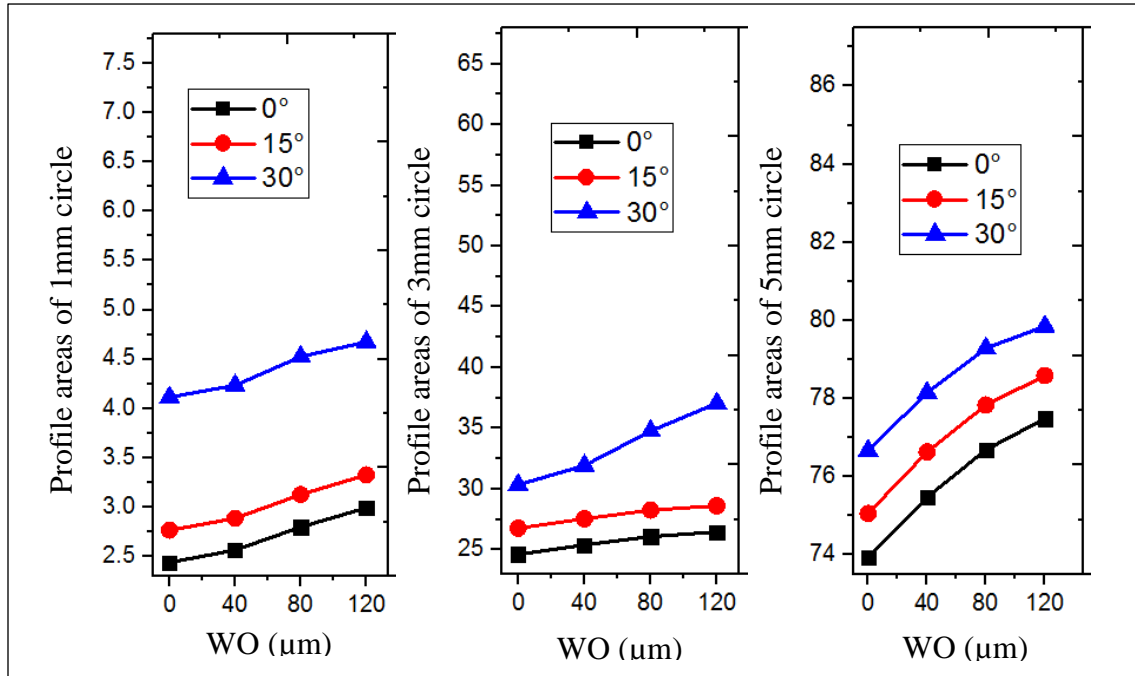
Figure 5.20 Effects plots for wire offset (WO) parameter on circular profile areas

5.5.1.2 Effect of wire guide distance (WGD) on Profile area

The WGD was the next contributing and significant parameter on all the profiles areas. Fig. 5.21, 5.22 and 5.23 shows the main effects plot at different taper angles. It shows a clear decrease in profile area as the WGD increases at 1mm for 0° and 15° angles, 3mm at 30° and 5mm at 0° and 30° angles for triangular profiles respectively. In case of square and circular profiles 1mm and 3mm in all the taper angles shows an increase in fig.5.22 and 5.23 respectively. This phenomenon of a decrease in the profile area was witnessed due to increase in wire length (L). As the WGD increases the wire length (L) increases, the wire lag/wire deflection also escalates (Sarkar et al., 2011). Hence, there would be an offset created that decreases the profile areas. There were small variations in different profile areas in fig. 5.21, 5.22 and 5.23. This variation was observed due to the stochastic vibrations of the wire during profiling (Puri and Bhattacharyya, 2008). These vibrations were caused because of the change in wire length due decrease in wire tension. As the wire length increases the wire tension decreases and vibration also increases (Puri and Bhattacharyya, 2003).
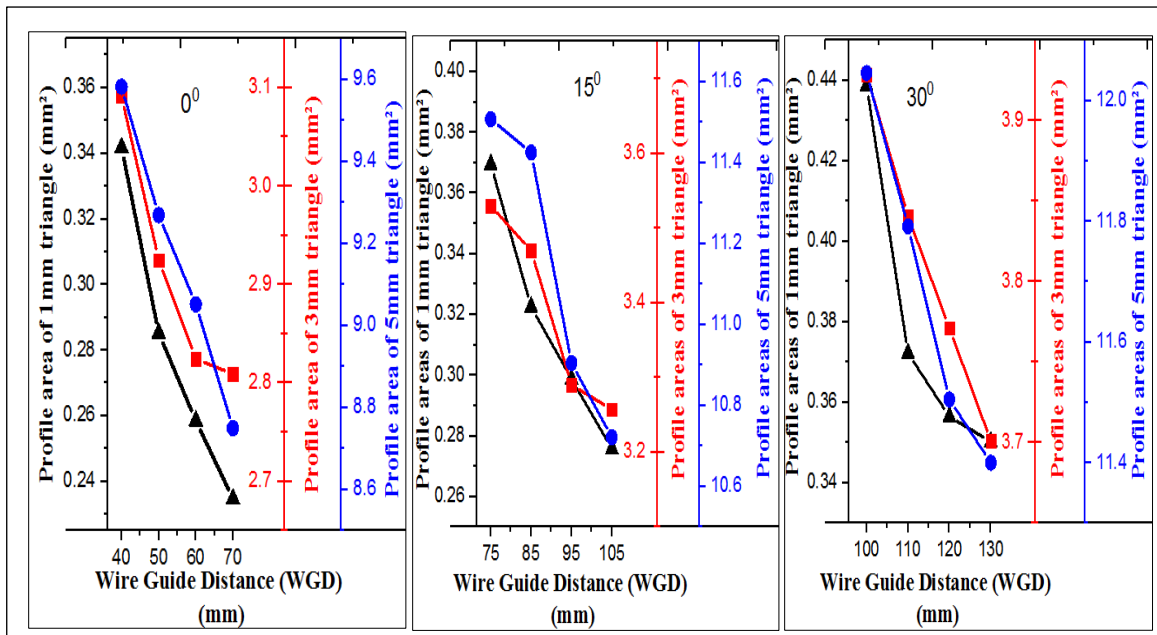
Figure 5.21 Effects plots for wire guide distance (WGD) parameter on triangular profile areas

128
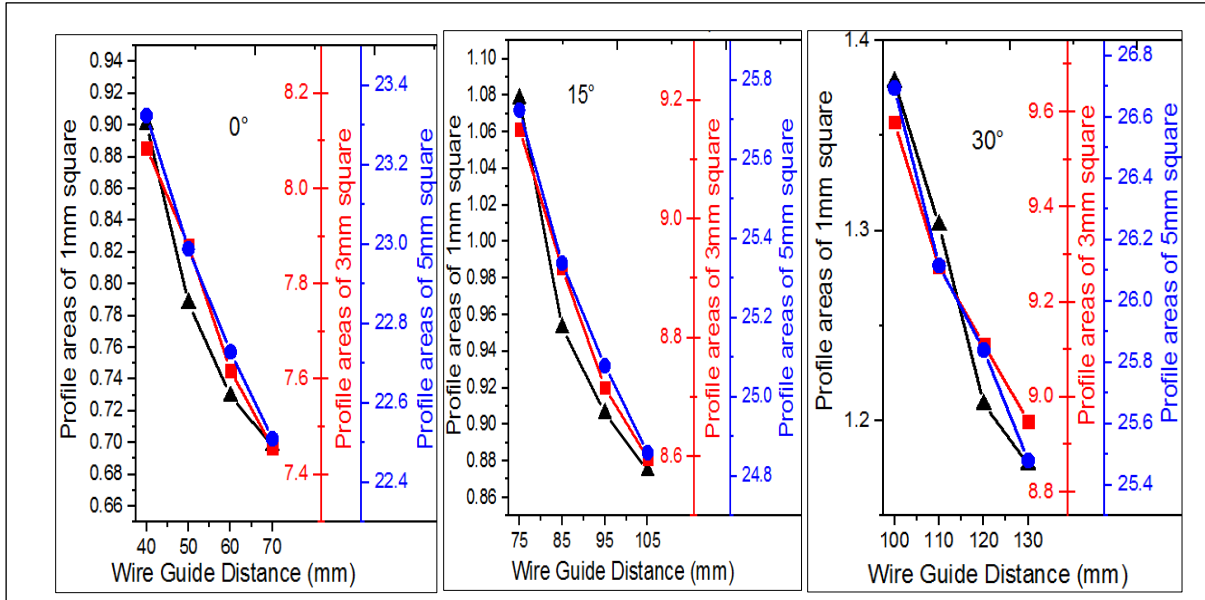
Figure 5.22 Effects plots for wire guide distance (WGD) parameter on square profile
areas
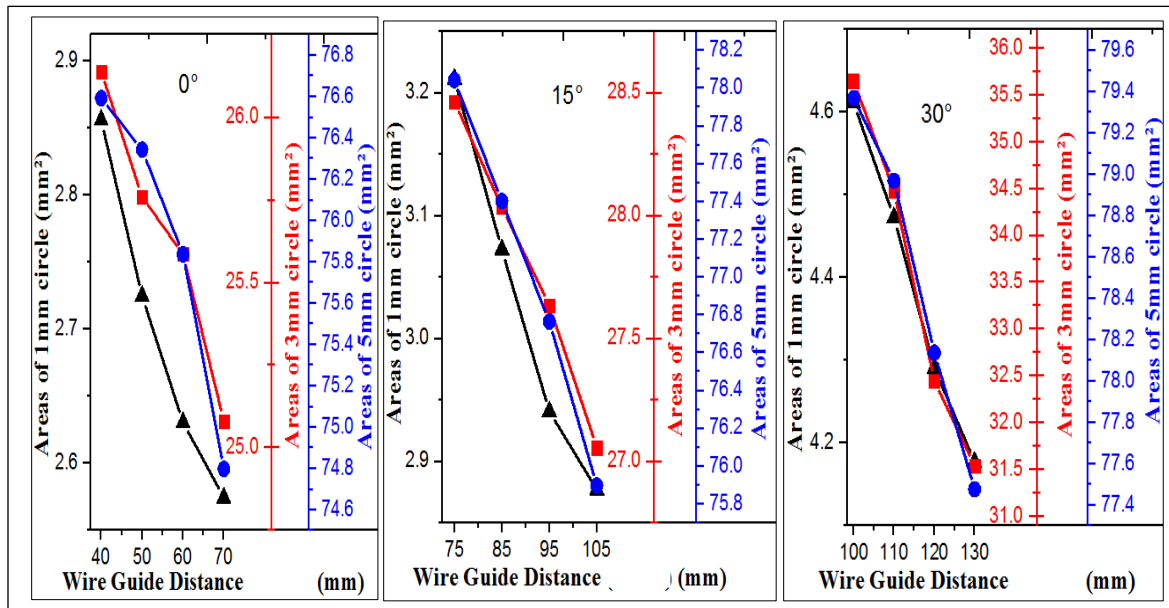
Figure 5.23 Effects plots for wire guide distance (WGD) parameter on circular profile
areas

5.5.1.3 Effect of cutting speed override (CSO) on Profile area

From the main effects plot in fig. 5.24, 5.25 and 5.26, it was noticed that as the CSO
increases the profile area decreases. The profiling speed was mainly influenced by CSO.

129

At higher CSO the profiling speed increases. All the taper angles shows a decreasing trend in profile areas as the CSO increases. At higher profiling speed the wire lag increases which reduced the profile areas due to increases in the corner error in outer parts as observed by Selvakumar et al. (2018). From fig. 5.24, 5.25 and 5.26 it can be observed that as the CSO parameter increases the profile area decreases. There were small variation in decrease that can be observed in fig. 5.24, 5.25 and 5.26. This was due to the higher discharge during machining. A similar phenomenon was observed by (Habib et al., 2017). Habib and Okada, 2016 stated that the profiling speed was found to have an inversely proportional trend to offset values during their exploration, when compared the trend of WO and CSO.

Figure 5.24 Effect of cutting speed override (CSO) on triangular profile areas

Figure 5.25 Effect of cutting speed override (CSO) on square profile areas

Figure 5.26 Effect of cutting speed override (CSO) on circular profile areas

5.5.1.4 Effect of Corner Dwell Time (CDT) on Profile area

Figure 5.27 Effect of cutting speed override (CSO) on triangular profile areas
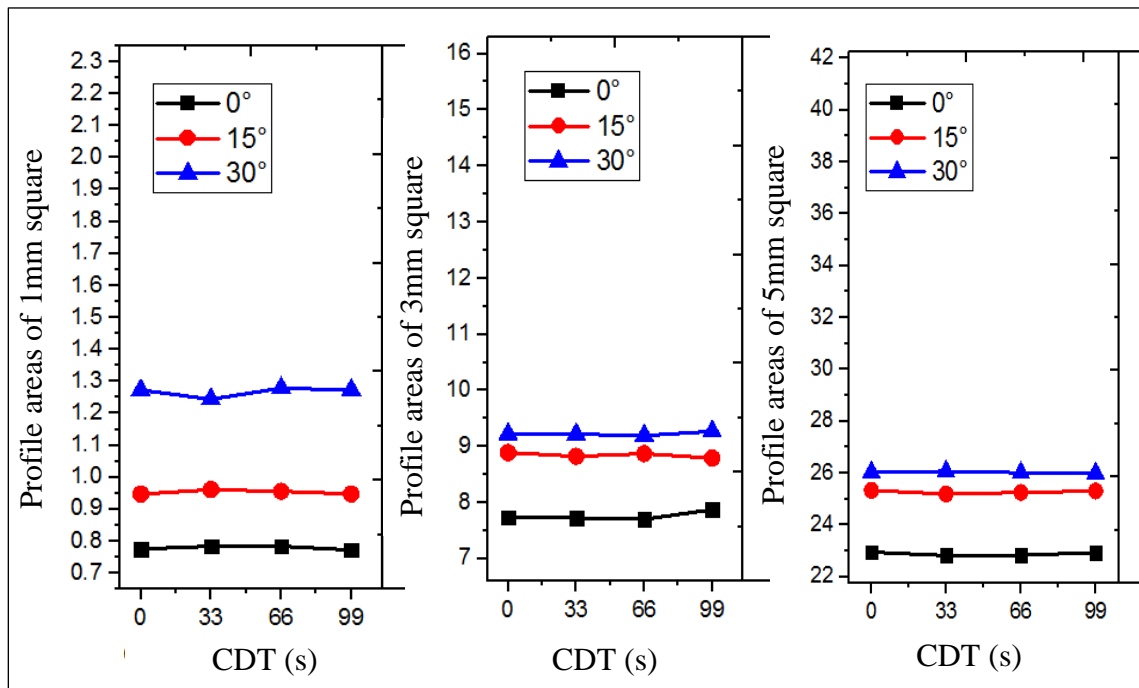
Figure 5.28 Effect of cutting speed override (CSO) on square profile areas

Figure 5.29 Effect of cutting speed override (CSO) on circular profile areas

It can also be observed from the ANOVA table 5.6 and Fig. 5.27, 5.28 and 5.29 the corner dwell time contributes least (1.4-0.42%) on all profile areas namely triangular, square and circular profiles. This is because of CDT mainly focuses on complex shapes and their formation during taper profiling. It also ensures smooth machining of complex taper profiles (Read and Zenyth, 2010).It is the dwell given to the wire during corner profiling for precise corner formation. The corner dwell time (CDT) influences mostly on corner outer areas. From the main effects plot, we can observe that there are small variations in fig. 5.27, 5.28 and 5.29, these variations were due to the sparking in the dwell position.

5.5.2 Variation of profile areas at different taper angles.

Fig.5.30, 5.31 and 5.32 shows the variation of areas at different taper angles that were machined from various parameters. It can be observed that each parameter yields different areas although the cutting parameters such as pulse on time, pulse off time, servo voltage, servo feed and wire feed are kept constant. This phenomenon was because of change in input parameters, especially WO, WGD and CSO. As the WGD increases, the wire length

133

also increases increasing the wire lag (Sakar et al., 2011). This wire lag influences the profile areas during machining. The WO controls the amount and direction of shift of the wire, this also leads to variation in areas of the profile. The effect of CSO was found to have an inverse relationship on the profile area compared with WO as observed from the main effect plots in fig. 5.17, 5.18, 5.20 and ANOVA table 5.6. As each combination of these input parameters had wire lag, overcut and wire deflection. Similar results were reported by Sakar et al., 2011, Habib and Okada (2016) and Habib (2017). It can be noticed that profile areas cut at 30° have the highest areas followed by 15° and 0° taper angles. This increase was seen throughout the main effects plots of profile areas from fig. 5.18 to 5.29, this is because as the taper angle increases the area available for machining also increases.
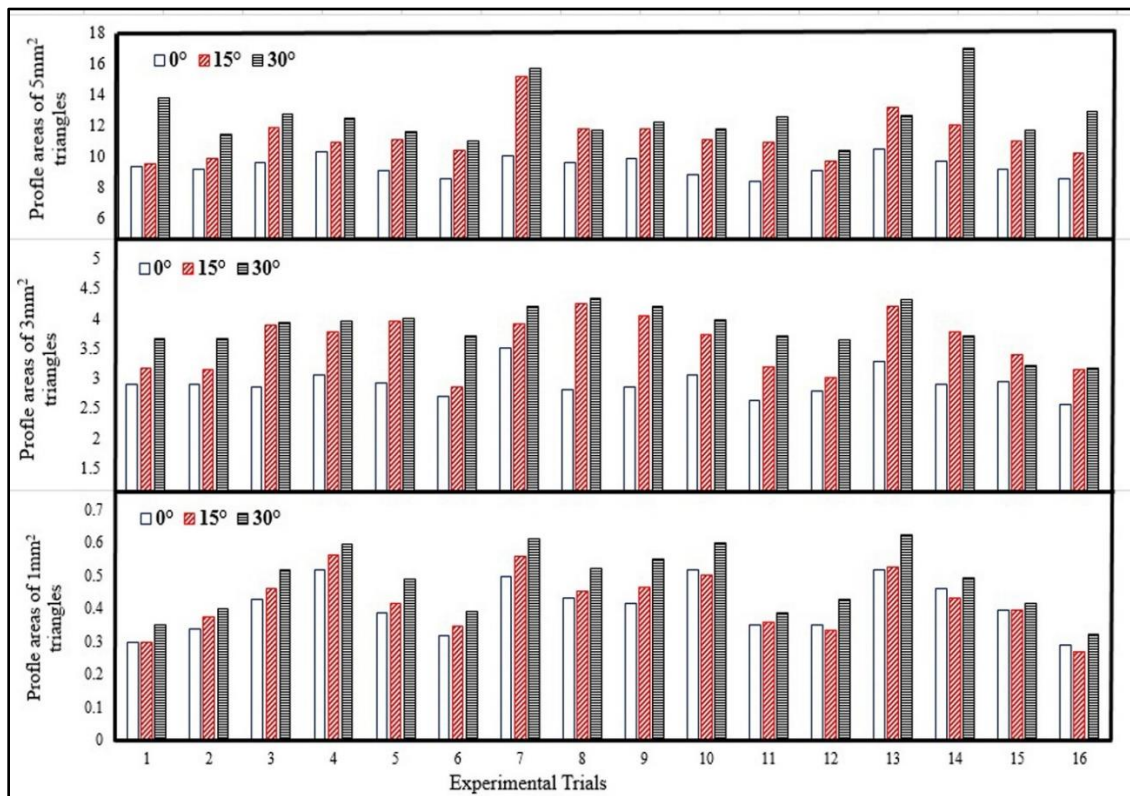
Figure 5.30 Variation of areas at different taper angles for 1mm, 3mm and 5mm triangle
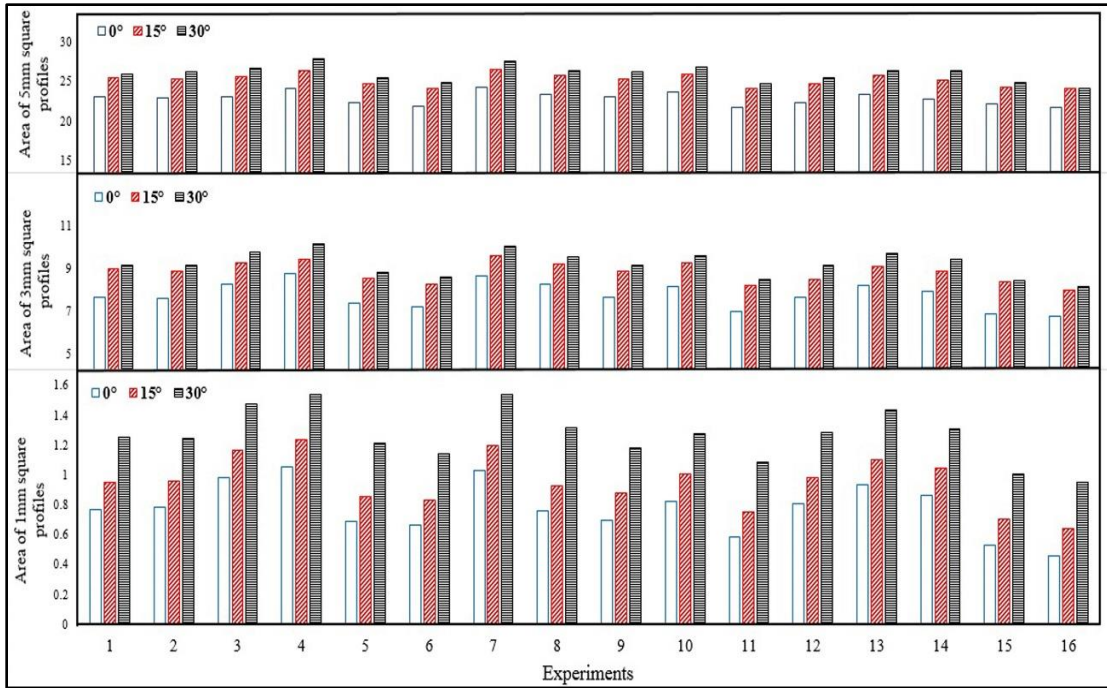
Figure 5.31 Variation of areas at different taper angles for 1mm, 3mm and 5mm square
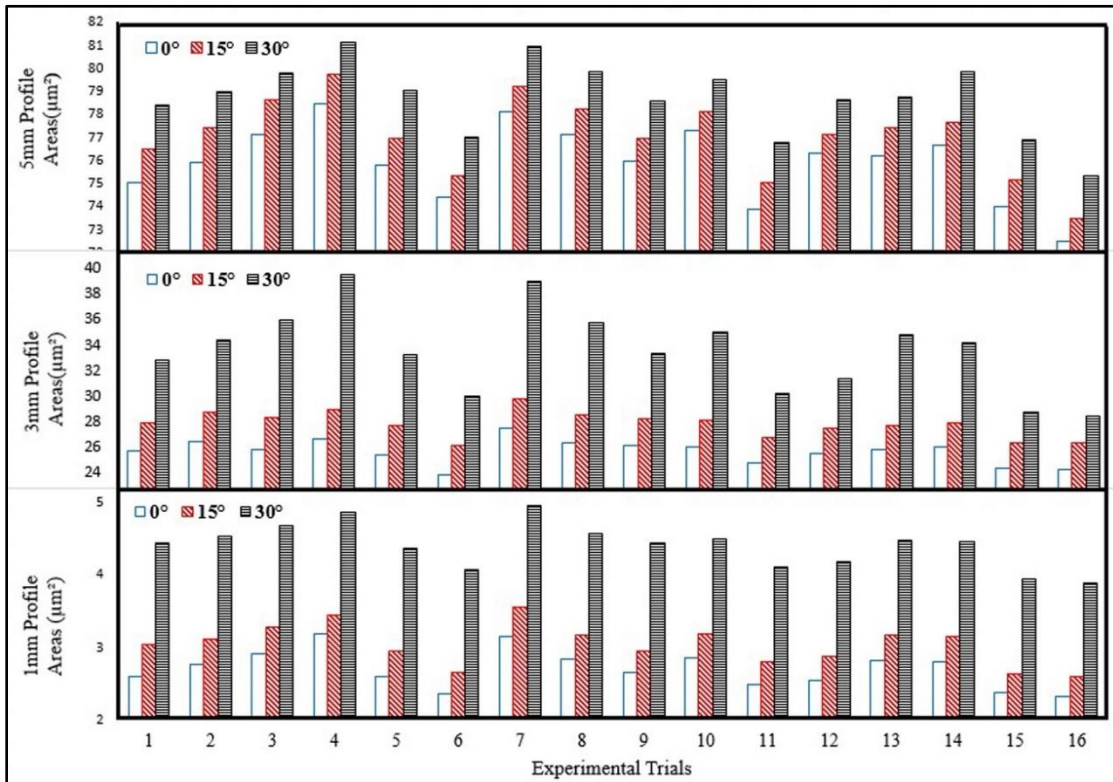
Figure 5.32 Variation of areas at different taper angles for 1mm, 3mm and 5mm circle

5.6 SUMMARY

In this chapter triangular profile was machined at different taper angles namely 0°, 15° and 30° at different profiling parameters such as WGD, WO, CDT and CSO. All the triangular, square and circular profile components were investigated with response parameters i.e. profiling speed, surface roughness, and profile area. Both profiling parameters and taper angular effects were investigated and following conclusion were drawn.

- The CSO was the significant and contributing parameter for profiling speed and surface roughness for all the profiles. It was noticed that as the CSO increased the profiling speed increases 2.065-2.192 times and the surface roughness also increases from 55.76 % to 64.62%.

- Comparing triangular, square and circular profile, the square profiles have the highest profiling speed due to geometry, although it has a higher number of corners compared to triangular profiles. In the case of circular profiles, the profiling speed is in between square and triangular profiles due to the curve path. Similar trends were seen in surface roughness also.

- As the taper angle increases, the profile roughness increases from 8.250-9.100% for all the profiles although the profiling speed decreases from 3.846-14.602%, due to the increase in cutting thickness.

- In case of the profile areas, WGD (wire guide distance) and WO (wire offset) were significant parameters. As WGD increases the profile areas was found to decrease from 5% to 32% and for WO parameter, as it increases the profile areas also increased to 0.86 to 1.13 times. As the slant angle increases, the areas of the profile also increases. The increase was found to range between 40%-68% in all the profiles.

CHAPTER 6

ASSESSMENT OF CORNERS, RECAST LAYER, MICROHARDNESS FOR DIFFERENT PROFILES

6.1 INTRODUCTION

In this chapter, all the profiles that were machined at different taper angles namely 0°, 15° and 30° using slant type taper fixture using suitable cutting parameters (Ton=115μs, Toff=44μs, SF=20mm/min, WF=6m/min and SV=40V) obtained from previous experiments were used to machining in chapter 4. The profiling parameters wire guide distance (WGD), corner dwell time (CDT), wire offset (WO) and cutting speed override (CSO) were considered for detailed studies. The output characteristics of profiles such as corner characteristics, recast layer thickness and microhardness were studied. However, for circular profiles as there are no corners, the corner error was investigated only for triangular and square profiles. The influence of the taper angle on these parameters was highlighted.

6.2 EFFECT OF MACHINING PARAMETERS ON THE CORNER

The corner is an important feature that forms a profile during machining. Fig. 6.1 and 6.2 shows different corner phenomenon that occurs during profiling. Corner error at outer profiles was formed due to the uncut region at sharp corners of the profile during WEDM. This corner error occurs due to the wire deflection as stated by Abyar et al. (2018). The corner error can only be observed at the corners as circular profiles have no corners it was only observed in triangular and square profiles. The corer shift observed at inner profiles was a shift in the corner or deviation of the tip. This was due to the weak tip/corner strength, the electromagnetic forces during machining causes the deviation in the tip. Similar effects were observed by Gong et al. (2016), Dodun et al. (2015) and Chen et al. (2018).
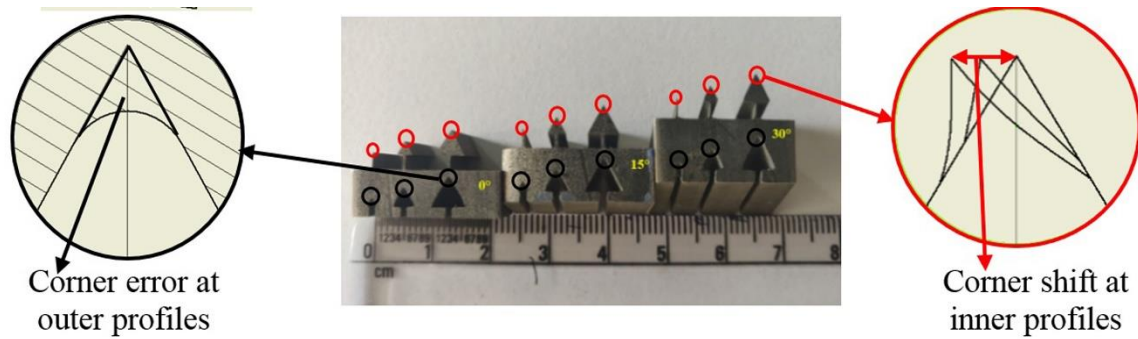
Figure 6.1 Different corner errors that were observed in triangular profiles.
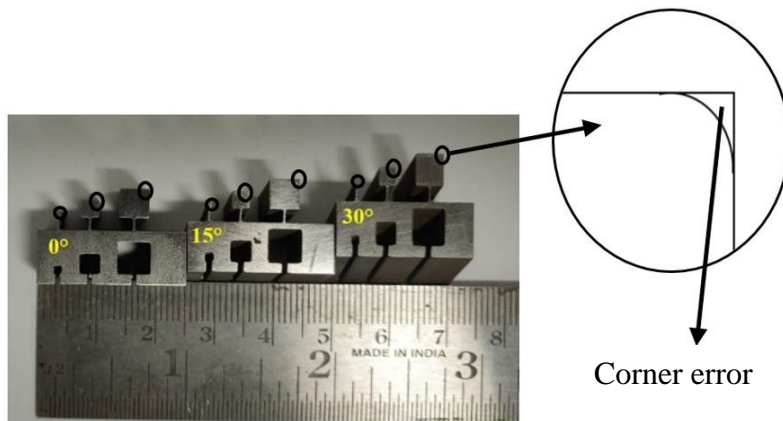
Figure 6.2 Corner errors that were observed in square profiles.

6.2.1 Analysis of Corner Error (CE)

Table 6.1 shows the triangular and square profiles at 0°, 15° and 30° taper angles respectively. Similar L_{16} experimental parameters were followed in the case of investigating corner errors as in profiling speed and surface roughness. The SEM images of the corner were observed and recorded with the help of Image J software, the corner errors were measured from SEM images. The 2nd corner of the machined profiles was considered for the investigation. From the corner errors, the ANOVA were plotted as shown in table 6.2. The ANOVA table indicates that the WDG is the major contributing factor followed by CSO, CDT and WO in case of corner errors for triangular profiles at all the taper angles. Whereas in square profile it indicates that WDG, CSO, WO and CDT are the major contributing factors. This is because of the corner geometry of the profile. The main effects plots obtained by the measured corner errors show the effects of the individual

138

parameters for all the 1mm, 3mm and 5mm profiles at different taper angles of 0°, 15° and 30° respectively.

Table 6.1 Triangular and square corner errors at different machining parameters

	Triangular Profiles			Square Profiles		
Sl. No.	Corner Errors (CE) (µm²) (E-01)			Corner Errors (CE) (µm²) (E-01)		
	1mm	3mm	5mm	1mm	3mm	5mm
0° Taper angle						
1	1521.912	1435.335	1297.385	3007.847	2926.458	3014.380
2	1558.446	1384.716	1318.586	3358.440	3305.417	2953.510
3	1594.677	1326.134	1102.714	4331.240	4588.090	4244.514
4	1419.563	1402.588	1239.918	4808.070	4953.681	4663.720
5	1897.645	1712.229	1516.769	4596.440	4807.639	4355.761
6	1865.024	1729.734	1669.163	4012.450	4599.045	4207.890
7	1543.739	1325.223	1204.981	4854.080	5159.036	4903.090
8	1508.843	1296.044	1190.765	5219.420	5375.657	5219.070
9	1945.981	2138.185	2238.096	6347.040	6253.837	6322.604
10	1718.970	1806.351	1768.944	6994.350	7111.337	6987.361
11	1763.462	1713.855	1846.068	4914.890	4821.441	4811.820
12	1595.295	1443.513	1421.519	4519.020	4561.754	4767.830
13	1858.686	1792.382	1779.001	7078.928	7255.012	6999.080
14	1779.684	1746.628	1688.715	6061.129	6018.941	6022.413
15	1957.648	2169.767	2121.656	6197.777	6110.535	5981.750
16	1892.969	2158.956	1956.339	5629.070	5433.611	5370.790
15° Taper angle						
1	1961.138	1921.658	2112.009	3707.825	3896.491	4054.347
2	1884.912	1955.686	2096.905	4158.424	4205.470	3953.515
3	1995.035	1909.922	2207.608	5131.217	5488.096	5244.575
4	1831.209	2016.284	2150.055	5608.098	5853.619	5663.767
5	2465.782	2399.656	2561.236	5396.457	5707.628	5355.758
6	2607.673	2438.754	2610.038	4812.491	5499.059	5207.835
7	1685.674	1726.638	2095.672	5654.041	6059.067	5903.022
8	2197.616	1883.572	2100.054	6019.431	6275.682	6219.076
9	2663.635	2603.281	2687.605	7157.057	7163.894	7322.644
10	2564.847	2286.983	2519.656	7854.398	7971.356	7837.362
11	2556.052	2409.864	2439.808	5764.810	5671.475	5661.877
12	2193.683	1938.639	2298..609	5369.050	5411.757	5617.898
13	2616.821	2321.292	2516.933	7998.982	8105.071	7709.080
14	2300.694	2381.941	2369.556	6911.128	6868.949	6872.438

15	2676.753	2604.256	2698.634	7032.797	6945.598	6831.726
16	2481.775	2490.125	2541.655	6489.011	6293.671	6220.723
30° Taper angle						
1	2283.032	2016.527	2203.091	4597.852	4716.448	5014.310
2	2006.695	2129.265	2026.662	4958.415	5105.447	4953.510
3	2139.676	1926.053	2199.663	5931.287	6388.094	6244.514
4	2133.214	1996.031	2043.278	6458.035	6753.623	6663.720
5	2418.828	2371.225	2458.876	6196.468	6607.691	6355.761
6	2666.672	2437.559	2576.654	5662.459	6399.087	6207.890
7	1996.736	1949.624	1956.736	6454.074	6959.046	6903.090
8	2136.788	1921.675	2156.785	6819.497	7175.622	7219.070
9	2677.559	3006.846	2577.536	7997.058	8063.812	8322.604
10	2407.545	2453.651	2457.568	8754.376	8871.314	8737.361
11	2425.484	2606.313	2425.455	6664.818	6571.442	6561.820
12	2355.028	2239.682	2265.096	6269.031	6311.757	6517.830
13	2732.893	2691.241	2722.864	8808.974	9055.028	8669.017
14	2452.562	2476.074	2432.573	7811.184	7768.948	7772.413
15	2756.511	2795.806	2706.520	7982.747	7845.550	7731.750
16	2591.282	2793.889	2611.245	7389.078	7193.617	7120.790

Table 6.2 ANOVA results for triangular and square profiles at different taper angles

Sl. No.	Factor	DF	Corner Error (µm²)					
			1mm		3mm		5mm	
			Sum of squares (E+06)	% Contribution	Sum of squares (E+06)	% Contribution	Sum of squares (E+06)	% Contribution
Triangular Profile								
0° Taper angle								
1	**WDG**	**3**	**25.254**	**52.984**	**81.013**	**58.373**	**120.264**	**65.130**
2	CDT	3	8.325	17.466	7.955	5.732	13.477	7.299
3	WO	3	3.962	8.313	6.929	4.993	8.013	4.339
4	CSO	3	9.305	19.522	36.219	26.097	35.853	19.416
5	Error	3	0.817	1.714	6.670	4.806	7.046	3.816
15° Taper angle								
1	**WDG**	**3**	**94.054**	**56.537**	**57.554**	**45.912**	**36.850**	**49.107**
2	CDT	3	15.171	9.120	12.768	10.185	8.535	11.374
3	WO	3	10.393	6.247	10.538	8.406	3.010	4.011
4	CSO	3	38.776	23.309	39.193	31.265	25.906	34.523
5	Error	3	7.963	4.787	5.305	4.232	0.739	0.985

140

			30° Taper angle					
1	**WDG**	**3**	**53.767**	**55.737**	**123.617**	**66.382**	**54.217**	**59.418**
2	CDT	3	12.033	12.474	17.124	9.195	10.750	11.781
3	WO	3	6.805	7.054	7.857	4.219	5.346	5.859
4	CSO	3	18.585	19.266	30.687	16.479	16.201	17.755
5	Error	3	5.276	5.469	6.937	3.725	4.733	5.187
			Square Profile					
			0° Taper angle					
1	**WGD**	**3**	**13.344**	59.569	**11.485**	55.129	**13.823**	63.402
2	CDT	3	1.079	4.817	0.123	0.590	0.085	0.390
3	WO	3	6.139	27.405	7.193	34.527	6.557	30.075
4	CSO	3	1.523	6.799	1.776	8.525	0.950	4.357
5	Error	3	0.316	1.411	0.256	1.229	0.387	1.775
			15° Taper angle					
1	**WGD**	**3**	**14.402**	62.509	**10.785**	49.820	**11.68**	55.479
2	CDT	3	0.175	0.760	0.152	0.702	0.17	0.807
3	WO	3	6.388	27.726	8.467	39.112	7.627	36.228
4	CSO	3	1.818	7.891	1.988	9.183	1.209	5.743
5	Error	3	0.257	1.115	0.256	1.183	0.367	1.743
			30° Taper angle					
1	**WGD**	**3**	**15.256**	65.626	**11.202**	58.365	**11.271**	55.321
2	CDT	3	0.064	0.275	0.123	0.641	0.073	0.358
3	WO	3	6.029	25.935	6.531	34.028	6.976	34.240
4	CSO	3	1.559	6.706	1.021	5.320	1.821	8.938
5	Error	3	0.339	1.458	0.316	1.646	0.233	1.144

6.2.1.1 Influence of Wire Guide Distance (WGD) on Corner Error

From the main effects plot in fig. 6.3 and 6.4, it can be noticed that the corner error increases with WDG. As the WDG increases, the corner error also increases due to the increase in guide length (L) during machining. As the guide length increases the deflection of the wire also increases due to its thin wire diameter and flexibility. This behaviour of the wire leads to an increase in lag (Puri and Bhattacharyya, 2003a; Abyar et al., 2019). Hence, an increase in wire lag is responsible for the increase in the uncut region area while machining the corners of the profile. This uncut region is called the corner error and it depends on the instantaneous wire movement during corner machining. There were

variations in increase at WGD=60mm for 0°, WGD=95mm for 15° and WGD=110 and 120mm for 30° in fig. 6.3 and 6.4. These variations in the increase of corner error were due to the different chaotic forces during machining on the wire (Habib, 2017; Puri and Bhattacharyya, 2003b). This causes vibrations due to the decrease in tension of the wire distance between the upper and lower guides (length of the wire) while machining (Habib, 2017; Abyar et al., 2019). In both triangular and square profiles, the WGD parameter has the same effect.
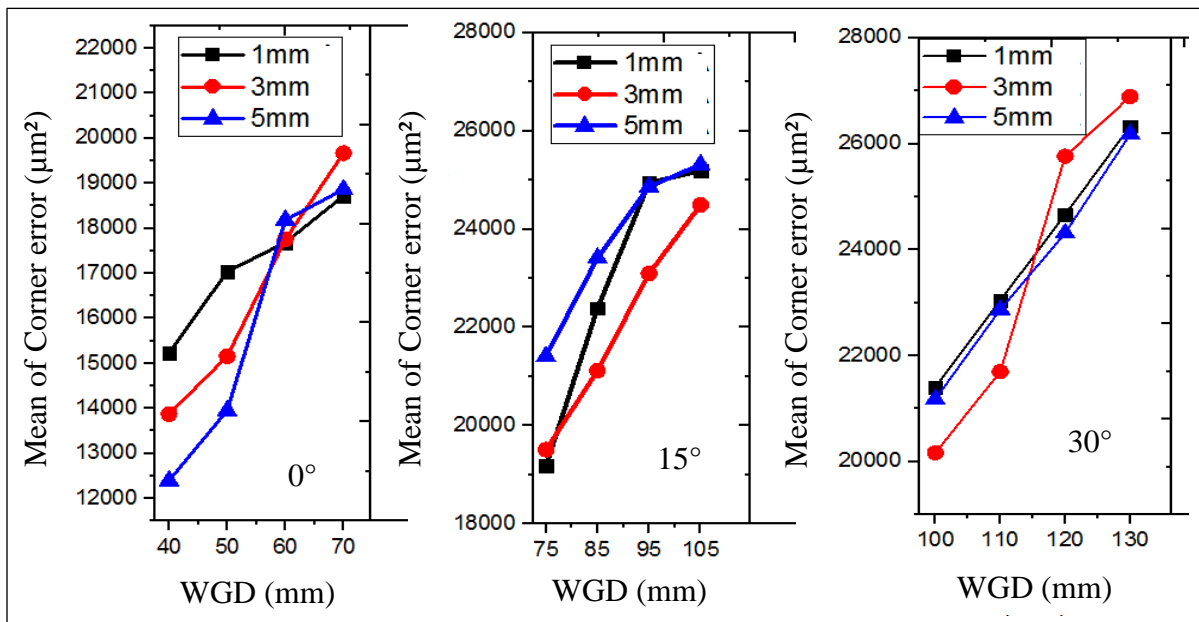
Figure 6.3 Effects of wire guide distance (WGD) in triangular profile
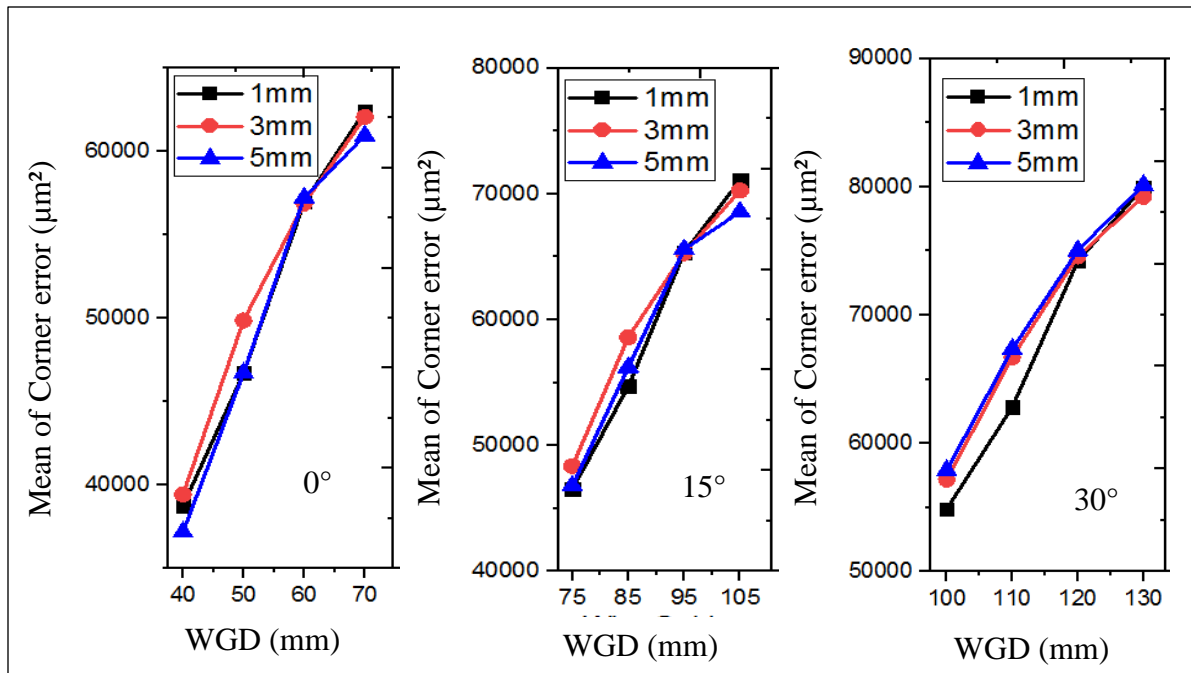
Figure 6.4 Effect of wire guide distance (WGD) in square profile

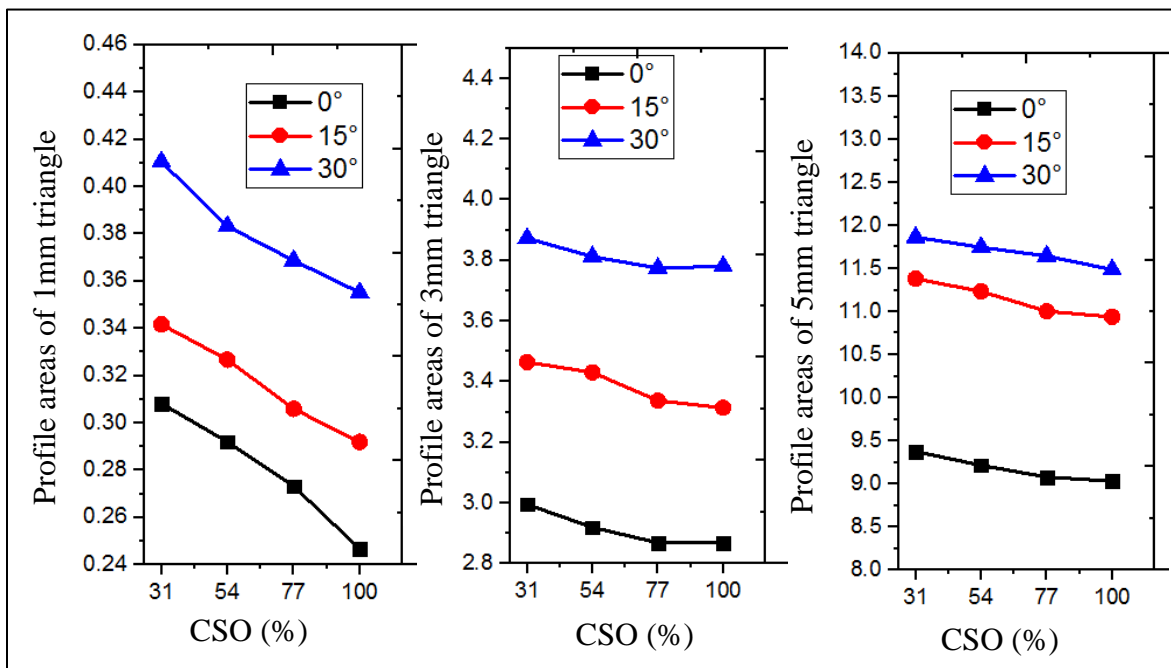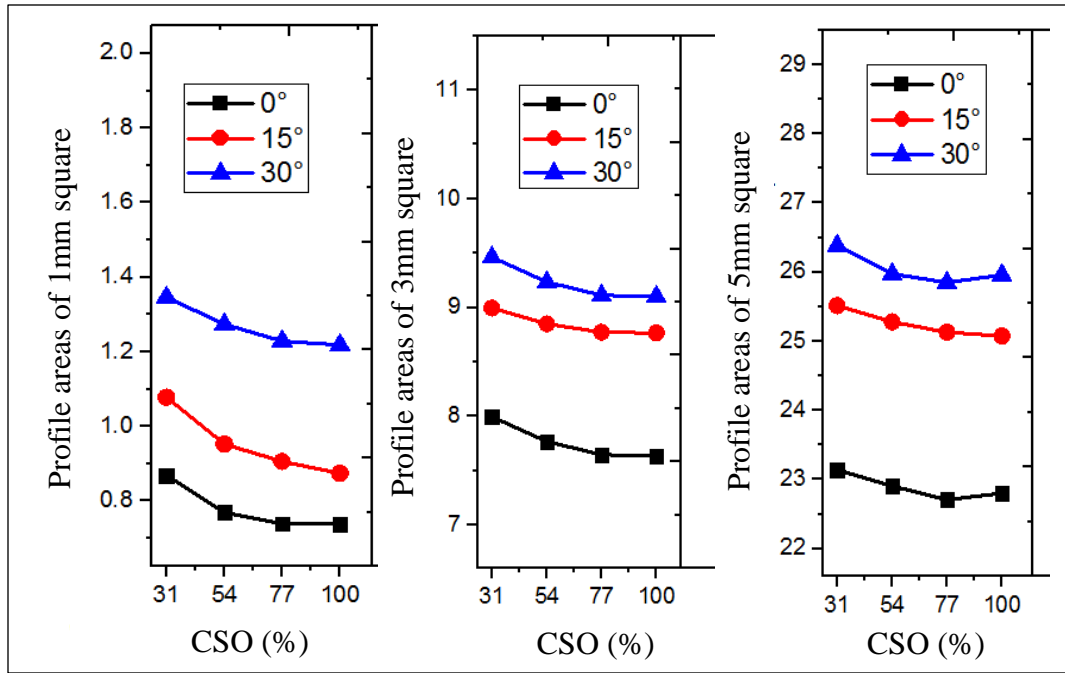## 6.2.1.2 Influence of Cutting Speed Override (CSO) on Corner Error
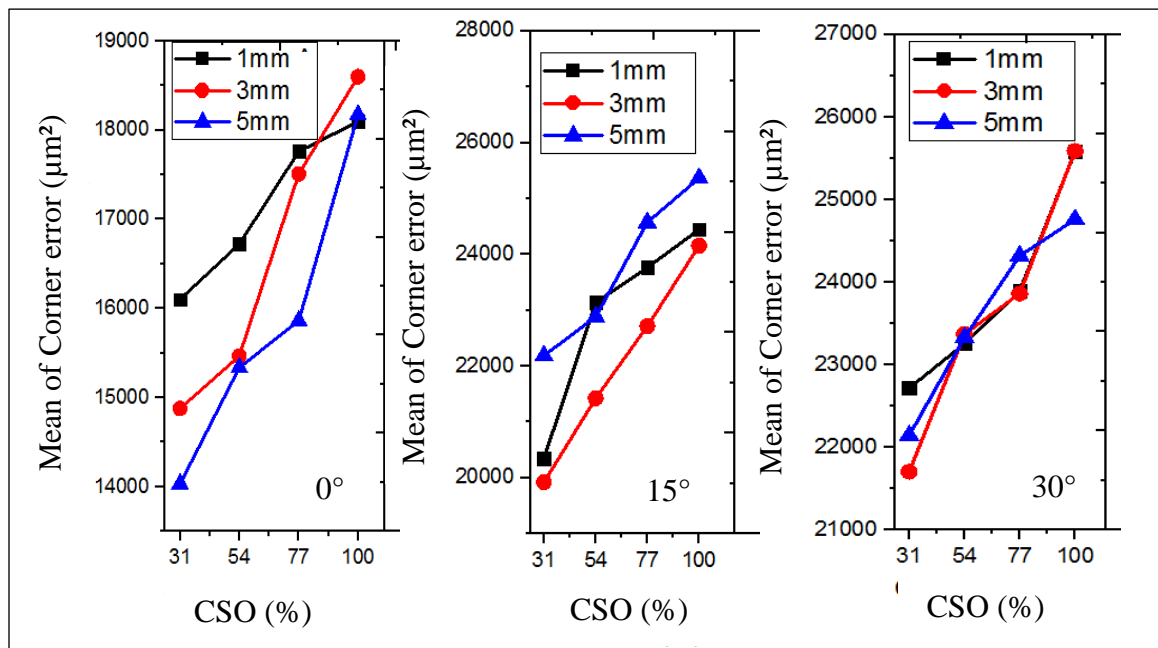
Figure 6.5 Effects of Cutting speed Override (CSO) for triangular profiles

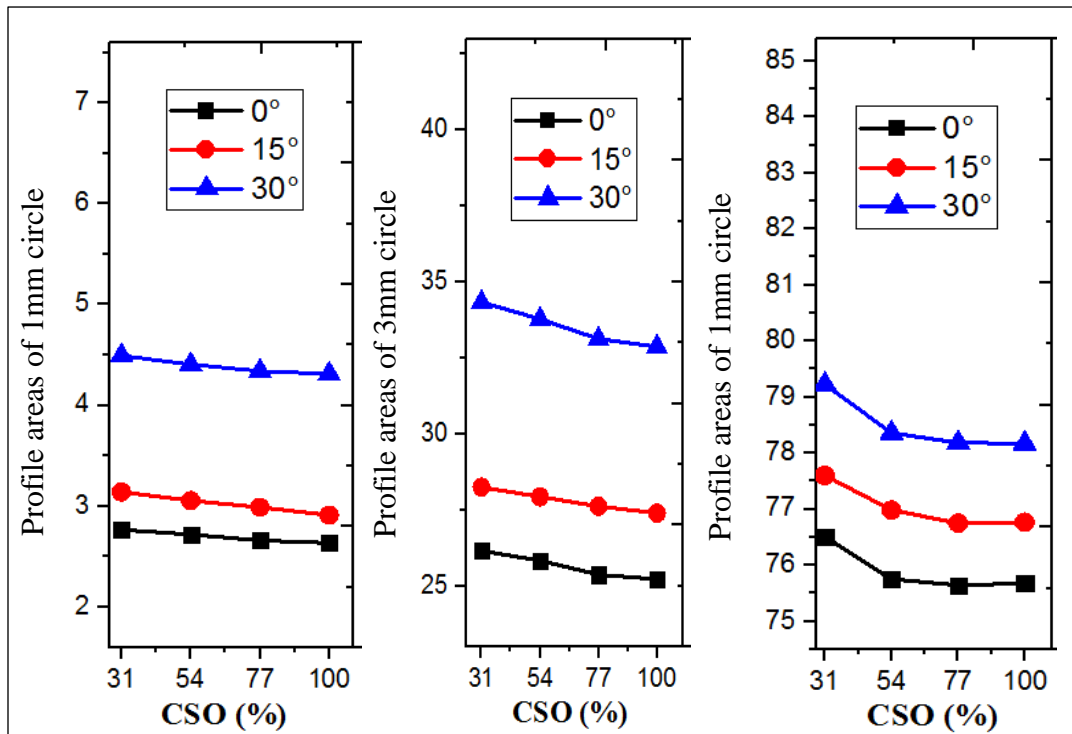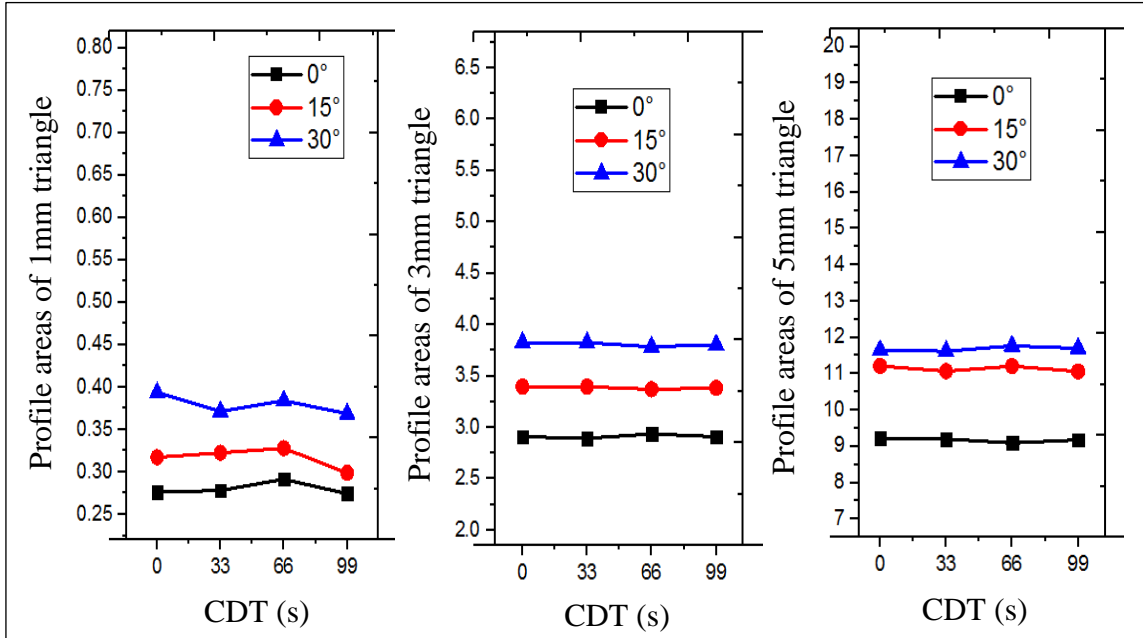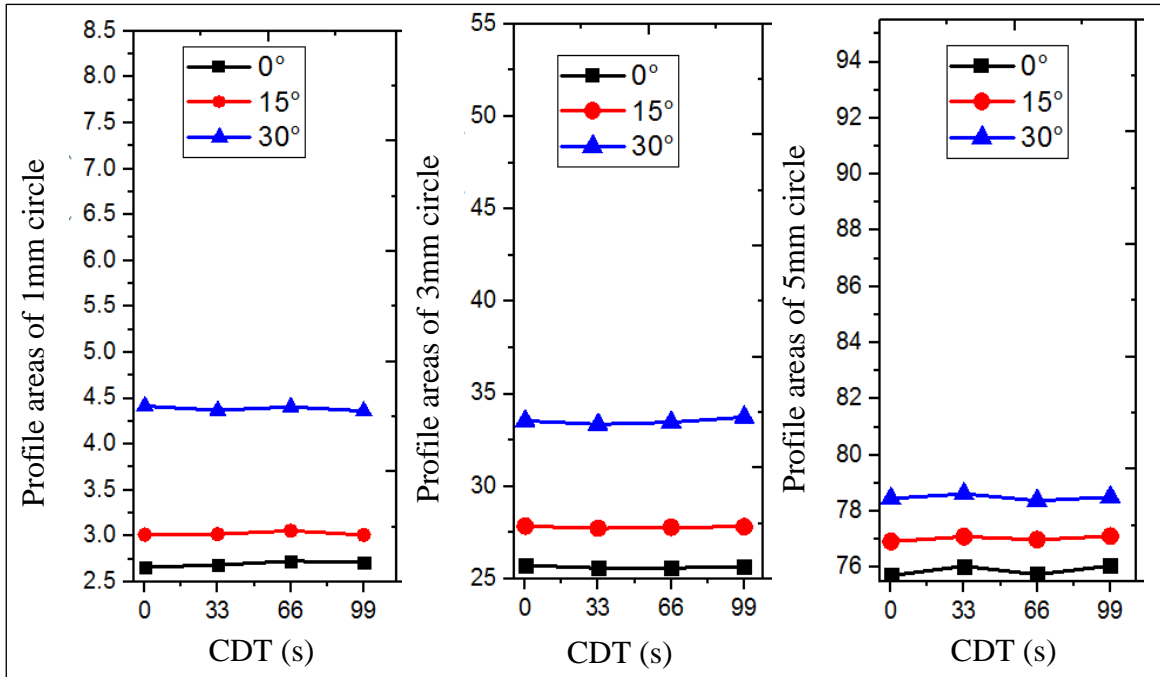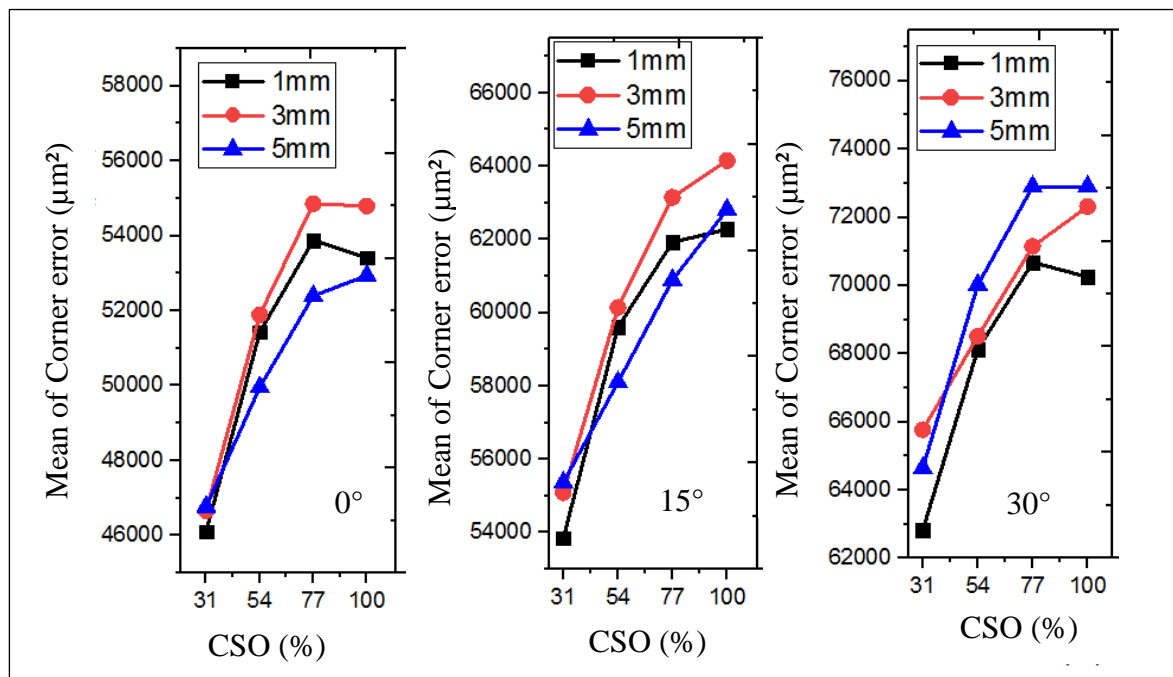Figure 6.6 Effect of cutting speed override (CSO) for square profiles

The CSO is an online parameter that varies the profiling speed without changing the machining parameters (Read and Zenyth, 2010). From fig. 6.5 and 6.6, it can be noticed that as the CSO increases the corner error also increases. As the CSO increases the profiling speed also increases, which increases the corner error. Selvakumar et al. (2018) also noticed similar results during their investigation of corner error and cutting speed. A clear increasing trend in corner error with CSO can be observed in fig. 6.5 for 5mm, 3mm at 15° and 5mm at 30° taper angle and in fig 6.6 for 5mm at 15°, 3mm at 30° taper angle. There was variation in the increase of the corner error at 77%, 54% and 77% for 0°, 15° and 30° taper angles respectively. This variation in the increasing trend of corner error was observed due to an increase in discharge energy with uneven forces on the wire (Habib, 2017). In the case of the square profile in fig. 6.6, the increase was noticed to be decreasing in 77% of CSO at all angles. These variations are because of the increasing profiling speeds, due to which the corner error becomes constant after a certain speed (Sanchez. J.A., 2007).

6.2.1.3 Influence of Corner-dwell Time (CDT) on Corner Error
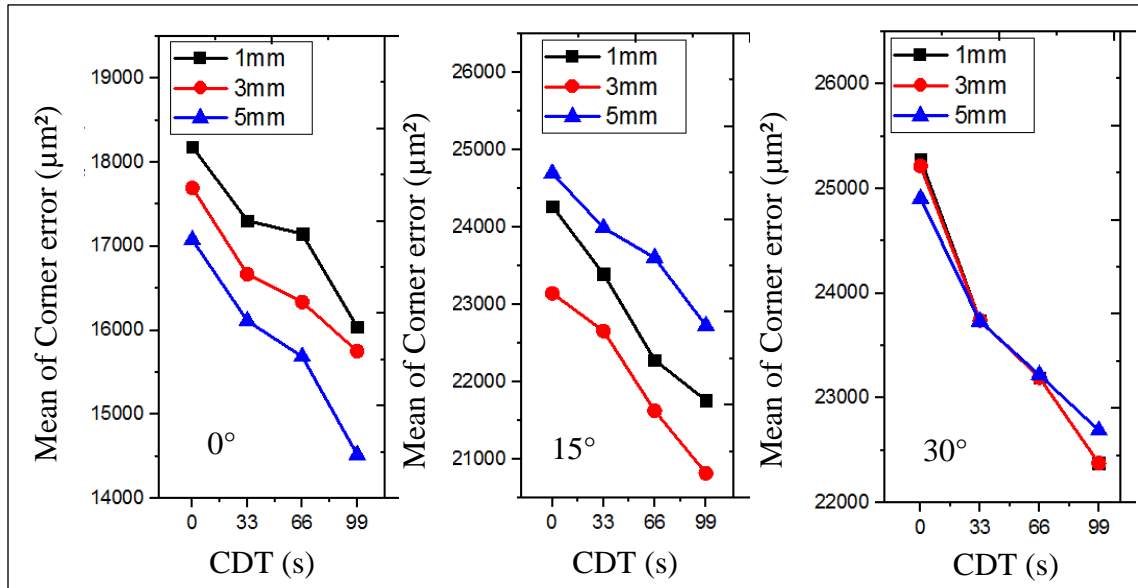
Figure 6.7 Effects of corner-dwell Time (CDT) for the triangular profile

CDT is dwell time is a period where the wire is made to stop at specific coordinates especially in corners to remove the uncut region. It can be noticed from the main effect plots in fig. 6.7 that as the CDT increases the corner error also decreases. The corner error is because during profiling the wire guide moves to the programmed coordinates. Although the wire wouldn't have reached the dwell position or the co-ordinate. As the CDT increases, the wire slowly travels to the required coordinate and the material removal rate decreases. So gradually the rate of decrease in corner error also decreases. Selvakumar et al., (2018) also found similar results during corner machining. There are variations in decrease at 33s and 66s in all the angles as seen in fig. 6.7 and 6.8. These variations are because of wire vibrations. These wire vibrations can also be due to flushing, sparking and discharging as at corners the wire would dwell at a coordinate without moving forward (Puri and Bhattacharyya, 2003, Habib, 2017). It can be observed that the CDT parameter can only decrease the corner error but it cannot be removed completely. It was also observed from ANOVA table 6.2 that the CDT parameter influences lesser on corner error

in square profiles than in triangular profiles due to the corner angle of the profile. As the angle of the profile or corner increases the influence of CDT decreases. This was due to the ease of wire travel also increases as the angle of the corner increases.
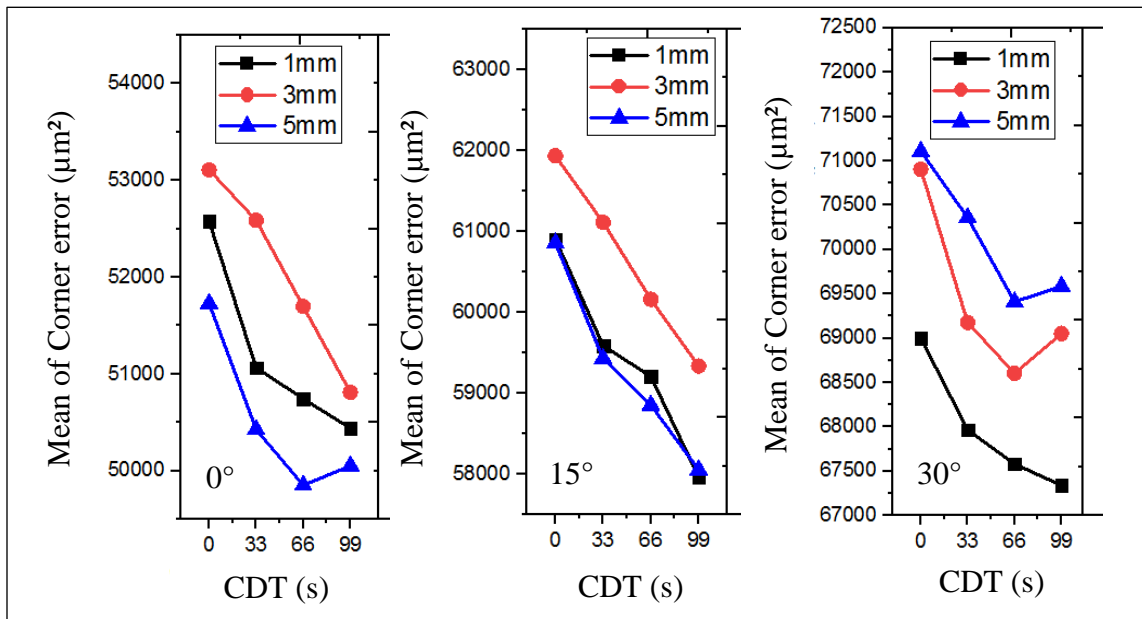
Figure 6.8 Effect of corner dwell time (CDT) for square profile

6.2.1.4 Influence of Wire Offset (WO) on Corner Error
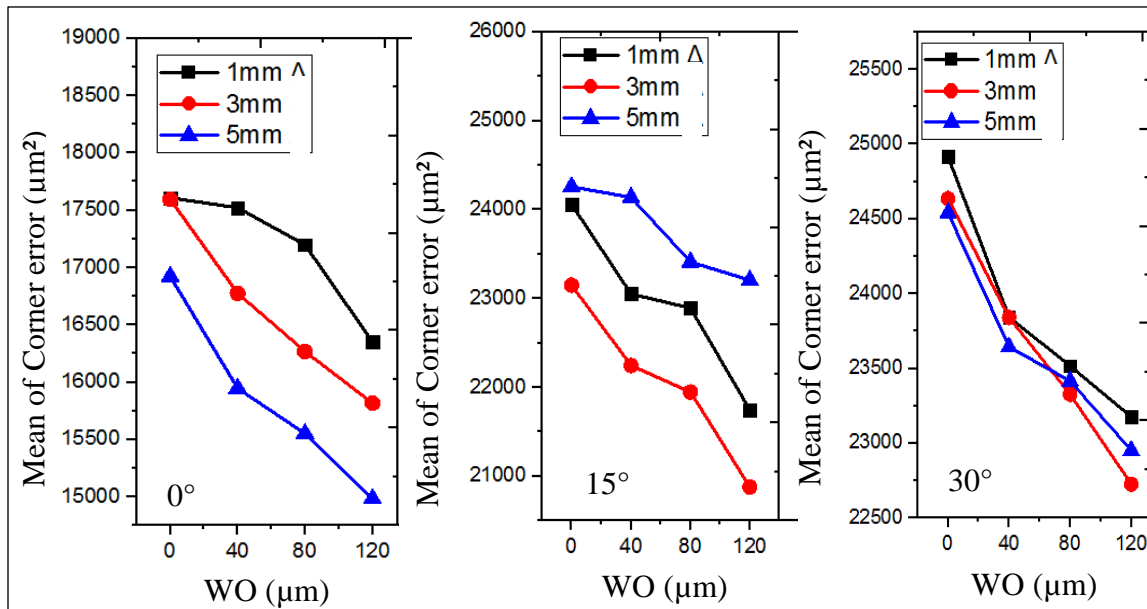
Figure 6.9 Effects of wire offset (WO) for triangular profile

146

From the main effects plot in fig. 6.9, it can be seen that the corner error decreases with the increase in the WO parameter. The wire offset parameter is the offset parameter where the programmed profile is offset to mention perpendicular distance and the profile is machined. The area of the machined profile is bigger than the programmed profile. This facilitates the wire to travel much efficiently in corners due to bigger curvature. Similar results were found in Naveed et al. (2017), Habib and Okada (2016) in there research. This results in the reduction of corner error as the uncut region reduces. It can be seen from the fig. 6.9, that there is a variation in the decrease of corner error at 40µm for 0°, 40µm to 80µm for 15° and 40 µm for 30° in fig.6.9. This recognizable variation in decrease was due to the combined variation in wire tension and profiling speed (Habib and Okada, 2016; Puri and Bhattacharyya, 2003). In case of square profile, it can be noticed that as the WO increases, the corner error also increases from fig. 6.10. This effect was noticed due to the increase in wire deflection as observed in Habib, S. and Okada, A. (2016). As the WO increases the corner error also increases as observed clearly in 3mm at 0°, 3mm at 15°, 5mm at 30° taper angles. Slight variations in the increase were noticed in 40µm and 80µm of WO at all the angles due to the combined variation in wire tension and profiling speed (Habib and Okada, 2016, Puri and Bhattacharyya, 2003). This contrasting behavior of WO parameter was observed due to the change in corner angle or geometry in case of trinagular profiles, as WO increased the corner error decreased because higher WO provided the wire to travel easy and remove the uncut material in the profile. In square profile, although the increase in WO parameter the corner error increases. This is due to the increase in wire deflection for fixed WGD parameter. Similar to the research observed by Sanchez. J.A. (2007) where it was stated that the corner error can be decreased but cannot be completely eliminated.

147
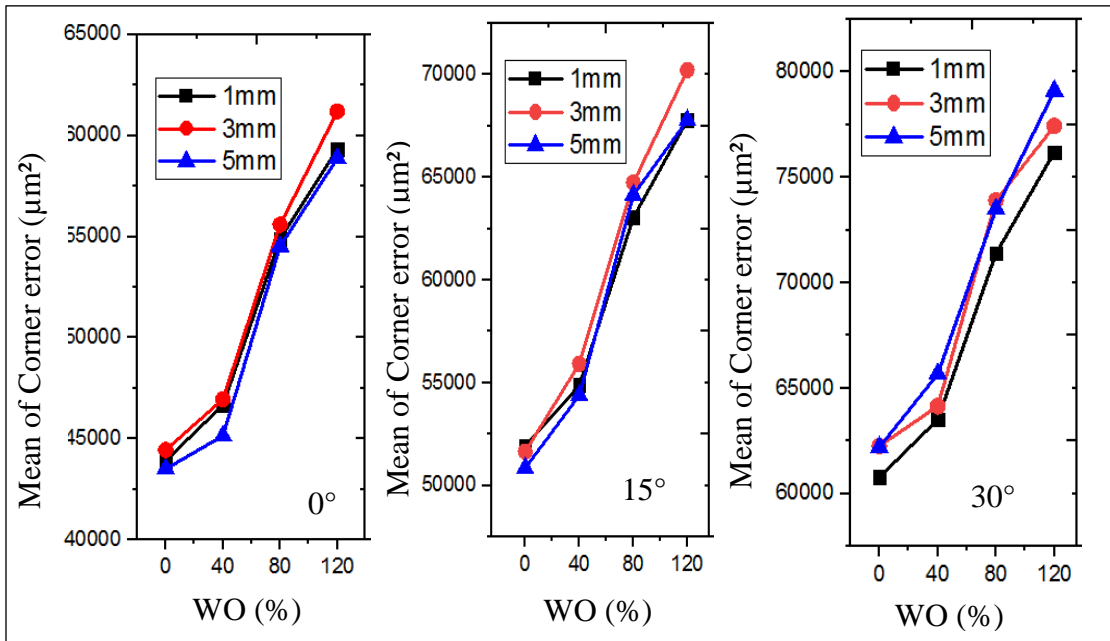
Figure 6.10 Effect of wire offset (WO) for square profile

6.2.2 Variation of Corner Error with Taper Angle and Profiling Speed
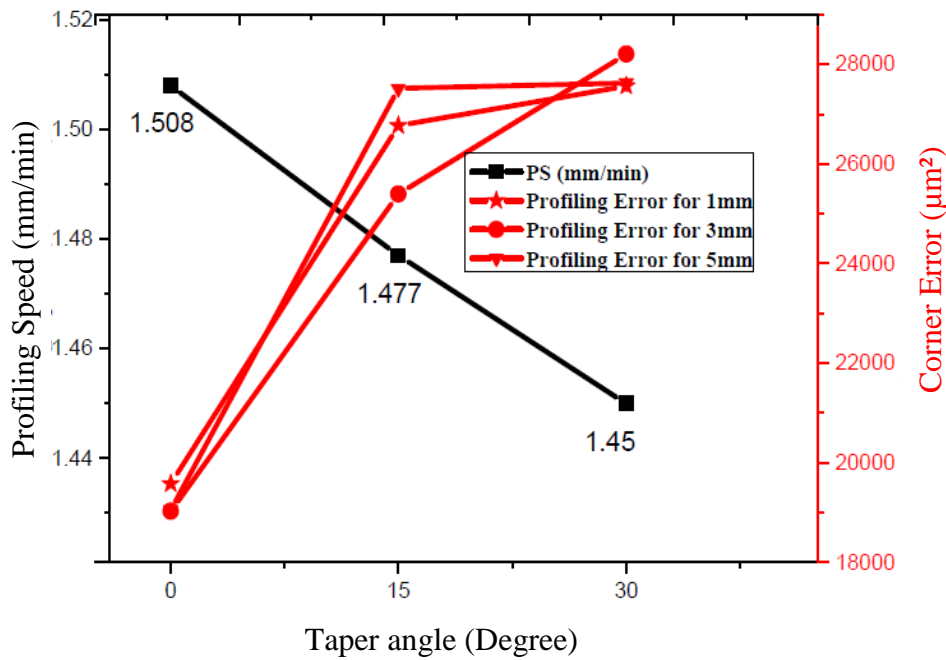
Figure 6.11 Variation of corner error at different taper angles for highest profiling speeds
in triangular profiles
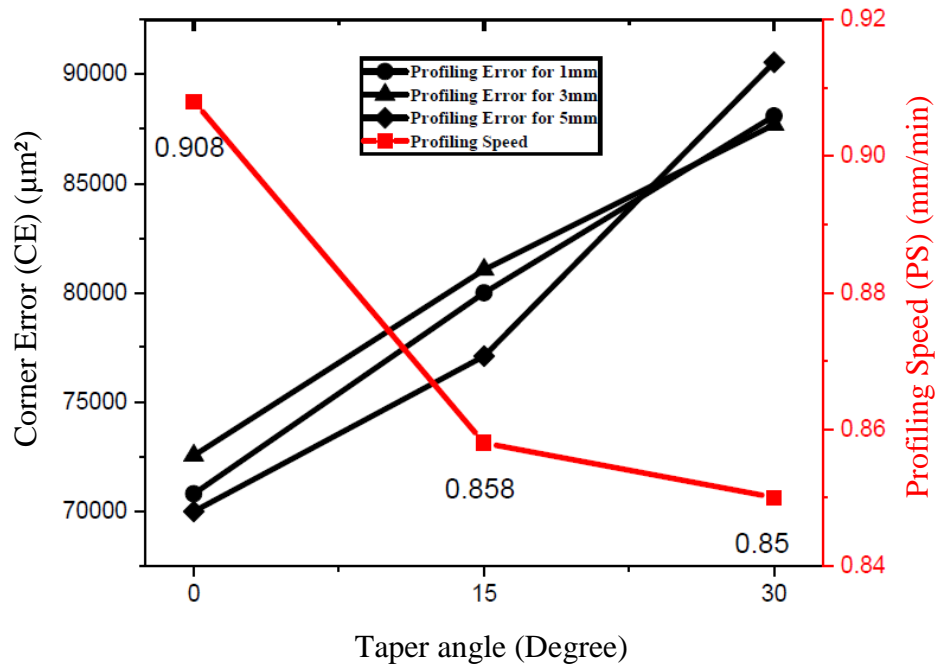
Figure 6.12 Variation of corner error with profiling speed at different taper angles in square profiles

From table 6.1, it can be seen that the highest corner errors were observed in the highest profiling speed parameters i.e. trial 15 (WGD=70mm at 0°,105mm at 15°,130mm at 30°, CDT=66s, WO=40μm, CSO=100%). Fig. 6.11 and 6.12 were plotted for corner errors at different taper angles for both triangular and square profiles. It can be observed that as the taper angle increases the profiling speed decreases. This phenomenon is due to an increase in cutting thickness as the taper angle increases. For the highest profiling speed parameters (WGD=70mm at 0°,105mm at 15°,130mm at 30°, CDT=66s, WO=40μm, CSO=100%) as the cutting thickness available for machining increases, the profiling speed decreases as it takes more time to melt. It can be observed from fig.6.11 that as the taper angles increase the corner error also increases although the profiling speed reduces which has contrasting behaviour as reported by Selvakumar et al. (2018). This contrasting phenomenon is due to the increase in taper angle which increases the cutting thickness. As the cutting thickness increases the bending of the wire also increases. This wire deflection leads to an increase in wire lag which results in a more uncut area (corner error) (Habib and Okada, 2016;

149

Samanta et al., 2016; Chen et al., 2018). So as the taper angle increases, the corner error also increased although the profiling speed decreases. The corner error not only depends on taper angle but also on many factors such as corner angle, profiling speed, wire lag and profile dimensions (Habib and Okada, 2016). It can be noticed in fig.6.11 and 6.12 that as the taper angle increased the corner errors also increases for both triangular and square profiles. Fig. 6.13 and 6.14 show the SEM images of the corner error that occurred at different taper angles for both the profiles.
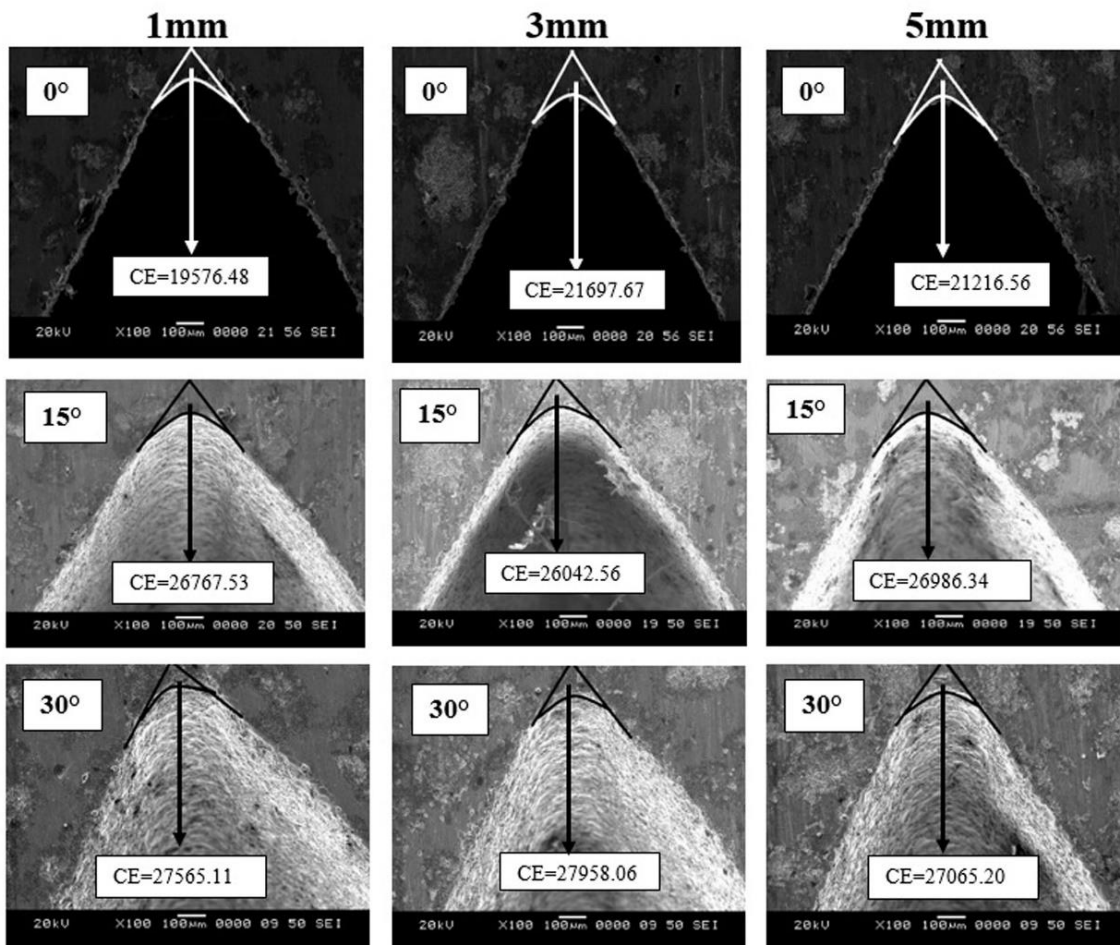
Figure 6.13 Corner Errors (CE) recorded at highest profiling speed parameters for triangular profiles

150
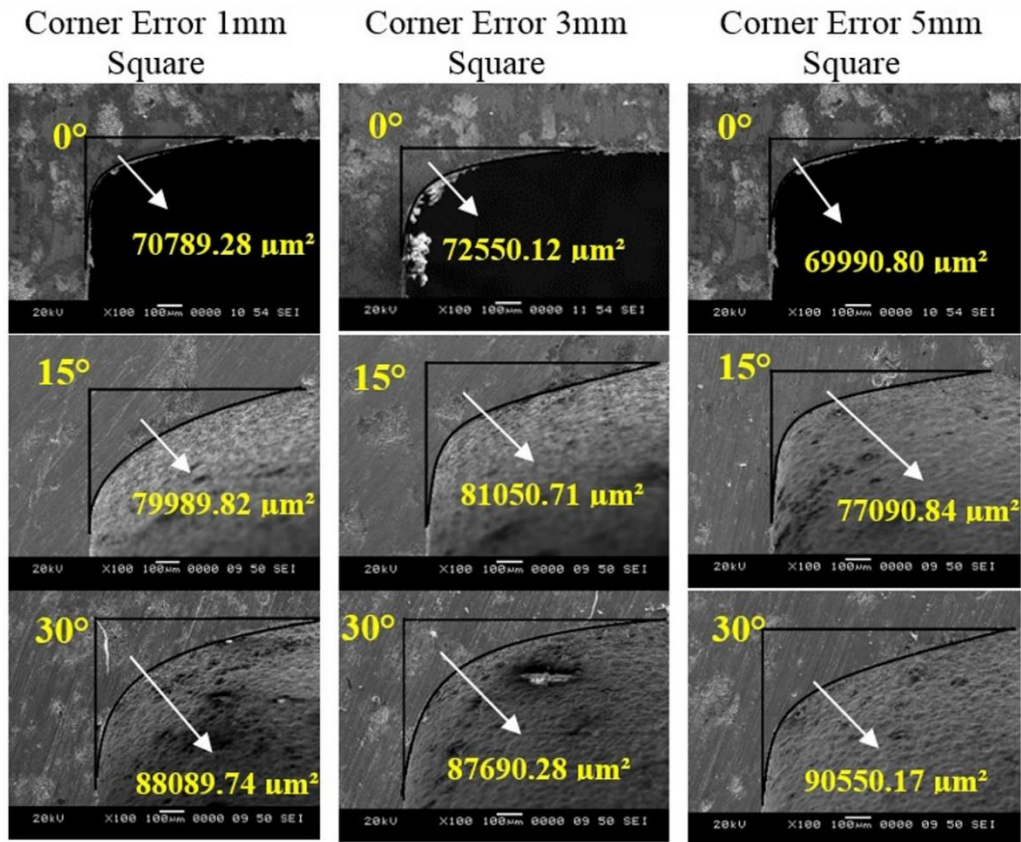
Figure 6.14 Variation of corner error at the highest profiling speed parameter for square profiles

6.2.3 Influence of machining on the triangular corners

In the case of the inner profile parts in the triangular profile, there was deformation of the apex machined which was observed similar to the effect highlighted by Gong et al. (2016), Dodun et al. (2015) and Chen et al. (2014). Trial 15 in table 6.3 yields the highest profiling parameters (WGD=70mm at 0°,105mm at 15°,130mm at 30°, CDT=66s, WO=40μm, CSO=100%） having profiling speeds of 1.45 mm/min, 1.477 mm/min, 1.45 mm/min for the taper angles 0°, 15° and 30° respectively. It was observed that at these highest profiling speeds, the highest shift or deviation was noticed at 15° and 30° angles. Fig. 6.15 shows the SEM images of the highest shift in apex observed for trial 15 at different taper angles. The highest shift of 47.925μm, 114.697μm, 122.699μm were observed at 30° taper angle for 1mm, 3mm and 5mm triangular profiles respectively. In the 15° taper angle the shift was 46.980μm, 108.779μm, 118.017μm for the profiles 1mm, 3mm and 5mm respectively.

151

Table 6.3 shows the corner shift at different parameters for 15° and 30° taper angle. It can be observed that 0° taper angle exhibited no shift in its apex as shown in SEM images in fig. 6.15. Although this phenomenon was observed in the literature for workpiece thickness of ≤5mm and in only acute angles, this was due to corner generated had lower strengths and high electromagnetic forces at the time of cutting (Chen et al., 2018; Gong et al., 2016). In the present study, the corner apex was observed to shift for a workpiece of a higher thickness (10mm). This shift was due to the lower strength of the corners at higher taper angles, hence the 30° taper angle showed the highest shift of apex was observed by SEM as shown in fig. 6.15. The shifting was always observed to be on the left side that is opposite to the direction of the wire path. This left-sided shift behaviour was due to the diamagnetic properties of the workpiece as reported by Dodun et al. (2015). But in square profile, this phenomenon is not observed due to strong corners.
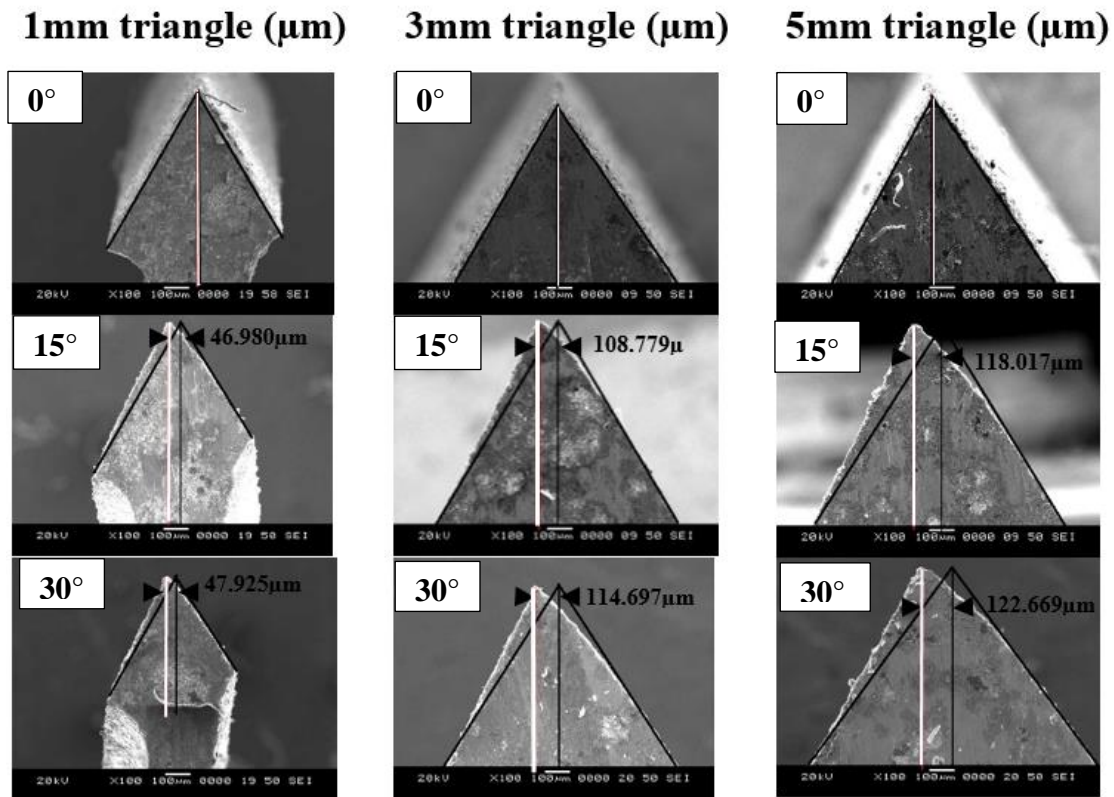
Figure 6.15 SEM images showing the shift in apex for highest profiling speed parameter (WGD=70mm at 0°,105mm at 15°,130mm at 30°, CDT=66s, WO=40μm, CSO=100%)

Table 6.3 Tapered corner shift for 15° and 30° taper angles

Trial No.	(a) Taper angle 15°			(b) Taper angle 30°		
	1mm profile (μm)	3mm profile (μm)	5mm profile (μm)	1mm profile (μm)	3mm profile (μm)	5mm profile (μm)
1	43.738	55.379	84.024	44.787	56.390	90.637
2	43.558	52.987	85.396	45.890	53.579	95.739
3	42.443	78.026	86.739	43.701	59.253	88.963
4	45.689	80.698	108.170	42.508	84.024	114.367
5	35.897	82.605	97.456	37.802	86.691	120.267
6	39.628	81.566	94.236	35.524	94.208	80.025
7	45.768	59.365	75.359	46.057	62.657	79.601
8	42.670	60.679	80.639	42.792	84.031	89.726
9	41.133	68.029	70.133	45.637	49.253	88.963
10	42.730	54.037	68.029	44.559	76.026	97.806
11	41.236	72.698	89.258	45.769	75.697	92.349
12	44.398	79.683	76.549	43.767	88.023	95.856
13	40.554	59.773	105.345	41.876	64.123	102.020
14	45.843	75.659	98.369	46.729	87.693	99.073
15	**46.980**	**108.779**	**118.017**	**47.925**	**114.697**	**122.669**
16	30.744	55.761	72.024	39.474	60.372	78.795

6.3 VARIATION OF RECAST LAYER THICKNESS AND MICRO-HARDNESS

During machining as the material was exposed to higher temperature, so the recast layer thickness and variation in hardness were observed. The recast layer thickness and the micro-hardness were measured for all the three profiles namely triangular, square and circular profiles. The profiles were polished and recast layer was measured using SEM. The microhardness was measured at different distances from the machined surface.

6.3.1 Analysis of recast layer thickness and microhardness

The recast layer was formed due to the melting of the material during machining. A part of the melt that was present on the material gets resolidified due to the dielectric fluid. Fig. 6.15 (a)-(f), 6.16 (a)-(f) and 6.17 (a)-(f) shows the variation of recast layer thickness for

the different tapered triangular, square and circular profile respectively. The lowest profiling speed parameters and highest profiling speed parameters were (WGD=60mm at 0°,95mm at 15°,120mm at 30°, CDT=99s, WO=40μm, CSO=31%) and (WGD=70mm at 0°,105mm at 15°,130mm at 30°, CDT=66s, WO=40μm, CSO=100%) for all the profiles. As the taper angle increases the profiling speed decreases for both parameters for all the profiles. This phenomenon was noticed due to the increase in the thickness of cut (t). In general, for a fixed parameter, the discharge energy remains constant, as the taper angle increases the workpiece thickness also increases. This reduces the length of cut which in turn reduces the profiling speed. The discharge energy gets distributed which leads to lower recast layer thickness as the taper angle increases. So at higher tapered profiles, the recast layer thickness decreases due to the increase in the thickness of cut. The discharge energy influences the recast layer thickness during machining as reported by Sharma et al. (2018). The recast layer decreased as the taper angle increased at the lowest and highest profiling speed parameters for all the profiles as shown in fig. 6.16 (a)-(f), 6.17 (a)-(f) and 6.18 (a)-(f) respectively. This recast layer was subjected to the micro-hardness test where the machined layer had lower micro-hardness as it was a resolidified layer. Fig. 6.19, 6.21 and 6.23 show the variation of micro-hardness from the nearest machined surface which is considered a reference point for all the profiles. Each micro-hardness value was recorded with a 20μm difference in distance from the reference point (machined zone). The lowest micro-hardness was recorded in the highest profiling speed parameter (WGD=60mm at 0°, CDT=99s, WO=40μm, CSO=31%) 0°and the highest micro-hardness was at 30° taper angle for the lowest profiling speed parameter (WGD=120mm at 30°, CDT=99s, WO=40μm, CSO=31%) at the machined surface. It was observed in profiles that both at the highest and lowest profiling speed the micro-hardness decreased at the reference point (machined zone). As the distance gradually increased i.e. away from the reference point (machined zone) the micro-hardness increased to the level of base metal micro-hardness i.e. (212 Hv). This was mainly due to the metallurgical changes in the material due to the discharge energy produced while machining as observed by Sharma et al. (2018). The recast layer due to the discharge energy leads to thermal degradation which makes the

154

material soft with low micro-hardness than that compared to the base metal. The EDS was taken on the recast layer and machined surface of the triangular and square profiles are shown in fig. 6.20 (a), (b) and 6.22 (a), (b) shows that the degradation in the material was due to the presence of O, Zn and Cu in the nickel superalloy. The presence of Zinc (Zn) and Copper (Cu) in base metal was due to the zinc-coated copper electrode and oxygen (O) due to dielectric water that was used in profiling. Similar results were found in OFAT profiling experiments and reported in section 4.3.5 of chapter 4.
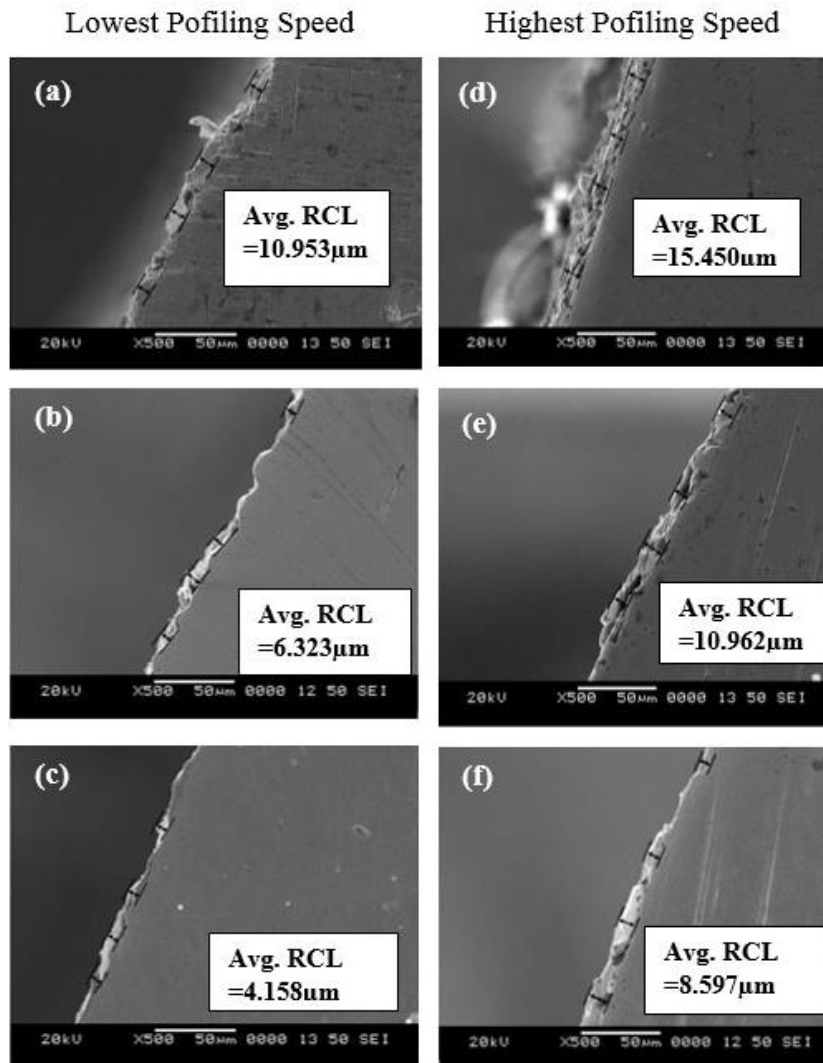
Figure 6.16 Variation of recast layer thickness at different taper angles for triangular profile

Lowest Profiling Speed   Highest Profiling Speed
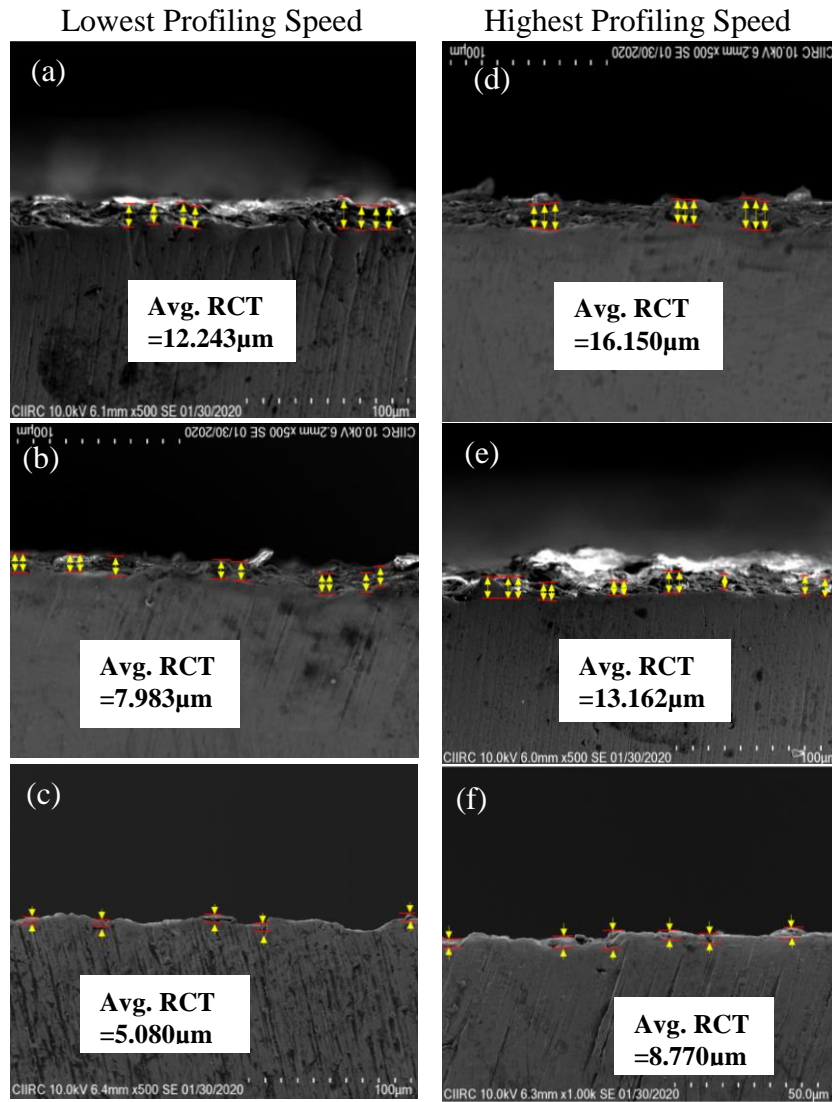
Figure 6.17 Variation of recast layer thickness at different taper angles for square profile.

Lowest Profiling speed Parameter   **Highest Profiling speed Parameter**
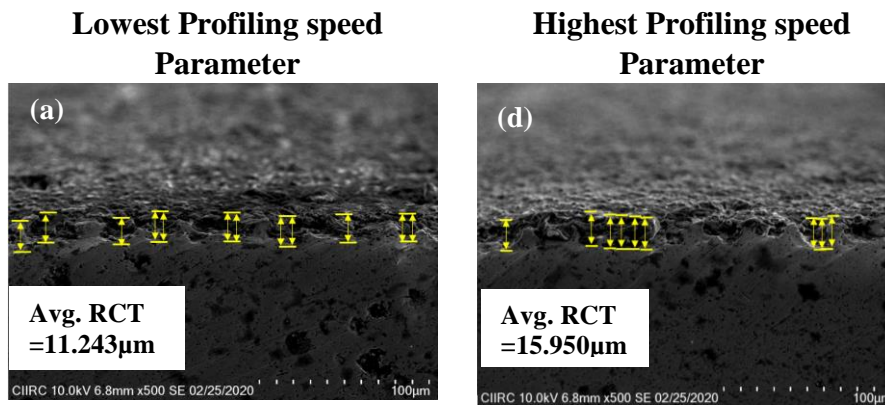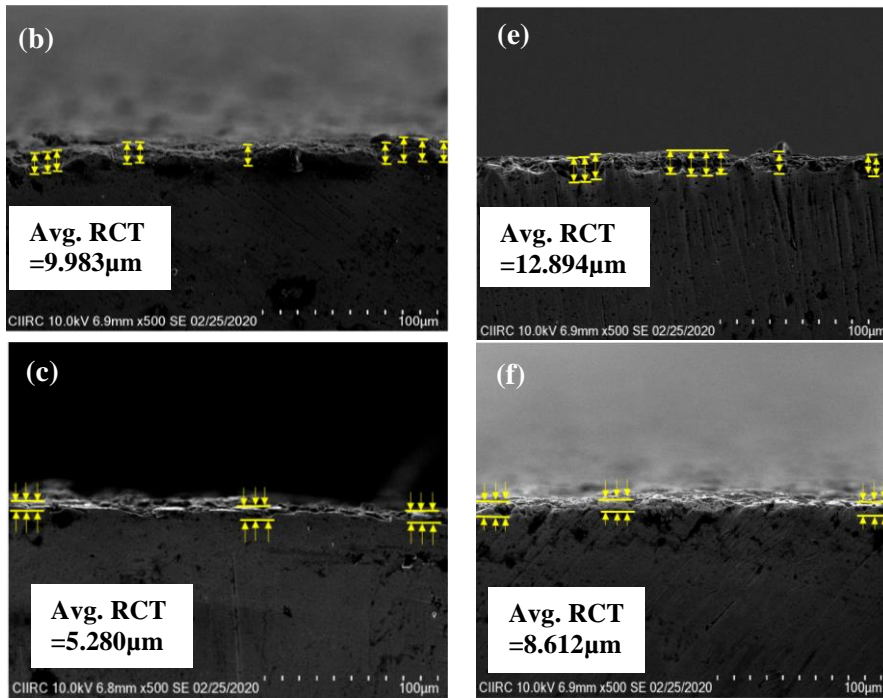
Figure 6.18 Variation of recast layer thickness at different taper angles for circular profile
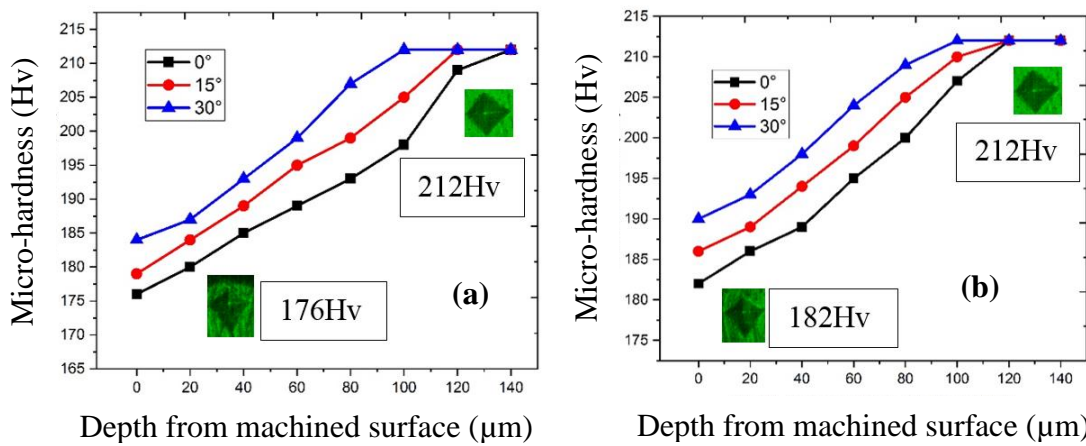
Figure 6.19 Variation of micro-hardness for (a) Highest and (b) Lowest profiling speed in triangular profile
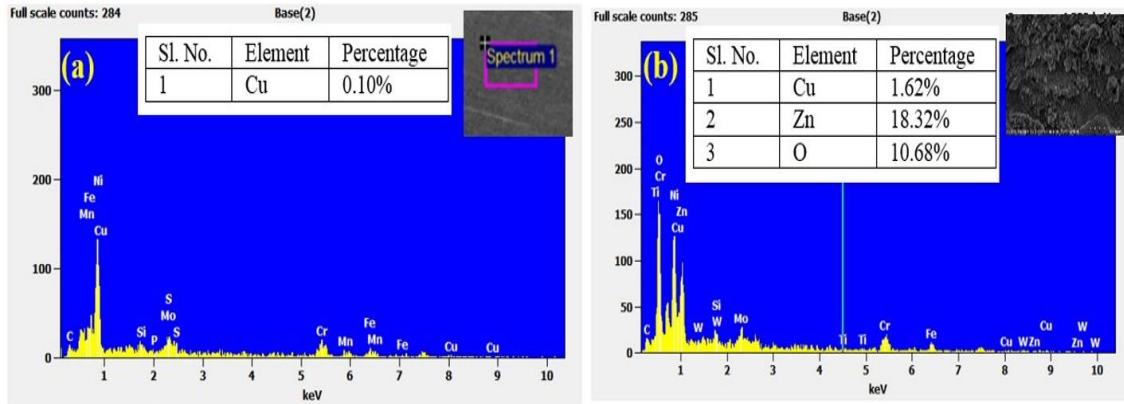
Figure 6.20 EDS of (a) As received (b) WEDmed surface
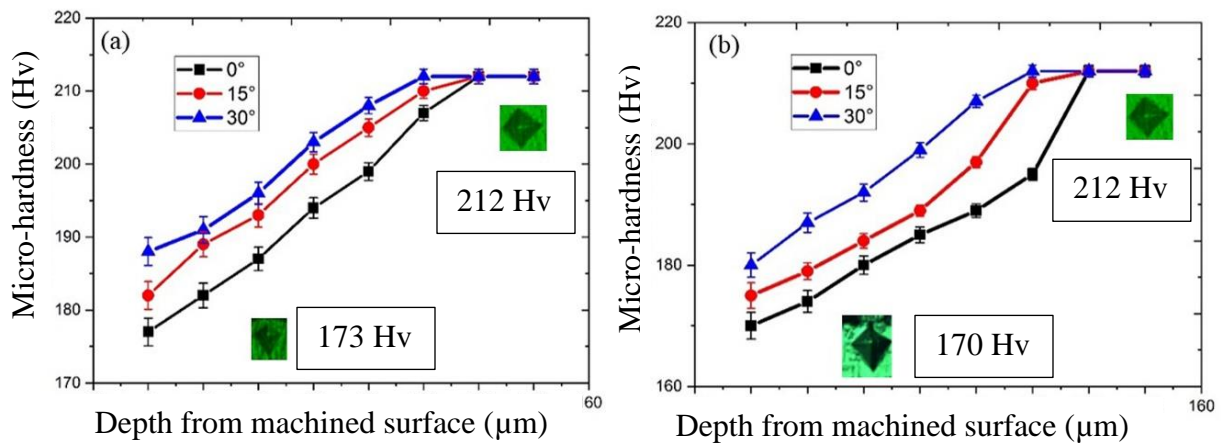
Figure 6.21 Micro-hardness at different taper angles for (a) Lowest and (b) Highest profiling speeds for square profiles
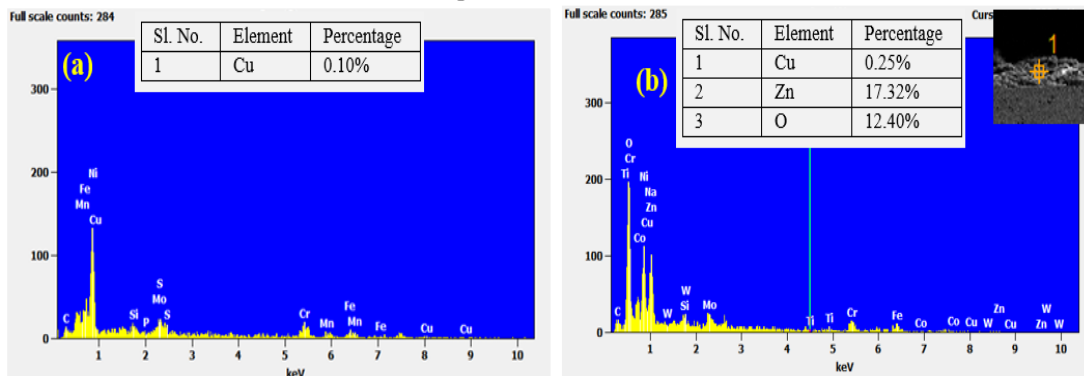
Figure 6.22 EDS for (a) As-received and (b) WEDMed surfaced
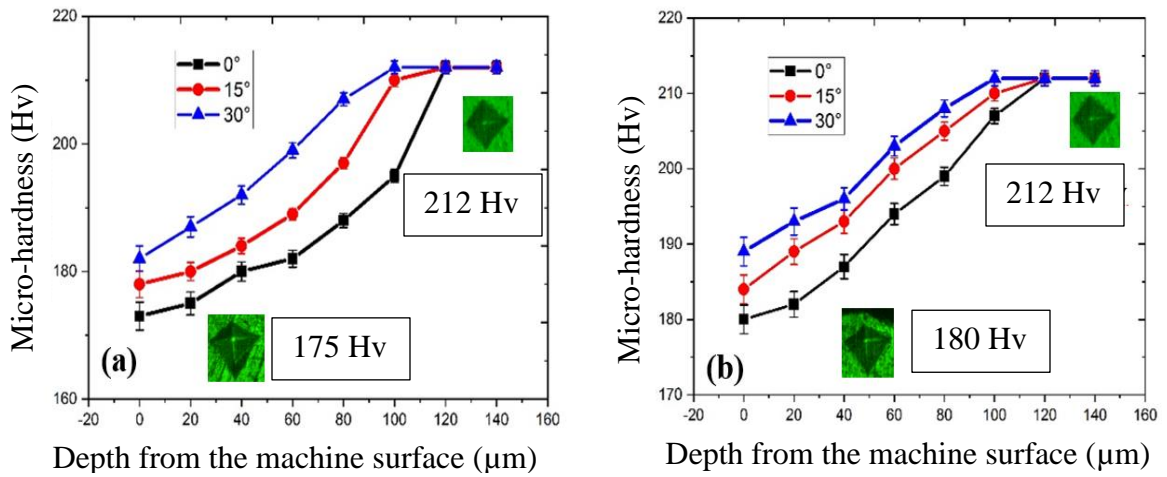
Figure 6.23 Micro-hardness at (a) Highest (b) Lowest profiling parameters for circular profiles

6.3.2 Compression recast layer and microhardness for different profiles
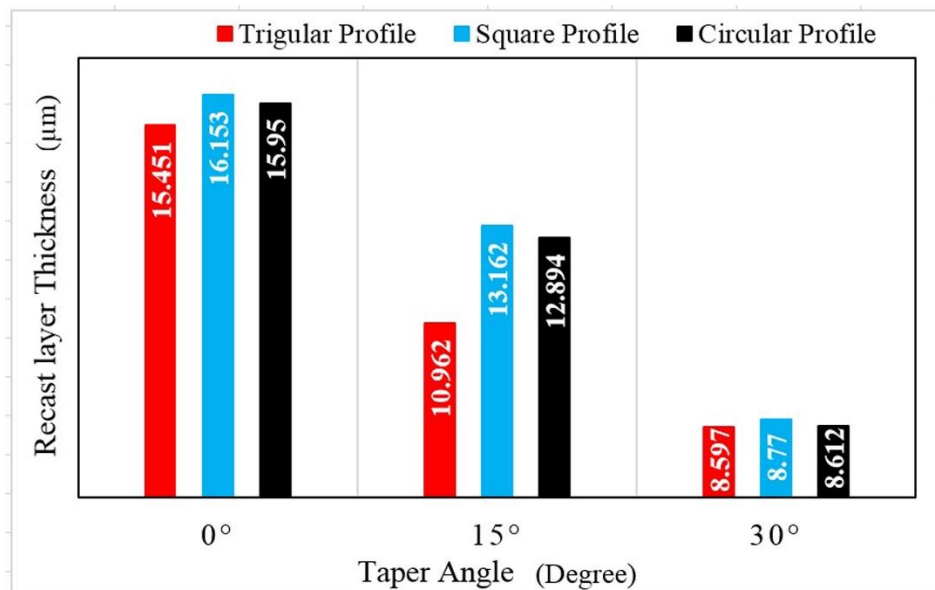
Figure 6.24 Variation of recast layer thickness in different profiles for highest profiling speed

Fig.6.24 and 6.25 show the recast layer thickness and micro-hardness for the highest profiling speed parameters. It follows similar trends as in section 5.4.3 where the profiling speed of the square profiles was the highest due to the CSO parameter followed by circular

profiles and triangular profiles have the least profiling speed. It can be observed that as the CSO increases the sparking increases increasing the discharge energy required for melting the material. So in square profiles, the material is exposed to more heat than in triangular profiles this leads to the highest recast layer thickness of 16.150μm at 0°. Where the triangular profiles have the least recast layer thickness of 15.45μm at 0°. This trend was also followed by profiling speed and surface roughness shown in chapter 5 sections 5.3.2 and 5.4.3. Contrasting trends were observed in microhardness of the profiles where square profiles have the least hardness and triangular profiles have the highest hardness values as shown in fig.6.25. The circular profiles have hardness and recast layer thickness in between triangular and square profiles. Similar trends were followed in profiling speed and surface roughness shown in chapter 5 sections 5.3.2 and 5.4.3.
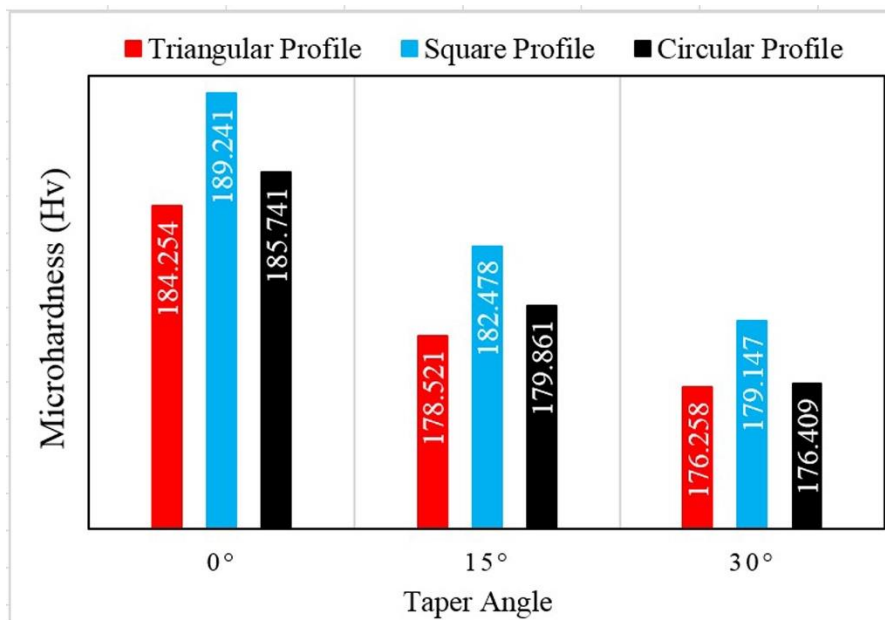
Fig. 6.25 Variation of microhardness in different profiles for highest profiling speed

6.4 SUMMARY

The tapered triangular, square and circular profiles at 0°, 15° and 30° taper angles were machined using WEDM with the aid of a novel fixture. Different input parameters like

WGD, WO CDT and CSO were investigated on profiling response characteristics. Based on the above investigation the following conclusions are drawn.

- In the case of corner error, the wire guide distance (WGD) parameter is the most influencing parameter. As WGD increases, the corner error also increased from 45.77 to 61.019%. The parameters yielding minimal errors were WGD=40mm for 0°, 75mm for 15°and 100mm for 30°, CDT=99s, WO=0μm and CSO=31% based on machining parameters.

- As the taper angle increases, although the speed decreases by 3.846% the corner error increases by 1.813-8.377 for both triangular and square profiles due to the wire deflection.

- Comparing the parameters in triangular and circular profiles, the WO parameter behaves contrastingly for different profiles, as WO increases the corner error increases in square profiles and corner error decreases in triangular profiles. This contrasting behaviour was due to the change in corner angle or geometry.

- The shift was only observed in triangular profiles. The highest shift of 47.93μm, 114.70μm, and 122.67μm at 30° taper corners for 1mm, 3mm, and 5mm profiles respectively at the highest profiling rates. This shift is due to the decrease in corner strength and electromagnetic forces and it was observed to be always opposite to the wire path.

- The recast layer thickness clearly shows a decrease from 53.25-45.02% and micro-hardness at the WEDMed surface increases 5.13-5.81% as the taper angle increases from 0° to 30°. This was because of increased (slant material thickness) material thickness and the effect of heat during machining.

CHAPTER 7

ARTIFICIAL NEURAL NETWORK (ANN) AND ADAPTIVE NEURAL FUZZY INTERFERENCE SYSTEM (ANFIS) MODELLING WITH EXPERIMENTAL VALIDATION

7.1 INTRODUCTION

The different profiles like triangular, square and circular profiles were machined at different profiling parameters like wire guide distance (WGD), corner dwell time (CDT), wire offset (WO) and cutting speed override (CSO) at 0°, 15° and 30° taper angles. The output characteristics like profiling speed and surface roughness were used for training, validation and testing of the developed model in both ANN and ANFIS modelling. An optimal model was developed, where the parameters were fed for the prediction of the profiling speed and surface roughness. The parameters used apart for training, validation and testing were also used for prediction which was validated by experimentation to check the efficiency of the developed model.

7.2 PREDICTION AND VALIDATION OF PROFILING SPEED AND SURFACE ROUGHNESS USING ANN AND ANFIS

Based on the experimental data, ANN and ANFIS modelling were performed. The optimal model were used to predict profiling speed and surface roughness with the accuracy of the prediction were demonstrated for different profiles. Different parameters were chosen to validate the accuracy of the models developed by comparing to experimentation. The parameters used to build the ANN and ANFIS models are described as follows.

7.2.1 Artificial Neural Network (ANN)

The prediction ANN tool of MATLAB is utilized to develop the Back-propagation neural network (BPNN) model for the prediction of machining areas for different parameters. The input of 48 iterations of profiling repeated for different parameters at different taper angles at 0°, 15° and 30° was considered for the ANN model. The total sets were divided randomly into 70% for training, 15% for validation and 15% for testing the model by the software. As backward propagation neural network (BPNN) integrated with Levenberg-Marquardt (LM) algorithm is most efficient as reported by Gosh et al. (2019) similar model and algorithm combinations are used to train the neural network for prediction of profiling speed. The profiling speed recorded was normalized between -1 to 1 for training the network. The tansig function and the pureline functions were used for training the neural network. The mean square error (MSE) performance function was used for training, testing and validation.

The 5-8-1-1 ANN architecture was found to be suitable for training the network in the prediction of profiling speed (PS) as in fig. 7.1.This architecture depends on the number of input and output parameters. The regression plot generated during the training of the 5-8-1-1 neural network. The model was trained until the overall R-value was found to be nearing 0.99 indicating the model efficiency. Similar architecture was used for both profiling speed and surface roughness as the input and output parameters remain same in number. The input parameters considered were wire guide distance (WGD), corner dwell time (CDT), wire offset (WO) and cutting speed override (CSO) and the output parameters were profiling speed (PS) and surface roughness (SR). Each output parameters were trained, validated and tested separately for different profiles for different responses.
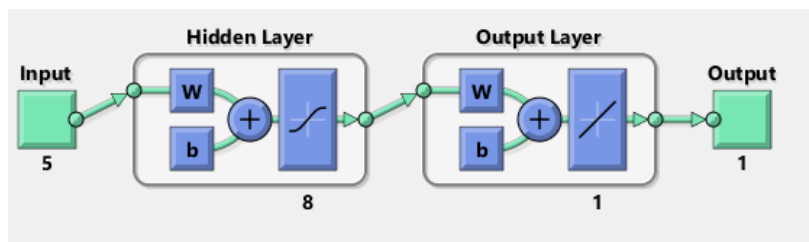
Figure 7.1 5-8-1-1 ANN architecture

163

7.2.2 Adaptive Neural Fuzzy Interference System (ANFIS)

In the case of the ANFIS model was modelling uses five network layers to perform the following fuzzy inference steps. As stated by Maher et al. (2016), it was concluded that the Gaussian membership function (gaussmf) gives the lowest errors. (No. of epochs 1000 and output function used was constant). Among the experimental parameters, the ratio of 80% of the data was considered for training the model and 20% were considered for the testing model. This ratio gave the lowest testing errors. There were 5 network layers used each network layer was assigned 2 membership function. The training to testing ratios, type and number of membership function were assigned based on different trials carried out during building the model.

7.3 PROFILING SPEED (PS)

The profiling speed was calculated as average of instantaneous cutting speed at various parameters for different profiles. The experimental data was as in chapter 5 in sections 5.3 and chapter 6 in section 6.3 and 6.7. All the data were used for obtaining the optimal ANN and ANFIS model.

7.3.1 Triangular profile

Table 7.1 shows the profiling speed (PS) for predicted, experimental and error in the prediction of different parameters for various taper angles. It can be observed from table that the ANFIS was more accurate than ANN. The average percentage error for the ANFIS model was 0.494% which is lesser than the ANN model having 1.312%.

Table 7.1 Predicted and experimental profiling speed (PS) for triangular profile

Sl. No.	WGD (mm)	CDT (s)	WO (μm)	CSO (%)	Profiling Speed (mm/min)				
					Predicted		Experi mental	% Error	
					ANN	ANFIS		ANN	ANFIS
0° Taper angle									
1	40	0	0	31	0.732	0.749	0.749	2.270	0.000
2	40	33	40	54	0.96	0.952	0.952	0.840	0.000
3	40	66	80	77	1.267	1.208	1.256	0.876	3.822

4	40	99	120	100	1.436	1.425	1.425	0.772	0.000
5	50	0	40	77	1.262	1.266	1.266	0.316	0.000
6	50	33	0	100	1.408	1.409	1.409	0.071	0.000
7	50	66	120	31	0.659	0.659	0.659	0.000	0.000
8	50	99	80	54	0.831	0.801	0.801	3.745	0.000
9	60	0	80	100	1.431	1.403	1.403	1.996	0.000
10	60	33	120	77	1.356	1.371	1.371	1.094	0.000
11	60	66	0	54	0.821	0.812	0.812	1.108	0.000
12	60	99	40	31	0.619	0.636	0.631	1.902	0.792
13	70	0	120	54	0.752	0.75	0.75	0.267	0.000
14	70	33	80	31	0.626	0.602	0.602	3.987	0.000
15	70	66	40	100	1.5	1.508	1.508	0.531	0.000
16	70	99	0	77	0.732	0.749	0.749	1.735	0.000
15° Taper angle									
17	75	0	0	31	1.303	1.326	1.326	0.956	0.574
18	75	33	40	54	0.528	0.52	0.523	0.628	0.000
19	75	66	80	77	0.641	0.637	0.637	1.102	0.000
20	75	99	120	100	1.101	1.089	1.089	0.428	0.000
21	85	0	40	77	1.409	1.403	1.403	1.935	0.000
22	85	33	0	100	1.115	1.137	1.137	0.786	0.000
23	85	66	120	31	1.41	1.399	1.399	1.346	0.000
24	85	99	80	54	0.527	0.52	0.52	0.300	2.549
25	95	0	80	100	0.665	0.684	0.667	0.643	0.000
26	95	33	120	77	1.39	1.399	1.399	0.360	0.000
27	95	66	0	54	1.115	1.111	1.111	1.810	1.508
28	95	99	40	31	0.675	0.673	0.663	8.182	0.000
29	105	0	120	54	0.595	0.550	0.550	0.305	0.000
30	105	33	80	31	0.654	0.656	0.656	1.075	0.000
31	105	66	40	100	0.564	0.558	0.558	0.677	0.000
32	105	99	0	77	1.487	1.477	1.477	2.566	4.400
30° Taper angle									
33	100	0	0	31	0.481	0.482	0.483	0.414	0.207
34	100	33	40	54	0.540	0.566	0.566	4.594	0.000
35	100	66	80	77	1.008	1.000	1.000	0.800	0.000
36	100	99	120	100	1.355	1.384	1.384	2.095	0.000
37	110	0	40	77	0.995	0.977	0.977	1.842	0.000
38	110	33	0	100	1.362	1.335	1.361	0.073	1.910
39	110	66	120	31	0.493	0.494	0.494	0.202	0.000
40	110	99	80	54	0.563	0.571	0.571	1.401	0.000
41	120	0	80	100	1.375	1.383	1.383	0.578	0.000
42	120	33	120	77	1.048	1.046	1.046	0.191	0.000
43	120	66	0	54	0.591	0.610	0.586	0.853	4.096

44	120	99	40	31	0.488	0.470	0.470	3.830	0.000
45	130	0	120	54	0.589	0.586	0.586	0.512	0.000
46	130	33	80	31	0.491	0.520	0.500	1.800	4.000
47	130	66	40	100	1.453	1.450	1.450	0.207	0.000
48	130	99	0	77	0.985	1.006	1.006	2.087	0.000

7.3.1.1 Validation of the optimal models
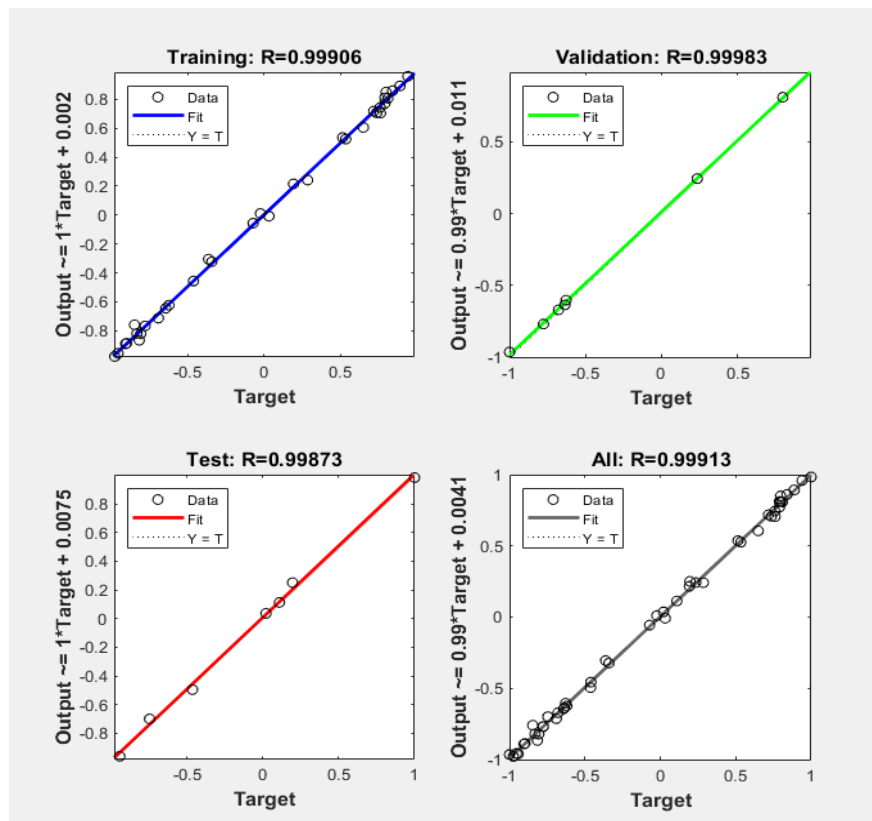
Figure 7.2 Regression plot of the optimum fitting model used for prediction.

The optimal model was obtained based on R-value in the regression plot as in fig.7.2. In case of ANFIS model minimal error was considered as optimal model. For validation, the input parameters are fed to the ANN and ANFIS model. The model was then made to simulate for the prediction of output profiling speed. The input parameters for validation were selected randomly from the experimental input parameters. Table 7.2 shows the validation input parameters, measured profiling speed, predicted profiling speed and %

error. The ANFIS model obtained the least error compared to the ANN models during experimental validation. It can be seen that the ANFIS model gives error ranging from 0-4.87% which indicates higher efficiency.

Table 7.2 Validation of ANN model by experiments

Sl. No.	WGD (mm)	CDT (s)	WO (µm)	CSO (%)	Profiling Speed (mm/min)				
					Predicted		Experi mental	% Error	
					ANN	ANFIS		ANN	ANFIS
0° Taper angle									
1	55	40	100	45	0.778	0.742	0.768	**1.302**	3.385
2	65	55	80	55	0.863	0.879	0.891	3.143	**1.347**
15° Taper angle									
3	90	50	75	65	0.852	0.881	0.902	5.543	2.328
4	80	70	55	95	1.355	1.325	1.263	**7.284**	**4.909**
30° Taper angle									
5	115	80	50	90	1.285	1.271	1.211	6.111	4.955
6	125	40	30	80	1.097	1.122	1.172	6.399	4.266

7.3.1.2 ANFIS model mapping of response parameters.

The ANFIS model gives the 3 dimensional mapping of input-output parameters mapping obtained from MATLAB. Fig.7.3 (a-d) shows the variation of the profiling speed with WGD, CDT, WO, CSO and taper angle. It can be noticed that as the taper angle increases the profiling speed decreases in all the fig. 7.3 (a-d). Similar trend were observed in chapter 5 section 5.3 from the main effects plot in fig.5.4, 5.5 and 5.6. In case of CSO parameter seen in fig.7.3 (d) that as CSO increases the profiling speed also increases. This influence of CSO parameter in the profiling speed as observed in the main effects plot in fig.5.4, 5.5 and 5.6 from chapter 5.
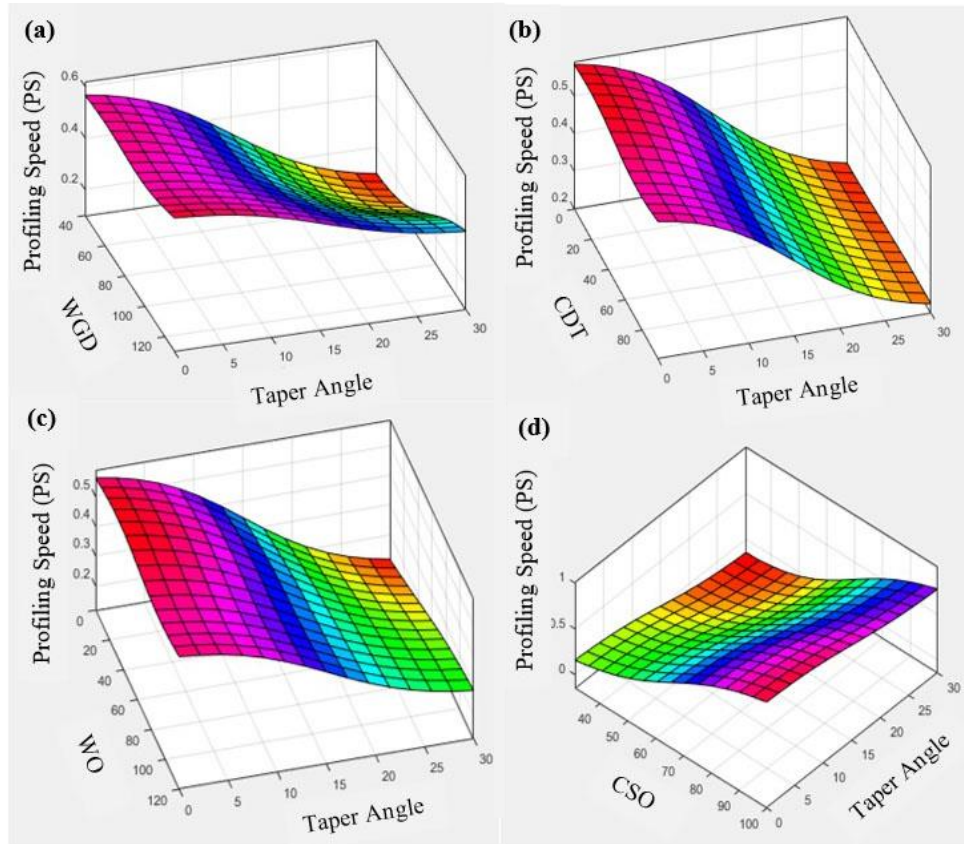
Figure 7.3 ANFIS mapping for profiling speed of triangular profile

7.3.2 Square profile

Table 7.3 shows the profiling speeds obtained at different parameters by experimental, ANN prediction, and ANFIS prediction. The average percentage error in ANFIS model was 0.744% whereas ANN model was 0.920%. This shows that the ANFIS model is accurate than ANN model.

Table 7.3 Predicted and experimental profiling speed for the square profile.

Sl. No.	WGD (mm)	CDT (s)	WO (µm)	CSO (%)	Profiling Speed (mm/min)				
					Predicted		Experi mental	% Error	
					ANN	ANFIS		ANN	ANFIS
0° Taper angle									
1	40	0	0	31	0.785	0.769	0.769	2.081	0.000
2	40	33	40	54	1.099	1.126	1.126	2.398	0.000
3	40	66	80	77	1.417	1.392	1.427	0.701	2.453

168

4	40	99	120	100	1.596	1.616	1.616	1.238	0.000
5	50	0	40	77	1.496	1.501	1.501	0.333	0.000
6	50	33	0	100	1.593	1.599	1.599	0.375	0.000
7	50	66	120	31	0.892	0.898	0.898	0.668	0.000
8	50	99	80	54	1.009	1.001	1.000	0.900	0.100
9	60	0	80	100	1.562	1.558	1.558	0.257	0.000
10	60	33	120	77	1.536	1.523	1.523	0.854	0.000
11	60	66	0	54	0.891	0.889	0.889	0.225	0.000
12	60	99	40	31	0.721	0.719	0.739	2.436	2.706
13	70	0	120	54	0.936	0.908	0.908	3.084	0.000
14	70	33	80	31	0.733	0.749	0.749	2.136	0.000
15	70	66	40	100	1.720	1.718	1.718	0.116	0.000
16	70	99	0	77	1.500	1.495	1.495	0.334	0.000
15° Taper angle									
17	75	0	0	31	0.743	0.693	0.723	2.766	4.149
18	75	33	40	54	0.895	0.876	0.876	2.169	0.000
19	75	66	80	77	1.295	1.289	1.289	0.465	0.000
20	75	99	120	100	1.519	1.490	1.490	1.946	0.000
21	85	0	40	77	1.352	1.345	1.345	0.520	0.000
22	85	33	0	100	1.545	1.507	1.507	2.522	0.000
23	85	66	120	31	0.764	0.754	0.754	1.326	0.000
24	85	99	80	54	0.846	0.901	0.855	1.053	5.380
25	95	0	80	100	1.498	1.493	1.493	0.335	0.000
26	95	33	120	77	1.465	1.479	1.479	0.947	0.000
27	95	66	0	54	0.875	0.872	0.876	0.114	0.457
28	95	99	40	31	0.712	0.715	0.705	0.993	1.418
29	105	0	120	54	0.859	0.858	0.858	0.117	0.000
30	105	33	80	31	0.712	0.708	0.718	0.836	1.393
31	105	66	40	100	1.628	1.628	1.628	0.000	0.000
32	105	99	0	77	1.420	1.513	1.427	0.491	6.027
30° Taper angle									
33	100	0	0	31	0.694	0.681	0.695	0.144	2.014
34	100	33	40	54	0.706	0.718	0.718	1.671	0.000
35	100	66	80	77	1.158	1.160	1.160	0.172	0.000
36	100	99	120	100	1.463	1.467	1.467	0.273	0.000
37	110	0	40	77	1.302	1.297	1.297	0.386	0.000
38	110	33	0	100	1.508	1.527	1.499	0.600	1.868
39	110	66	120	31	0.697	0.698	0.698	0.143	0.000
40	110	99	80	54	0.774	0.779	0.779	0.642	0.000
41	120	0	80	100	1.446	1.449	1.449	0.207	0.000
42	120	33	120	77	1.372	1.370	1.369	0.219	0.073
43	120	66	0	54	0.834	0.819	0.834	0.000	1.799

44	120	99	40	31	0.701	0.693	0.693	1.154	0.000
45	130	0	120	54	0.860	0.856	0.856	0.467	0.000
46	130	33	80	31	0.715	0.658	0.698	2.436	5.731
47	130	66	40	100	1.469	1.468	1.468	0.068	0.000
48	130	99	0	77	1.418	1.406	1.406	0.853	0.000

7.3.2.1 Validation of the optimal models

Fig. 7.4 shows the regression plots obtained in optimal ANN model. In case of ANFIS model minimal error was considered as optimal model. For validation, the input parameters are fed to the ANN and ANFIS model. The model was then made to simulate for the prediction of output profiling speed. Table 7.4 shows the validation input parameters, measured profiling speed, predicted profiling speed and % error. The ANFIS model obtained the least error compared to the ANN models during experimental validation. The ANN model yielded errors between 0-10% and the ANFIS model gave 0-5% errors indicating higher efficiency in prediction.
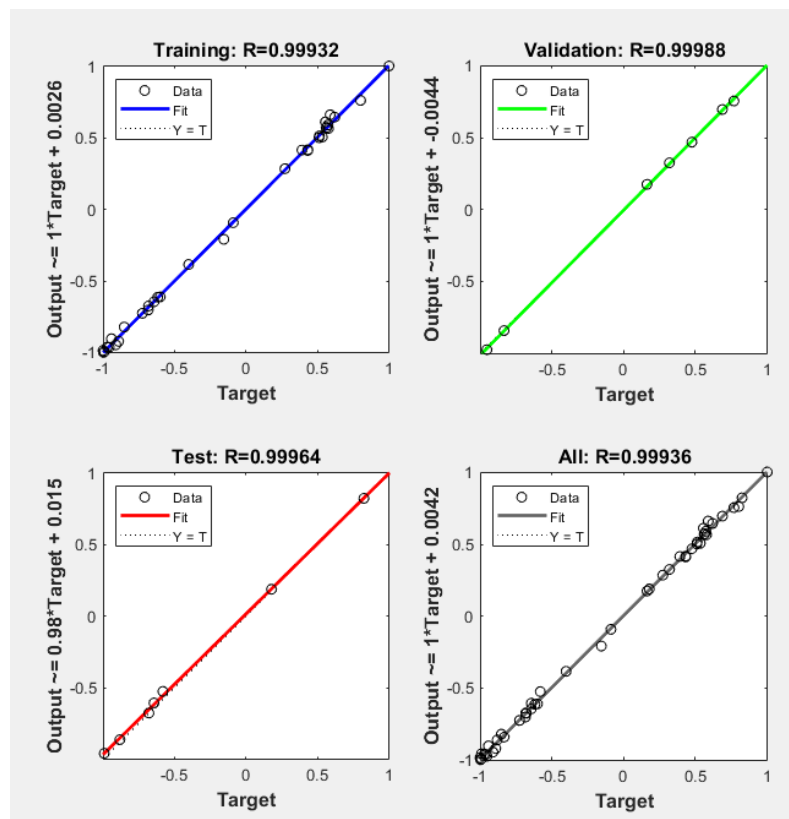
Figure 7.4 Regression plots for optimal model

Table 7.4 Experimental, ANN and ANFIS predicted profiling speeds

Sl. No.	WGD (mm)	CDT (s)	WO (µm)	CSO (%)	Profiling Speed (mm/min)				
					Predicted		Experi mental	% Error	
					ANN	ANFIS		ANN	ANFIS
0° Taper angle									
1	55	40	100	45	0.848	0.875	0.865	**1.965**	**1.156**
2	65	55	80	55	1.026	1.10	1.083	5.263	1.570
15° Taper angle									
3	90	50	75	65	1.109	1.240	1.207	8.119	2.734
4	80	70	55	95	1.326	1.400	1.474	**9.857**	**4.827**
30° Taper angle									
5	115	80	50	90	1.267	1.354	1.301	2.613	4.074
6	125	40	30	80	1.236	1.250	1.282	3.588	2.496

7.3.2.2 ANFIS model mapping of response parameters

From the ANFIS model, the Input and output relationship was obtained as shown in fig.7.5 (a-d) obtained from MATLAB. It shows a 3-dimensional variation of profiling speed with three taper angles for different input parameters. It can be concluded from the ANFIS mapping that the CSO parameter influenced the most on profiling speed as obtained from effect plots of square profile in in chapter 5. The mapping also clearly shows that as the taper angle increases the profiling speed also decreases. It can also be observed that the WGD and CDT have a very less effect on profiling speed. From fig.7.5 (c) it can be observed that as the WO parameter increases the profiling speed also increases. As the WO parameter increases the wire movement vibrations are limited. This increases the profiling speed due to lower wire vibration stated as by Habib and Okada (2016) which were not traced in the case of effects plots.
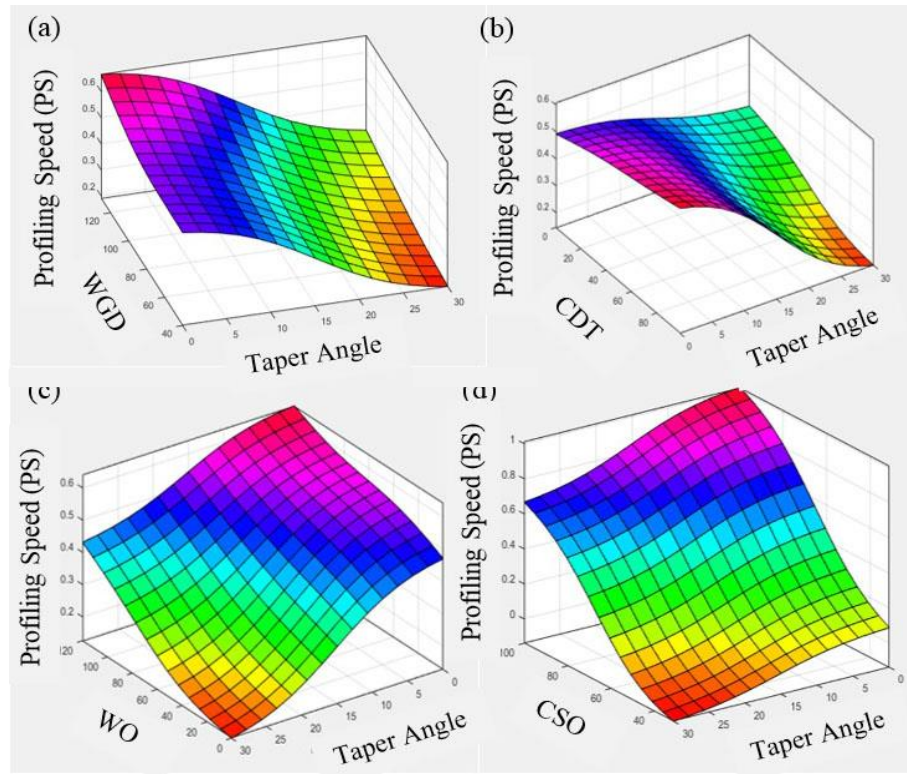
Figure 7.5 ANFIS mapping for profiling speed of square profile

7.3.3 Circular profile

The predicted experimental and error in profiling speeds for circular profiles were as in table 7.5. The average error was found to be 0.362% for ANFIS and 0.890% for ANN models. This shows that ANFIS is more accurate than ANN model.

Table 7.5 Predicted and experimental profiling speed for triangular profile

Sl. No.	WGD (mm)	CDT (s)	WO (µm)	CSO (%)	Profiling Speed (mm/min)				
					Predicted		Experi mental	% Error	
					ANN	ANFIS		ANN	ANFIS
0° Taper angle									
1	40	0	0	31	0.765	0.756	0.756	1.190	0.000
2	40	33	40	54	0.983	0.99	0.990	0.707	0.000
3	40	66	80	77	1.394	1.309	1.392	0.144	5.963
4	40	99	120	100	1.565	1.537	1.537	1.822	0.000
5	50	0	40	77	1.334	1.337	1.337	0.224	0.000

172

6	50	33	0	100	1.514	1.519	1.510	0.265	0.596
7	50	66	120	31	0.745	0.748	0.748	0.401	0.000
8	50	99	80	54	0.910	0.881	0.881	3.292	0.000
9	60	0	80	100	1.500	1.502	1.501	0.067	0.067
10	60	33	120	77	1.402	1.398	1.398	0.286	0.000
11	60	66	0	54	0.881	0.879	0.879	0.228	0.000
12	60	99	40	31	0.720	0.711	0.718	0.279	0.975
13	70	0	120	54	0.862	0.898	0.898	4.009	0.000
14	70	33	80	31	0.728	0.729	0.729	0.137	0.000
15	70	66	40	100	1.679	1.677	1.677	0.119	0.000
16	70	99	0	77	1.394	1.393	1.393	0.072	0.000
15° Taper angle									
17	75	0	0	31	0.714	0.719	0.719	0.695	0.000
18	75	33	40	54	0.855	0.85	0.850	0.588	0.000
19	75	66	80	77	1.274	1.263	1.263	0.871	0.000
20	75	99	120	100	1.512	1.502	1.501	0.733	0.067
21	85	0	40	77	1.261	1.263	1.263	0.158	0.000
22	85	33	0	100	1.464	1.468	1.468	0.272	0.000
23	85	66	120	31	0.712	0.712	0.712	0.000	0.000
24	85	99	80	54	0.831	0.838	0.838	0.835	0.000
25	95	0	80	100	1.470	1.456	1.456	0.962	0.000
26	95	33	120	77	1.276	1.274	1.274	0.157	0.000
27	95	66	0	54	0.856	0.835	0.843	1.542	0.949
28	95	99	40	31	0.697	0.701	0.701	0.571	0.000
29	105	0	120	54	0.804	0.814	0.813	1.107	0.123
30	105	33	80	31	0.694	0.693	0.693	0.144	0.000
31	105	66	40	100	1.606	1.602	1.602	0.250	0.000
32	105	99	0	77	1.300	1.298	1.311	0.839	0.992
30° Taper angle									
33	100	0	0	31	0.622	0.619	0.62	0.323	0.161
34	100	33	40	54	0.641	0.703	0.703	8.819	0.000
35	100	66	80	77	1.113	1.106	1.106	0.633	0.000
36	100	99	120	100	1.410	1.411	1.411	0.071	0.000
37	110	0	40	77	1.090	1.089	1.089	0.092	0.000
38	110	33	0	100	1.383	1.313	1.383	0.000	5.061
39	110	66	120	31	0.677	0.682	0.682	0.733	0.000
40	110	99	80	54	0.720	0.718	0.718	0.279	0.000
41	120	0	80	100	1.402	1.405	1.405	0.214	0.000
42	120	33	120	77	1.074	1.074	1.074	0.000	0.000
43	120	66	0	54	0.691	0.701	0.696	0.718	0.718
44	120	99	40	31	0.608	0.607	0.607	0.165	0.000
45	130	0	120	54	0.714	0.708	0.708	0.847	0.000

46	130	33	80	31	0.577	0.624	0.614	6.026	1.629
47	130	66	40	100	1.447	1.457	1.457	0.686	0.000
48	130	99	0	77	1.090	1.089	1.088	0.184	0.092

7.3.3.1 Validation of optimal models of ANN and ANFIS

Fig. 7.6 shows the regression plot for the optimal model in ANN model. Minimal error was considered as an indication of efficiency in case of ANFIS model. Table 7.6 shows different parameters that were used for validation and prediction of profiling speed as in triangular and square profile. The parameters were fed to the optimal models of ANN and ANFIS. These were also experimentally validated to know the efficiency of the models. The maximum error was found in the ANN model of 9.04% and the ANFIS model yielded a maximum error of 4.49%. This indicates ANFIS model was more accurate than the ANN model.
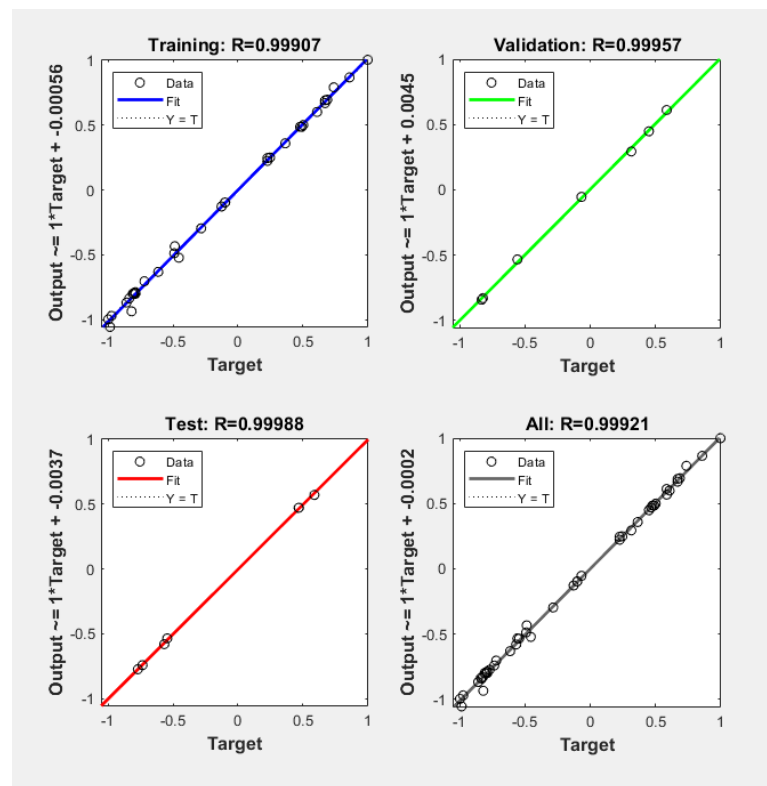
Figure 7.6 Regression plots for optimal model

Table 7.6 Validation of profiling speeds at different parameters

Sl. No.	WGD (mm)	CDT (s)	WO (µm)	CSO (%)	Profiling Speed (mm/min)				
					Predicted		Experimental	% Error	
					ANN	ANFIS		ANN	ANFIS
0° Taper angle									
1	55	40	100	45	0.752	0.853	0.822	8.516	3.771
2	65	55	80	55	0.937	0.976	0.965	2.902	1.140
15° Taper angle									
3	90	50	75	65	1.170	1.059	1.096	6.752	3.376
4	80	70	55	95	1.562	1.502	1.528	2.225	**1.702**
30° Taper angle									
5	115	80	50	90	1.351	1.323	1.350	**0.074**	2.000
6	125	40	30	80	1.106	1.158	1.217	**9.121**	**4.848**

7.3.3.2 ANFIS Mapping of response parameters
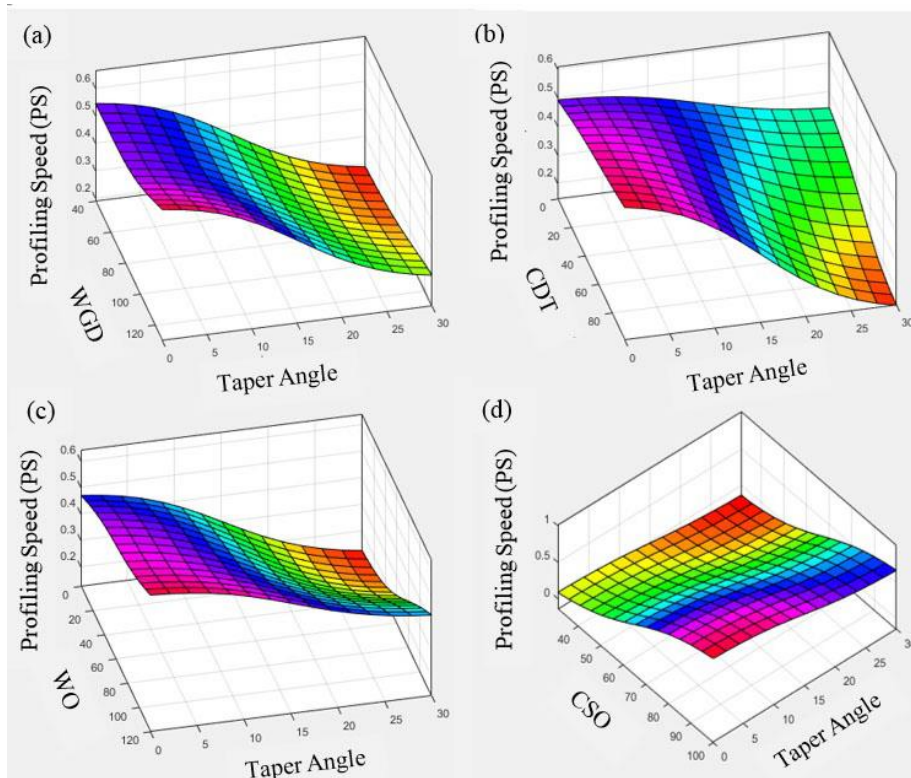
Figure 7.7 ANFIS mapping for profiling speed of circular profile

175

The ANFIS provides a behaviour of profiling speed by mapping input parameters to the output parameters from MATLAB. Fig. 7.7 (a-d) indicates the variation of profiling speed at different parameters. It can be seen from all the figures that as the taper angle increases the profiling speed decreases, similar to the main effects plot in chapter 5. Similar results were witnessed for triangular, square profiles.

7.4 SURFACE ROUGHNESS

The surface roughness was calculated as average surface roughness obtained at different profiles namely triangular, square and circular profiles. Chapter 5 shows the experimental data for surface roughness of different profiles. All the data were normalized and utilized for ANN and ANFIS modelling.

7.4.1 Triangular Profile

Table 7.7 shows the surface roughness obtained from prediction, experimental and % error for different experimental combinations. It can be observed from the table 7.7 that the ANFIS prediction gives lesser errors compared to ANN. The average error was found to be 0.369% for ANFIS which is lesser when compared to ANN having 0.874%.

Table 7.7 Experimental and predicted surface roughness at different taper angles

Sl. No.	WGD (mm)	CDT (s)	WO (µm)	CSO (%)	Surface roughness (µm)				
					Predicted		Experi mental	% Error	
					ANN	ANFIS		ANN	ANFIS
0° Taper angle									
1	40	0	0	31	0.449	0.447	0.447	0.447	0.000
2	40	33	40	54	0.510	0.518	0.518	1.544	0.000
3	40	66	80	77	0.584	0.576	0.576	1.389	0.000
4	40	99	120	100	0.773	0.756	0.756	2.249	0.000
5	50	0	40	77	0.659	0.656	0.656	0.457	0.000
6	50	33	0	100	0.697	0.692	0.692	0.723	0.000
7	50	66	120	31	0.470	0.476	0.476	1.261	0.000
8	50	99	80	54	0.626	0.629	0.629	0.477	0.000
9	60	0	80	100	0.803	0.799	0.799	0.501	0.000
10	60	33	120	77	0.777	0.794	0.794	2.141	0.000
11	60	66	0	54	0.523	0.517	0.517	1.161	0.000

12	60	99	40	31	0.427	0.427	0.426	0.235	0.235
13	70	0	120	54	0.654	0.662	0.662	1.208	0.000
14	70	33	80	31	0.576	0.567	0.567	1.587	0.000
15	70	66	40	100	0.911	0.908	0.908	0.330	0.000
16	70	99	0	77	0.737	0.736	0.736	0.136	0.000
15° Taper angle									
17	75	0	0	31	0.484	0.476	0.477	1.468	0.210
18	75	33	40	54	0.534	0.548	0.548	2.555	0.000
19	75	66	80	77	0.632	0.626	0.626	0.958	0.000
20	75	99	120	100	0.787	0.786	0.786	0.127	0.000
21	85	0	40	77	0.680	0.686	0.686	0.875	0.000
22	85	33	0	100	0.719	0.722	0.722	0.416	0.000
23	85	66	120	31	0.531	0.516	0.516	2.907	0.000
24	85	99	80	54	0.665	0.616	0.664	0.151	7.229
25	95	0	80	100	0.858	0.859	0.859	0.116	0.000
26	95	33	120	77	0.851	0.834	0.834	2.038	0.000
27	95	66	0	54	0.569	0.577	0.577	1.386	0.000
28	95	99	40	31	0.465	0.476	0.476	2.311	0.000
29	105	0	120	54	0.700	0.692	0.692	1.156	0.000
30	105	33	80	31	0.614	0.607	0.607	1.153	0.000
31	105	66	40	100	0.936	0.937	0.948	1.266	1.160
32	105	99	0	77	0.765	0.766	0.766	0.131	0.000
30° Taper angle									
33	100	0	0	31	0.700	0.711	0.705	0.709	0.851
34	100	33	40	54	0.780	0.779	0.779	0.128	0.000
35	100	66	80	77	0.895	0.902	0.902	0.776	0.000
36	100	99	120	100	1.094	1.094	1.094	0.000	0.000
37	110	0	40	77	0.932	0.929	0.929	0.323	0.000
38	110	33	0	100	0.984	1.000	0.982	0.204	1.833
39	110	66	120	31	0.742	0.741	0.741	0.135	0.000
40	110	99	80	54	0.922	0.923	0.923	0.108	0.000
41	120	0	80	100	1.175	1.145	1.145	2.620	0.000
42	120	33	120	77	1.170	1.178	1.178	0.679	0.000
43	120	66	0	54	0.820	0.771	0.822	0.243	6.204
44	120	99	40	31	0.684	0.682	0.682	0.293	0.000
45	130	0	120	54	0.959	0.964	0.964	0.519	0.000
46	130	33	80	31	0.844	0.845	0.845	0.118	0.000
47	130	66	40	100	1.249	1.247	1.247	0.160	0.000
48	130	99	0	77	1.040	1.039	1.039	0.096	0.000

7.4.1.1 Validation of the optimal model

Fig. 7.8 gives the regression plots obtained in training of ANN model indicating the efficiency of the model. The model having minimal error was considered as optimal model in case of the ANFIS model. Different parameters were chosen for validation of prediction models. The parameters were different from the parameters used for training, testing and validation. These parameters were fed to the optimal models to get the surface roughness. These parameters were validated using experiments. Table 7.8 indicates the predicted, experimental and error percentage. It can be seen that ANN the error varies from 0-9.128% and ANFIS error varies from 0-4.073% indicating the efficiency of the ANFIS model.
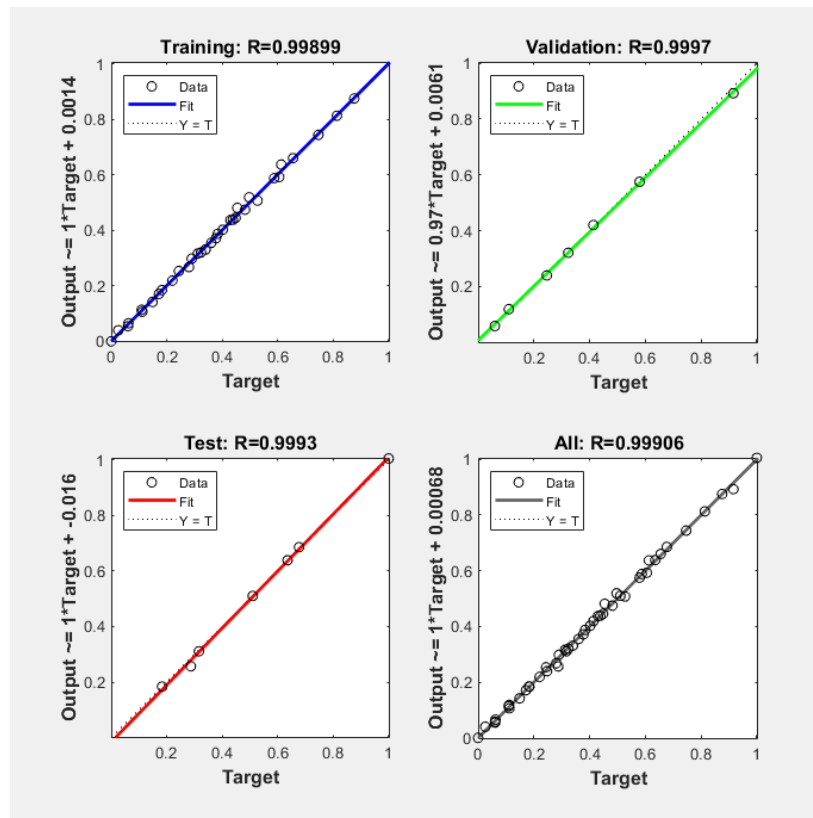
Figure 7.8 Regression plots for optimal model

Table 7.8 Validation of ANN and ANFIS models

Sl. No.	WGD (mm)	CDT (s)	WO (µm)	CSO (%)	Surface roughness (µm)				
					Predicted		Experi mental	%Error	
					ANN	ANFIS		ANN	ANFIS
0° Taper angle									
1	55	40	100	45	0.509	0.583	0.560	**9.128**	**4.073**
2	65	55	80	55	0.634	0.591	0.600	5.697	1.496
15° Taper angle									
3	90	50	75	65	0.655	0.658	0.660	**0.685**	**0.251**
4	80	70	55	95	0.761	0.697	0.710	7.233	1.841
30° Taper angle									
5	115	80	50	90	1.135	1.103	1.110	2.207	0.601
6	125	40	30	80	1.018	1.080	1.050	3.037	2.889

7.4.1.2 ANFIS mapping of response parameters
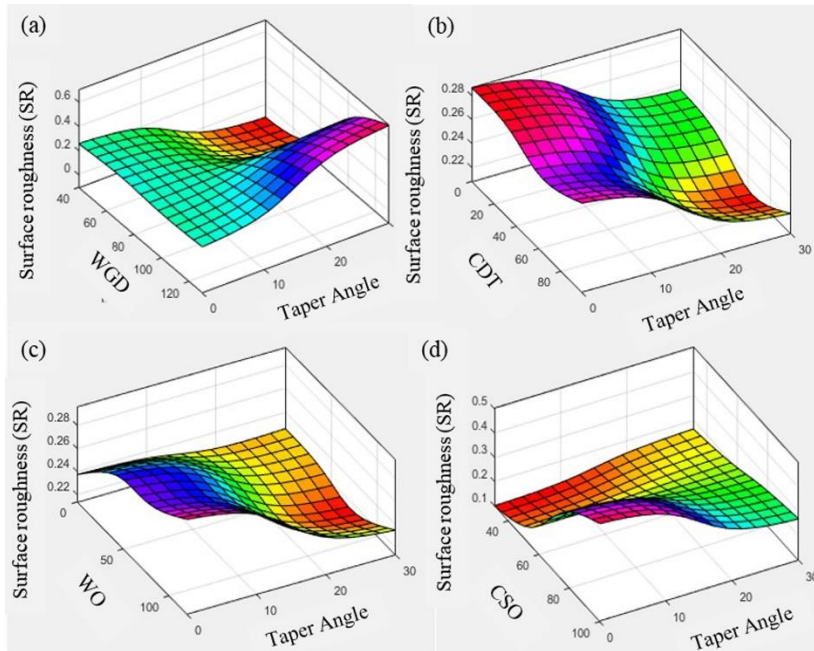
Figure 7.9 ANFIS mapping of surface roughness for triangular profile

The ANFIS provides a relationship between input and output parameters. In the present study WGD, CDT, WO, CSO and taper angle were the input parameters and surface roughness was the output parameter. Although the response plots give the variation of surface roughness the ANFIS mapping gives the 3-Dimensional graph behaviour of surface

roughness at different taper angle and for each input parameter. Fig.7.9 (a-d) shows the variation of the surface roughness for various machining parameters at different taper angle. It can be observed from the Fig. 7.9 (d) that as CSO increases cutting speed increase due to increase in discharge energy. This results in increase in the surface roughness also increases. This is similar to the results in main effect plots in chapter 5. Sharma et al. (2016) have also observed that with increase in discharge energy the surface roughness.

7.4.2 Square Profile

Table 7.9 represents the predicted experimental and error in surface roughness. It can be seen that the average percentage error of ANFIS was 0.228% that was lesser than the average percentage error of ANN being 0.739%. This indicates that ANFIS is accurate than ANN.

Table 7.9 Experimental and predicted surface roughness

Sl. No.	WGD (mm)	CDT (s)	WO (µm)	CSO (%)	Surface roughness (mm/min)				
					Predicted		Experi mental	% Error	
					ANN	ANFIS		ANN	ANFIS
0° Taper angle									
1	40	0	0	31	0.549	0.551	0.551	0.363	0.000
2	40	33	40	54	0.685	0.696	0.696	1.580	0.000
3	40	66	80	77	0.710	0.695	0.696	2.011	0.144
4	40	99	120	100	0.946	0.941	0.941	0.531	0.000
5	50	0	40	77	0.780	0.766	0.766	1.828	0.000
6	50	33	0	100	0.860	0.859	0.859	0.116	0.000
7	50	66	120	31	0.637	0.644	0.644	1.087	0.000
8	50	99	80	54	0.798	0.793	0.792	0.758	0.126
9	60	0	80	100	1.011	1.025	1.025	1.366	0.000
10	60	33	120	77	0.951	0.960	0.960	0.938	0.000
11	60	66	0	54	0.654	0.659	0.659	0.759	0.000
12	60	99	40	31	0.581	0.634	0.582	0.172	8.935
13	70	0	120	54	0.847	0.843	0.843	0.474	0.000
14	70	33	80	31	0.752	0.739	0.739	1.759	0.000
15	70	66	40	100	1.105	1.108	1.108	0.271	0.000
16	70	99	0	77	0.908	0.918	0.918	1.089	0.000
15° Taper angle									
17	75	0	0	31	0.599	0.592	0.595	0.672	0.504
18	75	33	40	54	0.698	0.689	0.689	1.306	0.000

19	75	66	80	77	0.768	0.762	0.762	0.787	0.000
20	75	99	120	100	0.984	0.984	0.984	0.000	0.000
21	85	0	40	77	0.835	0.839	0.839	0.477	0.000
22	85	33	0	100	0.902	0.906	0.906	0.442	0.000
23	85	66	120	31	0.653	0.641	0.641	1.872	0.000
24	85	99	80	54	0.813	0.823	0.823	1.215	0.000
25	95	0	80	100	1.045	1.030	1.030	1.456	0.000
26	95	33	120	77	1.000	0.996	0.996	0.402	0.000
27	95	66	0	54	0.685	0.692	0.692	1.012	0.000
28	95	99	40	31	0.590	0.592	0.592	0.338	0.000
29	105	0	120	54	0.852	0.854	0.854	0.234	0.000
30	105	33	80	31	0.729	0.730	0.730	0.137	0.000
31	105	66	40	100	1.144	1.124	1.137	0.616	1.143
32	105	99	0	77	0.926	0.919	0.919	0.762	0.000
30° Taper angle									
33	100	0	0	31	0.613	0.615	0.615	0.325	0.000
34	100	33	40	54	0.700	0.699	0.699	0.143	0.000
35	100	66	80	77	0.820	0.822	0.822	0.243	0.000
36	100	99	120	100	1.054	1.054	1.054	0.000	0.000
37	110	0	40	77	0.848	0.849	0.849	0.118	0.000
38	110	33	0	100	0.907	0.906	0.906	0.110	0.000
39	110	66	120	31	0.641	0.651	0.651	1.536	0.000
40	110	99	80	54	0.845	0.843	0.843	0.237	0.000
41	120	0	80	100	1.095	1.100	1.100	0.455	0.000
42	120	33	120	77	1.095	1.098	1.098	0.273	0.000
43	120	66	0	54	0.733	0.741	0.742	1.213	0.135
44	120	99	40	31	0.598	0.592	0.592	1.014	0.000
45	130	0	120	54	0.885	0.884	0.884	0.113	0.000
46	130	33	80	31	0.738	0.750	0.750	1.600	0.000
47	130	66	40	100	1.198	1.207	1.207	0.746	0.000
48	130	99	0	77	0.964	0.959	0.959	0.521	0.000

7.4.2.1 Validation of the optimal model

The model efficiency in case of ANN model was indicated by fig.7.10 and ANFIS model with least error was considered as optimum model for prediction. Table 7.10 shows the validation experiments and error percentage of prediction by ANN and ANFIS model. It can be seen from the table 7.10 that during ANN prediction the error percentage varies

from 0-9.20% and in the case of ANFIS the error percentage is from 0-4.67%. This shows that the ANFIS model has the least errors.
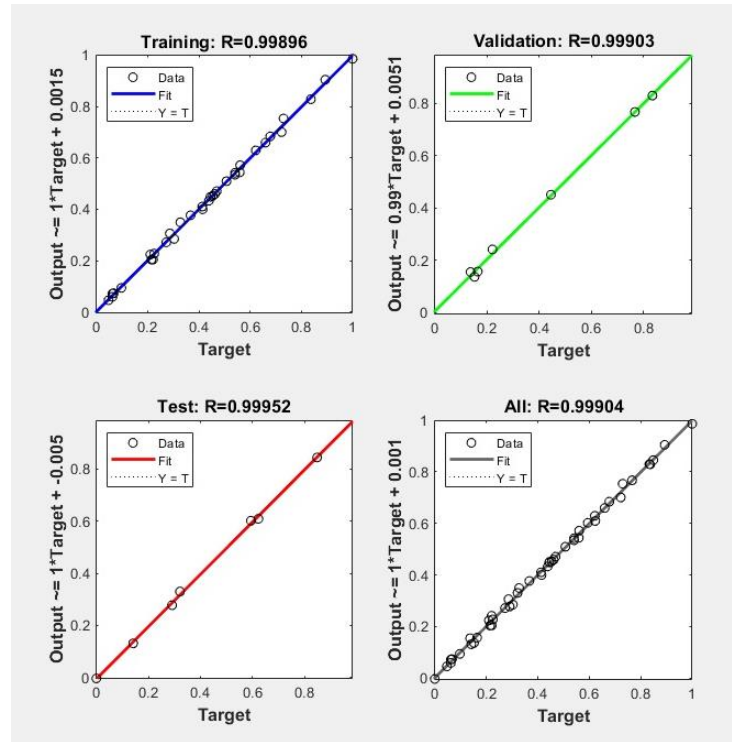
Figure 7.10 Regression plot for the optimal model

Table 7.10 Validation of ANN and ANFIS model for surface roughness

Sl. No.	WGD (mm)	CDT (s)	WO (µm)	CSO (%)	Surface roughness (µm)				
					Predicted		Experi mental	% Error	
					ANN	ANFIS		ANN	ANFIS
0° Taper angle									
1	55	40	100	45	0.753	0.722	0.690	**9.195**	**4.669**
2	65	55	80	55	0.846	0.762	0.790	7.046	3.515
15° Taper angle									
3	90	50	75	65	0.857	0.784	0.810	5.829	3.225
4	80	70	55	95	0.904	0.830	0.840	7.673	1.136
30° Taper angle									
5	115	80	50	90	1.013	1.038	1.070	5.356	2.953
6	125	40	30	80	0.959	0.988	0.990	**3.111**	**0.213**

7.4.2.2 ANFIS mapping of response parameters

The ANFIS model not only predicts the surface roughness but also gives the relationship between surface roughness and input parameters like WGD, WO, CDT, CSO and taper angles. The ANFIS mapping gives a 3-D plot where the surface roughness variation was mapped for different parameters as shown in fig.7.11 (a-d). Fig.7.11 (d) shows the effect of CSO parameters on surface roughness due to the increase in discharge energy as seen in triangular profiles.
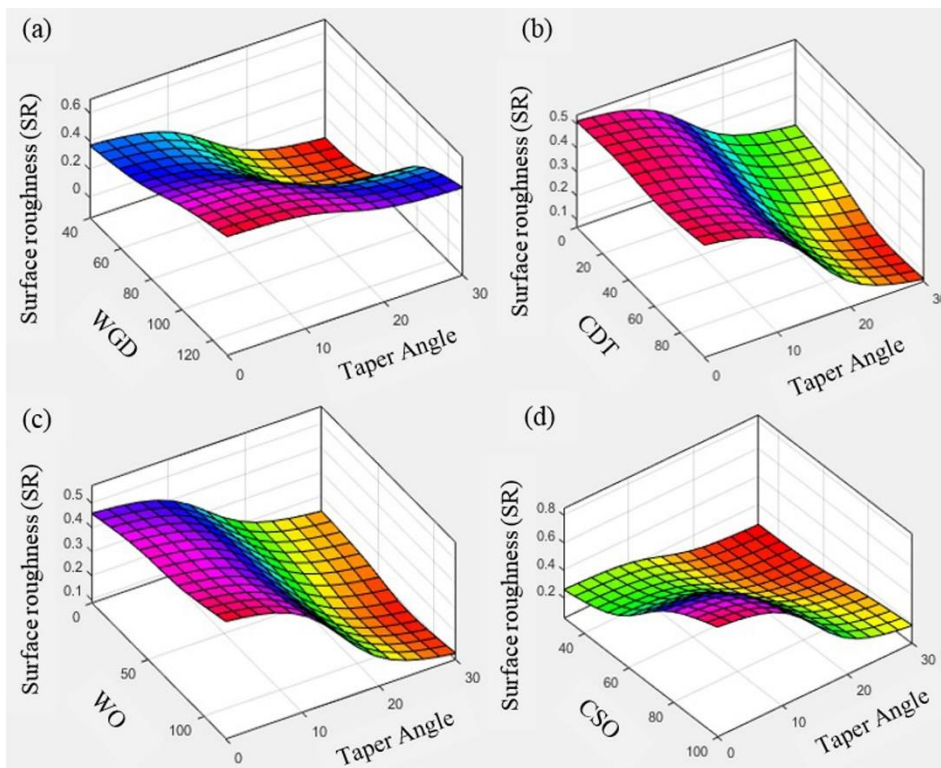
Figure 7.11 ANFIS mapping of surface roughness for square profile

7.3.3. Circular Profile

Table 7.11 represents the predicted, experimental and % error in surface roughness. It can be seen that ANFIS was more accurate than ANN as the average percentage error of ANFIS is 0.415% that was lesser than that of ANN model having 0.829%. This similar to the previous sections as triangular and square profile surface roughness.

Table 7.11 Experimental and predicted surface roughness at different taper angles

Sl. No .	WGD (mm)	CDT (s)	WO (µm)	CSO (%)	Surface Roughness (µm)				
					Predicted		Experi mental	% Error	
					ANN	ANFIS		ANN	ANFIS
0° Taper angle									
1	40	0	0	31	0.545	0.542	0.542	0.554	0.000
2	40	33	40	54	0.596	0.612	0.612	2.614	0.000
3	40	66	80	77	0.641	0.752	0.65	1.385	15.692
4	40	99	120	100	0.866	0.848	0.848	2.123	0.000
5	50	0	40	77	0.674	0.683	0.683	1.318	0.000
6	50	33	0	100	0.773	0.774	0.774	0.129	0.000
7	50	66	120	31	0.497	0.495	0.495	0.404	0.000
8	50	99	80	54	0.674	0.672	0.672	0.298	0.000
9	60	0	80	100	0.832	0.834	0.834	0.240	0.000
10	60	33	120	77	0.785	0.790	0.79	0.633	0.000
11	60	66	0	54	0.588	0.582	0.582	1.031	0.000
12	60	99	40	31	0.493	0.499	0.497	0.805	0.402
13	70	0	120	54	0.678	0.686	0.686	1.166	0.000
14	70	33	80	31	0.600	0.602	0.602	0.332	0.000
15	70	66	40	100	0.941	0.945	0.945	0.423	0.000
16	70	99	0	77	0.749	0.763	0.763	1.835	0.000
15° Taper angle									
17	75	0	0	31	0.574	0.576	0.576	0.347	0.000
18	75	33	40	54	0.618	0.617	0.617	0.162	0.000
19	75	66	80	77	0.687	0.678	0.678	1.327	0.000
20	75	99	120	100	0.873	0.871	0.871	0.230	0.000
21	85	0	40	77	0.723	0.713	0.712	1.545	0.140
22	85	33	0	100	0.804	0.805	0.805	0.124	0.000
23	85	66	120	31	0.536	0.531	0.531	0.942	0.000
24	85	99	80	54	0.713	0.719	0.719	0.834	0.000
25	95	0	80	100	0.876	0.887	0.887	1.240	0.000
26	95	33	120	77	0.860	0.851	0.851	1.058	0.000
27	95	66	0	54	0.617	0.618	0.618	0.162	0.000
28	95	99	40	31	0.522	0.522	0.522	0.000	0.000
29	105	0	120	54	0.704	0.715	0.715	1.538	0.000
30	105	33	80	31	0.621	0.622	0.622	0.161	0.000
31	105	66	40	100	0.997	0.999	1.001	0.400	0.200
32	105	99	0	77	0.784	0.782	0.783	0.128	0.128
30° Taper angle									
33	100	0	0	31	0.595	0.600	0.596	0.168	0.671

34	100	33	40	54	0.644	0.638	0.637	1.099	0.157
35	100	66	80	77	0.759	0.746	0.746	1.743	0.000
36	100	99	120	100	0.885	0.891	0.891	0.673	0.000
37	110	0	40	77	0.774	0.782	0.782	1.023	0.000
38	110	33	0	100	0.843	0.835	0.835	0.958	0.000
39	110	66	120	31	0.554	0.569	0.569	2.636	0.000
40	110	99	80	54	0.752	0.749	0.749	0.401	0.000
41	120	0	80	100	0.925	0.895	0.917	0.872	2.399
42	120	33	120	77	0.924	0.921	0.921	0.326	0.000
43	120	66	0	54	0.657	0.657	0.657	0.000	0.000
44	120	99	40	31	0.554	0.552	0.552	0.362	0.000
45	130	0	120	54	0.755	0.735	0.735	2.721	0.000
46	130	33	80	31	0.635	0.642	0.642	1.090	0.000
47	130	66	40	100	1.030	1.031	1.031	0.097	0.000
48	130	99	0	77	0.842	0.842	0.843	0.119	0.119

7.3.3.1 Validation of the optimal model
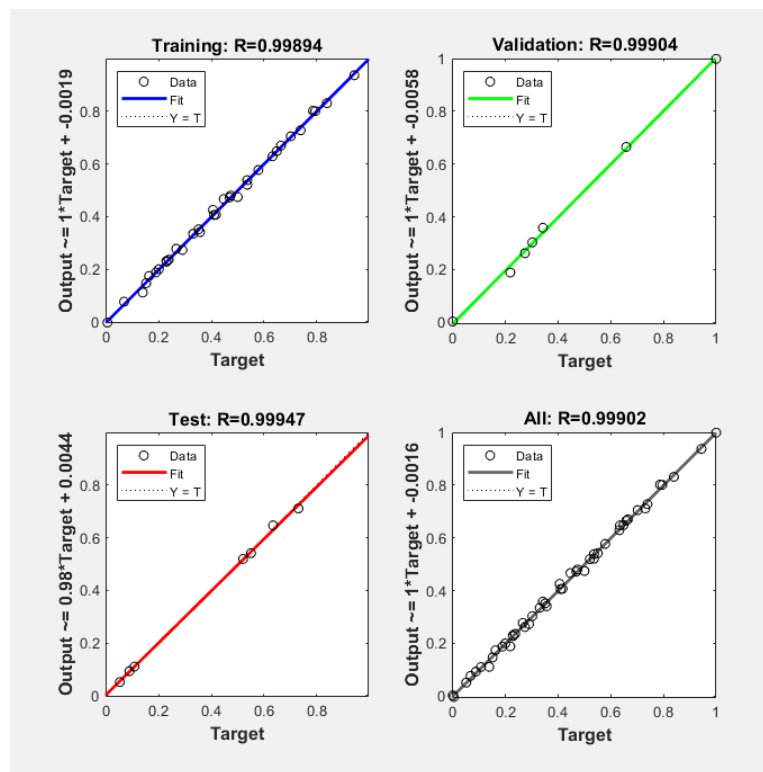
Figure 7.12 Regression plot for the optimal model

Fig. 7.12 indicates the regression model with R-value for optimized ANN model. In case of the ANFIS, models with minimum errors are considered for prediction. Table 7.12 indicates the predicted and experimental surface roughness of the circular profile. These parameters were fed to the optimal models to obtain predicted values. The parameters that were used for the prediction was validated experimentally. It can be seen that ANFIS error % varies from 0-4.1% and ANN error % varies from 0-8.9%. This indicated that the ANFIS is more reliable in prediction than ANN.

Table 7.12 Validation of ANN and ANFIS models

Sl. No.	WGD (mm)	CDT (s)	WO (μm)	CSO (%)	Surface Roughness (μm)				
					Predicted		Experi mental	% Error	
					ANN	ANFIS		ANN	ANFIS
0° Taper angle									
1	55	40	100	45	0.584	0.582	0.580	**0.714**	0.316
2	65	55	80	55	0.644	0.627	0.610	5.559	2.763
15° Taper angle									
3	90	50	75	65	0.680	0.679	0.660	3.101	2.856
4	80	70	55	95	0.806	0.739	0.740	**8.930**	**0.079**
30° Taper angle									
5	115	80	50	90	0.891	0.902	0.910	2.114	0.840
6	125	40	30	80	0.818	0.916	0.880	7.031	**4.064**

7.3.3.2 ANFIS mapping of response parameters

Fig. 7.13 (a-d) indicated the variation of surface roughness for different parameters at 0°, 15° and 30° taper angles. The ANFIS model also provides the relationship between input parameters and output parameter. Although this relationship can be seen in main effects plots the 3-Dimensional ANFIS plots provided by MATLAB show the clear variation of surface roughness (SR). Similar effects can be seen in triangular and square profiles.
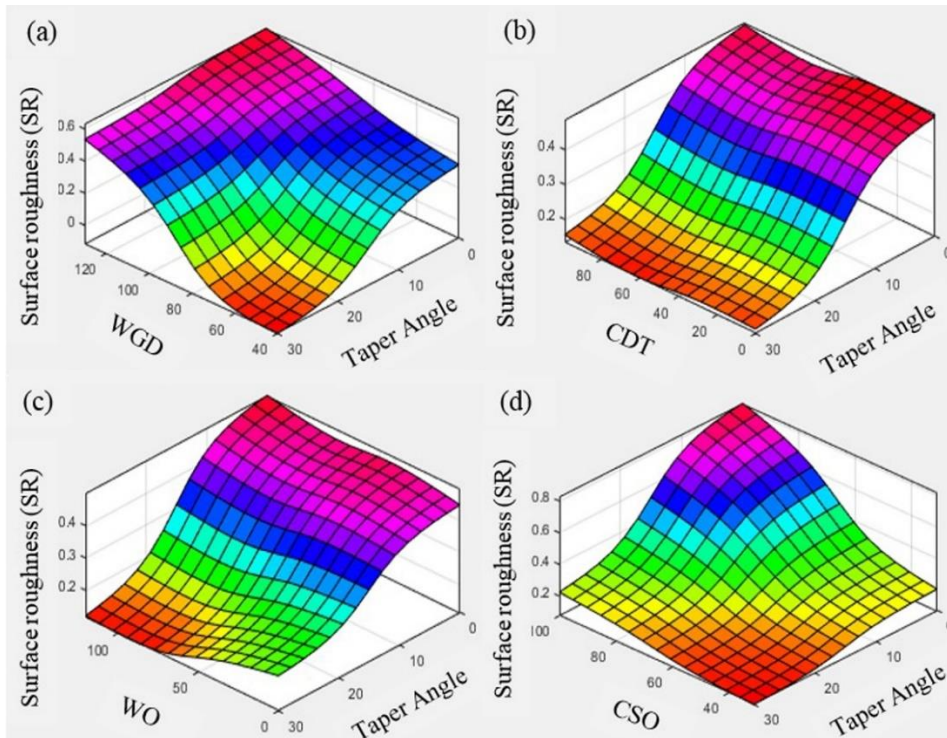
Figure 7.13 ANFIS mapping of surface roughness for circular profile

7.3 SUMMARY

The responses recorded in chapter 5 and chapter 6 were used for prediction modelling by an artificial neural network (ANN) and adaptive neural fuzzy interference system (ANFIS) tools. MATLAB software was used for modelling optimal model for responses i.e. profiling speed and surface roughness for triangular, square and circular profiles. The ANFIS model proved to be the most efficient and provided better understanding by 3-dimensional mapping of parameters. These results not only complemented the outcomes from the main effects plot but also provided clear variation for different input parameters and taper angle. These models were used to predict both profiling speed and surface roughness. Some of the important points that can be concluded are as follows

- The average errors were calculated to measure the efficiency of the ANN and ANFIS models. For prediction of profiling speed, it was calculated to be 1.312%,

0.920% and 0.890% for triangular, square and circular profiles respectively in ANN prediction models. In the case of the ANFS models, it was found to be 0.494%, 0.744% and 0.362% for triangular, square and circular profiles respectively. This shows ANFIS models is more efficient in the prediction of profiling speed as average errors are lesser than the ANN model.

- In the case of surface roughness, ANN was found to have the average error percentages of 0.874%, 0.739% and 0.829% for triangular, square and circular profiles respectively. Whereas, the ANFIS models predicted average errors of 0.369%, 0.228% and 0.415% for different triangular, square and circular profiles respectively. It was seen ANFIS models proved to have lesser errors and accurate models for prediction.

- The models were validated using experimentation where ANN models have prediction errors ranging from 0-10% whereas ANFIS models gave prediction errors ranging between 0-5%. This proves ANIFS models are more reliable and accurate compared to ANN models.

CHAPTER 8

CONCLUSION AND SCOPE FOR FUTURE WORK

8.1 CONCLUSION

The slant type taper fixture was used to machine all three profiles namely triangular, square and circular for different taper angles avoiding the bending of the wire unlike conventional taapering in WEDM. Hastelloy-X was used as the working material and it was machined for different profiles namely triangular, square and circular profiles. The input machine parameters considered for investigation were wire guide distance (WGD), corner dwell time (CDT), wire offset (WO) and cutting speed override (CSO). The output parameters such as profiling speed, surface roughness, profile areas, corner error, recast layer thickness and microhardness were examined for different taper angles. Finally, artificial neural network (ANN) and adaptive neuro-fuzzy interference system (ANFIS) for prediction of profiling speed and surface roughness for different profiles at 0°, 15° and 30° taper angles. From the above investigation, the following conclusions were drawn

1. Comparing all the profiles, the profiling speed of triangular profiles were found to be the least, followed by circular and sqaure profiles. The square profiles has the highest profiling speed. For the same parameters, there was an increase of 1.292-31.543% observed in the profiling speed due to its change in geometry from triangular to square profile due to CSO parameter. Among all the profiling parameters, the CSO parameters were the most significant with the highest contributing factor of 96.434-99.634%.The profiling speeds decreased from 40.554%-28.988% as the slant angle increased from 0° to 30°.

2. In the case of the surface roughness, the square profils have the highest surface roughness followed by circular profiles and triangular profiles. There in an increase in trinagular surface roughness by 0.316-21.252% compare to square profiles due to change in geometry. The CSO parameters were the most significant having contributing factor of 68.433-83.333%. As taper angle increases from 0° to 30° the

189

surface roughness also increased from 0-36.591% for triangular, square and circular profiles.

3. The WO and WGD were found to be the influencing factors in the case of profile areas apart from the taper angle. The WO parameter was the most influential factor having percentage contribution ranging from 59.332-74.677%. As the WO parameter increases from 0 to 120μm, the profile area escalates from 1.152 to 2.127 times. However, the effect of WGD on profile areas was found to be contrasting to the WO parameter, as WGD increased the profile area decreased from 4.541-32.358%. There was a maximum increase in the profile area ranging from 15.871-85.455% as the taper angle was increased from 0° to 30° for triangular, square and circular profiles.

4. The WGD parameter was the most influential factor with a percentage contribution of 45.914-66.385% on corner errors. As WGD increased the corner error also increase from 45.771-61.019% for triangular and square profiles. In case of WO parameter, as it increased the corner error decreased from 8.112-10.823% for triangular and increased from 29.122-39.845% in square profiles. This effect of the WO parameter influenced adversly to the corners of square profiles than corners triangular profiles due to the corner geometry. As the taper angle increased from 0° to 30°, the corner error also increased from 24.441-40.810% for both triangular and square profiles.

5. After profiling, the recast layer thickness was recorded for the highest and lowest cutting speed parameters. The highest recast layer thickness for the square profile was 16.150μm and 12.243 μm and the lowest recast layer thickness was 10.953 μm and 15.450μm found in the triangular profile at the highest and lowest cutting speed parameters respectively for 0° taper angle. As there is larger cutting area was exposed to heat at higher angles, the recast layer thickness decreases from 44.370-62.047% as the taper angle increased from 0° to 30° for triangular, square and circular profiles.

6. The micro-hardness of the machined surface was observed for the highest and lowest cutting speed parameters for all the three profiles. It was noticed that the lowest micro-hardness was observed in triangular profiles having 176Hv at 0° and square profiles having 189Hv at 30°. This was observed because at 0° the cutting surface area exposed to heat was lower. This increased heat effected zone which inturn lead to lower microhardness. As the taper angle increased from 0° to 30° the micro-hardness also increased from 4.545-5.749% in different profiles.

7. ANN and ANFIS were used in the prediction of profiling speed and surface roughness. The average percentage error of ANN ranged up to 0.920%-1.312% and 0.736%-0.874%, whereas the ANFIS model exhibited an average percentage error of 0.362%-0.494% and 0.228%-0.415% in the prediction of profiling speed and surface roughness respectively. It can be observed that the average percentage error of ANN models were approximately twice much as the ANFIS model irrespective of profile geometry. In the case of experimental validation, the ANFIS model showed errors ranging from 0-5% whereas the ANN model prediction errors ranged up to 0-10%. This proves ANFIS models were more accurate in prediction than ANN models.

8.2 SCOPE FOR FUTURE WORK

Hastelloy-X was machined using a slant type taper fixture for different profiles at 0°, 15° and 30° taper angles in the present study. Several areas are more fascinating for future studies and this will definitely help researchers to better understanding with in turn will help industry at large.

- As the present work only focuses on tapering and taper profiling, a better tapering system could be designed that enables to get circular tapered components (cone-shaped) avoiding bending of wire as in conventional tapering. So that parametric investigation of circular tapered components can be carried out in detail.

- The comparison of slant type tapering and conventional tapering can be further studied with respect to various input and output parameters for different tapering angles.

- In the current work, the tool wear was not considered for the study. So tool wear at different taper angles is another phenomenon that can be taken into consideration for further studies during taper machining in WEDM.

- From the present investigation, it was found tapering profiling parameters like wire guide distance (WGD), corner dwell time (CDT), wire offset (WO) and cutting speed override (CSO) also affects profile areas of different shapes. This study can be extended to geometrical features like circularity, cylindricity etc. at different taper angles can be still further explored with the aid of CMM.

- In the current work, we have observed that as the taper angle increase the wire vibration also increases. By adopting a high-speed camera and laser sensor the vibration of the wire and its effect at different wire guide distances on machining can be still explored. The effect of vibration on different geometrical features can be examined.

- With the recent boom in data science, different prediction models like servo vector mechanism, genetic algorithm, ANFIS with genetic algorithm can be utilized for accurate prediction of profiling speed, surface roughness, profile areas and many output parameters. From the industrial point of view by accurate prediction models, an optimal machining parameter and offset values for tolerances can be determined before machining the component, thus reducing the manufacturing cost.

REFERENCES

Abhilash P.M., and Chakradhar D. (2020). "ANFIS modelling of mean gap voltage variation to predict wire breakages during wire EDM of Inconel 718" *CIRP J. Manuf. Sci. Technol.*, 31, 153-164.

Abyar, H., Abdullah, A. and Akbarzadeh, A. (2019). "Prediction Algorithm for WEDM Arced Path Errors Based on Spark Variable Gap and Non uniform Spark Distribution Models." *J. Manuf. Sci. Eng.*, 141, 1-11.

Abyar, H., Abdullah, A., and Shafaroud, A.A. (2019). "Theoretical and experimental analysis of machining errors on small arced corners during WEDM finishing stages." *Mach. Sci. Technol.*, 23(5), 734-757, DOI: 10.1080/10910344.2019.1575410.

Ahmad, B., and Fitzpatrick, M.E. (2016). "Minimization and Mitigation of Wire EDM Cutting Errors in the Application of the Contour Method of Residual Stress Measurement." *Metall. Mater. Trans. A*, 47, 301–313. https://doi.org/10.1007/s11661-015-3231-7.

Ajay, B.T., Vitthal, P.M., and Rajyalakshmi, G. (2017). "WEDM machining on Aerospace Materials for improving Material Properties." *Mater. Today: Proc.*, 4 (8), 9107-9116.

Akhtar, W., Sun, J., Sun, P., Chen, W., and Saleem, Z. (2014). "Tool wear mechanisms in the machining of Nickel based super-alloys: A review." *Front. Mech. Eng.*, 9(2), 106-119.

Aldas, K., Ozkul, I., and Akkurt, A. (2014). "Modelling Surface Roughness in WEDM Process Using ANFIS Method." *J. Balk. Tribol. Assoc.*, 20(4), 548–558.

Ali, M.Y., Banu, A., and Al Hazza, M.H. (2020). "Analysis of kerf accuracy in dry micro-wire EDM." *Int. J. Adv. Manuf. Technol.*, 111, 597–608.

Ali, M.Y., Mustafizul Karim, A. N., Erry Yulian, Adesta, T., Ismail, A.F., Abdullah, A.A. and Idris, M.N. (2010). "Comparative study of conventional and micro WEDM based on machining of meso/micro Sized Spur Gear." *Int. J. Precis. Eng. Manuf.*, 11, 779–784.

Alshemary, A., Pramanik, A., Basak, A.K., and Littlefair, G. (2018). "Accuracy of duplex stainless steel feature generated by electrical discharge machining." *Meas.: J. Int. Meas. Confed.*, 130, 137–144.

Antar, M. T., Soo, S. L., Aspinwall, D. K., Jones, D., and Perez, R. (2011). "Productivity and workpiece surface integrity when WEDM aerospace alloys using coated wires," *Procedia Eng.*, 19, 3–8.

Antar, M.T., Soo, S.L., Aspinwall, D.K., Sage, C., Cuttell, M., Perez, R., and Winne, A.J. (2012). "Fatigue response of Udimet 720 following minimum damage wire electrical discharge machining." *Mater. Des.* , 42, 295-300.

Antar, M.T., Soo, S.L., Aspinwall, D.K., Sage, C., Cuttell, M., Perezd, R. and Winne, A.J. (2012). "Fatigue response of Udimet 720 following minimum damage wire electrical discharge machining." *Mater. Des.* , 42, 295–300.

Arun Kumar, N. E., and Suresh Babu, A. (2018). "Influence of input parameters on the near-dry WEDM of Monel alloy." *Mater. Manuf. Process.*, 33 (1), 85-92.

Aspinwall, D.K., Soo, S.L., Berrisford, A.E., and Walder, G. (2008). "Workpiece surface roughness and integrity after WEDM of Ti–6Al–4V and Inconel 718 using minimum damage generator technology." *CIRP Ann. Manuf. Technol.*, 57, 187–190.
Axinte, D., and Chiffre, D.L. (2008). "Effectiveness and resolution of tests for evaluating the performance of cutting fluids in machining aerospace alloys." *Cirp Ann.-Manuf. Techn.*, 57(1), 129–132.

Ayesta, I., Izquierdo, B., Flaño, O., Sánchez, J. A., Albizuri, J. and Avilés, R. (2016). "Influence of the WEDM process on the fatigue behavior of Inconel® 718," *Int. J. Fatigue*, 92, 220–233.

Ayesta, I., Izquierdo, B., Flaño, O., Sánchez, J.A., Albizuri, J., and Avilés, R. (2016). "Influence of the WEDM process on the fatigue behavior of Inconel® 718." *Int. J. Fatigue*, 92, 220–233.

Azam, M., Jahanzaib, M., Abbasi, J.A. and Wasim, A. (2016). "Modeling of cutting speed (CS) for HSLA steel in wire electrical discharge machining (WEDM) using moly wire." *J. Chin. Inst. Eng.*, 39(7), 802-808, DOI:10.1080/02533839.2016.1191377.

Azam, M., Jahanzaib, M., Abbasi, J.A., and Wasim A. (2016). "Modeling of cutting speed (CS) for HSLA steel in wire electrical discharge machining (WEDM) using moly wire" *J. Chin. Inst. Eng.*, 39(7), 802-808.

Azam, M., Jahanzaib, M., Abbasi, J.A., and Wasim, A. (2016). "Modeling of cutting speed (CS) for HSLA steel in wire electrical discharge machining (WEDM) using moly wire." *J. Chin. Inst. Eng.*, 39(7), 802-808, DOI:10.1080/02533839.2016.1191377.

Azhiri, R.B., Teimouri, R., Baboly, M.G., and Leseman, Z., (2014). "Application of Taguchi, ANFIS and grey relational analysis for studying, modeling and optimization of wire EDM process while using gaseous media." *Int. J. Adv. Manuf. Technol.*, 71, 279–295. https://doi.org/10.1007/s00170-013-5467-y.

Baburaja, K., Subbaiah, K. V., Vanaja, T., and Ramesh, N. N. (2017). "Resultant Surface Roughness Aluminium and Hastelloy C-276 Using Wire Electro Discharge Machining." *Mater. Today Proc.*, 4, (2), 1013–1018.

Banerjee, S., and Prasad, B. V. S. S. S. (2010). "Numerical evaluation of transient thermal loads on a WEDM wire electrode under spatially random multiple discharge conditions with and without clustering of sparks." *Int. J. Adv. Manuf. Technol.*, 48 (5–8), 571–580.

Beltrami, I., Bertholds, A., and Dauw, D. (1996). "A simplified post process for wire cut EDM." *J. Mater. Process. Technol.*, 58(4), 385–389. doi: 10.1016/0924-0136(95)02212-0.

Beri, N., Maheshwari, S., Sharma, C., and Kumar, A. (2010). "Technological Advancement in Electrical Discharge Machining with Powder Metallurgy Processed Electrodes: A Review." *Mat. Manuf. Process.*, 25(10), 1186-1197, DOI:10.1080/10426914.2010.512647.

Benjamin, J.S. (1970). "Dispersion strengthened super alloys by mechanical alloying." *Metall. Mater. Trans.*, 1(10), 2943–2951.

Bisaria, H., and Shandilya, P. (2019). "Processing of curved profiles on Ni-rich nickel–titanium shape memory alloy by WEDM." *Mater. Manuf. Process.*, 34(12), 1333-1341, DOI: 10.1080/10426914.2019.1594264.

Bochenek, K., and Basista, M. (2015). "Advances in processing of NiAl intermetallic alloys and composites for high temperature aerospace applications." *Prog. Aerosp. Sci.*, 79,136-146.

Bose, S., and Nandi, T. (2021). "Measurement of performance parameters and improvement in optimized solution of WEDM on a novel titanium hybrid composite." *Meas.: J. Int. Meas. Confed.*, 171, 108811.

Caiazzo, F., Cuccaro, L., Fierro, I., Petrone, G., and Alfieri, V. (2015). "Electrical Discharge Machining of René 108 DS Nickel Superalloy for Aerospace Turbine Blades", *Procedia CIRP*, 33, 382-387.

Cárach, J., Hloch, S., Hlaváček, P., Ščučka, J., Martinec, P., Petrů, J., Zlámal, T., Zeleňák, M., Monka, P., Lehocká, D., Krolczyk, J. (2016). "Tangential turning of Incoloy alloy 925 using abrasive water jet technology." *Int. J. Adv. Manuf. Technol.*, 82(9–12), 1747–1752.

Çaydaş, U., Hasçalık, A., and Ekici S. (2009). "An adaptive neuro-fuzzy inference system (ANFIS) model for wire-EDM." *Expert Syst. Appl.*, 36, 6135-6139.

Çaydaş, U., Hasçalik, A., and Ekici, S. (2009). "An adaptive neuro-fuzzy inference system (ANFIS) model for wire-EDM." *Expert Syst. Appl.*, 36 (3:2), 6135–6139.

Chalisgaonkar, R., and Kumar, J. (2015). "Multi-response optimization and modeling of trim cut WEDM operation of commercially pure titanium (CPTi) considering multiple user's preferences." *Int. J. Eng. Sci. Technol.*, 18(2), 125-134.

Chang, L., Chengzu, R., Guofeng, W., Yinwei, Y., and Lu, Z. (2015). "Study on surface defects in milling Inconel 718 super alloy." *J. Mech. Sci. Technol.*, 29(4), 1723–1730.

Chaudhari, R., Vora, J., Parikh, D. M., Wankhede, V., and Khanna, S. (2020). "Multi-response Optimization of WEDM Parameters Using an Integrated Approach of RSM–GRA Analysis for Pure Titanium." *J. Inst. Eng. India Ser. D*, 101, 117–126 (2020).

Chaudhary, T., Siddiquee, A.N., and Chanda, A.K. (2019). "Effect of wire tension on different output responses during wire electric discharge machining on AISI 304 stainless steel." *Def. Technol.*, 15, 541-544.

Chaudhary, T., Siddiquee, A.N., Chanda, A.K. (2019). "Effect of wire tension on different output responses during wire electric discharge machining on AISI 304 stainless steel." *Def. Technol.*, 15(4), 541-544, https://doi.org/10.1016/j.dt.2018.11.003.

Chen, Z., and Zhang G. (2018). "Study on magnetic field distribution and electro-magnetic deformation in wire electrical discharge machining sharp corner workpiece." *Int. J. Adv. Manuf. Technol.*, 98, 1913–1923.

Chen, Z., Huang, Y, Zhang, Z., Li, H., Ming, W., and Zhang, G. (2014). "An analysis and optimization of the geometrical inaccuracy in WEDM rough corner cutting", *Int. J. Adv. Manuf. Technol.*, 74, 917–929. doi: 10.1007/s00170-014-6002-5.

Chen, Z., Zhang, G., and Yan, H. A., (2018) "High-precision constant wire tension control system for improving workpiece surface quality and geometric accuracy in WEDM." *Precis. Eng.*, 54, 51–59.

Chen, Z., Zhang, G., Han, F., Zhang, Y., and Rong, Y. (2018). "Determination of the optimal servo feed speed by thermal model during multi-pulse discharge process of WEDM." *Int. J. Mech. Sci.*, 142-143, 359-369.

Chen, Z., Zhang, Y., Zhang, G., and Li, W (2018). "Modeling and reducing workpiece corner error due to wire deflection in WEDM rough corner-cutting." *J. Manuf. Process.*, 36, 557-564.

Chopra, K., Payla, A., and Mussada, E.K. (2019). "Detailed Experimental Investigations on Machinability of EN31 Steel by WEDM." *Trans. Indian. Inst. Met.*, 72, 919–927.
Choudhury, I.A. and El-Baradie, M.A. (1998). "Machinability of nickel-base super alloys: a general review." *J. Mater. Process. Technol.*, 77, 278–284.

Conde, A., Arriandiaga, A., Sanchez, J.A., Portillo, E., Plaza, S., and Cabanes, I. (2018). "High-accuracy wire electrical discharge machining using artificial neural networks and optimization techniques." *Robot. Comput. Integr. Manuf.*, 49, 24–38. doi: 10.1016/j.rcim.2017.05.010.

Conde, A., Sanchez, J. A., Plaza, S., and Ramos, J. M. (2016). "On the influence of wire-lag on the WEDM of low-radius free-form geometries." *Procedia CIRP*, 42 (17), 274–279.

Das, S., and Joshi, S.N. (2020). "Estimation of wire strength based on residual stresses induced during wire electric discharge machining." *J. Manuf. Process.*, 53, 406-419, ISSN 1526-6125.

Deka, S., Kar, S., and Patowari, P.K. (2020). "Machinability of Silicon and German Silver in Micro Electrical Discharge Machining: a Comparative Study." *Silicon*. https://doi.org/10.1007/s12633-020-00496-0.

Devarasiddappa, D., George, J., Chandrasekaran, M. and Teyi, N., (2016). "Application of Artificial Intelligence Approach in Modeling Surface Quality of Aerospace Alloys in WEDM Process." *Procedia Tech.*,1199–1208. doi: 10.1016/j.protcy.2016.08.239.

Dodun, O., Gonçalves-Coelho, A. M., Slătineanu, L., and Nagîţ, G. (2009). "Using wire electrical discharge machining for improved corner cutting accuracy of thin parts." *Int. J. Adv. Manuf. Technol.*, 858–864. doi: 10.1007/s00170-008-1531-4.

Ezilarasan, C., Senthil kumar, V.S., and Velayudham, A. (2013). "An experimental analysis and measurement of process performances in machining of Nimonic C-263 super alloy." *Meas.: J. Int. Meas. Confed.*, 46, 185–199.

Ezugwu, E.O. (2005). "Key improvements in the machining of difficult-to-cut aerospace superalloys." *Int. J. Mach. Tools Manuf.*, 45(12–13), 1353-1367, ISSN 0890-6955.

Ezugwu, E.O., Wang, Z.M., and Machado, A.R. (1999). "The machinability of nickel-based alloys: a review", *J. Mater. Process. Technol.*, 86, 1–16.

Fard, R.K., Afza, R.A., and Teimouri, R. (2013). "Experimental investigation, intelligent modeling and multi-characteristics optimization of dry WEDM process of Al–SiC metal matrix composite." *J. Manuf. Process.*, 15(4), 2013, 483-494.

Farooq, M.U., Ali, M.A., He, Y., Khan, A.M., Pruncu, C.I., Kashif, M., Ahmed, N., and Asif, N. (2020). "Curved profiles machining of Ti6Al4V alloy through WEDM: investigations on geometrical errors." *J. Mater. Res. Technol.*, 9(6), 16186-16201.

Firouzabadi, H. A. and Parvizian, J. (2015). "Improving accuracy of curved corners in wire EDM successive cutting." *Int. J. Adv. Manuf. Technol.*, 76, 447–459. doi: 10.1007/s00170-014-6270-0.

Garg, S. K., Manna, A., and Jain, A. (2016). "Experimental investigation of spark gap and material removal rate of Al/ZrO2 (P)-MMC machined with wire EDM." *J. Bra. Soc. Mech. Sci. Eng.*, 38(2), 481–491.

Garg, S. K., Manna, A., Jain, A. (2016). "Experimental investigation of spark gap and material removal rate of Al/ZrO2(P)-MMC machined with wire EDM." *J. Brazilian Soc. Mech. Sci. Eng.*, 38(2), 481–491.

Genna, S., Leone, C., Palumbo, B., and Tagliaferri, F. (2015). "Statistical Approach to Fiber Laser Microcutting of NIMONIC® C263 Superalloy Sheet Used in Effusion Cooling System of Aero Engines." *Procedia CIRP*, 33, 520-525.

Ghodsiyeh, D., Golshan, A., and Izman, S. (2014). "Multi-objective process optimization of wire electrical discharge machining based on response surface methodology." *J. Braz. Soc. Mech. Sci.*, 36, 301–313. doi: 10.1007/s40430-013-0079-x.

Ghosh, G., Mandal, P., and Mondal, S.C. (2019). "Modeling and optimization of surface rough." *Int. J. Mach. Tools Manuf.*, 100, 1223–1242.

Glenna, S., Leone, C., Palumbo, B., Tagliaferri, F. (2015). "Statistical Approach to Fiber Laser Microcutting of NIMONIC® C263 Superalloy Sheet Used in Effusion Cooling System of Aero Engines." *Procedia CIRP*, 33, 520-525.

Gong, Y.D., Sun, Y., and Wen, X.L. (2016). "Experimental study on accuracy and surface quality of TC2 in LS-WEDM multiple cuts." *J. Braz. Soc. Mech. Sci. Eng.*, 38(8), 2421-2433.

Goswami, A., and Kumar, J. (2014). "Optimization in wire-cut EDM of Nimonic-80A using Taguchi's approach and utility concept." *Eng. Sci. Technol. an Int. J.*, 17(4), 236–246.

Gowthaman, P.S., and Jeyakumar, S. (2019). "A Review on machining of High Temperature Aeronautics Super-alloys using WEDM." *Mater. Today: Proc.*, 18 (7), 2019, 4782-4791, ISSN 2214-7853.

Griffiths, M. (2019). "Ni-Based Alloys for Reactor Internals and Steam Generator Applications." Structural Alloys for Nuclear Energy Applications, 349-409, ISBN 9780123970466. https://doi.org/10.1016/B978-0-12-397046-6.00009-5.

Gupta, K., and Jain, N.K. (2013). "On Micro-Geometry of Miniature Gears Manufactured by Wire Electrical Discharge Machining", *Mat. Manuf. Process.*, 28(10), 1153-1159.

Habib, S. (2017). "Optimization of machining parameters and wire vibration in wire electrical discharge machining processes." *Mech. Adv. Mater. Mod. Process*, 3(1), 1–9. doi: 10.1186/s40759-017-0017-1.

Habib, S., and Okada, A. (2016). "Experimental investigation on wire vibration during fine wire electrical discharge machining process." *Int. J. Adv. Manuf. Technol.*, 84, 2265–2276. Han, F., Zhang, J. and Soichiro, I. (2007). "Corner error simulation of rough cutting in wire EDM", *Precis. Eng.*, 31(4), 331–336. doi: 10.1016/j.precisioneng.2007.01.005.

Hasçalýk∗, A., Çaydas, U., (2004). "Experimental study of wire electrical discharge machining of AISI D5 tool steel." *J. Mater. Process. Technol.*, 148, 362–367.

Hatami, S., Shahabi-Navid, M., and Nyborg, L. (2012). "Surface Preparation of Powder Metallurgical Tool Steels by Means of Wire Electrical Discharge Machining." *Metall. Mater. Trans. A*, 43, 3215–3226.

Haynes International, URL:http://www.haynesintl.com/company-information/our-heritage/elwood-haynes (April 6, 2021)

He, W., He, S., Du, J., Ming,W., Ma,J., Cao,Y., and Li,X., (2019). "Fiber orientations effect on process performance for wire cut electrical discharge machining (WEDM) of 2D C/SiC composite." *Int. J. Adv. Manuf. Technol.*, 102, 507–518.
Heilmaier, M., Krüger, M., Saage, H., Rösler, J., Mukherji, D., Glatzel, U., Völkl, R., Hüttner, R., Eggeler, G., Somsen, Ch., Depka, T., Christ, H. -J., Gorr, B., and Burk, S. (2009). "Metallic materials for structural applications beyond nickel-based superalloys." *JOM* , 61, 61–67 https://doi.org/10.1007/s11837-009-0106-7.

Hewidy, M.S., El-Taweel, T.A., and El-Safty, M. F. (2005). "Modelling the machining parameters of wire electrical discharge machining of Inconel 601 using RSM." *J. Mater. Process. Technol.*, 169(2), 328–336.

Hood, R., Soo, S.L., Aspinwall, D.K., Andrews, P., and Sage, C. (2012). "Radius end milling of Haynes 282 nickel based superalloy" *Proc. IMechE. B J. Eng. Manuf.*, 226 (10), 1745–1753.

Hsieh, S. F., Chen, S. L., Lin, H. C., Lin, M. H., and Chiou, S. Y. (2009). "The machining characteristics and shape recovery ability of Ti–Ni–X (X= Zr, Cr) ternary shape memory alloys using the wire electro-discharge machining." *Int. J. Mach. Tool. Manu.* , 49(6), 509–514.

Hsue, A. W. J., Yan, M. T. and Ke, S. H. (2007). "Comparison on linear synchronous motors and conventional rotary motors driven Wire-EDM processes." *J. Mater. Process. Technol.*, 192–193, 478–485. doi: 10.1016/j.jmatprotec.2007.04.046.

Hsue, A.W., and Su, H. (2004). "Removal analysis of WEDM's tapering process and its application to generation of precise conjugate surface." *J. Mater. Process. Technol.*, 149(1–3), 117-123.

Huang J.T., Liao Y.S., and Hsue W.J. (1999). "Determination of finish-cutting operation number and machining-parameters setting in wire electrical discharge machining" *J. Mater. Process. Technol.*, 87 (1–3), 69-81.

Ishfaq, K., Ahmad, N., Jawad, M., Ali, M.A., M. Al-Ahmari A. (2019). "Evaluating Material's Interaction in Wire Electrical Discharge Machining of Stainless Steel (304) for Simultaneous Optimization of Conflicting Responses." *Materials*, 12(12):1940. https://doi.org/10.3390/ma12121940.

Ishfaq, K., Ahmed, N., Rehman, A.U., and Umer, U., (2020). "WEDM of AA6061: an insight investigation of axial and lateral dimensional errors." *Mater. Manuf. Process.*, 35(7), 762-774. DOI: 10.1080/10426914.2020.1740251.

Ishfaq, K., Mufti, N.A., Mughal, M.P., Saleem, M.Q., and Ahmed, N. (2018). "Investigation of wire electric discharge machining of stainless-clad steel for optimization of cutting speed." *Int. J. Adv. Manuf. Technol.*, 96, 1429-1443.

Jadam, T., Datta, S., and Masanta, M. (2019). "Study of surface integrity and machining performance during main/rough cut and trim/finish cut mode of WEDM on Ti–6Al–4V: effects of wire material." *J. Braz. Soc. Mech. Sci. Eng.*, 41, 151 https://doi.org/10.1007/s40430-019-1656-4.

Jafari, R., Kahya, M., Oliaei, S. N. B., Ünver, H. Ö. and Özyurt, T. O. (2017). "Modeling and analysis of surface roughness of microchannels produced by μ-WEDM using an ANN and Taguchi method." *J. Mech. Sci. Technol.*, 31(11), 5447–5457.

Joseph D. R. (2000). "Nickel Cobalt and their alloys." ASM International, ISBN: 978-0-87170-685-0, 1-442.

Jothimurugan, R., and Amirthagadeswaran, K. S. (2016). "Performance of Additive Mixed Kerosene–Servotherm in Electrical Discharge Machining of Monel 400™." *Mater. Manuf. Process.*, 31, 432-438.

Kale, A., Khanna, N. A. (2017). "Review on Cryogenic Machining of Super Alloys Used in Aerospace Industry." *Procedia Manuf.*, 7, 2017, 191-197.

Kalpakjian, Serope, "Manufacturing engineering and technology." 3rd Edition, 1995.

Kanlayasiri, K., and Boonmung, S., (2007). "An investigation on effects of wire-EDM machining parameters on surface roughness of newly developed DC53 die steel." *Int. J. Mach. Tools Manuf.*, 187–188, 26–29.

Kanlayasiri, K., and Jattakul, P. (2013). "Simultaneous optimization of dimensional accuracy and surface roughness for finishing cut of wire-EDMed K460 tool steel." *Precis. Eng.*, 37(3), 556–561.

Kara, F., Aslantas, K., and Çiçek, A. (2016). "Prediction of Cutting Temperature in Orthogonal Machining Of Aisi 316l Using Artificial Neural Network." *Applied Soft Computing*, 38, 64–74.

Kinoshita, N., Fukui, M., and Kimura, T. (1984). "Study on the wire-EDM: in process measurement of mechanical behaviour of electrode wire." *Annls CIRP*, 33, 89–92.

Klocke, F., Vogtel, P., Gierlings, S., Lung, D., and Veselovac, D. (2013). "Broaching of Inconel 718 with cemented carbide." *Prod. Eng.*, 7, 593–600.

Klocke, F., Zeis, M., Klink, A., and Veselovac, D. (2013). "Experimental research on the electrochemical machining of modern titanium- and nickel-based alloys for aero engine components." *Procedia CIRP*, 6, 368 – 372.

Krishnan, S.A., and Samuel, G.L. (2013). "Multi-objective optimization of material removal rate and surface roughness in wire electrical discharge turning." *Int. J. Adv. Manuf. Technol.*, 67, 2021–2032. https://doi.org/10.1007/s00170-012-4628-8

Kumanan, S. and Nair, A. (2017). "Prediction of multi performance characteristics of wire EDM process using grey ANFIS." *IOP Conf. Ser.: Mater. Sci. Eng.*, 244, 012003, 1-9.

Kumar A., Kumar V., and Kumar J. (2015) Semi-empirical model on MRR and overcut in WEDM process of pure titanium using multi-objective desirability approach. *J. Braz. Soc. Mech. Sci. Eng.*, 37, 689–721.

Kumar, A., Kumar, V., Kumar, J. (2016). "Surface crack density and recast layer thickness analysis in WEDM process through response surface methodology." *Mach. Sci. Technol.*, 20, 201-230.

Kumar, S., Grover, S., and Walia, R.S. (2018). "Effect of hybrid wire EDM conditions on generation of residual stresses in machining of HCHCr D2 tool steel under ultrasonic vibration." *Int. J. Interact. Des. Manuf.*, 12, 1119–1137. https://doi.org/10.1007/s12008-018-0474-8.

Kumar, V., Jangra, K.K., Kumar, V., and Sharma, N. (2017). "WEDM of nickel based aerospace alloy: optimization of process parameters and modelling." *Int. J. Interact. Des. Manuf.*, 11, 917–929.

Kumar, V., Kumar, V., and Jangra, K.K. (2015). "An experimental analysis and optimization of machining rate and surface characteristics in WEDM of Monel-400 using RSM and desirability approach." *J. Ind. Eng. Int.*, 11, 297 –307.

Kus, A., and Motorcu, A.R. (2017). "Estimation of the optimum cutting parameters for surface roughness in wire electrical discharge machining of nickel based waspaloy using Taguchi method." *J. Fac. Eng. Archit. Gaz.*, 32 (1), 195-204.

Li, L., Wei, X. T., and Li, Y. (2014). "Surface integrity evolution and machining efficiency analysis of W-EDM of nickel-based alloy." *Appl. Surf. Sci.*, 313, 138–143.

Lin, C. T., Chung, I. F., and Huang, S. Y. (2001). "Improvement of machining accuracy by fuzzy logic at corner parts for wire-EDM." *Fuzzy Sets Syst.*, 122(3), 499–511. doi: 10.1016/S0165-0114(00)00034-8.

Lin, P.D., and Liao, T.T., (2009). "An effective-wire-radius compensation scheme for enhancing the precision of wire-cut electrical discharge machines." *Int. J. Adv. Manuf. Technol.*, 40, 324–331.

Liu, J. F., and Guo, Y. B. (2015). "Process Capability of Wire-EDM of NiTi Shape Memory Alloy at Main Cut and Trim Cut Modes." *Procedia Manuf.*, 1, 904–914.

Lynch, M.E., Williams, K., Cabrera, M., and Beccuti, T. (2021). "Surface finishing of additively manufactured IN718 lattices by electrochemical machining." *Int. J. Adv. Manuf. Technol.*, 113, 967–984.

Maher, I., Hui Ling, L., Sarhan, A. A. D., and Hamdi, M. (2015). "Improve wire EDM performance at different machining parameters - ANFIS modeling." *IFAC-PapersOnLine*, 28(1), 105–110.

Maher, I., Sarhan, A.A.D., Barzani, M.M., and Hamdi, M. (2015). "Increasing the productivity of the wire-cut electrical discharge machine associated with sustainable production." *J. Clean. Prod.*, 108, 247-255.

Maher, I., Sarhan, A.A.D., Marashi, H., Barzani, M.M., and Hamdi, M. (2016). "White layer thickness prediction in wire-EDM using CuZn-coated wire electrode − ANFIS modelling." *Trans. IMF.* 2016, 94, 204-210.

Maher, I., Sarhan, A.A.D., Marashi, H., Barzani, M.M., and Hamdi, M. (2016). "White layer thickness prediction in wire-EDM using Cu Zn-coated wire electrode − ANFIS modelling." *Trans. Inst. Met. Finish.* , 94, 204-210.

Majumder, H., Paul, T. R., Dey, V., Dutta, P. and Saha, A. (2017). "Use of PCA-grey analysis and RSM to model cutting time and surface finish of Inconel 800 during wire electro discharge cutting." *Meas. J. Int. Meas. Confed.*, 107, 19–30.

Mali, H.S., and Unune, D.R. (2017). "Machinability of Nickel-Based Superalloys: An Overview." Reference Module in Materials Science and Materials Engineering, https://doi.org/10.1016/B978-0-12-803581-8.09817-9.

Mandal, A., Dixit, A.R., Chattopadhyaya, S., Paramanik, A., Hloch, S. and Królczyk, G. (2017). "Improvement of surface integrity of Nimonic C 263 super alloy produced by WEDM through various post-processing techniques." *Int. J. Adv. Manuf. Technol.*, 93, 433–443. https://doi.org/10.1007/s00170-017-9993-x.

Mandal, A., Dixit, A.R., Das, A.K. and Mandal, N. (2016). "Modeling and Optimization of Machining Nimonic C-263 Superalloy using Multicut. Strategy in WEDM." *Mater. Manuf. Process.*, 31(7), 860-868, DOI: 10.1080/10426914.2015.1048462.

Manikandan, K., Ranjith kumar, P., kumar, D.R., and Palanikumar, K. (2020). "Machinability evaluation and comparison of Incoloy 825, Inconel 603 XL, Monel K400 and Inconel 600 super alloys in wire electrical discharge machining." *J. Mater. Res. Technol.*, 9(6), 12260-12272.

Manikandan, N., Balasubramanian, K., Palanisamy, D., Gopal, P.M., Arulkirubakaran, D., and Binoj, J.S. (2019). "Machinability Analysis and ANFIS modelling on Advanced Machining of Hybrid Metal Matrix Composites for Aerospace Applications." *Mater. Manuf. Process.*, 34(16), 1866-1881. DOI: 10.1080/10426914.2019.1689264.

Manjaiah, M., and Laubscher, R.F. (2017). "Study on recast layer thickness and residual stress during WEDM of SMAs." *Emerg. Mater. Res.*, 6(1), 82-88.

Manjaiah, M., Narendranath, S., Basavarajappa, S., and Gaitonde, V.N. (2018). "Investigation on material removal rate, surface and subsurface characteristics in wire electro discharge machining of Ti50Ni50-xCux shape memory alloy." *Proc. Inst. Mech. Eng. L*, 232(2), 164-177.

Manjaiah, M., Narendranath, S., Basavarajappa, S., and Gaitonde, V.N. (2015). "Investigation on material removal rate, surface and subsurface characteristics in wire electro discharge machining of Ti50Ni50-xCux shape memory alloy." Proc. Inst. Mech. Eng., 232 (2), 164-177.

Martowibowo, S. Y., and Wahyudi, A. (2012). "Taguchi Method Implementation in Taper Motion Wire EDM Process Optimization" *J. Inst. Eng. (India): C*, 93(4), 357–364. doi: 10.1007/s40032-012-0043-z.

Masanori Kunieda, and Chika Furudate, (2001). "High Precision Finish Cutting by Dry WEDM." *CIRP Ann.*, 50(1), 121-124, ISSN 0007-8506.

Mouralova, K., Benes, L., Bednar, J., Zahradnicek, R., Prokes, T., Matousek, R., Hrabec, P., Fiserova, Z., and Otoupalik, J. (2019). "Using a DoE for a comprehensive analysis of the surface quality and cutting speed in WED-machined had field steel." *J. Mech. Sci. Technol.*, 33(5), 2371-2386.

Mouritz, A.P. (2012). "Introduction to Aerospace Materials." 12 - Superalloys for gas turbine engines, *Woodhead Publishing*, 251-267, ISBN 9781855739468.

Mouritz, A.P. (2012). "Introduction to Aerospace Materials." Woodhead Publishing, 251-267.

Muhammad Wasif, Syed A. Iqbal, Anis Fatima, Saima Yaqoob, and Muhammad Tufail, Experimental investigation for the effects of wire EDM process parameters over the tapered cross-sectional workpieces of titanium alloys (Ti6Al-4V). *Mech. Sci.*, 11, 221–232, 2020.

Mukhuti, A., Rout A., and Tripathy, S. (2016). "Optimization of INCONEL 600 using wire EDM by MOORA and Taguchi's method." *International Conference on Electrical, Electronics, and Optimization Techniques*, 1577-1582.

Müller, F., and Monaghan, J. (2000). "Non-conventional machining of particle reinforced metal matrix composite." *Int. J. Mach. Tools Manuf.*, 40(9), 1351-1366, ISSN 0890-6955.

Mussada, E.K., Hua, C.C., and Rao, A.K.P. (2018). "Surface hardenability studies of the die steel machined by WEDM." *Mat. Manuf. Process.*, 33(16), 1745-1750, DOI: 10.1080/10426914.2018.1476695.

Nain, S.S., Sihag, P., and Luthra,S. (2018). "Performance evaluation of fuzzy-logic and BP-ANN methods for WEDM of aeronautics super alloy." *Methods X*, 5, 890-908.

Nair, A., and Kumanan, S. (2018). "Optimization of size and form characteristics using multi-objective grey analysis in abrasive water jet drilling of Inconel 617." *J. Braz. Soc. Mech. Sci. Eng.*, 40(12), pp.1-15.
Nair, A., and Kumanan, S. (2018). "Optimization of size and form characteristics using multi-objective grey analysis in abrasive water jet drilling of Inconel 617." *J. Braz. Soc. Mech. Sci. Eng.*, 40(121), 1-15.

Nani, V.M. (2017). "Complex phenomena study in dielectric fluid from gap during the W-EDM processing in ultrasonic field." *Int. J. Adv. Manuf. Technol.*, 92, 197–215.

Naveed, R., Mufti, N.A., Ishfaq, K., Ahmed, N., and Khan, S.A, (2019). "Complex taper profile machining of WC-Co composite using wire electric discharge process: analysis of geometrical accuracy, cutting rate, and surface quality." *Int. J. Adv. Manuf. Technol.*, 105, 411–423.

Naveed, R., Mufti,N.A., Mughal,M.P., Saleem, M.Q., and Ahmed, N. (2017). "Machining of curved profiles on tungsten carbide-cobalt composite using wire electric discharge process." *Int. J. Adv. Manuf. Technol.*, 93, 1367–1378.

Nayak, B.B., and Mahapatra, S.S. (2016). "Optimization ofWEDM process parameters using deep cryo-treated Inconel 718 as work material." *Int. J. Eng. Sci. Technol.*, 19 (2016) 161–170.

Newton, T.R., Melkote, S.N., Watkins, T.R., Trejo, R.M., and Reister, L. (2009). "Investigation of the effect of process parameters on the formation and characteristics of recast layer in wire-EDM of Inconel 718." *Mater. Sci. Eng. A*, 513–514, 208-215.

Nowotnik, A. (2016). "Nickel-Based Superalloys", Reference module in materials science and materials engineering, ISBN 9780128035818, (link: http://www.sciencedirect.com/science/article/pii/B9780128035818025741).

Orinakova, R., Turonova, A., Kladekova, D., Galova, M., and Smith, R.A. (2006). "Recent developments in the electrodeposition of nickel and some nickel-based alloys." *J. Appl. Electrochem.*, 36, 957–972 https://doi.org/10.1007/s10800-006-9162-7.

Ott,E., Bank, A., Anderson, J., Dempster, I., Gabb, T., Groh, J., Heck, K., Helmink, R., Liu, X., and Wusatowska- Sarnek, X. (2014). "Proceedings of the 8th International

Symposium on Superalloy 718 and Derivatives, The Minerals, M.M.S.9781119016601, 1-927 https://books.google.co.in/books?id=pgm4DQAAQBAJ.

Ozel, T., and Arisoy, Y.M. (2014). "Experimental and Numerical investigations on machining induced surface integrity in Inconel-100 nickel-base alloy." *Procedia CIRP*, 13, 302–307.

Padhi, P. C., Mahapatra, S. S., Yadav, S. N., and Tripathy, D. K. (2016). "Multi-Objective Optimization of Wire Electrical Discharge Machining (WEDM) Process Parameters Using Weighted Sum Genetic Algorithm Approach." *Int. J. Adv. Manuf. Syst.*, 15(2), 85-100.

Phate, M.R., and Toney, S.B. (2019). "Modeling and prediction of WEDM performance parameters for Al/SiCp MMC using dimensional analysis and artificial neural network." *Int. J. Eng. Sci. Technol.*, 22(2), 468-476.

Plaza, S., Ortega, N., Sanchez, J. A., Pombo I., and Mendikute, A. (2009). "Original models for the prediction of angular error in wire-EDM taper-cutting." *Int. J. Adv. Manuf. Syst.*, 44(5–6), 529–538. doi: 10.1007/s00170-008-1842-5.

Podder, B., and Paul, S. (2008). "Effect of machining environment on machinability of Nimonic 263 during end milling with uncoated carbide tool." *Int. J. Min. Met. Mater.*, 3, 104–119.

Pramanik, A., Basak, A.K., Dixit, A.R., and Chattopadhyaya, S. (2018). "Processing of duplex stainless steel by WEDM." *Mater. Manuf. Process.*, 33(14), 1559-1567.

Pramanik, A., Islam, M.N., Basak, A.K., Dong, Y., Littlefair, G., and Prakash, C. (2019). "Optimizing dimensional accuracy of titanium alloy features produced by wire electrical discharge machining." *Mat. Manuf. Process.*, 34(10), 1083-1090, DOI:10.1080/10426914.2019.1628259.

Puri, A.B. and Bhattacharyya, B. (2003). "Modelling and analysis of the wire-tool vibration in wire-cut EDM." *J. Mater. Process. Technol.*, 141(3), 295–301.

Puri, A.B., and Bhattacharyya, B. (2003). "An analysis and optimisation of the geometrical inaccuracy due to wire lag phenomenon in WEDM." *Int. J. Mach. Tool. Manu.*, 43, 151–159.

Rabinovich, S.G. (2006). Measurement Errors and Uncertainties. Theory and Practice. 3rd edition.

Rahim Jafari, Müge Kahya, Samad Nadimi Bavil Oliaei, Hakkı Özgür Ünver & Tuba Okutucu Özyur Modeling and analysis of surface roughness of microchannels produced by μ-WEDM using an ANN and Taguchi method. *J. Mech. Sci. Technol.*, 31, 5447–5457 (2017).

Rajyalakshmi, G. and Ramaiah, P.V. (2013). "Multiple process parameter optimization of wire electrical discharge machining on Inconel 825 using Taguchi grey relational analysis." *Int. J. Adv. Manuf. Technol.*, 69(5–8), 1249–1262.

Ramakrishnan, R., and Karunamoorthy, L. (2008). "Modeling and multi-response optimization of Inconel 718 on machining of CNC WEDM process." *J. Mater. Process. Technol.*, 207(1–3), 343-349.

Ranganath, S., Guo, C., and Hegde, P. (2009). "A finite element modeling approach to predicting white layer formation in nickel superalloys." *CIRP Ann. Manuf. Technol.*,58, 77–80.

Rao, M.S. and Venkaiah, N. (2015). "Parametric Optimization in Machining of Nimonic-263 Alloy using RSM and Particle Swarm Optimization." *Procedia Mater. Sci.*, 10, 70–79.

Razak, N.H., Rahman, M.M., and Kadirgama, K. (2012). "Response surface design model to predict surface roughness when machining Hastelloy C-2000 using uncoated carbide insert." *IOP Conf. Ser. Mat. Sci. Eng.*, 36, 12–22.

Razak, N.H., Rahman, M.M., and Kadirgama, K. (2014). "Experimental Study on Surface Integrity In End Milling Of Hastelloy C-2000 Superalloy." *Int. J. Automot. Mech. Eng.*, 9, 1578-1587.

Razzell, A.G. (2000). "Joining and Machining of Ceramic Matrix Composites." *Compre. Compos. Mater.* , Pergamon, 689-697, ISBN 9780080429939.

Read, B. E. Z. and Zenyth, B. A. (2010) 'Operating Manual for the Pulse Generator: ELPULS 15', Electronica Machine Tools Ltd., 1–20.

Reddy, V.C, Gowd, G.H., and Deva Kumar, M.L.S. (2018). "Empirical Modeling & Optimization of Laser Micro - Machining Process Parameters Using Genetic Algorithm." *Mater. Today: Proc.*, 5(2), 8095-8103.
Reddy, V.C., Gowd, G.H., and Kumar, M.L.S.D. (2018). "Empirical Modeling & Optimization of Laser Micro - Machining Process Parameters Using Genetic Algorithm", *Mater. Today*, 5 (2), 8095-8103.

Rees, A., Brousseau, E., Dimov, S. S., Bigot, S., and Griffiths, C. A. (2013). "Development of surface roughness optimisation and prediction for the process of wire electro-discharge grinding." *Int. J. Adv. Manuf. Technol.*, 64(9–12), pp. 1395–1410.

Reolon, .L.W., Laurindo, C.A.H., Torres, R.D., and Amorim, F.L. (2019). "WEDM performance and surface integrity of Inconel alloy IN718 with coated and uncoated wires." *Int. J. Adv. Manuf. Syst.*, 100, 1981–1991.

Roy A., and Narendranath, S. (2019). "Influence of dielectric flushing conditions during WEDM of TiNiCu shape memory alloys." *Emerg. Mater. Res.*, 8, 3, 376-386.

Saha, P., Singha, A., Pal, S.K., and Saha, P. (2008). "Soft computing models based prediction of cut-ting speed and surface roughness in wire electro-discharge machining of tungsten carbide cobalt composite." *Int. J. Adv. Manuf. Tech.*, 39, 74–84.

Sakar, S., Sekh, M., Mitra, S., and Bhattacharyya, B. (2011). "A novel method of determination of wire lag for enhanced profile accuracy in WEDM," *Precis. Eng.*, 35, 339-347.

Saleh, M., Anwar, S., El-Tamimi, A., Mohammed, M.K., and Ahmad, S. (2020). "Milling Microchannels in Monel 400 Alloy by Wire EDM: An Experimental Analysis." *Micromachines*, 11(5), 469. https://doi.org/10.3390/mi11050469.

Samanta, A., Sekh, M., and Sarkar, S. (2016). "Influence of different control strategies in wire electrical discharge machining of varying height job." *Int. J. Adv. Manuf. Technol.*, 100(5-8), 1299–1309.

Sanchez, J. A., Plaza, S., Ortega, N., Marcos, M. and Albizuri, J. (2008). "Experimental and numerical study of angular error in wire-EDM taper-cutting." *Int. J. Mach. Tools Manuf.*, 48(12–13), 1420–1428. doi: 10.1016/j.ijmachtools.2008.04.011.

Sanchez, J.A., Rodil, J.L., Herrero, A., Lacalle, L.N.L., and Lamikiz, A. (2007). "On the influence of cutting speed limitation on the accuracy of wire-EDM corner-cutting." *J. Mater. Process. Technol.*, 182(1–3), 574–579. doi: 10.1016/j.jmatprotec.2006.09.030.

Sarkar, S., Ghosh, K., Mitra, S., and Bhattacharyya, B. (2010). "An integrated approach to optimization of WEDM combining single-pass and multipass cutting operation." *Mater. Manuf. Process.*, 25(8), 799–807. doi: 10.1080/10426910903575848.

Sarkar, S., Mitra, S., Bhattacharyya B. (2006). "Parametric optimisation of wire electrical discharge machining of γ titanium aluminide alloy through an artificial neural network model." *Int. J. Adv. Manuf. Technol.*, 27, 501–508. DOI 10.1007/s00170-004-2203-7.

Sarkheyli, A., Zain, A. M., and Sharif, S. (2015). "A multi-performance prediction model based on ANFIS and new modified-GA for machining processes." *J. Intell. Manuf.*, 26(4), 703–716.

Selvakumar, G., and Thiruppathi Kuttalingam, K.G., Selvaraj, M., and Manohar, J. (2018). "Enhancing die corner accuracy using path modification strategy in wire electrical discharge machining of Monel 400." *Proc. Inst. Mech. Eng. C*, 232(2), 207-216.

Selvakumar, G., Jiju, K. B. and Veerajothi, R. (2016). "Experimental Study on Wire Electrical Discharge Machining of Tapered Parts", *Arab. J. Sci. Eng.*, 41(11), 4431–4439. doi: 10.1007/s13369-016-2145-z.

Selvakumar, G., Jiju, K.B., Sarkar, S., and Mitra, S. (2016). "Enhancing die corner accuracy through trim cut in WEDM." *Int. J. Adv. Manuf. Technol.*, 83:791-803.

Selvakumar, G., Kuttalingam, K.G.T., and Prakash, S.R. (2018). "Investigation on machining and surface characteristics of AA5083 for cryogenic applications by adopting trim cut in WEDM." *J. Braz. Soc. Mech. Sci. Eng.*, 40, 1-8.

Sen, R., Choudhuri, B., Barma, J.D., and Chakraborti, P (2020). "Surface integrity study of WEDM with various wire electrodes: experiments and analysis." *Mach. Sci. Technol.*, 24(4), 569-591, DOI: 10.1080/10910344.2019.1701019.

Shahane S., and S. S. Pande, (2016). "Development of a Thermo-Physical Model for Multi-spark Wire EDM Process," *Procedia Manuf.*, vol. 5, pp. 205–219.

Shahane, S., and Pande, S. S. (2016). "Development of a Thermo-Physical Model for Multi-spark Wire EDM Process." *Procedia Manuf.*, 5, 205–219. doi: 10.1016/j.promfg.2016.08.019.

Shandilya, P., Jain, P.K., Jain, N.K. (2013) "RSM and ANN Modeling Approaches For Predicting Average Cutting Speed During WEDM of SiCp/6061 Al MMC." *Procedia Eng.*, 64, 767-774, https://doi.org/10.1016/j.proeng.2013.09.152.

Sharma, P., Chakradhar, D. and Narendranath S. (2015). "Evaluation of WEDM performance characteristics of Inconel 706 for turbine disk application." *Mater. Des.* , 88, 558–566.

Sharma, P., Chakradhar, D., and Narendranath S. (2018). "Analysis and Optimization of WEDM Performance Characteristics of Inconel 706 for Aerospace Application." *Silicon*, 10, 921–930. https://doi.org/10.1007/s12633-017-9549-6.

Sharma, P., Chakradhar, D., and Narendranath, S., (2016). "Effect of wire material on productivity and surface integrity of WEDM-processed Inconel 706 for aircraft application." *J. Mater. Eng. Perform.* , 25(9), 3672-3681.

Sharman, A. R. C., Hughes, J. I., and Ridgway K. (2004). "Workpiece Surface Integrity and Tool Life Issues When Turning Inconel 718™ Nickel Based Superalloy." *Mach. Sci. Technol.*, 8(3), 399-414.

Sharman, A.R.C., Amarasinghe, A., Ridgway, K. (2008). "Tool life and surface integrity aspects when drilling and hole making in Inconel 718." *J. Mater. Process. Technol.*, 200(1–3), 424-432.

Sharman, A.R.C., Hughes, J.J., and Ridgway, K. (2004). "Workpiece Surface Integrity and Tool Life Issues When Turning Inconel 718™ Nickel Based Superalloy." *Mach. Sci. Technol.*, 8(3), 399-414.

Shinde, B., and Pawade, R. (2020). "Study on analysis of kerf width variation in WEDM of insulating zirconia." *Mater. Manuf. Process.*, 1010-1018. DOI: 10.1080/10426914.2020.1854468.

Shrivastava, P.K., and Pandey, A.K., (2018). "Geometrical quality evaluation in laser cutting of Inconel-718 sheet by using Taguchi based regression analysis and particle swarm optimization." *Infrared Phys. Technol.*, 89, 369-380.

Sines, G., and Carlson, R. (1952). "Hardness measurement for determination of residual stress." *Bull. Amer. Soc. Testing. Mater.* , 180, 35– 3.

Singh, B., and Misra, J.P. (2019). "Surface finish analysis of wire electric discharge machined specimens by RSM and ANN modelling." *Meas.: J. Int. Meas. Confed.*, 137, 225-237.

Singh, M.A., Das, K., and Sarma, D.K. (2018). "Thermal simulation of machining of alumina with wire electrical discharge machining process using assisting electrode." *J. Mech. Sci. Technol.*, 32, 333–343. https://doi.org/10.1007/s12206-017-1233-7.

Singh, M.A., Sarma, D.K., Hanzel, O., Sedláček, J., and Šajgalík, P. (2017). "Machinability analysis of multi walled carbon nanotubes filled alumina composites in wire electrical discharge machining process." *J. Eur. Ceram. Soc.*, 37(9), 3107-3114.

Soni, H., Narendranath, S., and Ramesh M. R. (2019). "Effects of Wire Electro-Discharge Machining Process Parameters on the Machined Surface of Ti50Ni49Co1 Shape Memory Alloy." *Silicon*, 11, 733–739.

Soni, H., Narendranath, S., and Rangarasaiah, R.M. (2017). "An experimental study of influence of wire electro discharge machining parameters on surface integrity of TiNiCo shape memory alloy." *J. Mater. Res.*, 2017, 1-9.

Sreenivasa Rao, M., and Venkaiah, N. (2015). "Parametric Optimization in Machining of Nimonic-263 Alloy using RSM and Particle Swarm Optimization." *Procedia Mater. Sci.*, 10, 70–79.

Straka, L., Čorný, I., Pitel, J., (2017). "Prediction of the Geometrical Accuracy of the Machined Surface of the Tool Steel EN X30WCrV9-3 after Electrical Discharge Machining with CuZn37 Wire Electrode." *Metals*, 7(11), 462, 2-19.

Sun, Y., Gong, Y., Cheng, J., and Cai, M. (2018). "Experimental investigation on carbon steel micro-rod machining by LS-WEDT." *Mater. Manuf. Process.*, 33(6), 597-605, DOI: 10.1080/10426914.2017.1339313.

Suresh Kumar, S., Erdemir, F., Varol, T., Thirumalai Kumaran, S., Uthayakumar, M., and Canakci, A. (2020). "Investigation of WEDM process parameters of AleSiCeB4C composites using response surface methodology." *Int. J. lightweight mater. manuf.*, 3, 127-135.

Thakur, A., and Gangopadhyay, S. (2016). "State of the art in surface integrity in machining of nickel based super alloys." *Int. J. Mach. Tools Manuf.*, 100, 25-54.

Thakur, A., Gangopadhyay, S., and Mohanty, A. (2015). "Investigation on Some Machinability Aspects of Inconel 825 during Dry Turning." *Mater. Manuf. Process.*, 30, 1026–1034.

Thakur, A., Mohanty, A., and Gangopadhyay, S. (2014). "Comparative study of surface integrity aspects of Incoloy 825 during machining with uncoated and CVD multilayer coated inserts." *Appl. Surf. Sci.*, 320, 829-837.

Tosun, N. (2003). "The effect of the cutting parameters on performance of WEDM." *KSME Int. J.*, 17, 816–824. https://doi.org/10.1007/BF02983395.

Vishnu Vardhana Naidu B, Varaprasad, K. C., and Prahlada Rao, K. (2021). "Machinability analysis on wire electrical discharge machining of stir casted AA2024/Al2O3/BN hybrid composite for aerospace applications." *Mater. Manuf. Process.*, DOI:10.1080/10426914.2020.1854466.

Wang, Y., He, D., Yang, L., and Xiong, W. (2017). "Formation mechanism of surface topography in low-speed wire electrical discharge machining Inconel 718 and its on-line prediction based on acoustic emission technology." *Adv. Mech. Eng.*, 9(4), 1–17.

Wasif, M., Iqbal, S.A., Fatima, A., Yaqoob, S., and Tufail, M. (2020). "Experimental investigation for the effects of wire EDM process parameters over the tapered cross-sectional workpieces of titanium alloys (Ti6Al-4V)" *Mech. Sci.*, 11, 221–232, https://doi.org/10.5194/ms-11-221-2020.

Wei, X. (2002). "Experimental study on the machining of a shaped hole in Ni-based super-heat-resistant alloy." *J. Mater. Process. Technol.*, 129(1–3), 143-147.

Wright, P.K., and Chow, J.G. (1982). "Deformation characteristics of nickel alloys during machining." *J. Eng. Mater. Technol.*, 104, 85–93.

Y.H. Guu (2005). "AFM surface imaging of AISI D2 tool steel machined by the EDM process." Appl. Surf. Sci. 242, 245–250.

Yan, H., Bakadiasa, K.D., Chen, Z., Yan, Z., Zhou, H., and Han, F. (2020). "Attainment of high corner accuracy for thin-walled sharp-corner part by WEDM based on magnetic field-assisted method and parameter optimization." *Int. J. Adv. Manuf. Technol.*, 106, 4845–4857.

Yan, M. T., and Fang, C. C. (2008). "Application of genetic algorithm-based fuzzy logic control in wire transport system of wire-EDM machine." *J. Mater. Process. Technol.*, 205(1–3), 128–137. doi: 10.1016/j.jmatprotec.2007.11.091.

Yan, M. T., and Huang, P. H. (2004). "Accuracy improvement of wire-EDM by real-time wire tension control." *Int. J. Mach. Tools Manuf.*, 44(7–8), 807–814. doi: 10.1016/j.ijmachtools.2004.01.019.

Yueqin, Z., Zhidong, L, Lixia, X., and Wei, W. (2016). "Interelectrode discharge mechanism in high-speed wire electrical discharge machining." *Int. J. Adv. Manuf. Technol.*, 84, 2637–2647. https://doi.org/10.1007/s00170-015-7891-7.

Yusoff, Y., Zain, A.M., Amrin, A., Sharif, S., Haron, H., and Sallehuddin, R., (2019). "Orthogonal based ANN and multiGA for optimization on WEDM of Ti–48Al intermetallic alloys." *Artif. Intell. Rev.*, 52, 671–706.

Yusoff, Y., Zain, A.M., Sharif, S., Sallehuddin, R., and Ngadiman, M.S. (2018). "Potential ANN prediction model for multiperformances WEDM on Inconel 718." *Neural. Comput. Applic.* , 30, 2113–2127.

Zhang, G., Li, H., Zhang, Z., Ming, W., Wang, N., and Huang, Y. (2016). "Vibration modeling and analysis of wire during the WEDM process." *Int. J. Adv. Manuf. Technol.*, 20, 173-186.

Zhang, Z., Huang, H., Ming, W., Xu, Z., Huang, Y., and Zhang, G. (2016). "Study on machining characteristics of WEDM with ultrasonic vibration and magnetic field assisted techniques." *J. Mater. Process. Technol.*, 234, 342-352.

Zhang, Z., Ming, W., Huang, H., Chen, Z., Xu,Z., Huang, Y, and Zhang, G. (2015). "Optimization of process parameters on surface integrity in wire electrical discharge machining of tungsten tool YG15." *Int. J. Adv. Manuf. Technol.*, 81, 1303–1317.

Zhu, Y., Farhadi, A., He, G., Liang, T., Gu, L., and Zhao, W. (2018). "High-efficiency machining of large aspect-ratio rotational parts by rapid contour approaching WEDM." *Int. J. Adv. Manuf. Technol.*, 94 (9–12), 3577–3590.

APPENDIX I

CNC PROGRAM FOR TRIANGULAR, SQUARE AND CIRCULAR PROFILE SLOTS

The programs used for cutting three profile shapes at different taper angles were as follows.

1. Triangular Profile

; 8.11.2018, 08:47:48

G71

G9

G27

G40

G47

G50

G90

G75

; Wire Compensation Definitions

D0=0

D1=0 ;(Offset Valves Given =0, 0.4, 0.8, 1.2)

;#1.0 Cavity=1 Rough-cut

G0 X-0.048673 Y0.084638 U0 V0

M0

G41 D0 ;D0=0

G1 X0 Y0.084638

G41 D1 ;D1= Offset values set

G1 X0 Y3.25

G1 X-2 Y3.25

G1 X-2 Y3
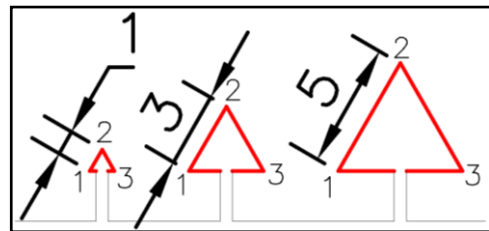
Programmed Triangular Profile

223

G1 X-2.87 Y3.5

G1 X-2 Y4

G1 X-2 Y3.75

G1 X0 Y3.75

G1 X0 Y8.25

G1 X-2 Y8.25

G1 X-2 Y7

G1 X-4.6 Y8.5

G1 X-2 Y10

G1 X-2 Y8.75

G1 X0 Y8.75

G1 X0 Y15.25

G1 X-2 Y15.25

G1 X-2 Y13

G1 X-6.33 Y15.5

G1 X-2 Y18

G1 X-2 Y15.75

G1 X0 Y15.75

G1 X0 Y25

M0

G41 D0 ;D0=0

G1 X0.020606 Y25.004429

G40

M0

2. Square Profile

; 9. 1.2019, 10:56:33

G71

G9

G27

G40

G47

G50

G90

G75

; Wire Compensation Definitions

D0=0

D1=0 ;(Offset Valves Given =0, 0.4, 0.8, 1.2)

;#1.0 Cavity=1 Rough-cut

G0 X0 Y0 U0 V0

M0

G41 D0 ;D0=0

G1 X0 Y3.25

G41 D1 ;D1= Offset values set

G1 X-2 Y3.25

G1 X-2 Y3

G1 X-3 Y3

G1 X-3 Y4

G1 X-2 Y4

G1 X-2 Y3.75

G1 X0 Y3.75

G1 X0 Y8.25
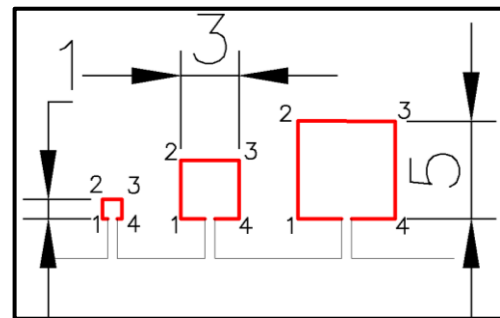
G1 X-2 Y8.25

G1 X-2 Y7

Programmed Square Profile

G1 X-5 Y7

G1 X-5 Y10

G1 X-2 Y10

G1 X-2 Y8.75

G1 X0 Y8.75

G1 X0 Y15.25

G1 X-2 Y15.25

G1 X-2 Y13

G1 X-7 Y13

G1 X-7 Y18

G1 X-2 Y18

G1 X-2 Y15.75

G1 X0 Y15.75

G1 X0 Y22

G1 X0 Y21.946291

M0

G41 D0 ;D0=0

G1 X0.003084 Y21.880896

G40

M0

3. Circular Profile

; 10. 1.2019, 09:00:28

G71

G9

G27

G40

G47

G50

G90

G75

; Wire Compensation Definitions

D0=0

D1=0 ;(Offset Valves Given =0, 0.4, 0.8, 1.2)

;#1.0 Cavity=1 Rough-cut

G0 X0 Y0 U0 V0

M0

G41 D0 ;D0=0

G1 X0 Y2

G41 D1 ;D1= Offset values set

G1 X-2 Y2

G2 X-2 Y2.5 I-1 J0.25

G1 X0 Y2.5

G1 X0 Y7

G1 X-2 Y7

G2 X-2 Y7.5 I-3 J0.25

G1 X0 Y7.5

G1 X0 Y16

G1 X-2 Y16

G2 X-2 Y16.5 I-5 J0.25
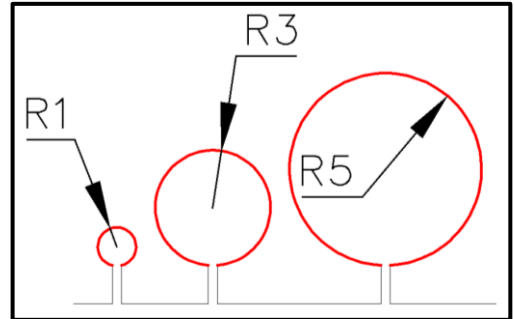
Programmed Circular Profile

227

G1 X0 Y16.5

M0

G41 D0 ;D0=0

G1 X0 Y22

G40

M0

LIST OF PUBLICATIONS

Sl. No.	Title of the paper	Authors (in the same order as in the paper. Underline the Research Scholar's name)	Name of the Journal/ Conference/ Symposium, Vol., No.,	Month & Year of Publication	Category *
1	Investigation on the effect of variation in cutting speeds and angle of cut during slant type taper cutting in WEDM of Hastelloy X	**I.V.Manoj**, Ranjit Joy and Narendranath S	Arabian Journal for Science and Engineering **(SCIE&SCOPUS) (IM-1.518)**	**September 2019**	1
2	Variation and artificial neural network prediction of profile areas during slant type taper profiling of triangle at different machining parameters on Hastelloy X by WEDM	**I.V.Manoj**, and Narendranath S	Journal of Process Mechanical Engineering. **(SCIE&SCOPUS) (IM-1.606)**	**July 2020**	1
3	Slant type taper profiling and prediction of profiling speed for a circular profile during in wire electric discharge machining using Hastelloy-X.	**I.V.Manoj**, and Narendranath S	Journal of Mechanical Engineering Science **(SCIE&SCOPUS) (IM-1.386)**	**March 2021**	1
4	Evaluation of WEDM performance characteristics and prediction of machining speed during taper square profiling on Hastelloy-X	**I.V.Manoj**, and Narendranath S	Australian Journal of Mechanical Engineering **(ESCI&SCOPUS) (IM-0.75)**	**July 2021**	1
5	Performance of profile characteristics at different machining parameters during wire electric discharge slant type taper profiling on Nicrofer 4722	**I.V.Manoj**, and Narendranath S	International Journal of Machining and Machinability of Materials Inderscience (Submitted)	**Under Review**	1

6	Wire Electric Discharge Machining at Different Slant angles during Slant Type Taper Profiling of Microfer 4722 Superalloy.	**I.V.Manoj**, and Narendranath S	Journal of Materials Engineering and Performance **(SCIE&SCOPUS)** **(IM-1.5)**	**August 2021**	1
7	Optimization and prediction of responses using ANN and ANFIS during taper profiling on Pyromet-680 using WEDM.	**I.V.Manoj,** Manjaiah.M, Narendranath S.	Journal of Materials Engineering and Performance **(SCIE&SCOPUS)** **(IM-1.5)**	**June 2022**	1
8	Examination of machining parameters and prediction of cutting velocity and surface roughness using RSM and ANN using WEDM of Altemp HX	**I.V.Manoj,** Hargovind Soni, Narendranath S, P M Mashinini, Fuat KARA	Advances in Materials Science and Engineering **(SCIE & SCOPUS)** **(IM-1.75)**	**January 2022**	1
9	Optimization and prediction of machining responses using response surface methodology and adaptive neural network by wire electric discharge machining of Alloy-X	**I.V.Manoj**, Narendranath S and Alokesh Pramanik	**Materials Science Forum (SCOPUS)**	**April 2021**	3
10	Investigation of machining parameters on corner accuracies for slant type taper triangle shaped profiles using WEDM on Hastelloy X.	**I.V.Manoj,** Ranjit Joy Narendranath S and Dumitru Nedelcu	Modern Technologies in Industrial Engineering, 2019, Iasi, Romania, June 19-22. (IOP Conference Series: Materials Science and Engineering) **(SCOPUS)**	**August 2019**	3
11	Investigation of cutting speed, recast layer and micro-hardness in angular machining using slant type taper fixture by WEDM of Hastelloy X	Ranjit Joy, **I.V.Manoj** and Narendranath S	Materials and Manufacturing Methods, 2019, NIT Trichy, July 05 – 07 (Materials Today: Proceedings) **(SCOPUS)**	**October 2019**	3

12	Analysis and Prediction of Cutting Speed for machining Slant triangular slot on Hastelloy X using WEDM.	**I.V.Manoj**, Narendranath S and Alokesh Pramanik	5th International Conference on Materials and Reliability, 2019, Maison Glad Jeju, Jeju, Republic of Korea. November 27-29.	**Abstract Accepted and presented**	4
13	Influence of machining parameters on taper square areas during slant type taper profiling using wire electric discharge machining	**I.V.Manoj** and Narendranath S	International Conference on Advances in Materials Processing & Manufacturing Applications (iCADMA 2020), NMIT Jaipur, November 05-06, 2020 (IOP Conference Series: Materials Science and Engineering) **(SCOPUS)**	**September 2020**	3
14	Effect of Profile Geometry and Cutting Speed Override Parameter on Profiling Speed During Tapering Using Wire Electric Discharge Machining	**I.V.Manoj** and Narendranath S	National Conference on Sustainable Machining Strategies for Better Performance (NCSMSBP 2020), NMIT funded by AICTE, New Delhi November 27 – 28, 2020 (Book Chapter:Lecture Notes in Mechanical Engineering by Springer) **(SCOPUS)**	**Accepted (3rd November 2020)**	3
15	Parametric Analysis and Response Surface Optimization of Surface Roughness and Cutting Rate in the Machining Using WEDM	**I.V.Manoj** and Narendranath S	Indo-Korean workshop on Multi-Functional Materials for Extreme Loading (Book Chapter Springer Nature: Composite Materials for Extreme Loading - Impact Mechanics, Composite Analysis.) **(SCOPUS)**	**Accepted**	3

16	Study and prediction of response parameter during oblique machining for different machining parameters by WEDM of Inconel-HX.	**I.V.Manoj** and Narendranath S	Advanced Materials and Manufacturing Processes (Book Chapter: Taylor and Francis) **(SCOPUS)**	**Accepted**	3
17	Machining and forecasting of square profile areas using artificial neural modelling at different slant angles by WEDM.	**I.V.Manoj** and Narendranath S	International Conference on Frontiers in Engineering, Science, and Technology (ICFEST-2020), Yenepoya Institute Of Technology on 18th and 19th December 2020. **(SCOPUS)**	**April 2021**	3
18	Assessment of wire electric discharge machining parameters and prediction of the areas of holes during machining using the artificial intelligent technique	**I.V.Manoj,** Hargovind Soni, P. M. Mashinini S.Narendranath	Artificial Intelligence and Machine learning in mechanical engineering **(SCOPUS)**	**Under Review**	3
19	Slant Type Taper Fixture	**I.V.Manoj** and Narendranath S	**Copyrights Diary Number:** 2378/2019-CO/L. **Reg. No:** L-81981/2019	**February 2019**	5

* Category: 1: Journal paper, full paper reviewed   2: Journal paper, Abstract reviewed

                   3: Conference/Symposium paper, full paper reviewed   4: Conference/Symposium paper, abstract reviewed

                   5: others (including papers in Workshops, NITK Research Bulletins, Short notes etc. (copyrights/patents).)

                   (If the paper has been accepted for publication but yet to be published, the supporting documents must be attached.)

Research Scholar: **Manoj.I.V**

Research Supervisor: **Dr. Narendranath S**

NAME: I.V.Manoj

FATHER'S NAME: Vijaya kumar. I

DATE OF BIRTH: 02/07/1990

NATIONALITY: Indian

PH. NO.: 919986754795, 917892606260

EMAIL ID.: vishalmanojvs@gmail.com, vishalmanojvs.177me006@nitk.edu.in

ADDRESS: D-608, Wing-2, Vaishnavi ARS Gardenia, No.2208, Subroto Mukherjee Road, T.Dasarahalli, Bengaluru, Karnataka 560057, India.

ACADEMIC CREDENTIALS

DEGREE	COLLEGE/INSTITUTE NAME	%/CPGA	YEAR OF PASSING
Ph.D (Manufacturing-Machining)	National Institute of Technology, Karnataka, India	84%/8.75 (FCD)	**Thesis submitted on** Dec-2021
M-Tech (Product Design and Manufacturing)	R.V.College Of Engineering, Bangalore, India.	78.03%/8.21 (FCD)	July-2015
B.E (Mechanical)	Acharya Institute Of Technology, Bangalore, India.	73.88%/7.78 (FCD)	Jun-2012
PUC (PCMB)	Christ College, Bangalore India.	72%/7.58 (FCD)	May-2008
10th(SSLC)	Christ School, Bangalore India.	87.68%/9.23 (FCD)	Mar-2006

PROFESSIONAL EXPERIENCE

ORGANIZATION/INSTITUTE	DESIGNATION	DURATION
Johson & Smith Co.	Maintenance Officer (grade-1)	01/06/2012-30/09/2013
CSIR-National Aerospace Laboratories (Propulsion Lab)	Project Student	01/05/2014-31/05/2015
Dayananda Sagar College of Engineering	Assistant Professor	20/07/2015-06/07/2017

AREA OF INTEREST

Nickel Based Super Alloys, Foil Bearings, Product Design and Development, and Non-conventional Machining.

DECLARATION

I hereby declare that the above information is true to the best of my knowledge and belief.

Place: Bangalore
Date: 22nd December 2021

(I.V.Manoj)

5% match (publications)
I. V. Manoj, Ranjit Joy, S. Narendranath. "Investigation on the Effect of Variation in Cutting Speeds and Angle of Cut During Slant Type Taper Cutting in WEDM of Hastelloy X", Arabian Journal for Science and Engineering, 2019

4% match (publications)
I. V. Manoj, S. Narendranath. "Wire Electric Discharge Machining at Different Slant Angles during Slant Type Taper Profiling of Microfer 4722 Superalloy", Journal of Materials Engineering and Performance, 2021

2% match (publications)
"Sustainable Machining Strategies for Better Performance", Springer Science and Business Media LLC, 2022

2% match (publications)
IV Manoj, S Narendranath. "Variation and artificial neural network prediction of profile areas during slant type taper profiling of triangle at different machining parameters on Hastelloy X by wire electric discharge machining", Proceedings of the Institution of Mechanical Engineers, Part E: Journal of Process Mechanical Engineering, 2020

1% match (publications)
IV Manoj, S Narendranath. "Slant type taper profiling and prediction of profiling speed for a circular profile during in wire electric discharge machining using Hastelloy-X", Proceedings of the Institution of Mechanical Engineers, Part C: Journal of Mechanical Engineering Science, 2021

1% match (Internet from 13-Dec-2021)
https://idr.nitk.ac.in/jspui/bitstream/123456789/14216/1/135065ME13F05.pdf

1% match (Internet from 01-Feb-2022)
https://www.hindawi.com/journals/amse/2022/5192981/

<1% match (Internet from 02-Feb-2022)
https://idr.nitk.ac.in/jspui/bitstream/123456789/16894/2/ABHINABA%20ROY%20-%20155017ME15P01.pdf

<1% match (publications)
I V Manoj, R Joy, S Narendranath, D Nedelcu. "Investigation of machining parameters on corner accuracies for slant type taper triangle shaped profiles using WEDM on Hastelloy X", IOP Conference Series: Materials Science and Engineering, 2019

<1% match (student papers from 22-Sep-2016)
Submitted to Rochester Institute of Technology on 2016-09-22

<1% match (publications)
I.V. Manoj, S Narendranath. "Machining and forecasting of square profile areas using artificial neural modelling at different slant angles by WEDM.", IOP Conference Series: Materials Science and Engineering, 2021

<1% match (publications)
I.V. Manoj, S Narendranath. "Machining and forecasting of square profile areas using artificial neural modelling at different slant angles by WEDM.", IOP Conference Series: Materials Science and Engineering, 2021

<1% match (Internet from 13-Dec-2021)
https://link.springer.com/content/pdf/10.1007/978-981-16-4138-1.pdf?code=a9fc5551-4377-443d-9b8c-7562e6a5d271&error=cookies_not_supported

<1% match (Internet from 07-Mar-2022)
https://link.springer.com/article/10.1007/s10311-022-01401-4?code=e0e0a504-99ce-4189-8222-2ba22c307a24&error=cookies_not_supported

<1% match (Internet from 05-Dec-2019)
https://link.springer.com/article/10.1007%2Fs40430-018-1192-7

<1% match (Internet from 12-Feb-2020)
https://link.springer.com/article/10.1007%2Fs00170-012-4628-8

<1% match (Internet from 08-Oct-2020)
https://link.springer.com/chapter/10.1007%2F978-3-030-43232-4_2

<1% match (Internet from 31-Mar-2020)
https://es.scribd.com/document/362385609/Final-Thesis-612ME311

<1% match (Internet from 28-Apr-2020)
https://es.scribd.com/document/235308748/h3125

<1% match (publications)
I. V. Manoj, S Narendranath. "Influence of machining parameters on taper square areas during slant type taper profiling using wire electric discharge machining", IOP Conference Series: Materials Science and Engineering, 2021

<1% match (publications)